Coupled Resonator Decoupling Networks

for Compact Antenna Arrays

of Advanced Communication Systems

ZHAO, Luyu

UMI Number: 3691915

UMI

Dissertation Publishing

UMI 3691915

ProQuest®

Author's Declarations

I hereby declare that I am the sole author of this thesis.

I authorize the Chinese University of Hong Kong to lend this thesis to other institutions or individuals for the purpose of scholarly research.

Signature

I further authorize the Chinese University of Hong Kong to reproduce this thesis by photocopying or by other means, in total or in part, at the request of other institutions or individuals for the purpose of scholarly research.

Signature

Abstract

Developements in next-generation advanced communication systems and devices have triggered multi-antenna systems for improved data throughput and transmission reliability. According to Shannon's theorem, to improve the channel capacity of a communication system, one method is to broaden the system bandwidth. Another method is to use the multiple-input-multiple-output (MIMO) technology. This technology uses multiple antennas at both transmitter and receiver to improve the channel capacity by several folds. Therefore, compact and broadband multi-antenna systems are very promising for future high-capacity wireless communication systems.

In parallel to advances in MIMO technologies, there is an irreversible trend that more and more communication protocols together with their respective antennas and radio transceivers are integrated into one compact unit. The radio systems of different protocols may work in very closely adjacent frequency bands or even overlapped bands. The coexistence of these multiple antennas has also become a concern from both industry and academic communities

However, since the number of antenna elements is increasing in more and more compact devices, the physical limitation on inter-element spacing cannot be easily transcended, which will lead to destructive mutual coupling interference as well as pattern/spatial dependent correlation. In a multi-antenna system, the signals at all antenna ports are coded differently either to increase the packet rate or simply because that they belong to different radio transceivers. If unwanted signals are coupled to the ports, the signal-to-noise ratio will be deteriorated. Furthermore, the far-field patterns of closely spaced antennas are highly correlated and the signal envelope correlation will become significantly large. All these negative impacts will greatly diminish the channel capacity and the data throughput. Such drawbacks

restrain the use of multiple antenna systems. It is therefore vital to develop a simple, broadband and effective decoupling technique for compact multiple antenna systems/arrays in advanced communication systems.

The major objectives of this thesis are (1) to innovate a new antenna decoupling technique called shunt type of *coupled resonator decoupling networks (S-CRDNs)* for wireless mobile terminal antennas; (2) to develop the synthesis theory and the design methodologies of the shunt type of CRDNs (S-CRDN) for various of antenna arrays; (3) to extend the theory and the design concept to dual band S-CRDNs, three port S-CRDNs and a LTCC S-CRDN module for mobile terminal applications; (4) to develop a cascaded type of *coupled resonator decoupling networks* (C-CRDN) for base station and wireless routers antennas; (5) to innovate a novel decoupling technique for multiple element antenna arrays with dummy antennas arrays; and more importantly, (6) to explore innovative applications with experimentally verified superiority.

Based on the characteristics of the coupled antennas, the synthesis theory of S-CRDNs starts from a set of required admittance polynomials, the targeted coupling matrix can be obtained from the polynomials analytically for a second-order S-CRDN. Possible coupling topologies of S-CRDNs include, but not limited to, a second-order all pole S-CRDN, a second-order S-CRDN with source-load coupling, a high-order S-CRDN network for dual band applications and a three port S-CRDN for three-element antenna arrays. Moreover, the concept of a "one-fit-all" S-CRDN module base on LTCC technology is also proposed and investigated, which makes an integrated S-CRDN module antenna independent as long as the frequency range matches.

The general theory of C-CRDN is developed in this thesis based on the circuit model of a 4-port coupled resonators network, which is proposed to solve the

antenna decoupling problem between two base station antennas, to which a high level of isolation between two adjacent frequency bands is required, for the first time. This type of CRDN is particularly useful when one antenna transmitting very high power energy in a vicinity to a receiver antenna that works in an adjacent frequency band with very high sensitivity.

A decoupling technique with appropriately designed dummy elements and their passive complex loading is also proposed in this thesis. The technique employs the characteristics of non-radiating antenna elements (dummy elements). Multiple dummy elements can be introduced to alter the mutual coupling characteristic the radiating antennas in the original compact array. Therefore, this technique is more suitable for decoupling problem of an array with multiple elements. It is demonstrated that for a four-element compact array, four dummy elements are sufficient to decouple the four radiating elements in a broadband sense. Additionally, each radiating element can be independently matched. This decoupling technique can be extended to antenna arrays with a high number of radiating elements.

Finally, necessary and important figures of merit for benchmarking a multiple element antenna array are introduced. Prototypes of multi-antenna systems with and without using proposed decoupling techniques are fabricated, measured and compared. A large number of experimental results have demonstrated the superiority and the significance of the proposed decoupling techniques for compact antenna arrays of advanced wireless communication systems.

Key Words — **Antenna decoupling, Compact antenna array, Coupled Resonator, Co-located transceivers, Dual-band, Decoupling network, IEEE 802.11, In-Device Coexistence (IDC), interference suppression, LTE, LTE-Advanced, Low temperature co-fired ceramic (LTCC), multiple input multiple output (MIMO), mutual coupling, microwave multi-port network, network synthesis,**

Wi-Fi.

論文摘要

下一代無線通訊系統與設備的飛速發展，極大的促進了多天線系統的開發與應用。多天線系統天生具有高數據吞吐率，并能夠確保傳輸的穩定性。根據香農定律，若想要提高一個系統的信道容量，要麼可以展寬系統帶寬，要麼可以適用多輸入多輸出（MIMO）系統。MIMO 技術在發射端和接收端安置多個天線，以同時發送多路數據，大大提高了數據的吞吐率和信道容量。理想的狀態下，信道容量隨著收發天線的個數可以線性成倍增加。因此，新一代的小型化多天線系統正在成為未來發展的趨勢。

與此同時，現今無線通訊系統的發展趨勢越來越朝著小型化，集成化以及多功能化發展。這就意味著，越來越多的通信協議及其收發機和天線，將會集成到一個越來越小的終端設備上。另外由於頻譜資源的稀缺，這些共同工作的系統的頻帶越來越寬，頻帶之間的距離也越來越近。這些多天線的共存問題，也日益成為學術界和工業界關心的焦點問題。

但是，當終端的尺寸越來越小，而天線的個數越來越多的時候，天線之間的物理距離這個瓶頸是無法逾越的。如此受限的距離，不但造成了天線之間的相互干擾較大，也造成了他們方向圖和信道的強相關。在多天線系統中，各個天線處的信號編碼是不同的（包括提高數據速率和提高通信可靠性兩種不同的模式）。如果無用的信號耦合到了不該到的端口或者天線處，就會極大的影響信噪比和通信質量。另外，如果多天線的方向圖和信道是相關的話，信號的包絡相關性就會變得異常的大。這些都是嚴重影響多天線系統的性能的因素。因此，設計一種簡單的，寬帶的，有效的解耦技術，對於多天線系統是至關重要的。

本論文的主要目標是：（1）開發一種新的天線解耦技術，叫做並聯型耦合諧振腔解耦網絡，專門針對手機終端。（2）研究針對此解耦網絡的綜合設計手段，以針對不同的多天線陣列，都能有效的設計。（3）將此技術推廣到雙頻，多頻，多端口的多天線系統中。并研究利用低溫共燒陶瓷技術實現此類器件的

小型化。（4）開發另一種級聯型耦合諧振腔解耦網絡，專門針對基站和路由器應用。（5）開發一種利用"假"天線進行解耦的新型技術。更重要的是 （6） 在實際使用場景中驗證所提出的各種解耦技術的有效性。

並聯型耦合諧振腔解耦網絡的綜合方法，需要受限根據耦合天線的特性和參數，得到一組電抗多項式，對於二階的網絡，所需要的耦合係數可以有這些多項式解析得到。實際上，並聯型耦合諧振腔解耦網絡的拓撲結構是多樣的，其中包括：兩階無交叉耦合型，兩階有交叉耦合及源負載耦合型，高階針對多頻的網絡以及三端口的網絡，專門針對三單元天線陣列。從並聯型耦合諧振腔解耦網絡，可以衍生出一種非常重要的基於低溫共燒陶瓷技術的"全能型"解耦網絡。這種網絡在頻率確定的情況下，可以適應各種不同的天線形式和耦合，非常適合在手機終端上廣泛採用。

本論文還討論了針對級聯型耦合諧振腔解耦網路的一般理論，以及其對應的電路模型和網絡參數。這種類型的網絡非常適合解決需要極高隔離度的基站天線解耦問題。這種網絡在本文中是業界首次提出的針對發射天線對領進頻帶接收機強幹擾的微波無線網絡解決方案。

另外，一種採用"假"天線配合其電抗負載進行解耦的方法也將在文中提到。這種技術利用了並不輻射的"假"天線的寄生特性，通過引入若干不同空間排布的假天線陣，來解決原有天線陣的強互耦問題。這種方法的優越性是可以針對多種不同單元數和不同陣列排布的陣列。

最後，本文將會一一討論多種評估多天線系統性能指標的參數。包括隔離度，效率，包絡相關性，信道容量乃至吞吐率。作為比較，多種多天線系統，包括採用解耦網絡技術和不採用解耦網路技術的天線陣的各種性能參數，都在文中做了詳細比較。大量的實驗證明了採用解耦網絡的多天線系統的優越性。

Terms and Abbreviations

AWGN	Additive White Gaussian Noise
BTS	Base Station
BER	Bit Error Rate
CAT	Computer-aided Tuning
CM	Coupling Matrix
CRDN	Coupled Resonator Decoupling Network
C-CRDN	Cascaded CRDN
DGS	Defected Ground Structure
EBG	Electromagnetic band-gap
EDGE	Enhanced Data rates for GSM Evolution
EMC	Electromagnetic Compatibility
FOM	Figure of Merit
GPRS	General Packet Radio Service
GSM	Global System for Mobile Communications
I.I.D.	Independent and Identically Distributed
LOS	Line of Sight
LTCC	Low Temperature Co-fired Ceramic
LTE	Long Term Evolution
LTE-A	Long Term Evolution Advanced
MAS	Multiple Antenna Systems
MEMS	Micro-electromechanical Systems
MIMO	Multiple-Input Multiple-Output
MOM	Method of Moments
NLOS	None Line of Sight
NFC	Near Field Communication
OTA	Over The Air

PCB	Printed Circuit Board
PEC	Perfect Electric Conductor
PIFA	Planar Inverted-F Antenna
PML	Perfect Matched Layer
QoS	Quality of Service
Rx	Receiver
S-CRDN	Shunt CRDN
SNR	Signal to Noise Ratio
SISO	Single Input Single Output
SVLTE	Simultaneous Voice and LTE
Tx	Transmitter
UMTS	Universal Mobile Telecommunications System
WCDMA	Wideband Code Division Multiple Access
WiMAX	Worldwide Interoperability for Microwave Access
WLAN	Wireless Local Area Network
XPD	Cross Polarization Discrimination

Acknowledgements

First of all, I would like to express my sincere gratitude to my supervisor, Prof. Ke-Li Wu, who paved the way for me toward the realm of microwave, wireless and antenna; who let me stand on his shoulders and created so many opportunities for me. His rigorous research attitude, profound knowledge and extraordinary foresight push me to the cutting edge of my research field. Everything I learnt from Prof. Wu will always be my lifetime treasures.

I am deeply and forever indebted to my parents for their love, support and encouragement throughout my entire life. I will never become who I am today without them. Thank them for bearing with me for all my shortcomings.

My sincere thanks to Dr. Lap K. Yeung for all the guidance and helpful discussions. Special thanks to our lab technician, Mr. Leo Fung, who help me in every possible aspect of my research. I do not know how to thank him enough for being such a nice person. I would also like to thank my former advisor Prof. Yin Yingzeng, who gave me the very first lesson in microwave and antenna. Words fail to describe how grateful I am to him.

Finally I must thank all my research-mates, colleagues and lifetime friends: Dr. Xiaobo Huang, Dr. Meng Meng, Dr. Hai Hu, Mr. Dacheng Wei, Mr. Tommy Hung, Dr. Xi Wang, Mr. Huan Meng, Dr. Li Wei, Mr. Xiaohu Fang, Prof. Kewei Qian, Mr. Zhenyuan Zhang, Mr. Ping Zhao, Ms. Yuhang Dou, Mr. Yang Jiang, Mr. Zhiliang Li, Mr. Jonathan Chik, Mr. Chenxi Zhai, for all the fruitful corporations and discussions. My sincere thanks go to Dr. Hongyang Wang, Mr. Li Liu, Mr. Xin Chen at the Raytech for their help and collaboration.

Table of Contents

List of Figures

xxi

List of Tables

Chapter 1

Introduction

1.1. A brief review of mobile communication

1.1.1 The Past

It is interesting to know that the mobile phone actually was emerged from automated services. The first fully automated mobile phone for vehicles was launched in Sweden in 1956, which allowed calls to be conducted in a car using a rotary dial [1]. It should be pointed out at that time, the telephones and base station equipment was provided by the Marconi Company, a telecommunication and engineering company founded by Guglielmo Marconi in 1897. As a matter of fact, in 1897, Marconi, the Father of Wireless, the Grandfather of Radio, the Great-Grandfather of the Cell Phone [2], installed a "firecracker" antenna to a car in England, which could be viewed as the first prototype of a mobile antenna [3].

After the first large scale commercial mobile phone network produced by Motorola in 1970s being put into use, it has gone through explosive changes ever since. In the 1990s, the 2G era of mobile communication began. The GSM and CDMA systems are two main competitors on the global mobile market, which are still in use in many parts around the world. Between the first ten year of the 21st century, an evolution of 3G technology emerged, which allows mobile networks and services to have higher data rates and better Quality of service (Qos). The High-Speed Downlink Packet Access (HSDPA) supports down-link speeds of up to 14.0 Mb/s. The fastest 3G-based

standard is the HSPA+ standard, which is commercially available since 2009 and offers 28 Mbit/s downlink (22 Mbit/s uplink) without using any multiple antenna techniques. The high connection speeds of 3G technology enabled a transformation in the industry: for the first time, media streaming of radio content to 3G handsets is made possible. This improvement was obtained through more complicated signal processing as well as more efficient frequency bandwidth utilization [1], [4].

1.1.2 The Status Quo

By 2009, it had become clear that, at some point, 3G networks would be overwhelmed by the growth of bandwidth-intensive applications like media streaming of HDTV content and instant video calls [1]. In early 2008, the ITU-R proposed a series requirements for 4G standards, named of the IMT-Advanced specification. The peak speed requirements for 4G service is set to 1 Gbit/s. The first-release versions of WiMAX and LTE support much less than 1 Gbit/s peak data rate, yet the two are still considered to be within the fourth generation. The world's first publicly available LTE service was launched in Stockholm by Ericsson and Nokia Siemens Networks systems and Oslo by a Huawei system on December 14, 2009 [6].
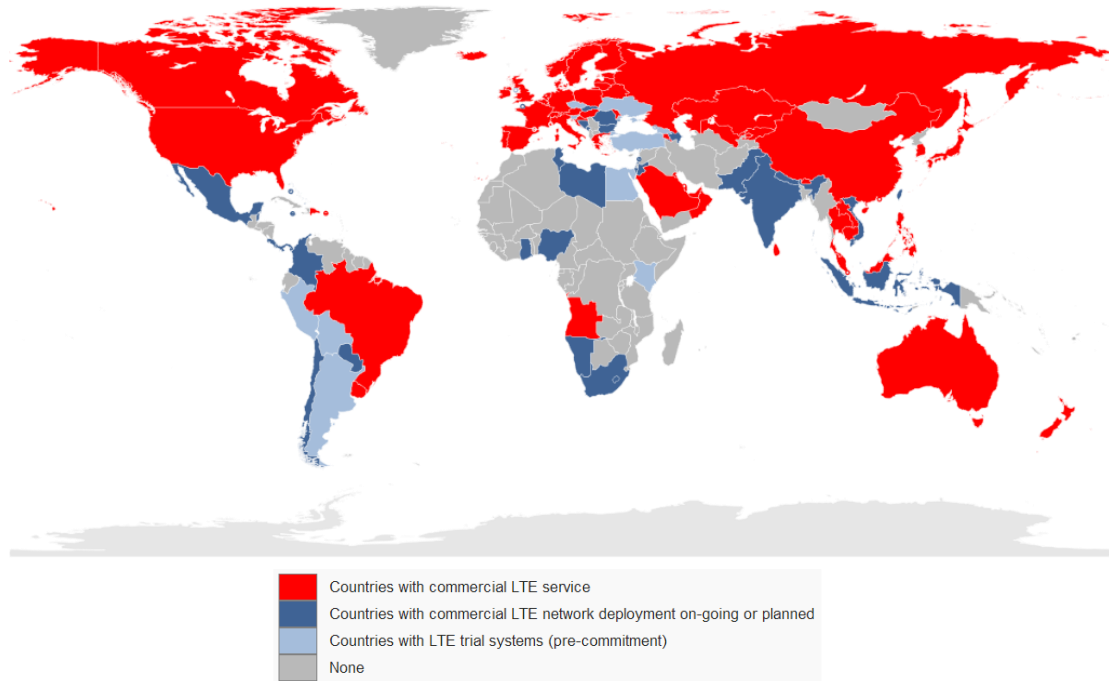
Figure 1.1 Adoption of LTE technology as of December 5, 2013 [5], [6].

According to GSMA INTELLIGENCE ANALYSIS, 264 LTE networks have been commercially launched across 101 countries between Dec. 2009 and Jan. 2014. The adoption status of LTE worldwide is shown in Fig. 1.1. It is expected that more than 2.5 billion 4G-LTE connections is possible in the year 2020, including both TDD and FDD schemes. At that time, 64% of the world's population will be covered by 4G-LTE services [7].

Orthogonal Frequency Division Multiplex (OFDM) and Multiple Input Multiple Output (MIMO) are two important enabling technologies of 4G-LTE, which have received tremendous attention in both industry and academic community. OFDM uses multiple sub-carriers that are multiplexed in a wide frequency spectrum, whereas MIMO provides a way of utilizing the multiple signal paths that exist between a transmitter and a receiver to significantly improve the data throughput on a given radio channel [8]. By using multiple antennas at a transmitter and a receiver along with some complex signal processing techniques, MIMO technology enables the system to set up parallel data streams on a single channel, thereby increasing the channel capacity by several times [9].

1.1.3 The Future

To further enhance the data throughput by up to 1000 times compared to 4G, more advanced mobile communication systems are under development, one of them is the LTE Advanced. In fact, the LTE-A is considered to be a key enabler to the "1000x mobile data challenge" – the challenge to increase the data capacity of today's network by 1000-times. The expected data rate of LTE-A is 3 Gbit/s downlink and 1.5 Gbit/s uplink as shown in Fig. 1.2 [10].
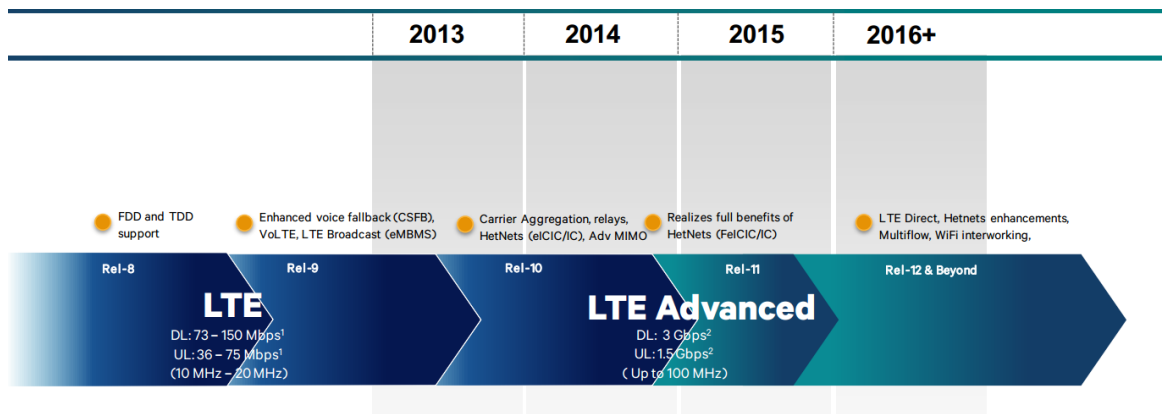
Figure 1.2 The LTE evolution road map [10].

Although 4G-LTE networks are still in deployment, the 5th generation of mobile communication has been on the agenda. An organization called METIS is formed, which aims at laying foundations for the 5G mobile communications. The objective is to have 100 times of connected devices with up to 10Gbps end-user data rate, lower latency and longer battery life [11].

One of the key technologies in Massive MIMO. With massive MIMO, a large antenna array is used, with a few hundred antennas simultaneously serving many tens of terminals in the same time-frequency band. The basic premise behind massive MIMO is to reap all the benefits of conventional MIMO, but on a much greater scale.

[12], [13].

1.1.4 The development of Wi-Fi

The IEEE 802.11 standards, or commonly known as Wi-Fi, is a technology that allows data transmission and exchange to be conducted wirelessly. The Wi-Fi occupies the 2.4GHz and 5GHz ISM bands. The Wi-Fi technology has its origins in a 1985 ruling by the US Federal Communications Commission that released the ISM bands for unlicensed use [14], [15]. The IEEE 802.11 family consists of a series of half-duplex modulation techniques that use the same basic protocol. IEEE 802.11b was the first widely accepted protocol, followed by 802.11a, 802.11g and 802.11n and even 802.11 ac [16]. IEEE 802.11n together with the up-to-date IEEE 802.11 ac (5G Wi-Fi), support MIMO and MU-MIMO (Multi-user MIMO) to further enhance the available throughput in a network, leading to a throughput of up to 1300 Mbit/s in 80 MHz channels in the 5 GHz band [17]. There are already chips and solutions for smartphones supporting 2 by 2 MIMO on the market, which promise doubled throughput and improved power efficiency [18].

1.2. Multiple antenna systems

Driven by the demand of ever greater throughput and spectrum efficiency, multiple antenna systems have become indispensable in wireless communication systems today and in the near future. There are basically two types of multiple antenna systems:

(1) *Intentionally formed multiple antenna system*, or MIMO. These antennas are intentionally installed, either to improve the data rate (spatial multiplexing) or to enhance the communication reliability (diversity) of a system.

(2) *Unintentionally formed multiple antenna system,* or Coexisted Multiple Antennas. Antennas belong to different radio communication systems of different protocols and working frequencies are integrated into one compact physical unit, such as LTE, Wi-Fi and GPS.

1.2.1. MIMO

The use of multiple receiving antennas intentionally for diversity dates back to Marconi's time, which was followed by the utilization of multiple antennas to form arrays for beam steering [19]. In the mid-1990s, researches done by the early pioneers of MIMO, mainly in Bell Labs, lay the foundation of MIMO wireless communication [20]-[22]. Multiple antennas enable a new dimension of multiplexing – the spatial multiplexing.

1.2.1.1. The Signal Model for MIMO Systems

There are several antenna configurations in a multiple antenna system. SISO (single input multiple output), SIMO (single input single output), MISO (multiple input single output) and MIMO (multiple input multiple output), which is shown in Fig. 1.3.
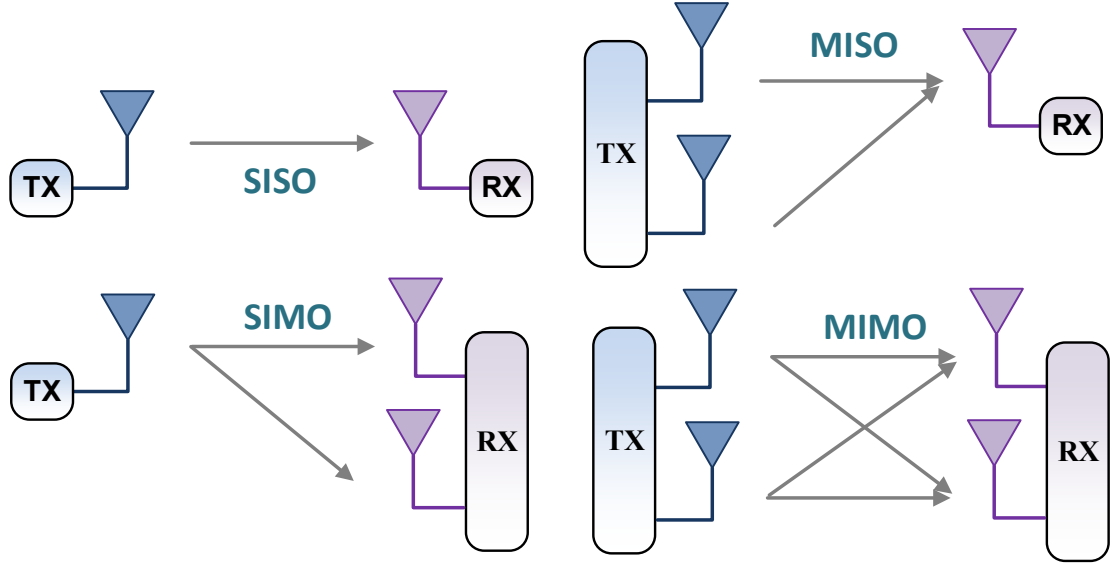
Figure 1.3 Different configurations in multiple antenna systems.

The signal model of MIMO is defined as [19]:

$$y = \sqrt{\frac{E_s}{N}} \mathbf{H}s + n \tag{1.1}$$

where y is a $M \times 1$ vector representing received signal. s is a $N \times 1$ tranmitted signal vector, while n is an additive noise vector having the same dimension as y. $\mathbf{H}$ is a $M \times N$ channel matrix. This model represents a single user MIMO over a fading channel with AWGN (Additive White Gaussian Noise). E_s is the total energy at the Tx within a symbol period.

The covariance matrix of $\mathbf{y}$ can be obtained from (1.1) and it is written as:

$$\mathbf{R}_{yy} = \frac{E_s}{N} \mathbf{H}\mathbf{R}_{ss}\mathbf{H}^H + N_0 \mathbf{I}_M \tag{1.2}$$

where $\mathbf{R}_{ss} = \mathcal{E}\{ss^H\}$ is the covariance of $\mathbf{s}$, N_0 is the noise power.

Following the method in [19], [20], the channel capacity of this MIMO system can be obtained as:

$$C = \log_2 \det\left(\mathbf{I}_M + \frac{E_s}{N \cdot N_0} \mathbf{H}\mathbf{R}_{ss}\mathbf{H}^H\right) \text{ bps/Hz} \tag{1.3}$$

If the channel is completely unknown to the Tx and the signals are uncorrelated as well as equal-powered at the Tx antennas:

$$\mathbf{R_{ss}} = \mathbf{I}_N \tag{1.4}$$

Then (1.3) can be simplified to:

$$C = \log_2 \det\left(\mathbf{I}_M + \frac{SNR}{N}\mathbf{HH}^H\right) \text{ bps/Hz} \tag{1.5}$$

where $SNR = \frac{E_s}{N_0}$ is the signal to noise ratio.

1.2.1.2. Influence of spatial fading correlation on the MIMO capacity

In practice, the assumption (1.4) is never valid. On one hand, the antennas at both Tx and Rx are always correlated because of limited antenna spacing and imperfect pattern orthogonality both for mobile terminals and base stations. On the other hand, the power cannot be equally distributed on every element in the MIMO antenna array. In this section, only the correlation effect are taken into consideration when doing capacity calculation, while the antenna radiation efficiency effect will be considered in **Chapter 5**.

Considering the effects of spatial correlation for a Rayleigh fading channel, the channel matrix can be modified as [19]:

$$\mathbf{H} = \mathbf{R_r}^{1/2} \cdot H_w \cdot R_t^{1/2} \tag{1.6}$$

Where H_w is the ideal channel matrix, with the spatial correlation at the transmitter and receiver $\mathbf{R_t}$ and $\mathbf{R_r}$ included, (1.5) now becomes:

$$C = \log_2 \left\{ det \left(I_M + \frac{SNR}{M} \mathbf{R_r}^{1/2} \cdot H_w \cdot R_t^{1/2} \cdot \left(R_t^{1/2} \right)^H \cdot H_w^H \cdot \left(R_r^{1/2} \right)^H \right) \right\} \quad (1.7)$$

It should be noted that $M = N$ is already assumed in (1.7) for simplicity. Since $\mathbf{R_r}$ and $\mathbf{R_t}$ are both Hermitian: $R_t^{1/2} = \left(R_t^{1/2} \right)^H$ and $R_r^{1/2} = \left(R_r^{1/2} \right)^H$. We can further simplify (1.7) as:

$$C = \log_2 \left\{ det \left(I_M + \frac{SNR}{M} \mathbf{R_r}^{1/2} \cdot H_w \cdot R_t \cdot H_w^H \cdot R_r^{1/2} \right) \right\} \quad (1.8)$$

Under high SNR condition: $SNR \gg 1$, (1.8) becomes:

$$C = \log_2 \left\{ det \left(\frac{SNR}{M} \mathbf{R_r}^{1/2} \cdot H_w \cdot R_t \cdot H_w^H \cdot R_r^{1/2} \right) \right\} \quad (1.9)$$

Using the property that $det(\mathbf{A} \cdot \mathbf{B}) = det(\mathbf{A}) \cdot det(\mathbf{B}) = det(\mathbf{B} \cdot \mathbf{A})$, (1.9) yields:

$$C \approx \log_2 det \left(\frac{SNR}{N} H_w H_w^H \right) + \log_2 det(R_r) + \log_2 det(R_t) \quad (1.10)$$

It can be proved that $\log_2 det(R_r) \leq 0$ and $\log_2 det(R_t) \leq 0$ [19], therefore, the higher the correlation, the smaller the channel capacity. To illustrate the effect of correlation on channel capacity, the channel capacity of a SISO system, an ideal 2 by 2 MIMO system, an ideal 3 by 3 MIMO system, and two 3 by 3 MIMO systems with different correlation values are compared with respect to different SNR level. The results are superposed in Fig. 1.4. For the 3 by 3 correlated MIMO system, the Tx are assumed to be ideal and the Rx are symmetrically correlated:

$$R_t = \begin{bmatrix} 1 & 0 & 0 \\ 0 & 1 & 0 \\ 0 & 0 & 1 \end{bmatrix}, R_r = \begin{bmatrix} 1 & \rho & \rho \\ \rho & 1 & \rho \\ \rho & \rho & 1 \end{bmatrix} \quad (1.11)$$

The correlation coefficients ρ are chosen to be 0.6 and 0.9 respectively.
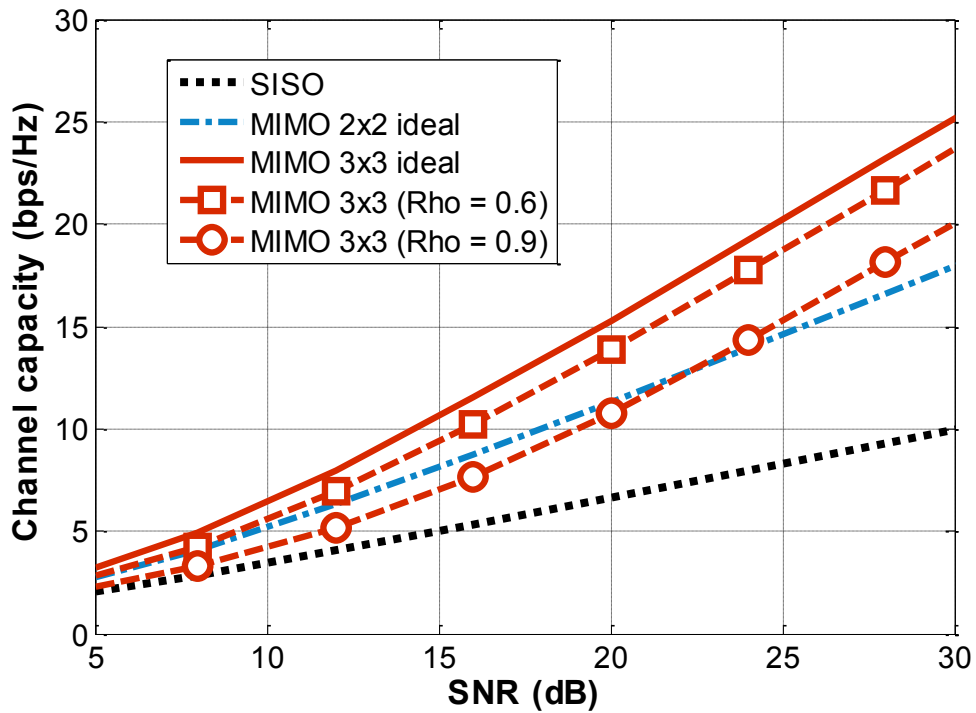
Figure 1.4 Channel capacities of different MIMO systems with respect to different SNR level.

It can be concluded from Fig. 1.4 that for ideal MIMO systems, the channel capacity can be increased linearly according to the number of antennas at Tx and Rx. However, when the correlation is large, the channel capacity will degrade significantly. A 3 by 3 MIMO system with high correlation behaves even poorer than an ideal 2 by 2 MIMO system. It is therefore vital that this correlation issue is tackled wisely and effectively.

1.2.2. Coexisted Multiple Antennas

In order to access various wireless networks and services ubiquitously, there is an irreversible trend in today's wireless communication technology that more and more communication systems of different protocols and working frequencies are integrated into one increasingly compact physical unit. Such trend impacts not only mobile terminals but also network infrastructure equipment such as base stations.

In a mobile unit, such as a mobile phone or a laptop computer, multiple wireless services, including GSM, UMTS, Wi-Fi, LTE, GPS and Bluetooth, coexist in a very compact space. The radio frequency interference among the systems that operate at the same frequency band can seriously affects the QoS. A typical example is the interference between Bluetooth and Wi-Fi modules in a laptop computer and a mobile phone.

In a today's wireless base station, antennas for 2G (GSM), 3G (UMTS) and 4G (LTE) wireless communication systems must coexist in close vicinity, which inevitably create radio frequency interference to each other. Although people have attempted to avoid such interference by adding filters and separating frequency bands of them as far as possible, the interference among the systems operating at close adjacent frequencies cannot be completely suppressed by bandpass filters when the spatial isolation is not sufficient. The coexistence interference issue among radio transceivers and antennas becomes increasingly important as the size of an integrated system is reducing that leads to decreasing of spatial isolation and the number of wireless systems is increasing.

Two typical coexistence scenarios for collocated antennas and transceivers in user equipment (UE) and a base station (BS) are shown in Figures 1.5.

(a)
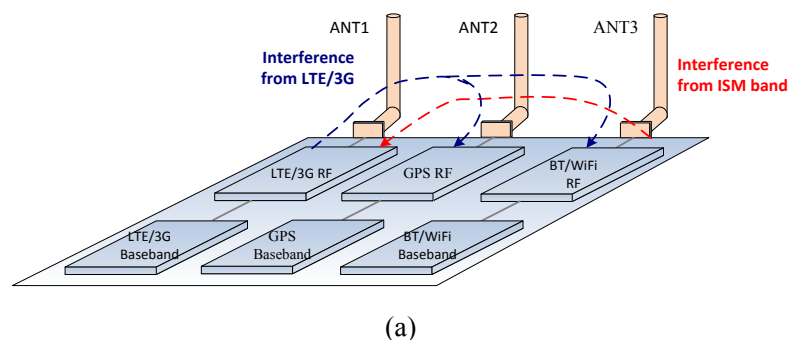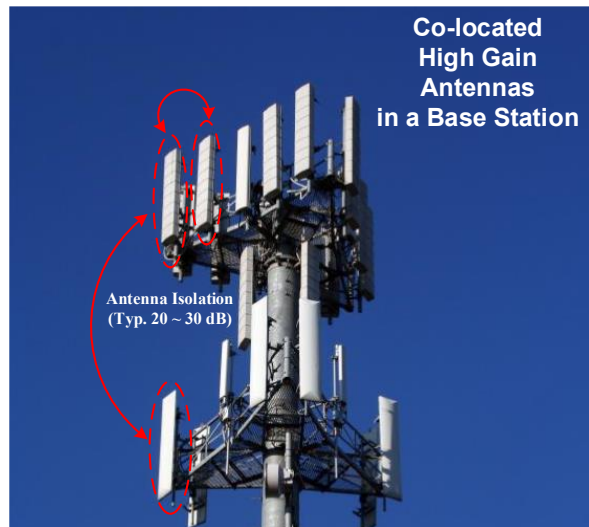
(b)

Figure 1.5 (a) Coexistence scenario of collocated wireless systems in one user equipment [23]. (b) Coexistence scenario of collocated base station antennas for different wireless systems.
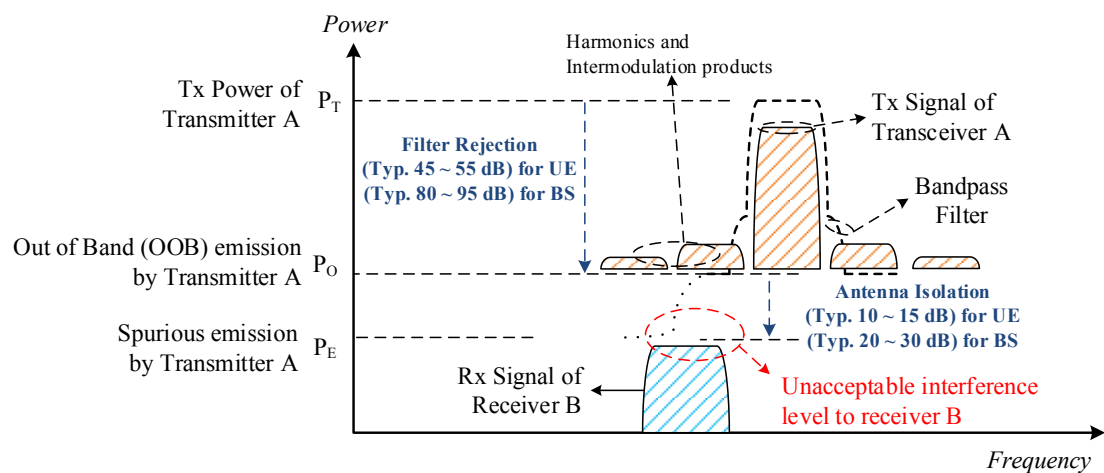
Figure 1.6 The coexistence interference from transmitter A to receiver B operating in adjacent frequency bands.

1.2.2.1. Two systems operating in adjacent frequency bands

Due to a compact proximity with critical electrical dimension less than half wavelengths for collocating different radio transceivers in the same UE, the radiated power from one transmitter may interfere a receiver of another communication system. Such interference is likely to happen when the separation of either the frequency bands

or two antennas is not sufficiently large. Within the same UE, as the two systems operate in two adjacent frequency bands, spatial isolation is low, no filter technology can offer sufficient signal attenuation in the adjacent band without introducing a significant insertion loss in its own working band. Although optimizing the orientations and locations of antennas may improve the isolation in certain extend, this kind of 'try and error' approach and is not systematic and should be considered as the 'last resource'. The mentioned interference problem is well illustrated in Figure 1.6, where transmitter A generates a signal of power P_T in its working frequency band. Denoting the inevitable parasitic emissions leaked to the adjacent frequency band as P_O, the ratio of P_T/P_O is defined as the Adjacent Channel Leakage Ratio (ACLR). A typical ACLR value is about 50 dB according to [23]. For a typical scenario of transmitted power of 20 dBm (100 mW) and receiver sensitivity of -100 dBm, if the filter rejection ($|S_{21}^F|_{dB}$) is 45 to 55 dB and antenna spatial isolation ($|S_{21}^A|_{dB}$) for a closely collocated antennas is 10 to 15 dB, the possible spurious emission P_E by transmitter A on radio B can be calculated as:

$$P_{E-UE} = P_T - ACLR - |S_{21}^F|_{dB} - |S_{21}^A|_{dB}$$
$$= 20dBm - 50dB - 45dB - 15dB = -90\ dBm > -100\ dBm \qquad (1.12)$$

which means that when the two antennas are closely collocated spurious emission may cause deadly interference and an effective means for improving the isolation of the two antennas is needed.

The coexistence interference issue in network infrastructure equipment is also severe. The newly added LTE network is deployed over the existing second generation (2G) and third generation (3G) mobile networks. Therefore, it can be foreseen that there will be growing concerns on the interference issue among the multiple wireless systems through their collocated base station antennas. Although the spacing between base station antennas serving the different systems might be several wavelengths, the transmitted power of one antenna could be as high as from 43 dBm to 46 dBm.

Moreover, inappropriately installed high gain antennas in a BS may lead to poor spatial isolation causing more severe interferences to adjacent receivers. For an LTE base station, if Rx sensitivity (P_r) is -110dBm, transmitted power $P_T = 46\ dBm$, filter rejection at the adjacent band ($|S_{21}^F|_{dB}$) is 80 dB, and an antenna spatial isolation ($|S_{21}^A|_{dB}$) is 20 dB, the possible spurious emission for a radio system in the adjacent frequency band of another radio system can be calculated as:

$$
\begin{aligned}
\text{P}_{E-BS} &= P_T - ACLR - |S_{21}^F|_{dB} - |S_{21}^A|_{dB} \\
&= 46\ dBm - 50dB - 80\ dB - 20dB = -104dBm > -110dBm \quad (1.13)
\end{aligned}
$$

which means that without appropriate spatial isolation, the spurious emission may also cause interference in its adjacent radio systems. Therefore, increasing the isolation between two antennas becomes an important subject for a successful operation and coexistence of multiple radio transceivers for both UEs and BSs.

An eminent example for this case is a pair of collocated TDD-LTE and Wi-Fi systems as the TDD LTE band 40 (2300 ~ 2400 MHz) is adjacent to the Industrial, Scientific and Medical (ISM) radio band (2400 ~ 2483.5 MHz). Since it is very difficult for RF filter technology to provide very high isolation in such a narrow guard band, strong interference may occur when the two systems have no sufficient antenna spatial isolation. Similarly, the ISM band can also interfere with FDD-LTE band 7 and TDD-LTE band 38 whose frequency band is around 2.6 GHz.

For BTSs, the WCDMA/IMT-200, the CDMA2000 and the TD-SCDMA bands are all in close proximity to LTE bands. These systems are likely to interfere with each other. Possible mutual interfering bands for the ISM band and LTE bands are shown in Fig. 1.7.
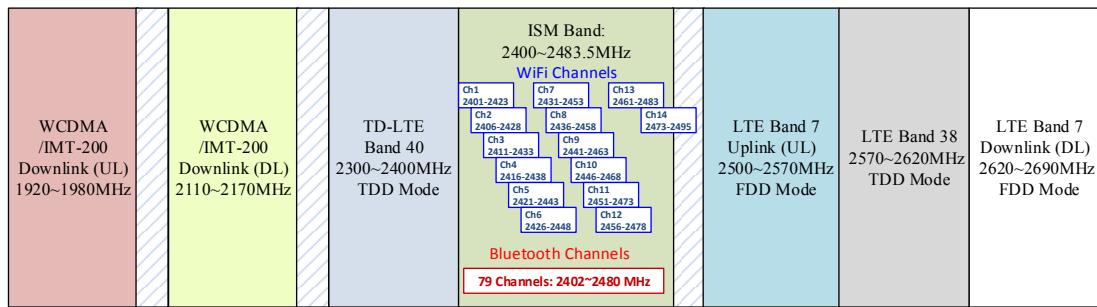
Figure 1.7 Possible mutual interfering bands near ISM band [23].

1.2.2.2. Two systems operating in the same frequency band

A Wi-Fi system that complies with IEEE 802.11 b/g/n/ac standards operates within the ISM radio band (2400 ~ 2483.5 MHz), which is the same as that for a Bluetooth (BT) enabled device. Since Wi-Fi and BT are complementary technologies, they will often be used simultaneously on the same UE.

To mitigate the interference to a BT system, BT uses FHSS (Frequency Hopping Spread Spectrum scheme) with about 1 MHz bandwidth. However, for a high data rate transmission, Wi-Fi uses DSSS (Direct Sequence Spread Spectrum scheme) with more than 20 MHz bandwidth. Therefore, when a BT system and a Wi-Fi system are turned on simultaneously in close proximity, the Wi-Fi system is more vulnerable in the interference combat. Many problematic reports of this kind of interference can be found by a Google search using key words of "interference", "Bluetooth" and "Wi-Fi".

To mitigate the interference problem for two collocated Bluetooth and Wi-Fi systems to maintain an acceptable performance and reliability, the current solutions are either collaboratively shifting the use of time or frequency, or simply placing the two units physically apart from each other as far as possible to increase the spatial isolation.

1.3. Literature Review

1.3.1. Antenna Decoupling

Significant attentions have been paid both by the industry and academic community to mitigating the above-mentioned interferences in a multiple antenna system. The method for reduction of mutual coupling and enhancement of spatial isolation, or termed as the ***antenna decoupling*** problem can be divided into five major categories:

(1) *The space, polarization and angle diversity scheme*:

The most obvious method to decouple two antennas is to increase the electrical distance between them [3], [9], [24]. When the angular spread of the channel covers the full sphere, the increased equivalent phase difference of the patterns of the two antennas will significantly de-correlate the received signals. However, in practice, a three dimensional uniform distribution of angular spread is seldom realized. Furthermore, for commonly used inverted-F and inverted-L antennas in mobile terminals, an increment in inter-element spacing might result in poorer isolation or correlation [25], [26]. Exploiting the orthogonal characteristics of radiated field between two antennas is an alternative choice [27], [28]. By exciting electric and magnetic mode on chassis, polarization diversity is achieved. Despite the benefit of this approach, the user's as well as the motor, camera and battery's influence on the orthogonality of two antennas are very significant, therefore, it is impractical for mobile terminals.

This type of solutions is quite straight forward and easy to use despite it occupies a large area. Several world leading companies have also proposed this type of solutions, such as Hewlett-Packard Development Company using spatial diversity [29] as well as Intel Corporation [30] and Qualcomm Incorporated [31] using polarization diversity. Cisco Technology proposed a solution based on angle diversity for wireless accessing point [32].

(2) *The eigen-modes decomposition scheme*:

A systematic decoupling scheme is to utilize orthogonal modes existing in compact antenna arrays and to diagonalize the scattering matrix of the coupled antennas using combinations of branch line couplers [33], [34] or lumped components [35]. Since different radiation modes have significantly different matching bandwidth and efficiency and some high Q mode resulting in a very narrow bandwidth, it might not be suitable for mobile terminals, instead, by making use of the orthogonal radiation modes, mode-based beam steering array can be built [36].

In the industry, the Koninklijke Philips Electronics N. V., commonly known as Philips, has proposed a concept of Virtual Antenna Array Decoupler (VAAD) which processes the received signal energy and decouple signals received from the closed spaced antennas by a digital signal processor or dedicated, passive, or electronic hardware [37]. [37] only proposed the mathematic relation that VAAD needs to realize. However, no any specific realization method is proposed in the patent. One possible method that is well known in the field to realize the mathematic relation is the above-mentioned mode-decomposition network.

(3) *The inserted network scheme*:

In 1970s', J. B. Andersen [38] proposed a necessary condition for the occurrence of no coupling between antennas and proved the concept by a transmission-line network inserted in-between the feeding ports and the coupled antennas. However, the element spacing in the design has to be fixed to some certain values, which limits its applications. A lumped element connected in shunt with the coupled antenna elements to achieve certain amount of isolation between the antenna ports [39]. Such decoupling element overcomes some major disadvantages of [38] and can be considered as a zero-th order decoupling network. However, due to limited choice of component values as well as its linearly monotonic admittance characteristic verses frequency at the frequency band of interest, its decoupling bandwidth is relatively narrow and is sensitive to surrounding influence including both hands and head. The neutralization line technique can also be used to achieve decoupling purpose [40], [41]. But the decoupling mechanism of such method is not well-understood since the neutralization line not only creates a second path of current flow but also perturbs the

radiated fields. Existing designs are ad-hoc and require further tuning and optimization.

Panasonic Corporation had also patented a solution based on lumped element decoupling [42], while another complicated solution is patented by Intel Mobile Communications recently, in which a tunable neutralization path is inserted between two PIFA antennas is implemented [43].

(4) *Artificial structure decoupling scheme*:

This scheme involves the use of sub-wavelength EM structures such as mushroom-like Electromagnetic Band Gap (EBG) structures [44], Defected Ground Structures (DGS) [45] and magnetic metamaterials [46]. These structures provide bandstop filtering characteristics in certain extent. A common issue for these structures is that they are all ad-hoc to particular antennas and their footprints are large. Another similar narrow band approach is to use a parasitic scatter/radiator [47]. Later this scheme is extended to three and four-element array by the author of this thesis [48], [49].

To use extra antenna-like isolation element is adopted by Apple Inc. very recently [50], [51]. The major concerns of this method are the required large space and its vulnerability to the human interference.

(5) Coupled resonator decoupling network (CRDN) scheme:

A preliminary result of decoupling a pair of coupled elements using a second-order coupled resonator network was first reported in 2012 by the author [52], in which not only the sequential but also a cross couplings are introduced for a broadband decoupling performance. Later, a thorough investigation both theoretically and experimentally is given in for second-order all pole Coupled Resonator Decoupling Networks (CRDNs) [53]. The scheme is broadband, antenna independent, and can be extend to dealing with multiple antennas [54]. It can be implemented by various passive integration technologies, such as Low Temperature Co-fired Ceramics (LTCC) [55] and silicon based Integrated Passive Device (IPD) technologies to be realized in a

very compact size, which can be easily adopted in a mobile terminal.

1.3.2. Dual-Band Decoupling Schemes

Significant attentions have been paid to mitigating the mutual coupling in a multiple antenna system. But such endeavors have been mostly constrained to single band applications, which cannot fulfill the requirement for multi-band systems. For example, emerging Long Term Evolution (LTE) systems may operate in 700 MHz, 2.3 GHz and 2.6 GHz bands and the widely used IEEE 802.11 WLAN devices can occupy both the 2.4 GHz and 5.2/5.8 GHz bands. As the single band decoupling solutions become mature, endeavors are now extended to multi-band solutions.

Many of the existing methods on dual-band decoupling problems simply extend the single band decoupling method to the context of a dual band problem. For example, [56] and [57] intended to decouple a pair of dual band antennas operating at two bands (803-820 MHz and 2440-2900 MHz for [56], UMTS (1920-2170 MHz) and WLAN (2400-2484 MHz) for [57]) with a defected ground structure (DGS), respectively. As it is widely known, DGSs are antenna-dependent and are not easy to design for a dual band application. Not to mention that the footprint of them are excessively large. Besides, these structures can have noticeable influence on the radiation pattern and efficiency. [58] uses the neutralization-line technique for dual band applications. But it is also antenna-dependent and must be designed by intuition. Additionally, it is obvious that currents induced on the line affect the radiation power pattern. A scheme using a lumped or semi-lumped element decoupling network for two dual band antennas is also proposed [59], [60]. The limitation for such scheme is on bandwidth and losses. A dual-band version of mode-decomposition technique [61], [62] and a combination of this technique with a passive decoupling network technique [63] are also proposed. There are three obvious issues in [61]-[63]: the network size is excessively large; the modes' Q and efficiency are different for different modes; and the insertion loss of the decoupling network is not negligible.

1.3.3. Decoupling Solutions for Coexistence Interference

In recent years, the coexistence interference problem has received tremendous attentions by the industry. Many world leading telecommunication companies have invested in developing technologies for mitigating the issues. The prominent companies among them include Apple, Qualcomm, Intel and Samsung Electronics. Some contributions from academia are also available. Although there are many preliminary attempts from industry and academic communities to avoid such interference by adding filters and increasing isolation between two antennas as far as possible, the interference among the systems operating at adjacent frequencies cannot be sufficiently suppressed if the spatial isolation is not sufficient. The coexistence interference issue among radio transceivers and antennas becomes increasingly important as the size of an integrated system decreasing and the number of wireless systems increasing. Current solutions can be divided into four categories:

(1) Signalling based solutions that require coordination between the collated transceivers [64], [65];

(2) Active interference suppression solutions that need complex active circuitry and control algorithm [66]-[68];

(3) Antenna isolation enhancement solutions by passive networks [34], [36], [44], [45], [47], [69].

(4) Using high selection filters [70], [71]. This solution uses very high Q bandpass and bandstop/notch filters, whose theory and implementation are very mature, for interference suppression. However, for collocated systems with same or contiguous frequency bands it is almost impossible to realize a high isolation between them by traditional filter technologies, since the limitation of selectivity cannot be easily transcended.

There are relatively fewer effective solutions related to the coexistence issue of base station antennas, because the problem for base station coexistence is more severe and more difficult to deal with than that for a UE. Some of the analysis has been done in [72] and the 3GPP specification [73]. As pointed out in [73] that "*The current state-of-the art technology does not allow a single generic solution for co-location*

with other system on adjacent frequencies for 30dB BS-BS minimum coupling loss".

Therefore, the 3GPP has established very stringent limitations on the BS spurious emissions for other co-located BSs. There is much to be done to improve the performance of collocated base station antennas.

1.4. Organization of the Thesis

The reminder of this thesis is organized as the following:

Chapter 2 will be focus on the first type of coupled resonator decoupling network (CRDN), the shunted type (S-CRDN). The S-CRDN is always connected to the coupled antennas in shunt for decoupling purpose. The synthesis and design procedures for a second-order all pole S-CRDN, a second order S-CRDN with source-load couplings, a dual-band S-CRDN for two-element array and a third-order three port S-CRDN for three-element array will be elaborated. Several design examples are given to prove the concept. Meanwhile, an LTCC-version of CRDN module especially designed for two element array decoupling in a mobile terminal will be discussed in detail, showing the potential of a compact decoupling network in practical applications.

Chapter 3 presents the novel concept of the second type of CRDN, the Cascaded CRDN (C-CRDN). The C-CRDN is a 4-port microwave network that is cascaded with two strongly coupled antennas in the system for decoupling purpose. It can further improve the isolation between the interfering antennas even though the original isolation is below 20dB. Therefore, it is quite suitable for high power applications, where high Q resonators are needed. The circuit model and design method will also be given in Chapter 3 with two practical examples trying to solve the coexistence problems of TD-LTE and Wi-Fi in a Femtocell.

Chapter 4 introduces a general decoupling theory using dummy antenna arrays.

The concept is to use an array of dummy antenna elements that are terminated with optimum loads to decouple a given antenna array. The theory is applied to a symmetric four element array and an isosceles triangular compact array. Based on the theory, a novel "Cheesecake" array for Distributed Antenna Systems (DAS) is proposed.

Several important figures of merit for benchmarking a MIMO antenna array are discussed in a great detail in Chapter 5. The isolation, radiation efficiency, Envelop Correlation Coefficient (ECC), channel capacity and throughput for decoupled antenna arrays together with their coupled counterparts are investigated. Meanwhile, the human's interferences on these figures of merit are studied experimentally, showing the supremacy of the proposed decoupling techniques over others for real-world applications.

Concluding remarks are given in Chapter 6.

1.5. Reference

[1] [Online]. Available: http://en.wikipedia.org/wiki/History_of_mobile_phones

[2] Calvin D. Trowbridge Jr., "Marconi: Father of Wireless, Grandfather of Radio, Great-Grandfather of the Cell Phone, The Story of the Race to Control Long-Distance Wireless," BookSurge Publishing, February 24, 2010.

[3] R.Vaughan and J. B. Andersen, *Channels, Propagation and Antennas for Mobile Communications.* London, U.K.: The Institute of Electrical Engineers, 2003.

[4] E. C. Niehenke, "Wireless Communications: Present and Future," *IEEE Microwave Magazine,* vol.15, no.2, pp.26-35, March-April 2014.

[5] [Online]. Available:
https://gsmaintelligence.com/analysis/2013/11/global-lte-network-forecasts-and-assumptions-201317/408/

[6] [Online]. Available: http://en.wikipedia.org/wiki/LTE_(telecommunication)

[7] [Online]. Available:

https://gsmaintelligence.com/images/analysis/entries/2014-02-24-infographic-lte.
png

[8] G. L. Stuber, J. R. Barry, S. W. McLaughlin, Y. Li, M. A. Ingram, and T. G. Pratt,
"Broadband MIMO-OFDM wireless communications," *Proc. IEEE*, vol. 92, no. 2,
pp. 271–294, Feb. 2004

[9] M. A. Jensen and J. W.Wallace, "A review of antennas and propagation for MIMO
wireless communications," *IEEE Trans. Antennas Propag.*, vol., 52, no. 11, pp.
2810–2824, Nov. 2004

[10][Online].

Available: http://www.qualcomm.com/media/documents/files/lte-advanced-an-e
volution-built-for-the-long-haul.pdf

[11]A. Osseiran, "Challenges and Scenarios of the fifth Generation (5G) Wireless
Communications System", [Online]. Available:

https://www.metis2020.com/wp-content/uploads/presentations/W@kth_METIS_
overview_scenarios_20131115_web.pdf

[12]T. L. Marzetta, "Noncooperative cellular wireless with unlimited numbers of base
station antennas," IEEE Trans. Wireless Commun., vol. 9, no. 11, pp. 3590–3600,
Nov. 2010.

[13]E. Larsson, O. Edfors, F. Tufvesson, T. Marzetta, "Massive MIMO for next
generation wireless systems," *IEEE*, *Communications Magazine*, vol.52, no.2,
pp.186-195, February 2014.

[14][Online].

Available: http://www.britannica.com/EBchecked/topic/1473553/Wi-Fi

[15][Online]. Available: https://en.wikipedia.org/wiki/WiFi

[16][Online]. Available: https://en.wikipedia.org/wiki/802.11

[17][Online]. Available:

http://www.smallnetbuilder.com/wireless/wireless-features/32238-ac1900-innova
tion-or-3d-wi-fi

[18] [Online]. Available: http://www.broadcom.com/products/features/5gwifi.php

[19] A. Paulraj, R. Nabar, and D. Gore, Introduction to Space-Time Wireless Communications. Cambridge, U.K.: Cambridge Univ. Press, 2003.

[20] I. E. Telatar. Capacity of Multi-Antenna Gaussian Channels, Tech. Rep. Bell Labs, Lucent Technologies (1995). [Online]. Available: http://mars.bell-labs.com/papers/proof/proof.pdf

[21] G. J. Foschini Jr., "Layered space-time architecture for wireless communication in a fading environment when using multi-element antennas," *Bell Labs Tech. J.*, pp. 41−59, Autumn, 1996.

[22] G. J. Foschini Jr. and M. J. Gans, "On limits of wireless communication in a fading environment when using multiple antennas," *Wireless Personal Commun.*, 311−335, Mar. 1998.

[23] 3GPP TR 36.816: "Study on signalling and procedure for interference avoidance for in-device coexistence," V11.2.0, 2011.

[24] C. B. Dietrich, Jr., K. Dietze, J. R. Nealy, and W. L. Stutzman, "Spatial, polarization, and pattern diversity for wireless handheld terminals," *IEEE Trans. Antennas Propag.,* vol. 49, no. 9, pp. 1271−1281, 2001.

[25] M. Pelosi, M. B. Knudsen, and G. F. Pedersen, "Multiple antenna systems with inherently decoupled radiators," *IEEE Trans. Antennas Propag.*, vol. 60, pp. 503−515, Feb. 2012.

[26] Z. N. Chen, X. N. Low, and T. S. P. See, "Analysis and optimization of compact suspended plate MIMO antennas," *IEEE Trans. Antennas Propag.,* vol. 59, no. 1, pp. 263−270, Jan. 2011.

[27] H. Li, Y. Tan, B. K. Lau, Z. Ying, and S. He, "Characteristic mode based tradeoff analysis of antenna-chassis interactions for multiple antenna terminals," *IEEE Trans. Antennas Propag.*, vol. 60, no. 2, pp.490−502, Feb. 2012.

[28] H. Li, Z. T. Miers, B. K. Lau, "Design of Orthogonal MIMO Handset Antennas Based on Characteristic Mode Manipulation at Frequency Bands Below 1 GHz," *IEEE Trans. Antennas Propag.*, vol.62, no.5, pp.2756−2766, May 2014.

[29] Dou et al., "Internal diversity antenna architecture," U. S. Patent US 7940223 B2,

May. 10, 2011.

[30] Suh et al., "Multi-band highly isolated planar antennas integrated with front-end modules for mobile applications," U. S. Patent US 8077095 B2 Dec. 13, 2011.

[31] Gainey et al., "Integrated, closely spaced, high isolation, printed dipoles," U. S. Patent US 7733285 B2, Jun. 8, 2010.

[32] Theobold, "Multichannel access point with collocated isolated antennas," U. S. Patent US 6933909 B2, Aug. 23, 2005.

[33] J. C. Coetzee and Y. Yu, "Port decoupling for small arrays by means of an eigenmode feed network", *IEEE Trans. Antennas and Propag.,* vol. 56, no. 6, pp.1587-1593, Jun 2008.

[34] C. Volmer, J. Weber, R. Stephan, K. Blau, and M. A. Hein, "An eigen-analysis of compact antenna arrays and its application to port decoupling," *IEEE Trans. Antennas Propag.*, vol. 56, no. 2, Feb. 2008.

[35] J. Weber, C. Volmer, K. Blau, R. Stephan, and M. A. Hein, "Miniaturized antenna arrays using decoupling networks with realistic elements," *IEEE Trans. Microw. Theory Tech.*, vol. 54, no. 6, pp. 2733–2740, Jun.2006.

[36] L. K. Yeung and Y. E. Wang, "Mode-based beamforming arrays for miniaturized platforms," *IEEE Trans. Microw. Theory Tech.,* vol. 57, no. 1, pp. 45-52, Jan. 2009.

[37] Van Der Merwe et al., "Wireless communication system with diversity/MIMO array branch decoupling," U. S. Patent US 7876850 B2, Jan. 25, 2011.

[38] J. B. Andersen and H. H. Rasmussen, "Decoupling and descattering networks for antennas," *IEEE Trans. Antennas Propag.* vol., 24, no. AP-6, pp. 841-846, Nov. 1976.

[39] S. Chang, Y. –S. Wang, and S. –J. Chung, "A decoupling technique for increasing the port isolation between strongly coupled antennas," *IEEE Trans. Antennas Propag.* vol. 56, no. 12, pp. 3650-3658, Dec. 2008.

[40] A. Diallo, C. Luxey, P. L. Thuc, R. Staraj, and G. Kossiavas, "Study and reduction of the mutual coupling between two mobile phone PIFAs operating in the DCS1800 and UMTS bands," *IEEE Trans. Antennas Propag.* vol. 54, no. 11, pp. 3063-3073, Nov. 2006.

[41] S.-W. Su, C.-T. Lee, and F.-S. Chang, "Printed MIMO-antenna system using neutralization-line technique for wireless USB-dongle applications," *IEEE Trans. Antennas Propag.*, vol. 60, no. 2, pp. 456–463, Feb. 2012.

[42] Iwai et al., "Array antenna apparatus having at least two feeding elements and operable in multiple frequency bands," U. S. Patent US 7557761 B2, Jul. 7, 2009.

[43] Knudsen et al., "Minimizing mutual coupling," U. S. Patent US 8170510 B2, May. 1, 2012.

[44] F. Yang and Y. R. Samii, "Microstrip antennas integrated with electromagnetic band-gap EBG structures: A low mutual coupling design for array applications," *IEEE Trans. Antennas Propag.* vol. 51, no. 10, pp. 2936-2946, Oct. 2003.

[45] C. Y. Chiu, C. H. Cheng, R. D. Murch, and C. R. Rowell, "Reduction of mutual coupling between closely-packed antenna element," *IEEE Trans. Antennas Propag.* vol. 55, no. 6, pp. 1732-1738, Jun. 2007.

[46] M. M. Bait-Suwailam, M. S. Boybay, and O. M. Ramahi, "Electromagnetic coupling reduction in high-profile monopole antennas using single-negative magnetic metamaterials for MIMO applications," *IEEE Trans. Antennas Propag.*, vol. 58, no. 9, pp. 2894–2902, Sep. 2010.

[47] B. K. Lau and J. B. Andersen, "Simple and efficient decoupling of compact arrays with parasitic scatterers," *IEEE Trans. Antennas Propag.*, vol. 60, no. 2, pp. 464－472, Feb. 2012.

[48] L. Zhao and K.-L. Wu, "Decoupling of an Isosceles Triangular Three Element Array with One Reactively Loaded Dummy Element", *2014 IEEE International Microwave Symposium,* June, 2014.

[49] L. Zhao and K.-L. Wu, "A Decoupling Technique for Four-element Symmetric Arrays with Reactively Loaded Dummy Elements", *IEEE Trans. Antennas Propag.*, vol. 62, no. 8, pp. 4416－4421, August. 2014.

[50] Schlub et al., "Antenna isolation for portable electronic devices," U. S. Patent US 7916089 B2, Mar. 29, 2011.

[51] Schlub et al., "Handheld electronic devices with isolated antennas," U. S. Patent US 8094079 B2, Jan. 10, 2012.

[52] Luyu Zhao, L. K. Yeung and Ke-Li Wu, "A novel second-order decoupling network for two-element compact antenna arrays, "*Microwave Conference Proceedings (APMC), 2012 Asia-Pacific*, pp.1172−1174, 4-7 Dec. 2012.

[53] Luyu Zhao, L. K. Yeung and Ke-Li Wu, "A Coupled Resonator Decoupling Network for Two-Element Compact Antenna Arrays in Mobile Terminals," *IEEE Trans. Antennas Propag.*, vol.62, no.5, pp.2767−2776, May 2014.

[54] Luyu Zhao and Ke-Li Wu, "A broadband coupled resonator decoupling network for a three-element compact array," *Microwave Symposium Digest (IMS), 2013 IEEE MTT-S International* , 2-7 June 2013.

[55] Kewei Qian, Luyu Zhao and Ke-Li Wu, "An LTCC Coupled Resonator Decoupling Network for Two Antennas of the Same Frequency Bands", submitted to *IEEE Trans. Microw. Theory Tech.*.

[56] M. S. Sharawi, A. B. Numan, M. U. Khan, and D. N. Aloi, "A dual-element dual-band MIMO antenna system with enhanced isolation for mobile terminals," *IEEE Antennas Wireless Propag. Lett.*, vol. 11, pp. 1006-1009, 2012.

[57] Y. Ding, Z. Du, K. Gong, and Z. Feng, "A novel dual-band printed diversity antenna for mobile terminals," *IEEE Trans. Antennas Propagat.*, vol. 55, no. 7, pp. 2088–2096, Jul. 2007.

[58] X. M. Ling and R. L. Li, "A novel dual-band MIMO antenna array with low mutual coupling for portable wireless devices," *IEEE Antennas Wireless Propagat. Lett.,* vol. 10, no. 1, pp. 1039–1042, 2011.

[59] X. Tang, K. Mouthaan, and J. C. Coetzee, "Dual-band decoupling and matching network design for very closely spaced antennas," in *Proc. Eur. Microw. Conf.,* 2012, pp. 49–52.

[60] C.-Y. Lui, Y.-S. Wang, and S.-J. Chung, "Two nearby dual-band antennas with high port isolation," presented at the IEEE Antennas Propagat. Symp. Dig., San Diego, CA, Jul. 2008.

[61] P.-L. Chi, C.-J. Lee, and T. Itoh, "A compact dual-band metamaterials-based rat-race coupler for a MIMO system application," in *IEEE MTT-S Int. Microw. Symp. Dig.*, Jun. 15–20, 2008, pp. 667–670.

[62] P. Chi and T. Itoh, "Miniaturized dual-band directional couplers using composite right/left-handed transmission structures and their applications in beam pattern diversity systems," *IEEE Trans. Microw. Theory Tech.*, vol. 57, no. 5, pp. 1207–1215, May 2009.

[63] K.-C. Lin, C.-H. Wu, C.-H. Lai, and T.-G. Ma, "Novel dual-band decoupling network for two-element closely spaced array using synthesized microstrip lines," *IEEE Trans. Antennas Propag.,* vol. 60, no. 11, pp. 5118–5128, Nov. 2012.

[64] 3GPP TR 36.816: "Study on signalling and procedure for interference avoidance for in-device coexistence," V11.2.0, 2011.

[65] Z. Hu, R. Susitaival, Z. Chen, I.-K. Fu, P. Dayal, and S. Baghel, "Interference avoidance for in-device coexistence in 3GPP LTE-advanced: Challenges and solutions," *IEEE Commun. Mag.*, vol. 50, no. 11, pp. 60–67, Nov. 2012.

[66] J. I. Choi, M. Jain, K. Srinivasan, P. Levis, and S. Katti, "Achieving single channel, full duplex wireless communication," in *Proc. 16th Annu. Int. Conf. Mobile Comput. Netw.,* 2010, pp. 1–12.

[67] A. Raghavan, E. Gebara, E. Tentzeris, and J. Laskar, "Analysis and design of an interference canceller for collocated radios," *IEEE Trans. Microwave Theory Tech.,* vol. 53, no. 11, pp. 3498–3508, Nov. 2005.

[68] H. Habibi, E. J. G. Janssen, R. G. M. Hilkens, Y. Wu, D. Milosevic, P. G. M. Baltus, J. W. M. Bergmans, "Experimental Evaluation of an Adaptive Nonlinear Interference Suppressor for Multimode Transceivers," *IEEE Journal on Emerging and Selected Topics in Circuits and Systems,* vol.3, no.4, pp.602-614, Dec. 2013.

[69] A. S. Konanur, K. Gosalia, S. H. Krishnamurthy, B. Hughes, and G. Lazzi, "Increasing wireless channel capacity through MIMO systems employing co-located antennas," *IEEE Trans. Microwave Theory Tech.*, vol. 53, pp. 1837–1844, Jun. 2005.

[70] H. Khatri, P. S. Gudem, and L. E. Larson, "Integrated RF interference suppression filter design using bond-wire inductors," *IEEE Trans. Microw. Theory Techn.,* vol. 56, no. 5, pp. 1024–1034, May. 2008.

[71] K. Rambabu, M. Y.-W. Chia, K. M. Chan, and J. Bornemann, "Design of Multiple-Stopband Filters for Interference Suppression in UWB Applications," *IEEE Trans. Microw. Theory Techn.,* vol. 54, no. 8, pp. 3333–3338, Aug. 2006.

[72] M. H. Ng, S.-D. Lin, J. Li, and S. Tatesh, "Coexistence studies for 3GPP LTE with other mobile systems," IEEE Communications Magazine, vol. 47, issue 4, pp. 60-65, Apr. 2009.

[73] 3GPP TS 36.104, "Evolved Universal Terrestrial Radio Access (LTE): Base Station (BS) Radio Transmission and Reception," v. 10.2.0, May 2011.

Chapter 2

Shunt type CRDN (S-CRDN)

2.1. Problem description

2.1.1 Working mechanism and Circuit model of A CRDN
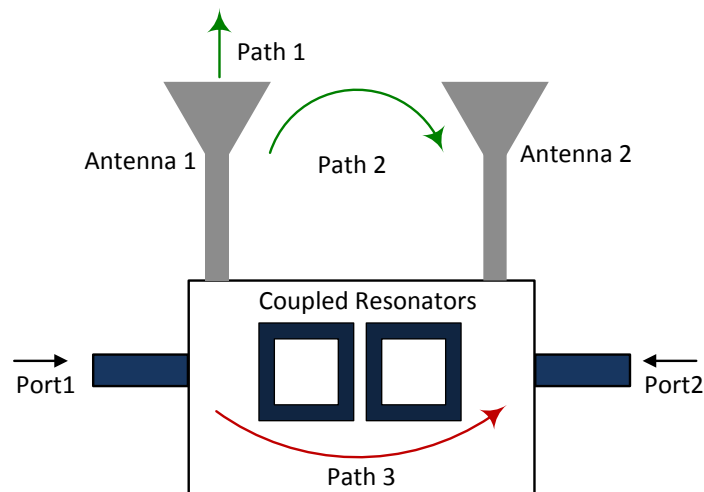
Figure 2.1 Basic mechanism of the CRDN.

    The basic working mechanism of the shunt-type CRDN in decoupling two strongly coupled antennas is shown in Fig. 2.1. Assuming perfectly matched ports, the power fed to port 1 can only be dispensed through three different ways. One way is to go through antenna 1 and then radiates into free space (path 1). Another way is to leak to port 2 through the unwanted mutual coupling between antenna 1 and antenna 2 (path 2). The third way is to go through the CRDN and flows out again from port 2 (path 3). With properly chosen characteristics of the CRDN, the undesired power coupling due

to path 2 can be mostly canceled by the signal through path 3. As a result, there will be no current induced on port 2 and decoupling of the two signal ports can thus be achieved.

From the network point of view, a pair of tightly coupled antennas can always be represented by a microwave two-port network, which can be described by a 2-by-2 admittance matrix ($\mathbf{Y}^A$) with **complex** entries:

$$\mathbf{Y}^A = \begin{bmatrix} Y_{11}^A & Y_{12}^A \\ Y_{21}^A & Y_{22}^A \end{bmatrix} \tag{2.1}$$
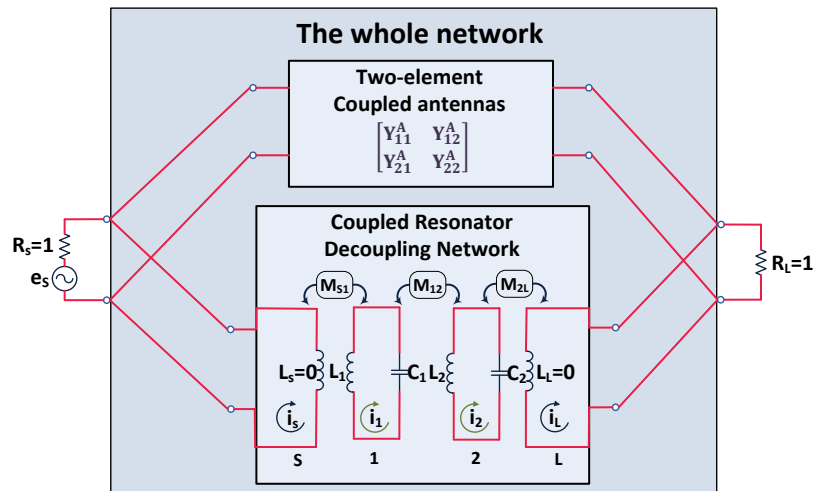
Figure 2.2 Network representation of two coupled antennas in shunt with a second order CRDN.

For the decoupling configuration shown in Fig. 2.1, the decoupling network consisting of a series of coupled resonators (i.e. CRDN) is connected to the pair of coupled antennas in shunt. The two matched ports of the decoupled whole network are terminated by two unit loads, which indicates that the system is matched. Assuming the CRDN is lossless network, the entries in its admittance matrix $\mathbf{Y}^F$ must be purely imaginary. Obviously, the total admittance is the sum of the two individual admittance matrices as:

$$\mathbf{Y} = \begin{bmatrix} Y_{11} & Y_{12} \\ Y_{21} & Y_{22} \end{bmatrix} = \begin{bmatrix} Y_{11}^A + Y_{11}^F & Y_{12}^A + Y_{12}^F \\ Y_{21}^A + Y_{21}^F & Y_{22}^A + Y_{22}^F \end{bmatrix} \tag{2.2}$$

Notice that the overall network is reciprocal but not necessarily symmetric. The scattering parameters of the overall network can be obtained from the admittance parameters by [1]

$$S_{11} = \frac{(1 - Y_{11})(1 + Y_{22}) + Y_{12}Y_{21}}{(1 + Y_{11})(1 + Y_{22}) - Y_{12}Y_{21}}, \tag{2.3}$$

$$S_{21} = \frac{-2Y_{21}}{(1 + Y_{11})(1 + Y_{22}) - Y_{12}Y_{21}}, \tag{2.4}$$

$$S_{22} = \frac{(1 + Y_{11})(1 - Y_{22}) + Y_{12}Y_{21}}{(1 + Y_{11})(1 + Y_{22}) - Y_{12}Y_{21}}. \tag{2.5}$$

It can be seen, from (3), that the two ports of the whole network will be well isolated within a given frequency range if

$$Y_{21}(\omega_B) = Y_{21}^A(\omega_B) + Y_{21}^F(\omega_B) \approx 0, \tag{2.6}$$

where ω_B is the bandpass radian frequency variable.

Since Y_{21}^F is purely imaginary, (2.6) implies following two decoupling conditions:

$$\mathrm{Re}\left\{Y_{21}^A(\omega_B)\right\} \approx 0 \tag{2.7a}$$

and

$$j \cdot \mathrm{Im}\left\{Y_{21}^A(\omega_B)\right\} + Y_{21}^F(\omega_B) \approx 0 \tag{2.7b}$$

Having had (2.7) satisfied, (2.3) and (2.5) can be simplified to:

$$S_{11} \approx \frac{1 - Y_{11}^A - Y_{11}^F}{1 + Y_{11}^A + Y_{11}^F} \qquad (2.8a)$$

and

$$S_{22} \approx \frac{1 - Y_{22}^A - Y_{22}^F}{1 + Y_{22}^A + Y_{22}^F} \qquad (2.8b)$$

from which the decoupling and matching conditions can be obtained as:

$$\text{Re}\left\{ Y_{kk}^A(\omega_B) \right\} \approx 1, \quad k = 1, 2 \qquad (2.9a)$$

and

$$j \cdot \text{Im}\left\{ Y_{kk}^A(\omega_B) \right\} + Y_{kk}^F(\omega_B) \approx 0, \quad k = 1, 2 \qquad (2.9b)$$

2.1.2 The Mutual Admittance of Coupled Antennas

2.1.2.1 The real part of mutual admittances:

1. The theory:

Since the CRDN is a passive network with purely imaginary admittance/impedance parameters, condition (2.7a) must be satisfied before using CRDNs. The most efficient and convenient method is to insert a section of transmission line at the antenna port. For single band applications, a section of uniform line whose characteristic impedance Z_0 is the same as the coupled antenna port impedance will be sufficient.

For the originally coupled antenna array, we assume its ports are matched to the characteristic impedance (admittance) of the system, so we can write:

$$[S^A] = \begin{bmatrix} 0 & |S_{21}| \cdot e^{j\phi} \\ |S_{21}| \cdot e^{j\phi} & 0 \end{bmatrix} \tag{2.10}$$

Inserting two transmission lines with the same characteristic impedance and electrical length of θ at the ports, the resultant scattering matrix is:

$$[S^{A'}] = \begin{bmatrix} 0 & |S_{21}| \cdot e^{j(\phi-2\theta)} \\ |S_{21}| \cdot e^{j(\phi-2\theta)} & 0 \end{bmatrix} \tag{2.11}$$

Using the S-to-Y transformation, the mutual admittance can be obtained as:

$$Y_{21}^{A'} = Y_0 \frac{-2|S_{21}| \cdot e^{j(\phi-2\theta)}}{1-|S_{21}|^2 \cdot e^{j2(\phi-2\theta)}} \tag{2.12}$$

Finding the real part of $Y_{21}^{A'}$, and setting it to zero will result in the following relation:

$$(2|S_{21}| - 2|S_{21}|^3) \cdot \cos(\phi - 2\theta) = 0 \tag{2.13}$$

The solution of (2.13) can now be easily found as:

$$\theta = \frac{1}{2}(\phi - \frac{\pi}{2} \pm k\pi) \quad k = 0,1,2,... \tag{2.14}$$

It should be noted that equation (2.14) will only be valid at a single frequency point. It is normally chosen to be the center frequency of the band we are interested in. But sometimes it is better to choose another frequency point to minimize the sum of $Y_{21}^{A'}$ within the band of interest, normally, this frequency point should not be far away from the center frequency.

2. An EM example:

One EM simulation example is shown to illustrate the admittance transformation process for two coupled cone-shaped antennas shown in Fig. 2.3 (a). The resonance frequency (f_0) is chosen to be 2.45GHz. There are four criterions for choosing a proper transmission line length θ:

> ➢ **Criterion 1-1**: Setting θ such that $Re\left(Y_{21}^{A}{}'\right) = 0$ at the center frequency f_0, such that $Im\left(Y_{21}^{A}{}'\right)$ is positive.

> ➢ **Criterion 1-2**: Setting θ such that $Re\left(Y_{21}^{A}{}'\right) = 0$ at the center frequency f_0, such that $Im\left(Y_{21}^{A}{}'\right)$ is negative.

> ➢ **Criterion 2-1**: Setting θ such that $Re\left(Y_{21}^{A}{}'\right)$ is minimized within a narrow band of interest.

> ➢ **Criterion 2-2**: Setting θ such that $Re\left(Y_{21}^{A}{}'\right)$ is minimized within a wide band of interest.

All criterions are used in this example and their resultant transformed mutual admittance parameters are compared in Fig. 2.3 (b). It should be noted that for **Criterion 1**, there are in general two solutions for θ, one will result in positive $Im(Y_{21}^{A}{}')$ at f_0, while the other results in negative $Im(Y_{21}^{A}{}')$. According to the size constraint of practical design, one of these two solutions with smaller θ is normally used. However, in some cases, the slope of $Im(Y_{21}^{A}{}')$ might also be considered, as shown in Fig. 2.3 (b).

For **Criterion 2**, one can minimize $Re\left(Y_{21}^{A}{}'\right)$ within a wide band or a relative narrow band. In this example, *Criterion 2-1* is set as to minimize $Re(Y_{21}^{A}{}')$ within 2.4GHz to 2.5 GHz such that $|Re(Y_{21}^{A}{}')|$ is smaller than 0.003 and *Criterion 2-1* is set as to minimize $Re(Y_{21}^{A}{}')$ within 2.4 GHz to 2.5 GHz such that $|Re(Y_{21}^{A}{}')|$ is smaller than 0.01. Using these four criterions, four different solutions of θ can be obtained, and the $Re(Y_{21}^{A}{}')$ and $Im(Y_{21}^{A}{}')$ for these four solutions are superposed in Fig. 2.3 (b).

Criterion 1-1:

$f_0 = 2.45$ GHz $Re(Y_{21}^A{}')$ equals to zero, $Im(Y_{21}^A{}')$ is positive $\quad \theta = 89.3°$

Criterion 1-2:

$f_0 = 2.45$ GHz $Re(Y_{21}^A{}')$ equals to zero, $Im(Y_{21}^A{}')$ is negative $\quad \theta = 24.9°$

Criterion 2-1:

within 2.4 GHz to 2.5 GHz $Re(Y_{21}^A{}')$ smaller than 0.003 $\quad \theta = 95.16°$

Criterion 2-2:

within 2.3 GHz to 2.6 GHz $Re(Y_{21}^A{}')$ smaller than 0.01 $\quad \theta = 106°$
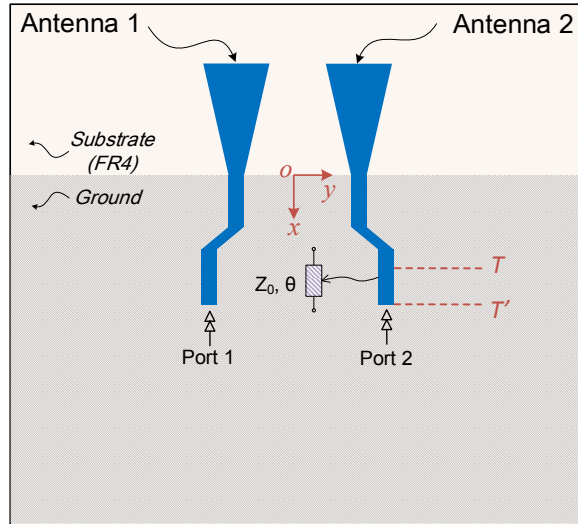
(a)
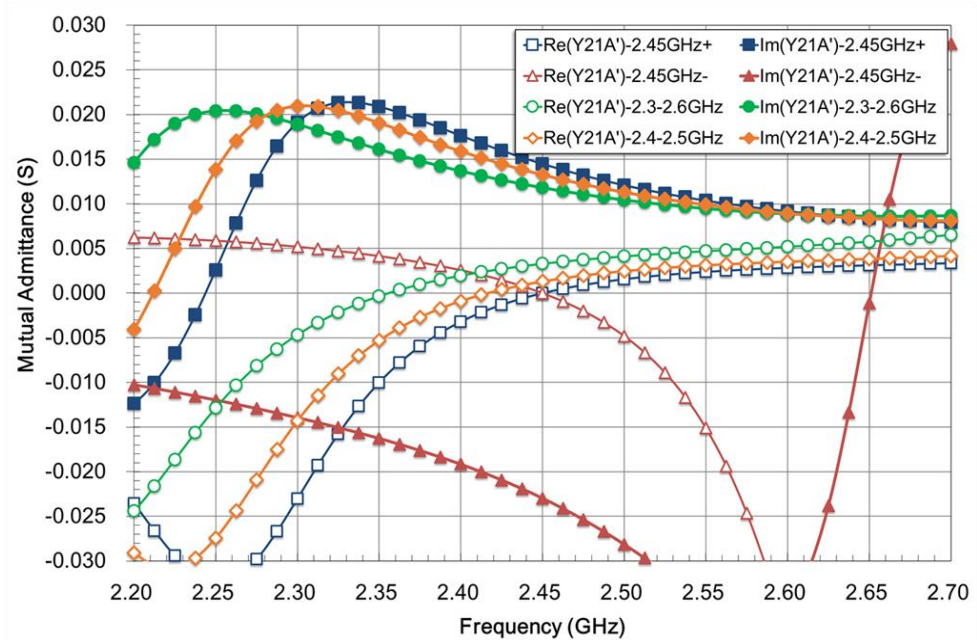
(b)

Figure 2.3 (a) Admittance transformation for a pair of coupled cone-shaped printed antennas. (b) The $Re(Y_{21}^A{}')s$ and $Im(Y_{21}^A{}')s$ for different criterions.

2.1.2.2 The imaginary part of mutual admittances:

To have a thorough understanding about the characteristic of coupled antennas, several kinds of coupled antennas are studied by EM simulation in this section, such as: coupled PIFA antennas (Fig. 2.4), coupled cone-shaped printed antennas (Fig. 2.5), coupled cylindrical monopoles (Fig. 2.6) and one printed inverted-F antennas and one cone-shaped printed antenna that are coupled (Fig. 2.7). If only the spacing D between the antennas are to be changed while other dimensions such as ground size, electrical length of the antennas are adjusted to maintain matching performances, different mutual admittances are expected to be observed, which are also superposed in Figs. 2.4, 2.5, 2.6 and 2.7, respectively. It is assumed that proper transmission lines are already included in these admittances using **Criterion 1** from the last section. It should also be mentioned that in these plots, the admittances are transformed to the lowpass frequency domain with reference to unit terminations and designated fractional bandwidth (FBW) by:

$$s = \frac{1}{FBW} \left(\frac{\omega_B}{\omega_0} - \frac{\omega_0}{\omega_B} \right) \tag{2.15}$$

There are several intriguing findings from these results:

1) The real part of mutual admittances can always be transformed to zero at the frequency point of interest. However, for different antenna form factor and spacing, the slope of $Re(Y_{21}^{A\prime})$ can be quite different.

2) Having had $Re(Y_{21}^{A\prime}) = 0$ at the frequency point of interest, the $Im(Y_{21}^{A\prime})$s of all types of antennas can be approximated by the function of $y_{21} = ks + b$,

$$y_{21} = ks + b \tag{2.16}$$

while s is the frequency variable in the low-pass domain and k is the slope, b is a constant. For most cases, the k is very close to zero and $Im(Y_{21}^{A\prime})$ can be treated as

a constant within a certain band of interest, such as most of the curves in Fig. 2.5 (c) and Fig. 2.7 (c).

3) For the same type of coupled antenna pairs, the value of $Im(Y_{21}^{A\prime})$ is mainly dependent on the spacing D or coupling level.

Dimensions (Unit: mm)

L_G=60
L_A=24.5
W_A=5
H_A=8
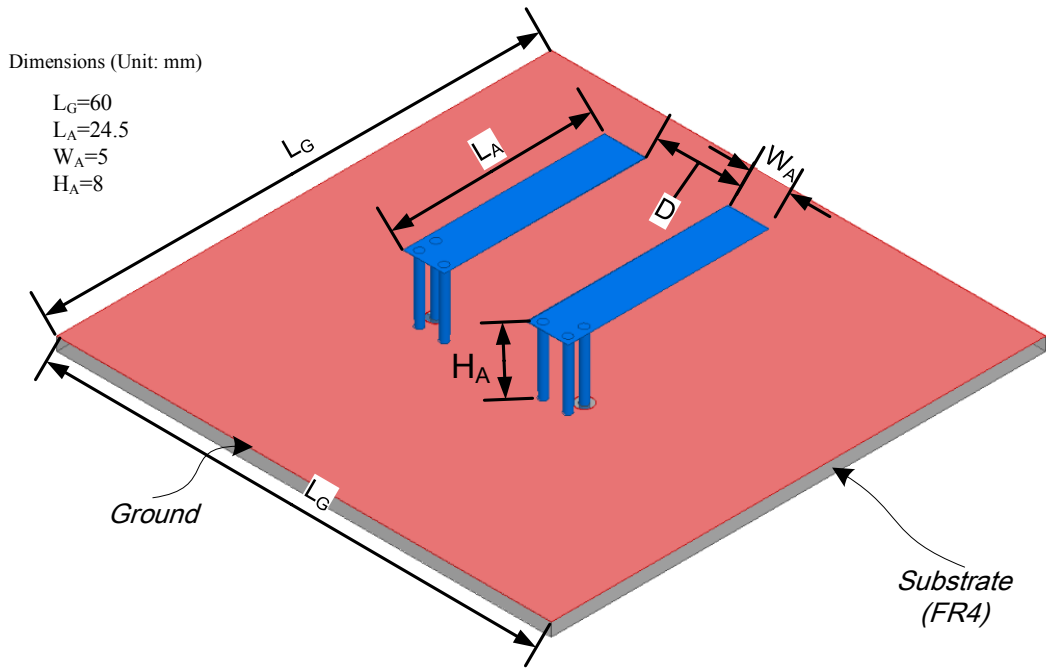
(a)
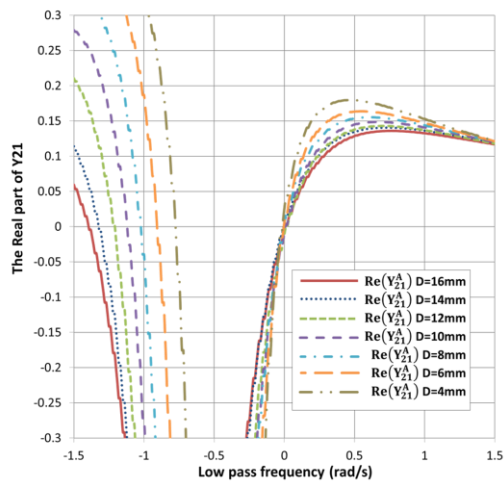
(b)
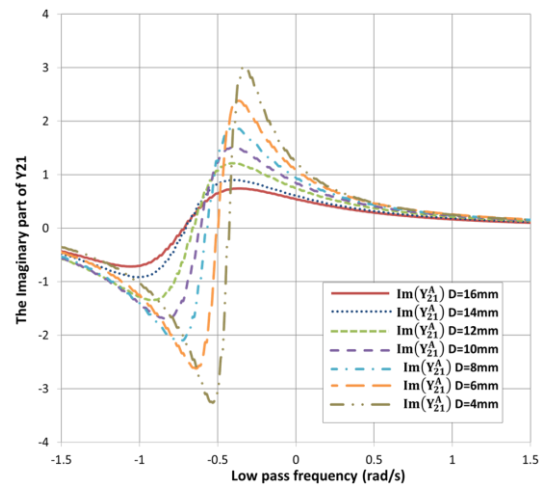
(c)

Figure 2.4 (a) The physical layout; (b) The real part of mutual admittance; and (c) The imaginary of mutual admittance of two coupled PIFA antennas.
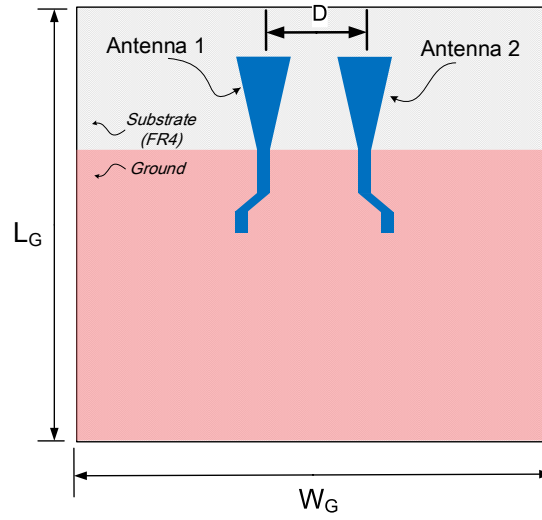
(a)
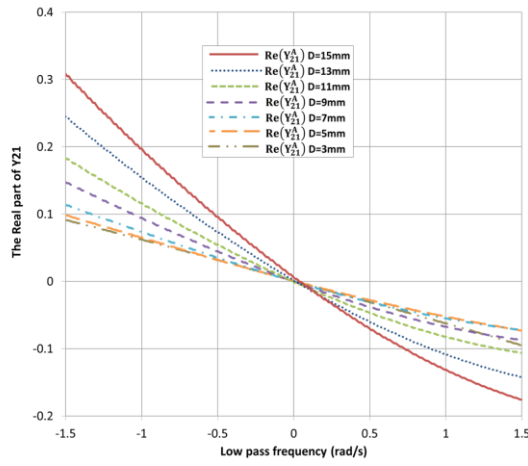
(b)
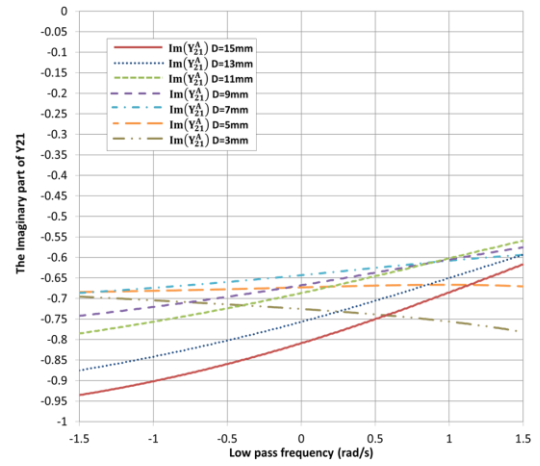
(c)

Figure 2.5 (a) The physical layout; (b) The real part of mutual admittance; and (c) The imaginary of mutual admittance of two coupled cone-shaped printed antennas.
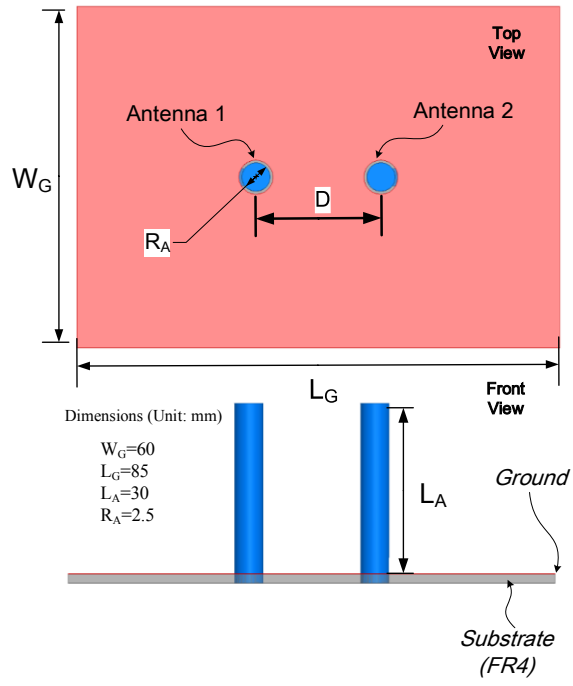
(a)
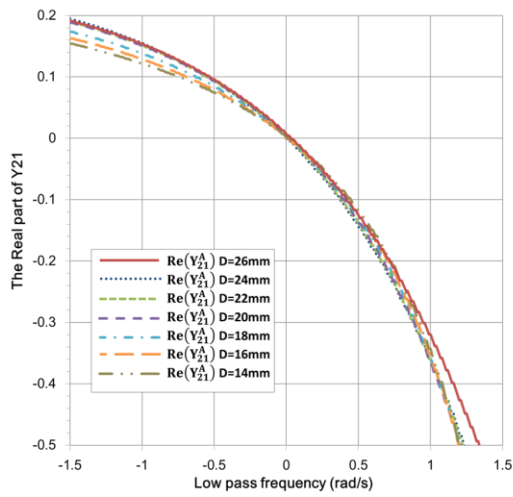
(b)
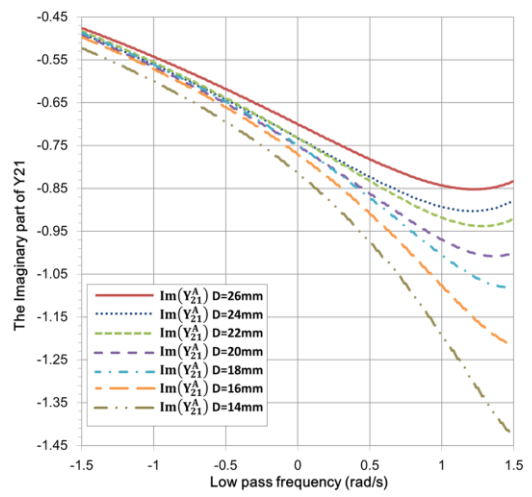
(c)

Figure 2.6 (a) The physical layout; (b) The real part of mutual admittance; and (c) The imaginary of mutual admittance of two coupled cylindrical monopoles.
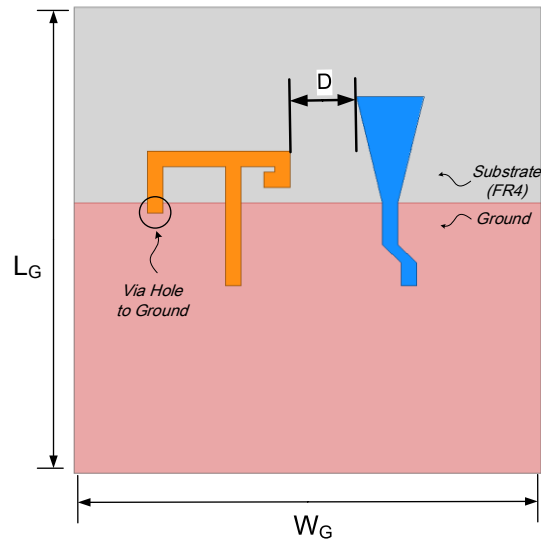
(a)
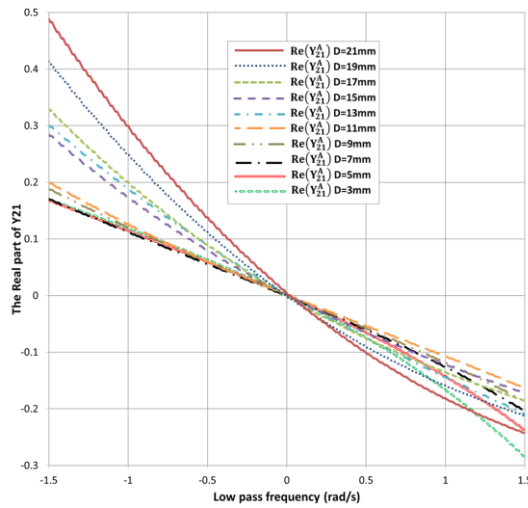
(b)
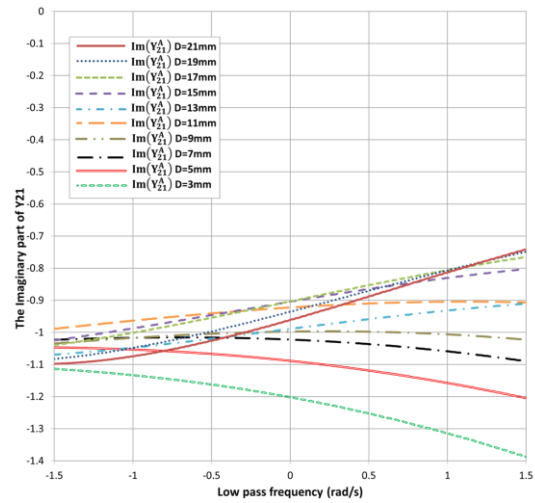
(c)

Figure 2.7 (a) The physical layout; (b) The real part of mutual admittance; and (c) The imaginary of mutual admittance of one printed inverted-F antenna and one cone-shaped antenna that are coupled to each other.

A constant $Im(Y_{21}^A)$ for many types of coupled antennas is an important discovery. One explanation of such phenomenon can be found in [2], where the classic coupled resonator circuit model in filter synthesis and design [3] are to represent two strongly coupled antennas. Its dual circuit model are used in this thesis as shown Fig. 2.8. Following simple circuit nodal analysis, the mutual admittance can be found to be

nearly constant within a certain band of interest. Detailed deduction of its lossless form will be elaborated in section 2.2.1.
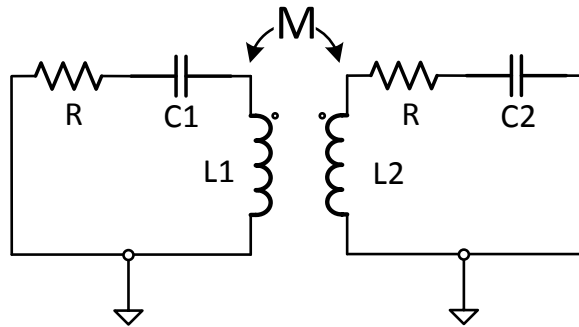
Figure 2.8 Circuit model for two coupled antennas.

2.2. A Second Order S-CRDN

It is already shown in **Section 2.1.2.2** that the mutual admittance for two coupled antennas can be describe by a linear function and most of the time a constant. The next step is to find a proper network configuration, that have similar but opposite mutual admittance, such that the mutual couplings between antennas can be cancelled out completely within the band of interest. A Coupled Resonator Decoupling Network (CRDN) seems to be the best option at hand because of its unique features in providing a constant mutual admittance while maintaining a matching condition. More importantly, since the strongly coupled antennas can also be treated as two coupled lossy resonators, it seems that using coupled resonators to connect in shunt (S-CRDN) with the coupled antennas to decouple them is a rational choice.

The concept of coupling matrix (CM), which is developed for designing bandpass filters, can be applied to describe the CRDN as shown in Fig. 2.2. The design process of this network starts with synthesizing the rational functions for the admittance parameters using the requirements imposed by (2.7) and (2.9). Up till now, there are two types of S-CRDN: the all pole type and the cross coupled type. They will be discussed in detail in the subsequent sections.

2.2.1. All pole S-CRDNs

2.2.1.1 The synthesis theory

For a second-order CRDN without any finite transmission zeroes (all pole), the mutual admittance can be expressed as:

$$Y_{21}^F(s) = \frac{j\gamma}{(s - jp_1)(s - jp_2)} \qquad (2.17)$$

where γ is a real constant, jp_1 and jp_2 are two system poles. Although the low pass frequency variable $s = \sigma + j\omega$ is defined in the complex plane, we can always evaluate the function in the imaginary $j\omega$ axis.

Without loss of generality, it can be assumed that $p_1 < p_2$. It is worth mentioning that for the lowpass prototype circuit of a coupled resonator network, the rational function $Y_{21}^F(s)$ is not necessarily a quotient of even to odd or odd to even polynomials. This is because frequency invariant reactances (FIRs) and an extra inverter element are introduced in the second-order lowpass prototype [4] (See Appendix A1). However, with appropriate approximation in converting the rational function to a network realization, the resultant network can always be described by a quotient of even to odd or odd to even polynomials. Furthermore, $Y_{21}^F(s)$ may not be positive real [5] (See also **Appendix A2**).

The partial fractional expansion of (2.17) is expressed as:

$$Y_{21}^F(s) = \frac{r_1^{21}}{s - jp_1} + \frac{r_2^{21}}{s - jp_2} \qquad (2.18)$$

where residues $r_1{}^{21} = \gamma / (p_1 - p_2)$ and $r_2{}^{21} = \gamma / (p_2 - p_1)$. Notice that the residues of $Y_{21}^F(s)$ must be real but with opposite signs. In general, the residues of $Y_{11}^F(s)$ and $Y_{22}^F(s)$ can be obtained through [4]:

$$\sqrt{r_k^{11} \cdot r_k^{22}} = \pm r_k^{21}, \quad k = 1, 2 \tag{2.19}$$

Based on the residues of $Y_{21}^F(s)$, proper signs in (2.19) must be chosen. For a realizable passive network, $Y_{11}^F(s)$ and $Y_{22}^F(s)$ must be positive real [5].

Then to find the rational functions $Y_{11}^F(s)$ and $Y_{22}^F(s)$ from (2.19), two positive scaling coefficients c and d need to be introduced with which the residues can be expressed as:

$$
\begin{aligned}
r_1^{11} &= c \cdot \left| r_1^{21} \right| = \frac{c|\gamma|}{(p_2 - p_1)}, & r_2^{11} &= d \cdot \left| r_1^{21} \right| = \frac{d|\gamma|}{(p_2 - p_1)}, \\
r_1^{22} &= \frac{1}{c} \cdot \left| r_2^{21} \right| = \frac{|\gamma|}{c(p_2 - p_1)}, & r_2^{22} &= \frac{1}{d} \cdot \left| r_2^{21} \right| = \frac{|\gamma|}{d(p_2 - p_1)},
\end{aligned}
\tag{2.20}
$$

The absolute signs in (10) ensure $Y_{11}^F(s)$ and $Y_{22}^F(s)$ to be positive real. Therefore, the rational functions $Y_{11}^F(s)$ and $Y_{22}^F(s)$ can now be expressed as:

$$Y_{11}^F(s) = \frac{c|\gamma|}{(s - jp_1)(p_2 - p_1)} + \frac{d|\gamma|}{(s - jp_2)(p_2 - p_1)}, \tag{2.21a}$$

$$Y_{22}^F(s) = \frac{|\gamma|}{c(s - jp_1)(p_2 - p_1)} + \frac{|\gamma|}{d(s - jp_2)(p_2 - p_1)}. \tag{2.21b}$$

By substituting (2.17) and (2.21) into (2.7b) and (2.9b), parameters γ, p_1, p_2, c and d can be determined analytically and the transversal $N + 2$ coupling matrix for the decoupling network can then be obtained by following the procedure given in [4]. The

results are given here:

$$m_{S1} = \frac{r_1^{21}}{\sqrt{r_1^{22}}}, \quad m_{S2} = \frac{r_2^{21}}{\sqrt{r_2^{22}}},$$

$$m_{L1} = \sqrt{r_1^{22}}, \quad m_{L2} = \sqrt{r_2^{22}}, \tag{2.22}$$

$$m_{11} = -p_1, \quad m_{22} = -p_2, \quad m_{SL} = 0.$$

where m_{S1}, m_{S2}, m_{L1}, m_{L2} and m_{SL} are the coupling coefficients between source to resonator 1, source to resonator 2, load to resonator 1, load to resonator 2, and source to load, respectively. Entries m_{11} and m_{22} are the self-couplings of resonator 1 and resonator 2, respectively.

To obtain the coupling matrix for a folded coupling structure, which is more convenient to realize than the transversal one, a matrix similarity transformation with pivot (2, 3) can be applied [4]. The transformed coupling matrix can be analytically expressed by

$$m_{S1}' = \sqrt{\frac{|\gamma| \cdot (c+d)}{(p_2 - p_1)}}, \quad m_{2L}' = \sqrt{\frac{|\gamma| \cdot (c+d)}{cd \cdot (p_2 - p_1)}},$$

$$m_{12}' = \frac{\gamma}{|\gamma|} \sqrt{\frac{d}{c}} \cdot \frac{c}{c+d} \cdot (p_2 - p_1), \quad m_{11}' = \frac{-(cp_1 + dp_2)}{c+d},$$

$$m_{22}' = \frac{-(cp_2 + dp_1)}{c+d}, \quad m_{SL}' = 0. \tag{2.23}$$

For a symmetrical decoupling network with symmetrical poles, $c = d = 1$ and $-p_1 = p_2 = p$, the coupling matrix can be simplified to

$$m_{S1}' = m_{L2}' = \sqrt{\frac{|\gamma|}{p}}, \quad m_{12}' = \frac{\gamma p}{|\gamma|},$$

$$m_{11}' = m_{22}' = 0, \quad m_{SL}' = 0. \tag{2.24}$$

It has been theoretically shown from the above derivation that a decoupling network can be realized by a coupled resonator network whose coupling coefficients are solely determined by the poles and residues of the network, and eventually depend on the properties of the coupled antennas.

2.2.1.2 Design Procedures with an illustrative example

To illustrate the design procedure, a compact antenna array working at 2.6 GHz (LTE band 7) as shown in Fig. 2.9 (a) is considered. The array is composed of one cone-shaped monopole and one meandered monopole. The center-to-center distance between the two elements D is 16.55 mm ($0.14\lambda_0$) and the edge-to-edge distance S is 3.9 mm ($0.03\lambda_0$). Other dimensions are also shown in Fig. 2.9 (a). The simulated and the measured S-parameters are shown in Fig. 2.9 (b), in which an isolation of poorer than 8 dB at 2.6 GHz is observed, although both antennas can be well matching without any external matching networks. An isolation of around 8 dB means that more than 10% percent of the radiated power is coupled to the other antenna rather than radiating to the free space. In other word, the approximate radiation efficiency loss is estimated to be more than 10%.

Dimensions (Unit: mm)

W_{A1}=12.15 L_{A2}=4.35
L_{A1}=18.9 L_{A3}=7.15
L_F=7.95 L_{A4}=10.3
S_F=3.45 L_{A5}=12.15
L_E=4.15 L_{A6}=6.4
W_F=3.15
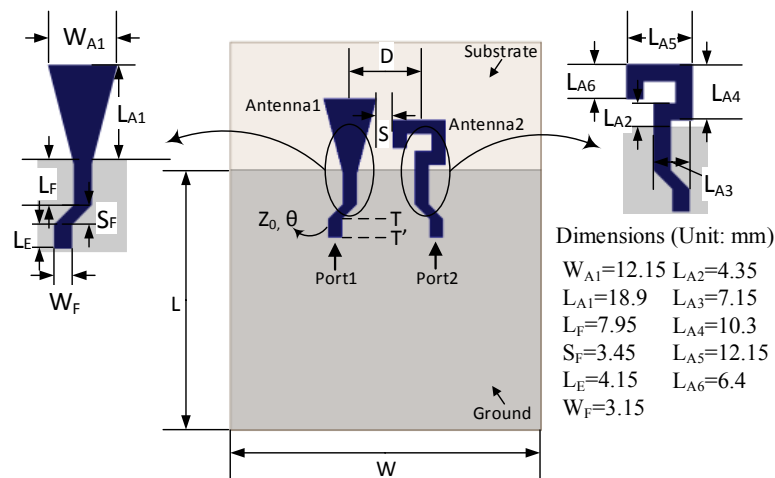
(a)
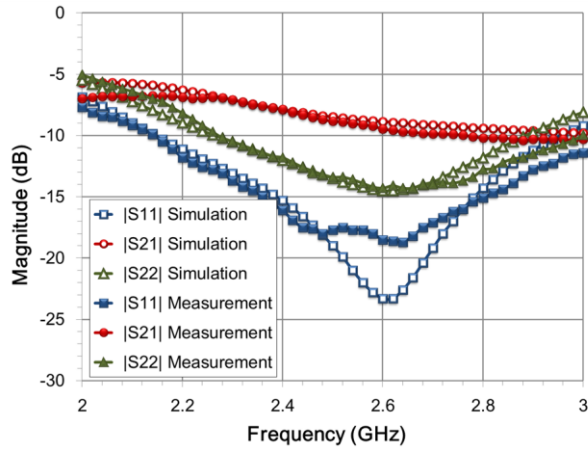
(b)
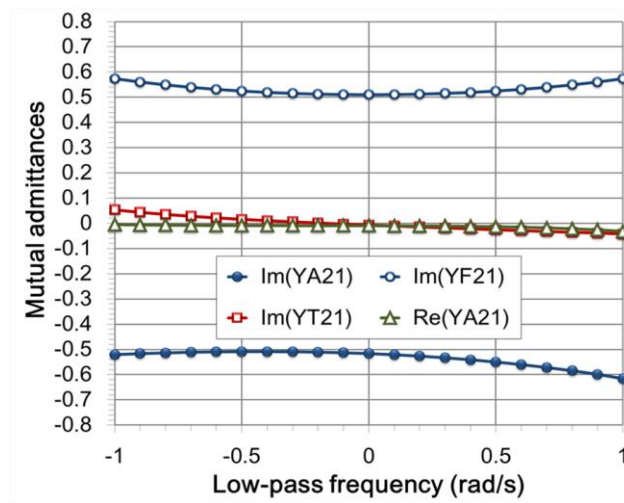
(c)
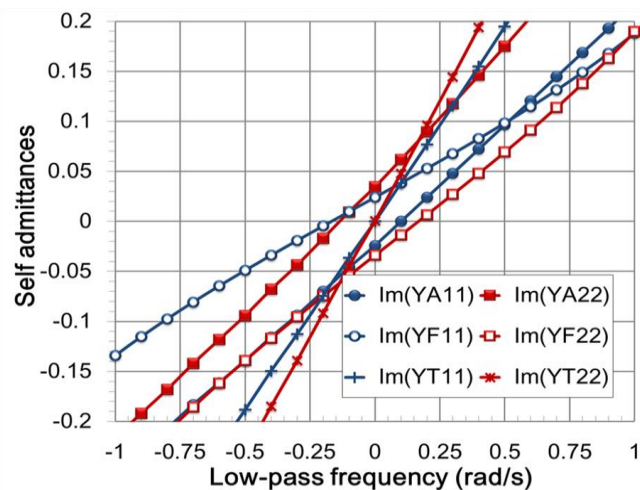
(d)

Figure 2.9 (a) An asymmetric two-element compact array. (b) Simulated and measured S-parameter of the array. (c) Simulated Y_{21} of the array and a CRDN.   (d) Simulated normalized Y_{11} and Y_{22} of the array and a CRDN.

In order to determine parameters γ, p_1, p_2, c, and d and to obtain the coupling coefficients, the admittance parameters of the coupled antennas are transformed to the lowpass frequency domain with reference to unit terminations and designated fractional bandwidth (*FBW*) by (2.15).

1. Mutual Admittance Transformation:

A section of transmission line with its electric length determined by (2.14) is first introduced at each antenna port so that $\text{Re}\{Y_{21}^A\} = 0$ at the center frequency. Fig. 2 (c) shows the simulated Y_{21}^A in lowpass domain.

2. Decoupling and Matching Design:

It can be observed in Fig. 2.9 (c) that $Im(Y_{21}^A)$ is almost constant within the pass band ($s \in [-1,1]$). Therefore, Y_{21}^F is desired to be relatively constant within the band of interest. In other words, because the slope of Y_{21}^F at $s = 0$ is proportional to $(p_1 + p_2)$ according to (2.17), it is necessary to have $p_2 = -p_1 = p > 0$. One can then use the value of Y_{21}^F at $s = 0$ to approximate the value of Y_{21}^F within the decoupling band. As illustrated by Fig. 2.9 (c), the optimum Y_{21}^F that satisfies (2.7b) should be opposite to $j \cdot Im\{Y_{21}^A(0)\}$, that is:

$$\text{Im}\left\{Y_{21}^F(s)\right\}\Big|_{s\in[-j,j]} \approx \text{Im}\left\{Y_{21}^F(0)\right\} = \gamma\Big/p^2 = -\text{Im}\left\{Y_{21}^A(0)\right\} \tag{2.25}$$

To achieve a broadband impedance matching, $\text{Re}\{Y_{11}\}$ ($\text{Re}\{Y_{22}\}$) should be the same as $\text{Re}\{Y_{11}^A\}$ ($\text{Re}\{Y_{22}^A\}$) provided that $\text{Im}\{Y_{11}\}$ ($\text{Im}\{Y_{22}\}$) approaches zero in a broadband sense. From Fig. 2.9 (d), it is observed that, in general, $\text{Im}\{Y_{11}^A\}$ and $\text{Im}\{Y_{22}^A\}$ can be different in terms of their slopes and zero locations. Therefore, to satisfy (2.9b) at the center frequency ($s = 0$) for both ports, the following relations

are obtained by setting $s = 0$ in (2.21a) and (2.21b):

$$Y_{11}^F(0) = j \cdot \frac{|\gamma|(d-c)}{2p^2} = -j \cdot \text{Im}\{Y_{11}^A(0)\} \qquad (2.26a)$$

$$Y_{22}^F(0) = j \cdot \frac{|\gamma|(c-d)}{2cdp^2} = -j \cdot \text{Im}\{Y_{22}^A(0)\} \qquad (2.26b)$$

Since $c > 0$ and $d > 0$, it is obvious that:

$$\text{Im}\{Y_{11}^F(0)\} \cdot \text{Im}\{Y_{22}^F(0)\} < 0, \qquad (2.27)$$

which suggests that the center frequency ω_0 should be chosen in the way that $Y_{11}^A(0)$ and $Y_{22}^A(0)$ have different signs. Although this new ω_0 is different from the original center frequency of the antennas, two extra matching circuits can still be added to each port to match the decoupled antennas at the original center frequency. In this example, if $f_0 = \omega_0/2\pi$ is chosen to be 2.55 GHz, (2.26a) and (2.26b) can be satisfied simultaneously as shown in Fig. 2(d).

In some applications, the two coupled antenna might work at different center frequencies. For instance, one antenna may resonant at around 2.3 GHz as a TD-LTE antenna while another antenna might work at 2.4GHz ISM band as a Wi-Fi antenna. Thus, to decouple them, equations (2.26a) and (2.26b) must be satisfied simultaneously, resulting in an asymmetric CRDN.

For a given antenna configuration, the slope of Y_{11}^A is an inherent characteristic depending on the Q value of the antennas. In order to optimally fulfill the impedance matching condition (2.9b), one needs to minimize the slope of Y_{11}^F at the resonant frequency and to use this slope information to represent the slope of Y_{11}^F within the decoupling frequency band. Closely examining the slope,

$$\left. \frac{d\left[Y_{11}^{F}(s)\right]}{ds}\right|_{s=0} = \frac{\left|\gamma \cdot (3c - d)\right|}{2p^3} \propto \frac{1}{p^3} \tag{2.28}$$

one can find that it is inversely proportional to p^3. Therefore, a large p results in a small slope of Y_{11}^{F} within a frequency band and consequently good impedance matching can be obtained providing that a proper γ is chosen to achieve a good isolation according to (2.25). The same conclusion can be drawn for Y_{22}^{F}. Having had p chosen as large as the network realization allows, parameters γ, c, and d can be determined by (2.25) and (2.26). Consequently, the coupling coefficients in (2.23) can be obtained. It is also observed in Fig. 2 (d) that when a CRDN is added to the original coupled antenna pair, despite of improved isolation, its Q-factor increases and, consequently, the matching bandwidth decreases. The reason for this is that for two strongly coupled antennas, one antenna acts as a lossy load for the other antenna thus by Fano-limits the matching bandwidth might be greater than the decoupled ones. However, despite the matching bandwidth, the radiation efficiencies for both antennas are sacrificed for coupled antennas [2]. As a matter of fact, this decoupling technique, including all the other decoupling techniques based on inserted network scheme trades matching bandwidth for isolation and efficiency. But if antennas are designed properly, taking both decoupling and matching into consideration, the overall decoupling and matching performance can still meet design specifications.

The importance of choosing a large p for broadband matching is studied parametrically and is presented in Fig. 2.10, where the circuit in Fig. 2.2 is used with the coupled antennas shown in Fig. 2.9 (a). The decoupling bandwidths with $|S_{11}| \leq -10$ dB and $|S_{21}| \leq -20$ dB for $p = 1$, $p = 3$ and $p = 6$ are 112 MHz, 244 MHz and 317 MHz, respectively. It is seen from (2.23) and (2.24) that the maximum p is stipulated by the maximum achievable inter-resonator coupling m_{12} when realizing a CRDN. Therefore, to obtain an optimum matching performance, it is advisable to maximize

m_{12} when designing the decoupling network. For different realization technologies, such as microstrip and multilayer LTCC, the maximum realizable p can be quite different. It is interesting to observe from Fig. 2.10 that a trade-off between the isolation level and the decoupling bandwidth can be made by choosing an appropriate value of parameter p. For example, for $p=1$, a narrow band with more than 30dB isolation performance can be observed while for $p=3$, a broad band with about 20dB isolation performance is obtained.
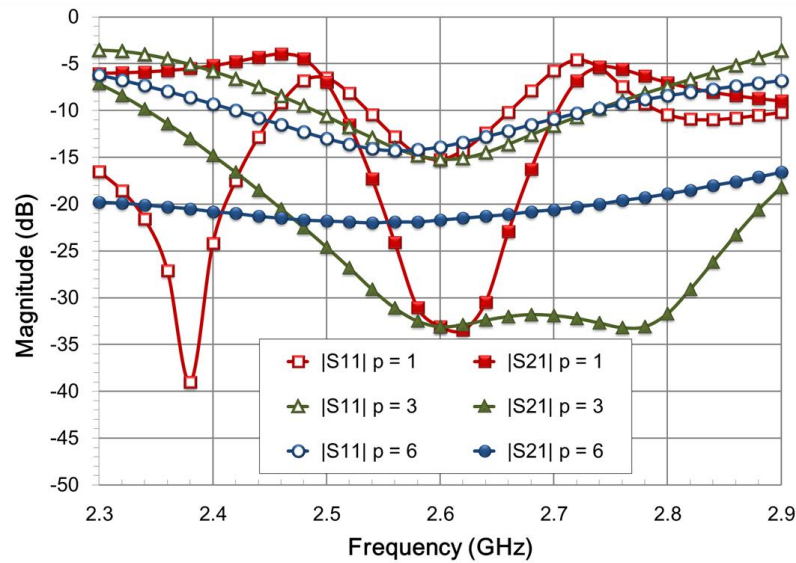
Figure 2.10 Decoupling and matching performances with different p values.

Due to the in-house fabrication constraints, the minimum line width and spacing for a PCB prototype are limited to 0.2 mm. In this example p is designed to be 3. It can be seen from Fig. 2.9 (c) that the imaginary part of Y_{21}^A is nearly a constant of -0.51 over a wide frequency band. According to (2.25), γ is found to be -4.59.

As shown in Fig. 2(d), the calculated $\text{Im}\{Y_{11}^A(0)\} = -0.024$ and $\text{Im}\{Y_{22}^A(0)\} = 0.034$. Therefore, using (2.26), c and d are found to be 0.7954 and 0.8895, respectively. Finally, with γ, p, c and d determined, the coupling coefficients for the decoupling network are obtained from (2.23). The designed lowpass coupling matrix is listed in Table 2-1 with designed fractional bandwidth FBW = 10%.

Table 2-1 Coupling coefficients of designed and realized decoupling networks for Example 1 and Example 2 (Designed FBW = 10%)

	Designed (Asym. CRDN)	Realized (Asym. CRDN)	Designed (Sym. CRDN)	Realized (Sym. CRDN)
m_{S1}	1.1353	1.1315	1.2369	1.2421
m_{2L}	1.3497	1.2227	1.2369	1.2421
m_{12}	2.9953	3.0794	3.0000	2.7142
m_{11}	-0.1675	-0.1846	0.0000	0.0000
m_{22}	0.1675	0.1847	0.0000	0.0000

3. Microstrip Realization of the CRDN

Dimensions (Unit: mm)
L_1=9.5 W_3=0.8
L_2=9.7 g_1=0.35
L_3=9.9 F_1=2.1
W_1=2.2 F_2=1.9
W_2=6.0
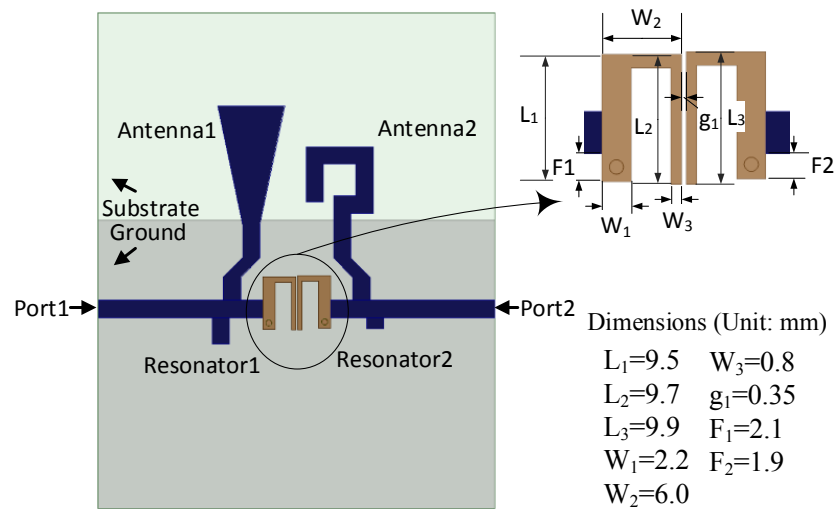
(a)
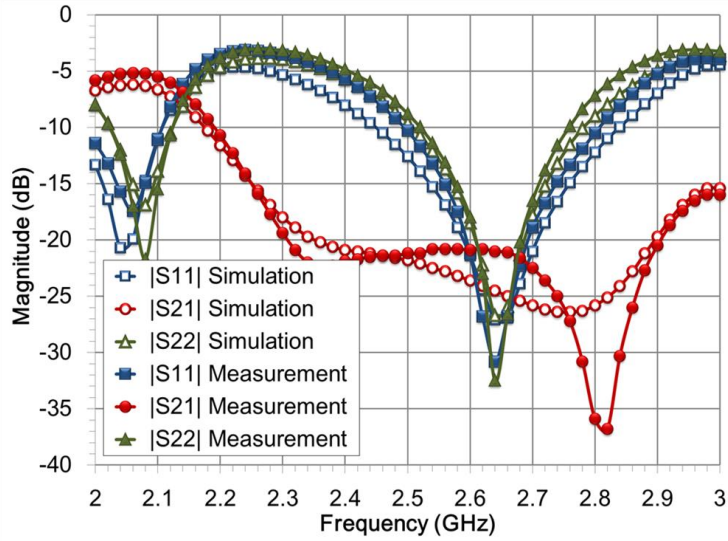
(b)

Figure 2.11 (a) Layout of the decoupled asymmetric antenna array. (b) Simulated and measured responses of the decoupled array.

The overall physical layout of the decoupled antenna array is shown in Fig. 11 (a). The coupling matrix is realized using two short-circuited and folded quarter-wavelength resonators with edge inter- resonator coupling. The smaller the gap g_1, the bigger the inter-resonator coupling m_{12}. The input/output couplings are realized by the tapped-line configuration. If one wants to increase the I/O couplings, one has to increase the variable $F1$ and $F2$. The resonant frequency of each resonator is determined by the self-coupling. With appropriate layout design, the physical dimensions are tuned by comparing the extracted coupling coefficients to the synthesized ones until the overall responses match the desired one. Details on how to design a microstrip resonator and required couplings can be found in many text books [6].

Notice that two additional matching stubs are used to broaden the matching bandwidth. Fig. 2.11 (b) shows the simulated and measured magnitudes of S-parameters of the decoupled array. The realized coupling matrix is extracted using the circuit model specified in Fig. 2.2 and is given in Table 2-1 as well for comparison. It is seen from Fig. 2.11 (b) that the decoupling bandwidth with $|S_{21}| \leq -20$ dB is about

23% and the impedance matching bandwidth with $|S_{11}| \leq -10$ dB and $|S_{22}| \leq -10$ dB is about 9.2%. For the commonly accepted 6 dB return loss requirement for mobile terminals, the matching bandwidth of this decoupled array is about 15%.

4. Working mechanism of a CRDN

To explain the working mechanism of this CRDN, EM simulated current distributions on the decoupled and the coupled arrays with excitation at port 1 are plotted in Figs. 2.12 (a) and (b), respectively. It can be observed from Fig. 2.12 (a) that the current induced by the antenna-to-antenna coupling at the terminated port (port 2) is well canceled by the current introduced through the CRDN.

(a)   (b)
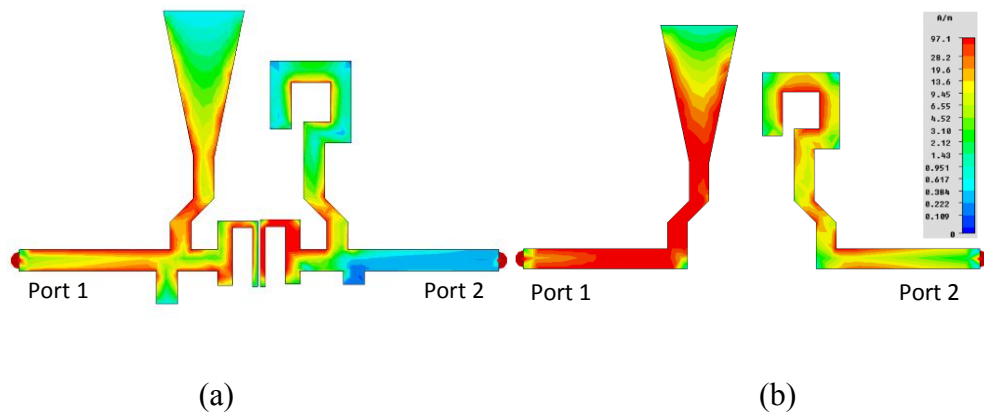
Figure 2.12 (a) Current distributions of two antennas with a CRDN; and (b) current distribution of the same antennas without a CRDN, when port 1 is excited.

5. Decoupling of a symmetrical array:
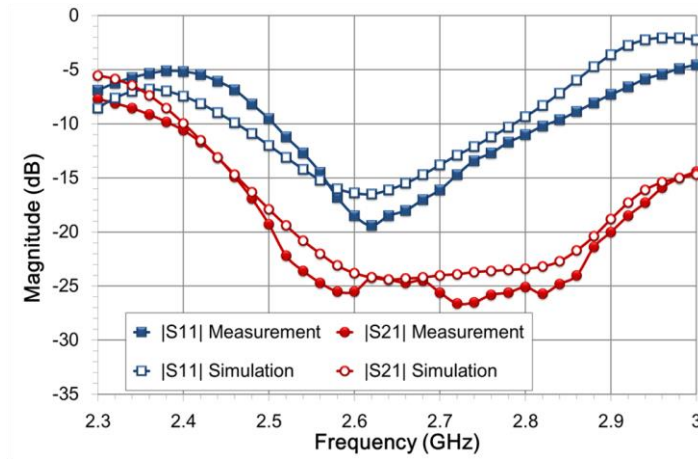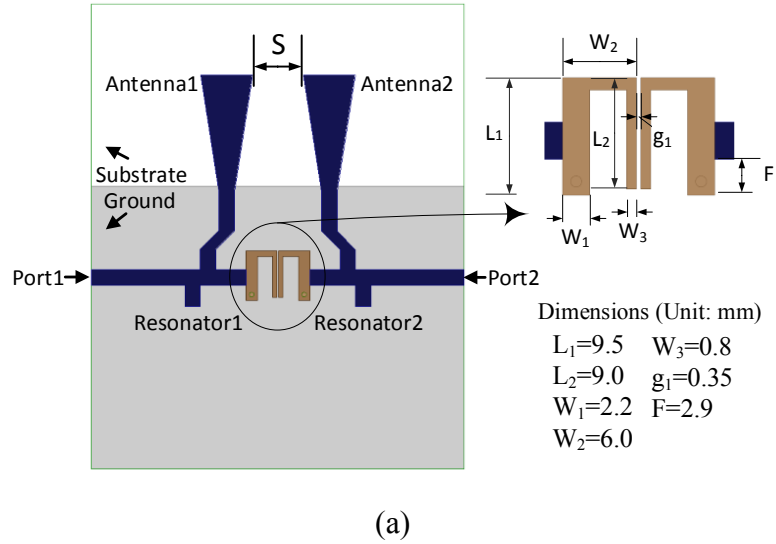
Figure 2.13 (a) Layout of the decoupled symmetric antenna array. (b) Simulated and measured responses of the decoupled array.

The decoupling theory is applied to a symmetric array in this example, in which a pair of symmetric cone-shaped monopole antennas is considered. The ground size and substrate thickness are the same as the antennas in Fig. 2.11 (a). The edge to edge spacing (S) between the two elements is 9.8 mm ($0.084\lambda_0$).

For the symmetric array, a symmetric decoupling network can be synthesized and designed according to (2.24). The synthesized lowpass coupling matrix is listed in Table 2-1. According to the coupling matrix, the physical dimensions of the resonators are determined and depicted in Fig. 2.13 (a). Two extra matching stubs are added.

Simulation and measurement results are shown in Fig. 2.13 (b) with the corresponding extracted coupling matrix listed in Table 2-1. The decoupling bandwidth for $|S_{21}| \leq -20$ dB is about 15% and the matching bandwidth for $|S_{11}| \leq -6$ dB is about 19%.

2.2.2. A S-CRDN with Source-load Couplings

For complicated scenarios, such as coupled antennas in Figs. 2.4 and 2.6, where $\mathrm{Im}(Y_{21}^A)$ is not a constant within the frequency band of interest, the all-pole type S-CRDN might not be the optimum decoupling solution. Meanwhile, closely examining the mutual admittance of all kinds of coupled antennas in Section 2.1.2, one could find that the imaginary part of mutual admittance cannot be approximated by a constant if the band of interest becomes wider. The second order S-CRDN with a source-load coupling is then developed to handle such complicated decoupling problems.

2.2.2.1 The synthesis theory

The circuit model describing shunt connected two-element compact array and a two-port S-CRDN with cross couplings is shown in Fig. 2.14, where all the ports are matched to unit terminations.
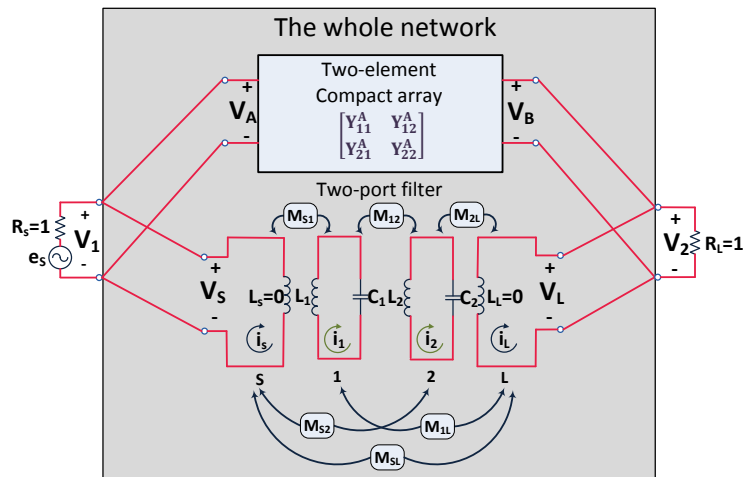
The admittance polynomials of the S-CRDN with all possible cross-couplings can be expressed as:

$$Y_{21}^C(s) = \frac{\gamma(s-z_1)(s-z_2)}{(s-p_1)(s-p_2)} \tag{2.29a}$$

and

$$Y_{11}^C(s) = \frac{\alpha(s-\beta)}{(s-p_1)(s-p_2)} \tag{2.29b}$$

which is the same as a fully canonical second-order filter network with a source-load coupling [4]. The variables z_1 and z_2 are two zeroes and p_1 and p_2 are two poles of the polynomial, while γ is a constant. Similar to Section 2.2.1.1, the partial fractional expansion of (2.29a) is expressed as:

$$Y_{21}^C(s) = \gamma + \frac{r_1^{21}}{s-p_1} + \frac{r_2^{21}}{s-p_2} \tag{2.30}$$

The two residues r_1^{21} and r_2^{21} can easily obtained as:

$$r_1^{21} = \frac{\gamma(p_1-z_1)(p_1-z_2)}{(p_1-p_2)} \tag{2.31a}$$

and

$$r_2^{21} = \frac{\gamma(p_2-z_1)(p_2-z_2)}{(p_2-p_1)} \tag{2.31b}$$

Similarly, the partial expansion for polynomials of the self-admittances can be

expressed as:

$$Y_{11}^C(s) = \frac{r_1^{11}}{s - p_1} + \frac{r_2^{11}}{s - p_2} \tag{2.32}$$

and

$$Y_{22}^C(s) = \frac{r_1^{22}}{s - p_1} + \frac{r_2^{22}}{s - p_2} \tag{2.33}$$

For a realizable passive network, i.e. an S-CRDN, the following residue conditions must be satisfied [4], [5]:

$$\begin{cases} \sqrt{r_1^{11} \cdot r_1^{22}} = \left| r_1^{21} \right| = \left| \frac{\gamma(p_1 - z_1)(p_1 - z_2)}{(p_1 - p_2)} \right| \\ \sqrt{r_2^{11} \cdot r_2^{22}} = \left| r_2^{21} \right| = \left| \frac{\gamma(p_2 - z_1)(p_2 - z_2)}{(p_2 - p_1)} \right| \end{cases} \tag{2.34}$$

For simplicity, if the CRDN is assumed to be symmetric, (2.34) can be simplified to:

$$\begin{cases} r_1^{11} = r_1^{22} = \left| r_1^{21} \right| \\ r_2^{11} = r_2^{22} = \left| r_2^{21} \right| \end{cases} \tag{2.35}$$

Comparing (2.34) and (2.35) with (2.29), the residue conditions lead to the following two constraints:

$$\gamma p^2 - [\gamma(z_1 + z_2) + \alpha]p + (\gamma z_1 z_2 + \alpha\beta) = 0 \tag{2.36a}$$

and

$$\gamma p^2 - [\gamma(z_1 + z_2) - \alpha]p + (\gamma z_1 z_2 - \alpha\beta) = 0 \tag{2.36b}$$

It should be noted that $p_2 = -p_1 = p > 0$ is already assumed in (2.36). Since there are more variables than conditions, it is more convenient to formulate the decoupling and matching conditions (2.7) and (2.9) as the following single objective constrained non-linear optimization problem:

$$\min f(x) = w_1 \cdot \sum_{i=1}^{N_s} \left| 1 - Y_{11}^A(s_i) - Y_{11}^C(s_i) \right|^2$$

$$+ w_2 \cdot \sum_{i=1}^{N_s} \left| Y_{21}^A(s_i) + Y_{21}^C(s_i) \right|^2$$

Subject to

$$\gamma p^2 - [\gamma(z_1 + z_2) + \alpha]p + (\gamma z_1 z_2 + \alpha\beta) = 0$$
$$\gamma p^2 - [\gamma(z_1 + z_2) - \alpha]p + (\gamma z_1 z_2 - \alpha\beta) = 0$$

(2.37)

where N_s is the sampling frequency points and the weight w_1 and w_2 are normally chosen to be 1.

For any given coupled antennas, if proper γ, p, α, β, z_1 and z_2 are determined by (2.37), an S-CRDN with cross couplings can be analytically synthesized following classic coupling matrix synthesis procedures in [4]. If the N+2 coupling matrix is defined as:

$$[m] = \begin{bmatrix} 0 & m_{S1} & m_{S2} & m_{SL} \\ m_{S1} & m_{11} & 0 & m_{1L} \\ m_{S2} & 0 & m_{22} & m_{2L} \\ m_{SL} & m_{1L} & m_{2L} & 0 \end{bmatrix}$$

(2.38)

Substitute all the residues and poles in (2.30), (2.32) and (2.33), we have the synthesized coupling matrix as:

$$[m] = \begin{bmatrix} 0 & r_1^{21}/\sqrt{r_1^{22}} & r_2^{21}/\sqrt{r_2^{22}} & \gamma \\ r_1^{21}/\sqrt{r_1^{22}} & -p_1 & 0 & \sqrt{r_1^{22}} \\ r_2^{21}/\sqrt{r_2^{22}} & 0 & -p_2 & \sqrt{r_2^{22}} \\ \gamma & \sqrt{r_1^{22}} & \sqrt{r_2^{22}} & 0 \end{bmatrix} \qquad (2.39)$$

The coupling matrix in (2.39) has a transversal coupling topology, which is difficult to realize [4]. It is then desirable to transform the matrix into other topologies that are convenient to implement. Unlike the all-pole type of CRDNs, (2.39) will not be transformed to a folded coupling matrix because the folded topology is not very convenient to realize in the symmetric CRDN configuration as shown in Fig. 2.15 (a). Instead, the full matrix topology in Fig. 2.15 (b) is used since it is naturally symmetric. Detailed matrix rotation process to rotate a transversal matrix into a full matrix topology will be given in Appendix A3.
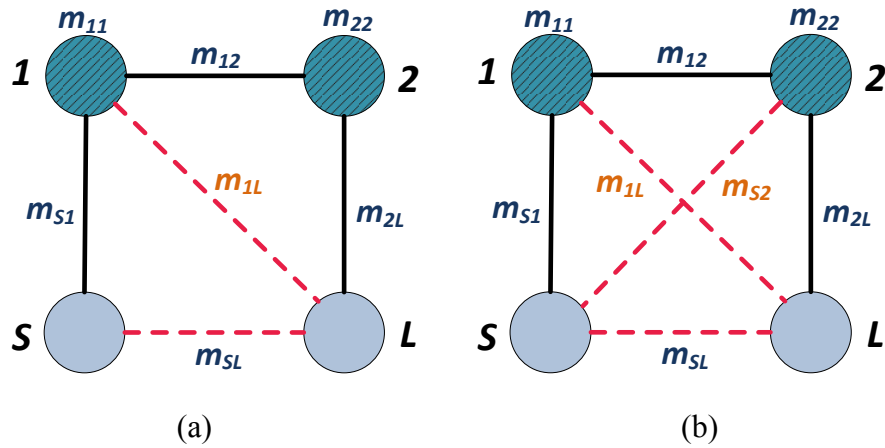
Figure 2.15 Routing diagram for (a) The folded topology; and (b) The full matrix topology for S-CRDN with all possible cross couplings.

2.2.2.2 Design Procedures with an illustrative example
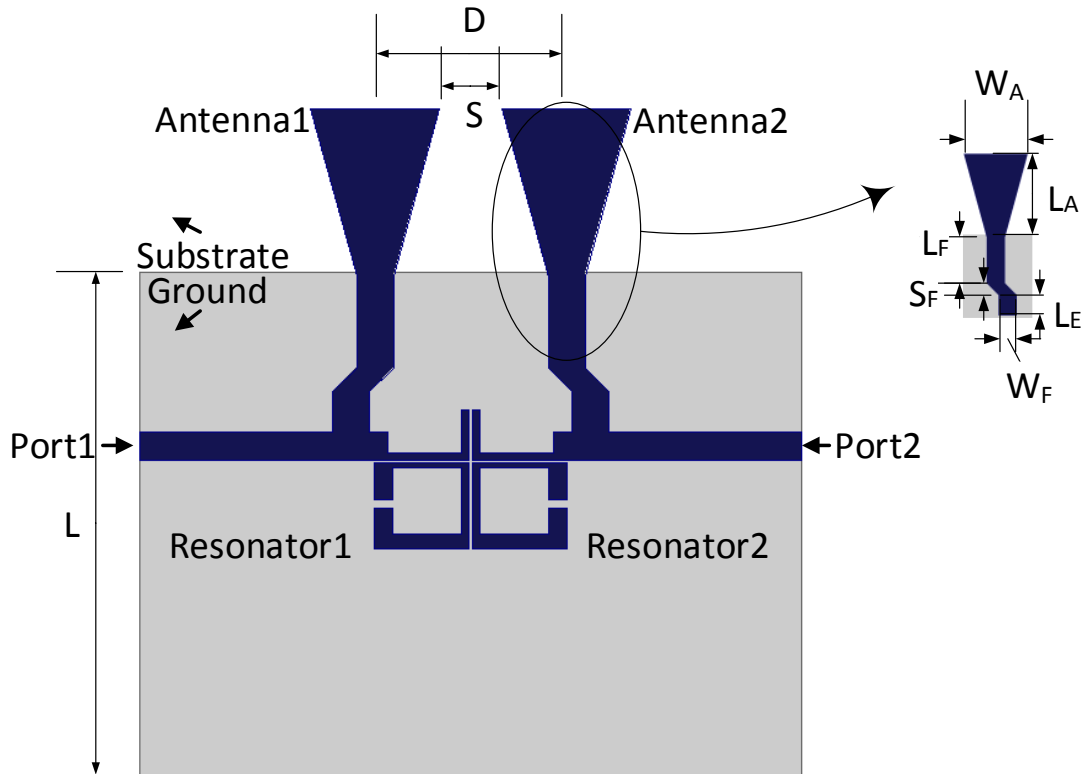
Figure 2.16 A pair of coupled cone-shaped printed antennas decoupled S-CRDN with cross couplings.

1. Coupled Antennas under investigation:

A practical example is presented here to illustrate the design procedures of a second order S-CRDN with all possible cross couplings (the full matrix topology). In this example, a pair of printed cone-shaped monopole antennas both resonating at 2.45 GHz are placed close to each other (0.16 λ_0) on an FR-4 printed-circuit board. A microstrip second-order coupled-resonator filter is then designed and inserted between the two antennas for decoupling and matching. The overall structure is shown in Fig. 2.16. Notice that the PCB has a relative dielectric constant of 4.3 and a thickness of 1.6 mm. Various design dimensions of the structure are summarized in Table 2-2. The isolation between the two antennas near the resonant frequency is around 9 dB, which is poor. Efficient decoupling means must be taken.

Table 2-2 Dimensions of the coupled antennas and the S-CRDN (unit: millimeters)

Name	Size	Name	Size	Name	Size
L	55	L_E	4.4	W_{SL}	0.8
W	72	W_F	4	g_1	1
L_A	18.2	L_R	9.3	g_2, g_3, g_4	0.3
W_A	14	W_R	10.3	L_1	8
L_F	10	S_F	2.6	L_2	4.7

2. Microstrip realization of S-CRDN:

The coupling matrix of the S-CRDN is obtained after all the poles and zeroes of the admittance polynomials are determined by optimization (2.37), which is shown in Table 2-3.

Table 2-3 Coupling coefficients of the designed and realized S-CRDN

	m_{S1}, m_{2L}	m_{11}, m_{22}	m_{S2}, m_{1L}	m_{12}	m_{SL}
Designed	0.5606	-1.4858	0.8682	1.8333	0.2063
Realized	0.5275	-1.5032	0.8100	1.8422	0.2139

The next step is to realize the synthesized coupling matrix by a pair of microstrip resonators. The square ring open loop resonator [6] is used in this thesis as shown in Fig. 2.17. The resonant frequency of such resonator is determined by the line length and the loading capacitor, whose capacitance is mainly controlled by the gap g_1. The input/output coupling m_{S1} and m_{2L} use the coupled-line coupling scheme. The bigger the g_3, the smaller the couplings will be. The inter-resonator coupling is realized by

placing the two resonators back-to-back, resulting a strong magnetic coupling. If electric inter-resonator coupling is desired, one should place the resonator in a way that the loading capacitors are facing each other, creating strong couplings through the E-field. The source-load coupling are generated by placing the end of the input and output feed line in close proximity. In general, if we increase the length L_2, the source load coupling m_{SL} can be enhanced. In microstrip realization, stray couplings from input feed line to resonator 2 and from output feed line to resonator 1 are expected to happen. By manipulating the distance between the feed lines and the resonators, the cross couplings m_{S2} and m_{1L} can also be controlled.
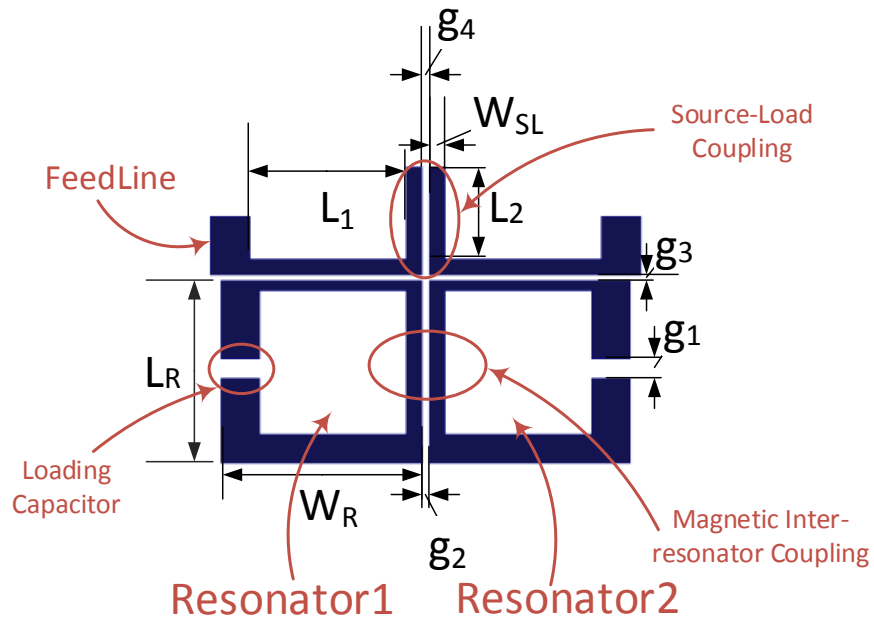
Figure 2.17 Microstrip realization of a second-order S-CRDN and its coupling mechanisms.

The initial size of the S-CRDN are generated by simple calculation. The total length of the line of resonators are around a quarter wavelength. After every iteration of EM simulation, the circuit model in Fig.2.14 is used to extract the respective realized coupling coefficients. Then it is compared with the designed coupling coefficients in Table 2-3. It is then tuned until the designed coupling coefficients are almost the same as the designed ones. This procedure is similar to a computer-aided

tuning (CAT) procedure in filter tuning [7], [8]. The final realized coupling coefficients are also shown in Table 2-3.

3. Decoupling and matching performance:

Simulated and measured scattering parameters of the decoupled array are plotted in Fig. 2.18. The decoupling bandwidth with $|S_{21}| \leq -20$ dB is 21%, while the matching bandwidth with $|S_{11}| \leq -10$ dB is 11%.
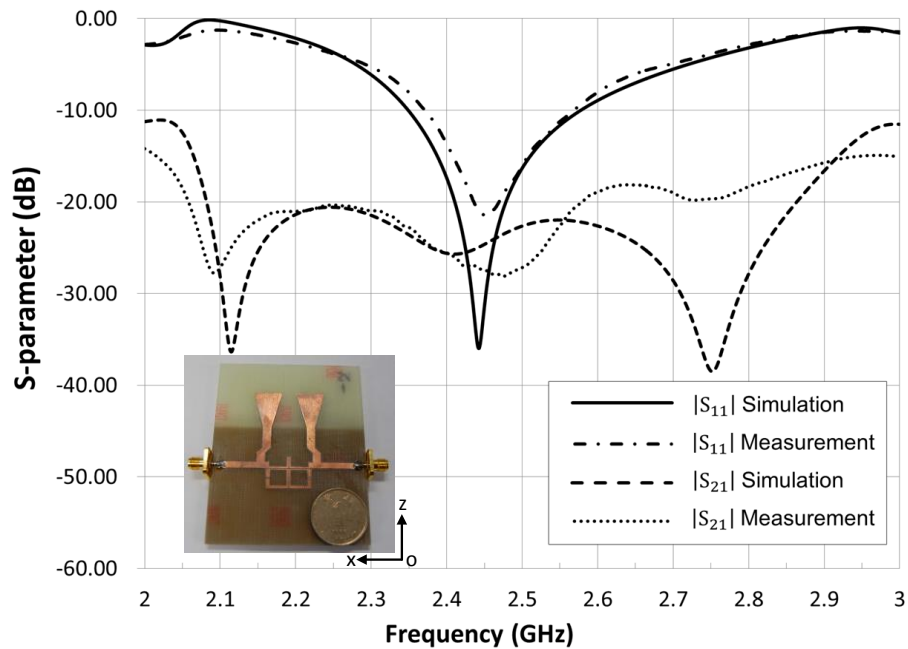
Figure 2.18 Simulated and measured scattering parameters of the decoupled array.

The simulated current distribution with port 1 excited is given in Fig. 2.19. The intentional coupling is clearly shown in region A. Such coupling cancels out the unwanted antenna-to-antenna coupling shown in region B. As a result, there is almost no current induced in region C compared to region D.
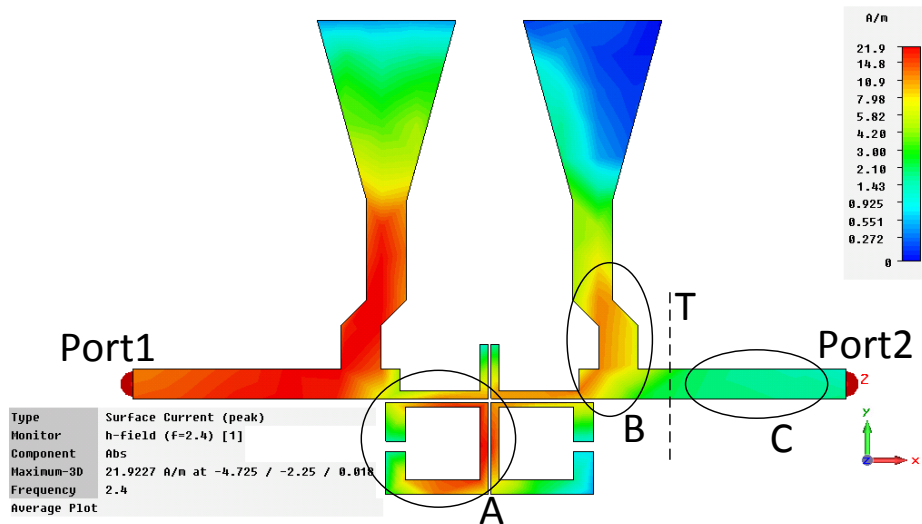
(a)
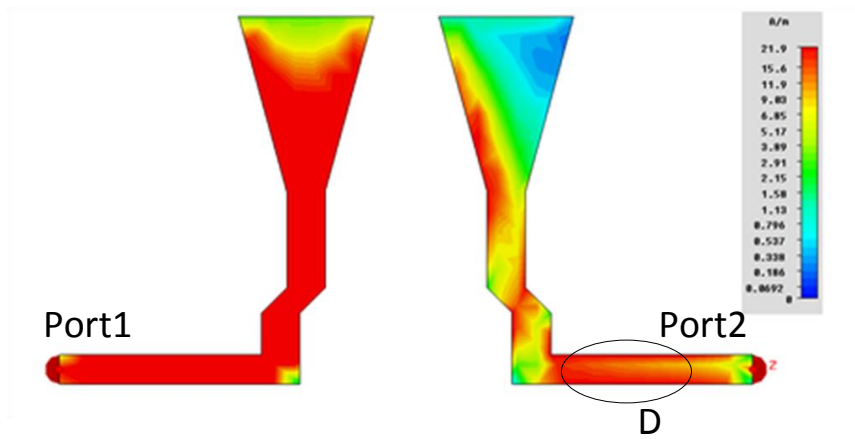
(b)

Figure 2.19 Simulated current distribution of the (a) decoupled antennas; and (b) coupled antennas when Port 1 is excited.

2.2.2.3 Comparison between the all pole S-CRDN and the S-CRDN with source-load coupling.

1. The slope of $y_{21}(s)$:

The mutual admittance polynomial for an all pole S-CRDN is already given in (2.17), the derivative of $y_{21}^{F}(s)$ at $s = 0$ is given by:

$$k_{21} = \frac{d\left[Y_{21}^F(s)\right]}{ds}\Bigg|_{s=0} = \frac{-\gamma \cdot (p_1 + p_2)}{p_1^2 p_2^2} \qquad (2.40)$$

If $p_1 = -p_2$, then $k_{21} = 0$, which means that $y_{21}^F(s)$ is almost constant near resonance.

For S-CRDN with cross couplings on the other hand, the slope of $y_{21}^C(s)$ at s = 0 can be obtained as:

$$\frac{\partial\left(y_{21}^C(s)\right)}{\partial s}\Bigg|_{s=0} = \gamma \cdot \frac{-p_1 p_2 (z_1 + z_2) + z_1 z_2 (p_1 + p_2)}{p_1^2 p_2^2} \qquad (2.41)$$

For simplicity, symmetric pole locations are assumed, which means $p_2 = -p_1 = p$, equation (2.41) can be further simplified as:

$$\frac{\partial\left(y_{21}^C(s)\right)}{\partial s}\Bigg|_{s=0} = \gamma \cdot \frac{z_1 + z_2}{p^2} \qquad (2.42)$$

Choosing the two zeroes z_1 and z_2 properly such that $z_1 + z_2 \neq 0$, then the slope of $y_{21}^C(s)$ is mainly determined by the constant γ. Since it is seen in (2.39) that $m_{SL} = \gamma$, it is obvious that the slope of $y_{21}^C(s)$ can be easily controlled by the realized source load couplings.

2. An Example:

To compare the decoupling performance of these two kinds of S-CRDNs, the coupled cylindrical monopoles in Fig. 2.6 with inter-element spacing D = 25 mm is used as an illustrative example. Both the all pole S-CRDN and the S-CRDN with source-load couplings are designed to decouple the antenna, the simulation results are shown in Fig. 2.20. The decoupling bandwidth ($|S_{21}| < -15$dB) for the S-CRDN with source-load couplings is about 28% wider compared to the all pole S-CRDN.
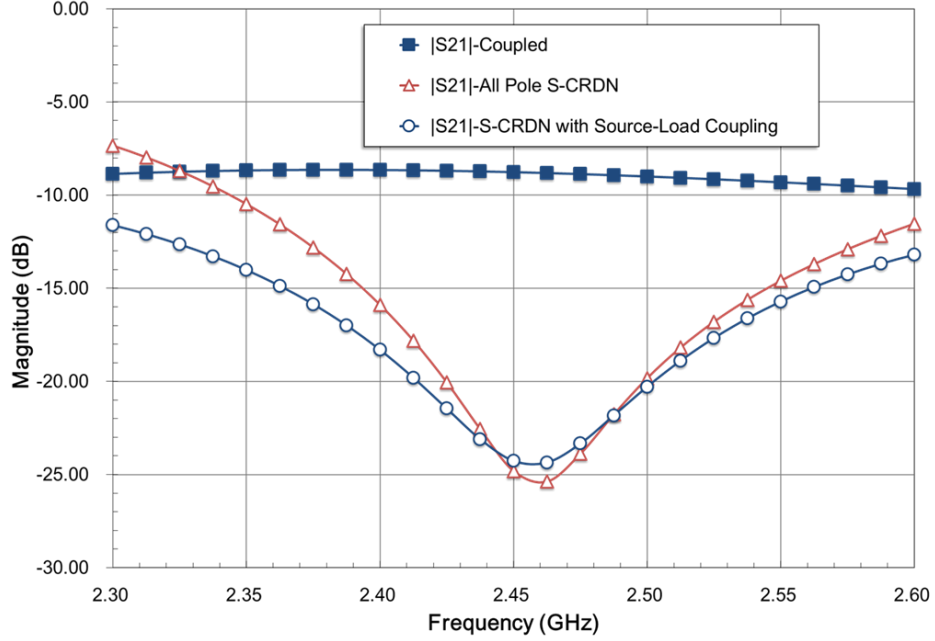
Figure 2.20 The comparison between two kinds of S-CRDN w.r.t. isolation bandwidth.

2.3. A "One-Fit-All" CRDN module

2.3.1. The antenna dependency issue of decoupling techniques

In practical applications, the form factors, e.g. inter-element spacing, ground plane size, etc., of an antenna array plays an important role to the mutual admittances between the antenna elements. Most existing decoupling techniques require a complete redesign if any of such factors is changed. However, an intriguing feature of the proposed CRDN technique is that only the input/output coupling coefficients m_{S1} and m_{2L} are required to be modified whenever the form factors have changed, as shown in (2.23) and (2.24). In other words, a generic S-CRDN can be designed and used to decouple any two-element antenna arrays by modifying only the input and output couplings.

To demonstrate this unique feature of the S-CRDN, a series of EM simulations have been carried out. Nine symmetric coupled antenna arrays similar to the one in Fig. 2.13 (a) with different inter-element spacing (4 mm to 112 mm) and two

68

different ground plane sizes (54×72 mm^2 and 54×170 mm^2) are examined. The simulated S and Y parameters are shown in Fig. 2.21. It should be pointed out that transmission lines of suitable length (determined by (2.14)) are already included in all these arrays.

Several important conclusions can be drawn from Fig. 2.21. Firstly, the isolation (S_{21}^A) of coupled antennas is closely related to the ground size as well as the element spacing. Generally, the isolation increases as the element spacing increases. The coupled arrays with small ground (SG) size are easier to be decoupled as compared to those with large ground (LG) because of the edge diffraction effect. Secondly, the imaginary part of the mutual admittance also depends on the element spacing and ground size. Its variation range is relative large for the decoupling network to cover. Thirdly, when designing the S-CRDN, both the real and imagery parts of the mutual admittance have to be considered. Finally, for small ground cases, if the element spacing is more than 22 mm, then the original isolation is more than 15 dB. Therefore, the performance is acceptable even without a decoupling network. However, for large ground cases, the element spacing has to be more than 110 mm to have an isolation of 15 dB.

The proposed all pole S-CRDN can be used to decouple all these arrays with the same inter-resonator coupled m_{12} with only different input and output couplings. For illustration purpose, four S-CRDNs are designed to decouple the arrays with element spacing 8 mm and 22 mm. The corresponding synthesized coefficients are listed in Table 2-4. However, if we use CRDN 1 for both Array 1 and Array 2, which only differ in ground size, the isolation will degrade significantly as can be seen in Fig. 2.21 (d). Therefore, the decoupling technique is sensitive to ground size, which makes the antenna independent feature important.
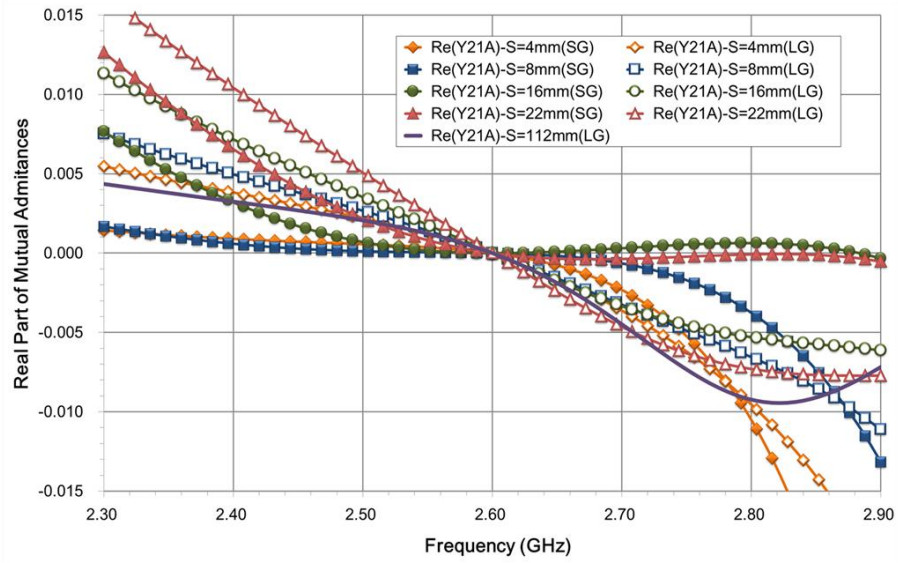
(a)
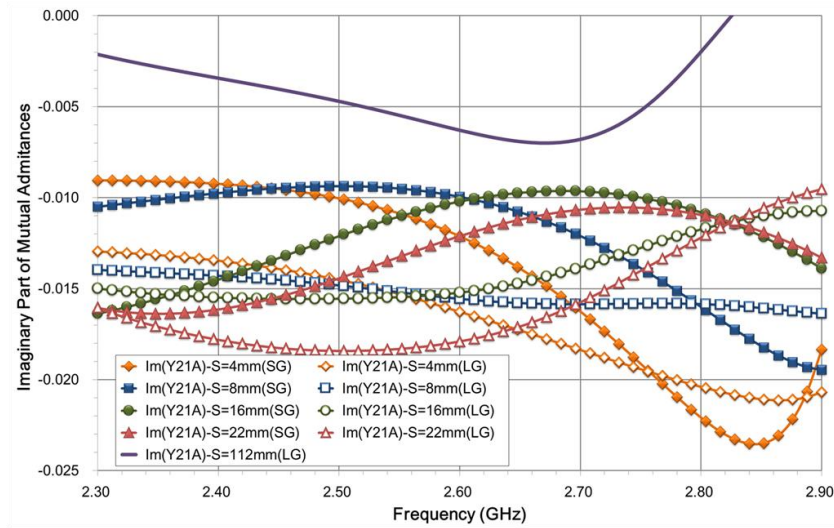
(b)
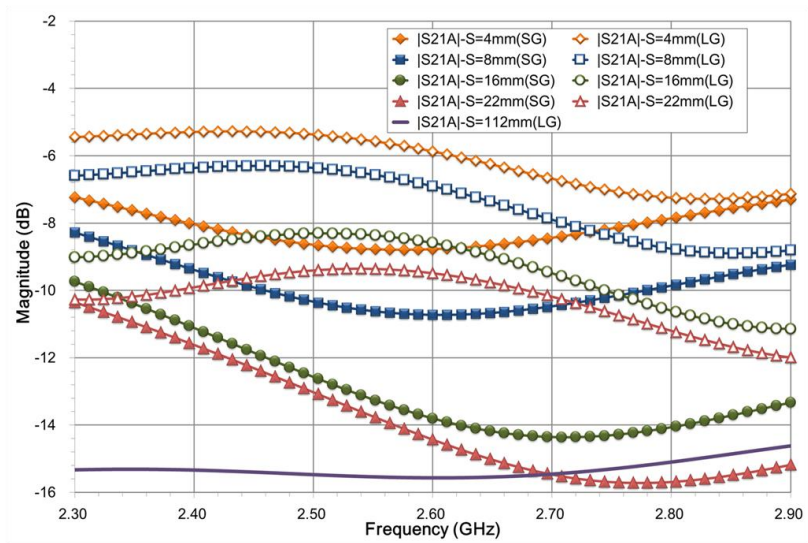
(c)
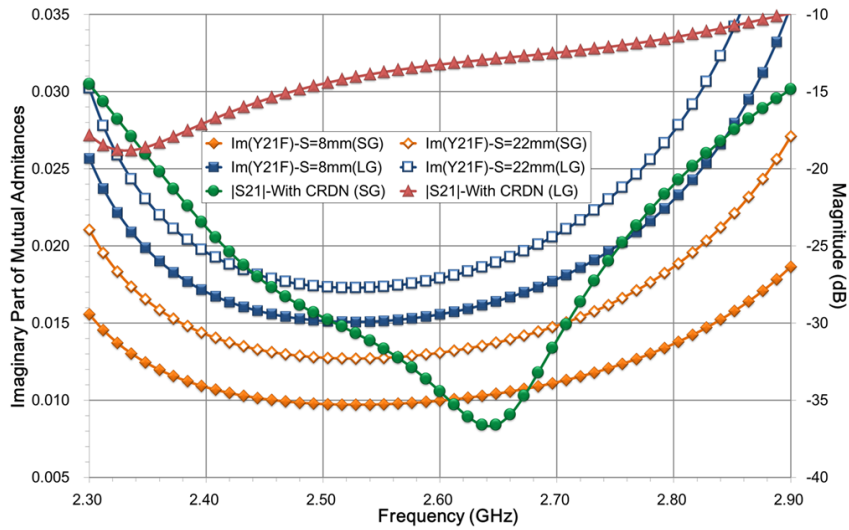
(d)

Figure 2.21 (a) Simulated real parts and; (b) Simulated imaginary parts of mutual admittance of the nine symmetric coupled antenna arrays (c) Simulated isolations of the nine symmetric coupled antenna arrays (d) Simulated Y_{21} for the four CRDNs which are used to decouple Array 1~4 and the isolations for Array 1 and Array 2 using CRDN1.

Table 2-4 Coupling coefficients of designed CRDNs For Array 1~4 (Designed FBW = 10%)

	CRDN1 FOR ARRAY1 S = 8, SG	CRDN2 FOR ARRAY2 S = 8, LG	CRDN3 FOR ARRAY3 S = 22, SG	CRDN3 FOR ARRAY3 S = 22, LG
m_{S1}, m_{2L}	1.2156	1.5168	1.3913	1.6250
m_{12}	**3.0000**	**3.0000**	**3.0000**	**3.0000**
m_{11}, m_{22}	0.0000	0.0000	0.0000	0.0000

2.3.2. An LTCC miniaturized CRDN module

In order to achieve good isolation between two strongly coupled antennas in a mobile terminal, a small footprint and surface mountable device that is independent to the form factors of the antennas would be highly desirable. In this section, an

integrated CRDN module for two strongly coupled antennas of arbitrary form factors is proposed. The CRDN is composed of two parts: a two-port multilayered LTCC device that consists of two tightly coupled semi-lumped element resonators; and an L or C component along with a transmission line external to each terminal of the LTCC device for personalized the required I/O couplings, which allows the LTCC CRDN device to be adopted for different antenna form factors. Furthermore, it will be shown that a trade-off between the decoupling level and decoupling bandwidth for a given operating frequency band can also be achieved by adjusting the couplings. Therefore, with one consolidated LTCC device, which is designed for a given frequency band, and two adjustable I/O couplings, the integrated CRDN is a 'one-fit-all' scheme for a wide range of wireless terminals with different antenna configurations.

2.3.2.1 The network representation
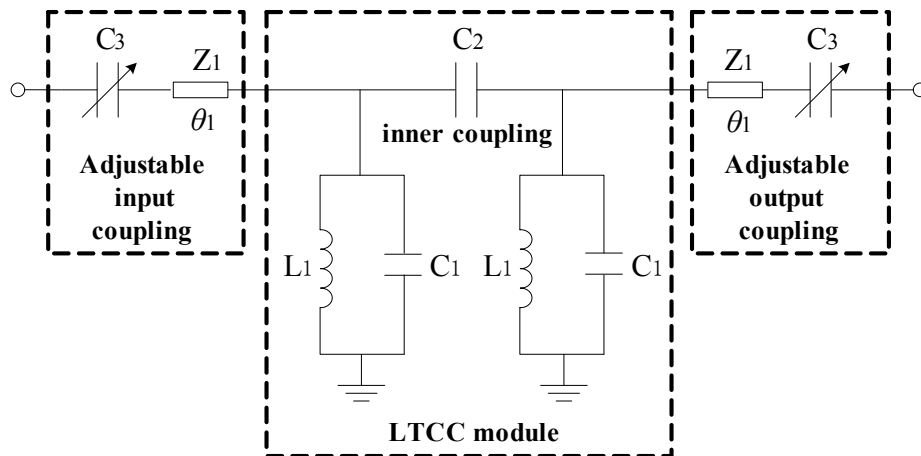
Figure 2.22 Architecture of the proposed integrated S-CRDN scheme.

The schematic circuit of the decoupling network is depicted in Fig. 2.22, where a well-known second-order coupled resonator filter topology is adopted. For simplicity, it is assumed that $Z_1 = Z_0 = 50 \ \Omega$. Denoting the $[ABCD]$ matrix of the LTCC device by $\overline{[ABCD]}$, which can be expressed as:

$$\overline{A} = \overline{D} = \frac{\omega^2 L_1 (C_1 + C_2) - 1}{\omega^2 L_1 C_2} \tag{2.43a}$$

$$\overline{B} = \frac{1}{j\omega C_2} \tag{2.43b}$$

$$\overline{C} = \frac{2}{j\omega L_1} + 2 j\omega C_1 - \frac{1}{j\omega^3 L_1^2 C_2} - \frac{\omega C_1^2}{j C_2} + \frac{2 C_1}{j\omega L_1 C_2} \tag{2.43c}$$

Having had the [*ABCD*] matrix of the LTCC device and left- and right- cascaded with those of the input and the output coupling circuits, one can find the overall [*ABCD*] matrix of the decoupling network, from which the *Y* parameters of the decoupling network can be found as:

$$Y_{11}^N = Y_{22}^N = \frac{D}{B} \tag{2.44a}$$

$$Y_{21}^N = \frac{-1}{B} \tag{2.44b}$$

where *D* and *B* are given by

$$
\begin{aligned}
B = {} & 2 j \overline{A} (\cos\theta_1 + \frac{\sin\theta_1}{Z_0 \omega C_3}) \cdot (Z_0 \sin\theta_1 - \frac{\cos\theta_1}{\omega C_3}) \\
& + \overline{B}(\cos\theta_1 + \frac{\sin\theta_1}{Z_0 \omega C_3})^2 - \overline{C}(Z_0 \sin\theta_1 - \frac{\cos\theta_1}{\omega C_3})^2
\end{aligned}
\tag{2.45a}
$$

$$
\begin{aligned}
D = {} & \overline{A} \cdot [\cos\theta_1 \cdot (\cos\theta_1 + \frac{\sin\theta_1}{Z_0 \omega C_3}) - \sin\theta_1 \cdot (\sin\theta_1 - \frac{\cos\theta_1}{Z_0 \omega C_3})] \\
& + \frac{j\overline{B}}{Z_0} \sin\theta_1 \cdot (\cos\theta_1 + \frac{\sin\theta_1}{Z_0 \omega C_3}) + j\overline{C} \cos\theta_1 (Z_0 \sin\theta_1 - \frac{\cos\theta_1}{\omega C_3})
\end{aligned}
\tag{2.45b}
$$

The decoupling and matching conditions can be specified by substituting (2.44) into

(2.7) and (2.9) for obtaining proper values of L_1, C_1, C_2, C_3, and θ_1. Specifically, parameters L_1 and C_1 determine the working frequency of the network; the inter-resonator coupling is controlled by C_2; parameter C_3 is crucial and is to be adjusted for different mutual couplings to be mitigated; and θ_1 is a variable for compensating the frequency offset introduced by C_3.

2.3.2.2 The "one-fit-all" feature

From equations (2.44) and (2.45), it is shown that admittance parameters of the decoupling network depend on the values of θ_1 and C_3 while the $\boxed{ABCD}$ matrix remains unchanged. In other words, different mutual admittances of a CRDN can be achieved by tuning I/O couplings only when the LTCC device is fixed for a given frequency band. For instance, the simulated imaginary part of Y_{11}^N for a 2.45 GHz band decoupling network with different C_3 value for I/O couplings is presented in Fig. 2.23. It can be seen that when L_1, C_1 and C_2 are fixed, different levels of $\mathrm{Im}\{Y_{21}^N\}$ (from 0.008 to 0.019) can be obtained by adjusting C_3 and θ_1, while $\mathrm{Im}\{Y_{11}^N\}$ remains to be zero at 2.45 GHz for good matching in all cases.
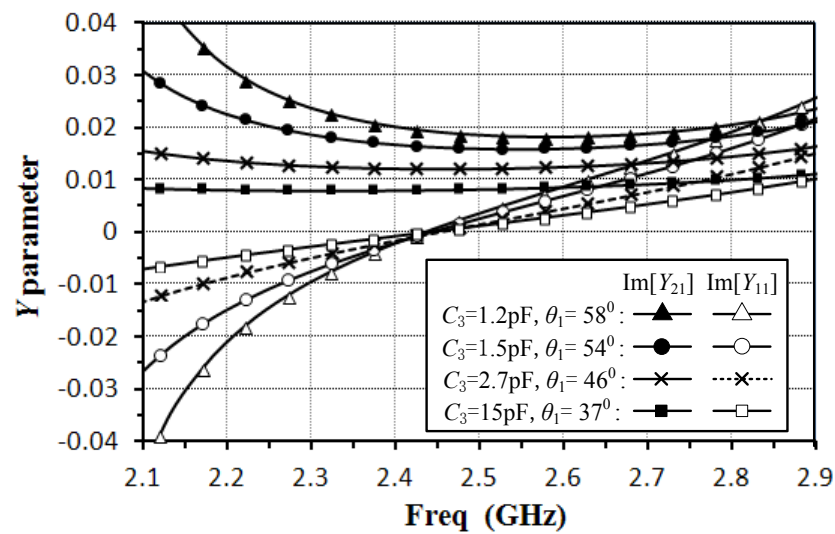
Figure 2.23 Simulated admittance parameters of the decoupling network with different I/O couplings.

74

Moreover, it should be mentioned that antennas with positive $\text{Im}\{Y_{21}^A\}$ can also be decoupled by this network topology with corresponding negative $\text{Im}\{Y_{21}^N\}$ realized by using inductive I/O components. This feature further justifies that the proposed decoupling network can provide a "one-fit-all" solution for any type of antenna coupling and a wide range of antenna configurations.

2.3.2.3 Decoupling Bandwidth Analysis

For various types of practical coupled antennas, such as patches, monopoles, or PIFAs, $\text{Im}\{Y_{21}^A\}$ is almost a constant in the vicinity of the resonant frequency in most cases. According to Eq. (2.7), if a wide decoupling bandwidth is required, Y_{21}^N of the decoupling network needs to be as constant as possible and be opposite to $\text{Im}\{Y_{21}^A\}$ within the band of interest, that is to say:

$$\text{Im}\{Y_{21}^N(\omega)\}\big|_{\omega \in [\omega_r - \Delta\omega,\, \omega_r + \Delta\omega]} \approx \text{Im}\{Y_{21}^N(\omega_r)\} = -\text{Im}\{Y_{21}^A(\omega_r)\} \qquad (2.46)$$

where $[\omega_r - \Delta\omega,\ \omega_r + \Delta\omega]$ is the frequency band of interest. In other words, the decoupling bandwidth, which is related to the slope of Y_{21}^N at ω_r, becomes wider as the slope approaches zero.
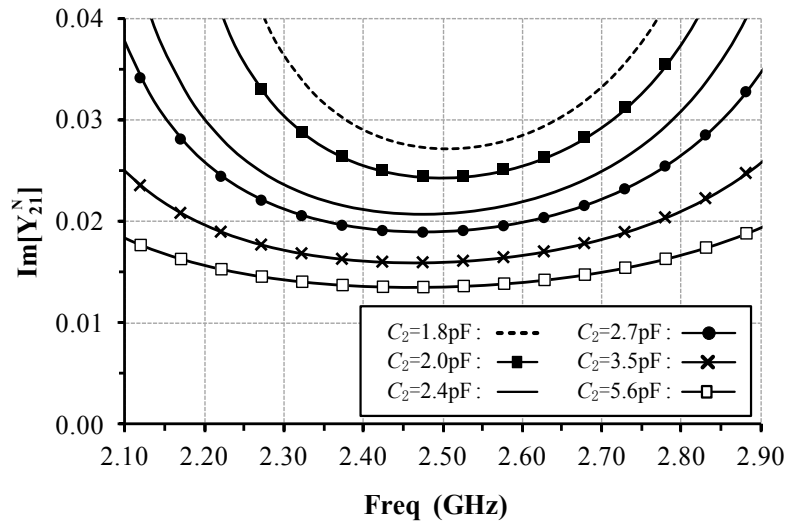
Figure 2.24 Simulated slopes of $\text{Im}\{Y_{21}^N\}$ against various values of C2.

Previous research has shown that the coupling between the two resonators has direct impact on the slope of Y_{21}^N at the resonant frequency [9]. In this section, a capacitive mutual coupling is utilized. It is obvious that $\text{Im}\{Y_{21}^N\}$ can be approximately equal to a constant over a wider frequency band as the value of C_3, the I/O capacitance increases. This fact is illustrated in Fig. 2.24. Therefore, the mutual coupling between the two resonators is designed to be as large as possible to realize a flat $\text{Im}\{Y_{21}^N\}$, while its absolute value can be independently adjusted by changing the I/O couplings, as can be seen in Fig. 2.23.

2.3.2.4 Design Examples of LTCC CRDN modules

To validate the proposed decoupling scheme and its design theory, two examples concerning different antenna coupling mechanisms are presented. In both cases, the coupled antennas are fabricated on an FR4 substrate with relative dielectric constant of 4.4 and thickness of 1.6 mm. The two resonators and the coupling capacitor of the decoupling network are integrated into an LTCC device whose relative dielectric constant is 9.2 and loss tangent is 0.002 at the frequency of interest. With an 8-layer vertical structure, the LTCC device is with dimensions of $3.2 \times 2.5 \times 1.2$ mm^3.

1. Example 1: CRDN module for a Symmetric Array

A symmetric 2.45 GHz printed two-element antenna array and the corresponding LTCC decoupling device will be discussed in this section. The configuration of the entire network, the detailed layout of the LTCC device and the EM model of the device together with the PCB board to be mounted are illustrated in Fig. 2.25. As can be seen, two wideband coupled monopole antennas separated by distance D are printed on a 90 mm $\times$ 72 mm FR4 board. The other antenna relevant dimensions are $W_2 = 3$ mm, $W_3 = 9.8$ mm and $S_3 = 19.4$ mm. A section of transmission line of length

S_2 and characteristic impedance of Z_0 is inserted at each antenna port to satisfy (2.14).
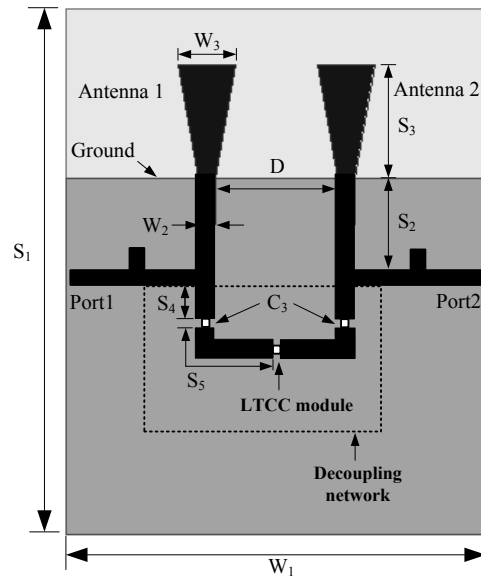
(a)
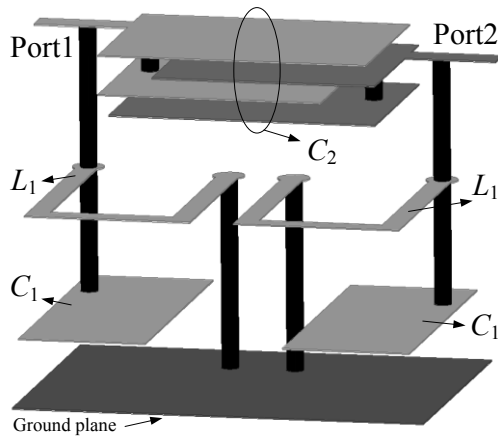
(b)
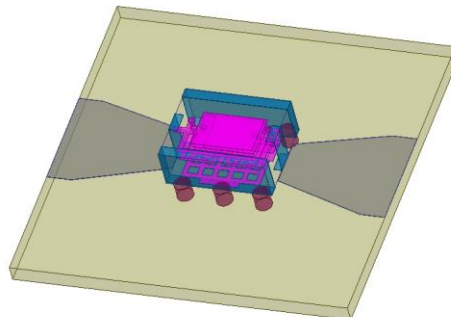
(c)

Figure 2.25 Configurations of (a) the symmetric 2.45 GHz testing antenna array; (b) the layout of the LTCC CRDN device; (c) EM model of the LTCC device surface mounted on a PCB board.

The parameters L_1, θ_1, C_1, C_2 and C_3 are designed by enforcing the decoupling and matching conditions stipulated by Eqs. (2.7) and (2.9) through the known relations Eqs. (2.43) – (2.45). Beside, two open stubs are utilized near ports 1 and 2 for increasing the matching bandwidth. With the predesigned LTCC device and proper I/O couplings, different types of coupled antennas working at 2.45 GHz band can be decoupled with good impedance matching.
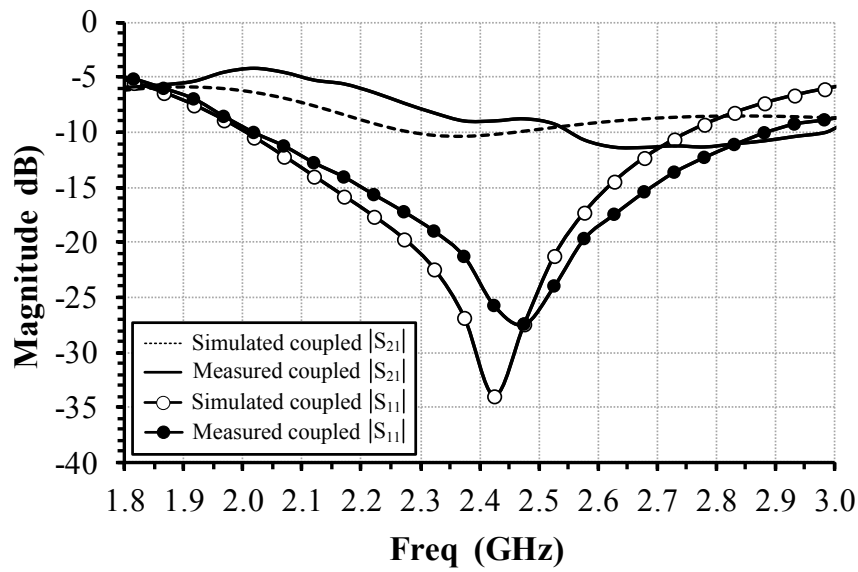
(a)
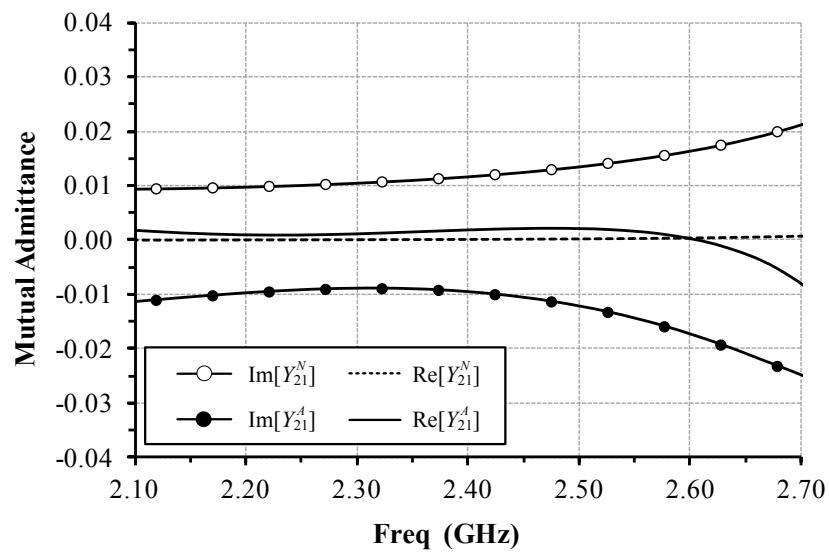
(b)
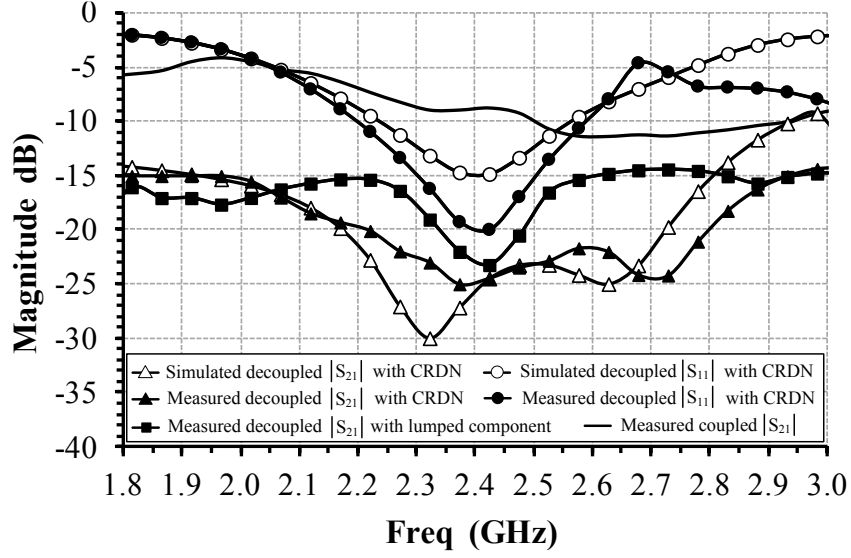
(c)

Figure 2.26 (a) Simulated and measured S-parameters of coupled array A1; (b) (simulated and measured?) Mutual admittances of antenna array A1 and the decoupling network; (c) Simulated and measured responses of the decoupled array A1.

Antenna pairs with $D = 0.26\ \lambda_g$ and $D = 0.32\ \lambda_g$ are investigated for different coupling circumstances, where λ_g is the guided wavelength at the operating frequency of 2.45 GHz. In the case of array A1 ($D = 0.26\lambda_g$), the simulated and measured S-parameters of the original coupled array are given in Fig. 2.26 (a), in which the isolation of about 8 dB of the coupled array in the working frequency band is also superimposed. In order to realize $\mathrm{Re}\{Y_{21}^A\} = 0$ at the resonant frequency, the inserted transmission line has a length of $S_2 = 19$ mm. The $\mathrm{Im}\{Y_{21}^N\}$ is designed to be 0.012 to cancel the $\mathrm{Im}\{Y_{21}^A\}$ that is about -0.012 over a certain frequency band according to (14) as shown in Fig. 2.26 (b). Due to the compact volume and LTCC fabrication constraints, the mutual coupling C_2 is limited to 6 pF. The other parameters of the decoupling network are chosen as follows: $L_1 = 4.2$ nH, $C_1 = 1.0$ pF, $C_3 = 0.5$ pF, $S_4 = 4$ mm and $S_5 = 7.9$ mm. Fig. 2.26 (c) shows the simulated and measured S-parameters of the entire decoupled network. It can be seen that the decoupling bandwidth with $|S_{21}| \leq -20$ dB is about 24% (580 MHz), while the impedance matching bandwidth with $|S_{11}| \leq -10$ dB is about 17% (400 MHz). For

comparison, the same antennas are decoupled by a lumped element designed by the same procedure given in [10]. It is seen from Fig. 2.26 (c) that the decoupling bandwidth with $|S_{21}| \leq -20$ dB using a lumped element is about 6% (150 MHz).

In the case of array A2 ($D = 0.32\lambda_g$), the isolation of the original coupled array is about 10 dB in the operating frequency band. In this case, $S_2 = 16.3$ mm is utilized for realizing $\text{Re}\{Y_{21}^A\} = 0$ and the corresponding $\text{Im}\{Y_{21}^A\}$ is about -0.008. With the same LTCC device, the other circuit parameters of the CRDN are tuned to realize $\text{Im}\{Y_{21}^N\} = 0.008$ and $\text{Im}\{Y_{11}^N\} = 0$ in the frequency band of interest, resulting in C_3 = 1.8 pF, $S_4 = 3.1$ mm and $S_5 = 9.2$ mm. Fig. 2.27 shows the simulated and measured S-parameters of the decoupled array A2. The decoupling bandwidth with $|S_{21}| \leq -20$ dB is about 14% (360 MHz), and the impedance matching bandwidth with $|S_{11}| \leq -10$ dB is about 15% (370 MHz). Similarly, by contrast, the same array decoupled by a lumped element has a decoupling bandwidth of about 3.7% for 20 dB isolation.
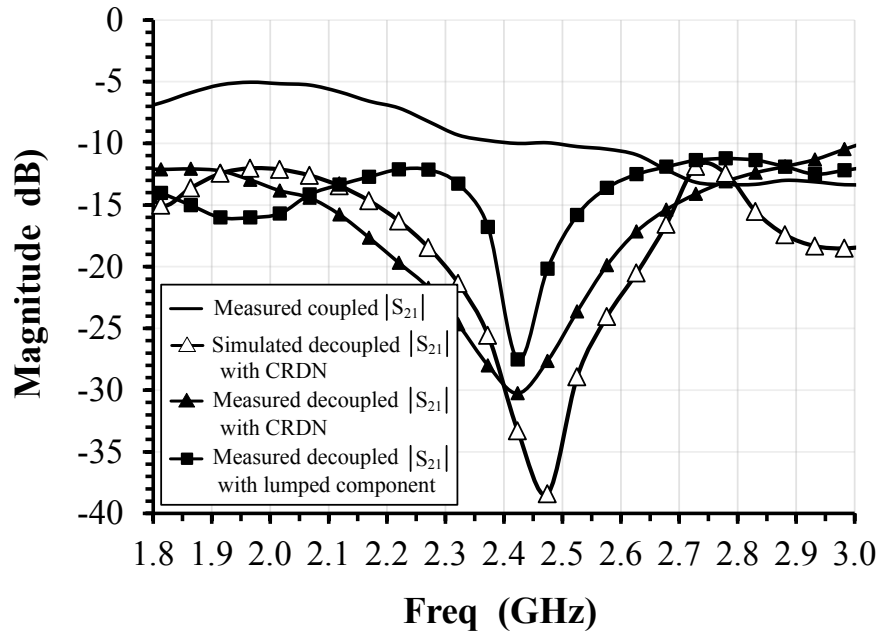
(a)
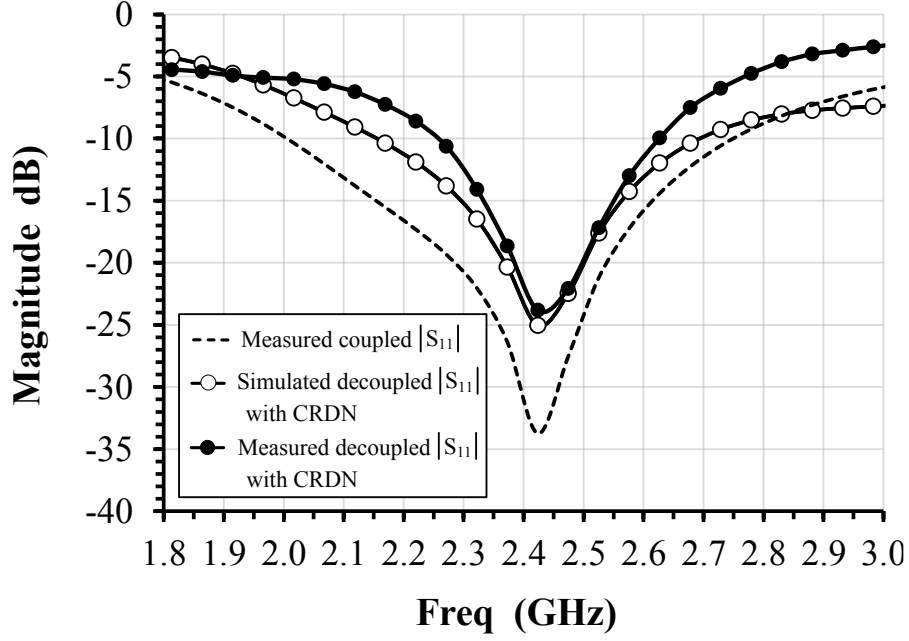
(b)

Figure 2.27 (a) Simulated and measured isolations of coupled and decoupled array A2; (b) Simulated and measured reflection coefficients of coupled and decoupled array A2.

2. Example 2: LTCC CRDN module for an Asymmetric Array

In order to demonstrate the effectiveness of the LTCC CRDN device, an asymmetric 2.45 GHz antenna array with two different types of antennas is concerned in this section. The geometries of the antennas and corresponding CRDNs are depicted in Fig. 2.28. A PIFA and a monopole antenna are printed on an FR4 substrate with the size of 120 mm × 120 mm. The dimensions of the antennas are as follows: $W_2 = 3$ mm, $W_3 = 9$ mm, $S_2 = 0.2$ mm, $S_3 = 7$ mm and $S_7 = 18.4$ mm. Similarly, a section of transmission line is introduced according to (2.14), and $D = 0.56 \lambda_g$ and $D = 0.69 \lambda_g$ cases are investigated in this example. Also, two open stubs are used for broadening matching bandwidth.
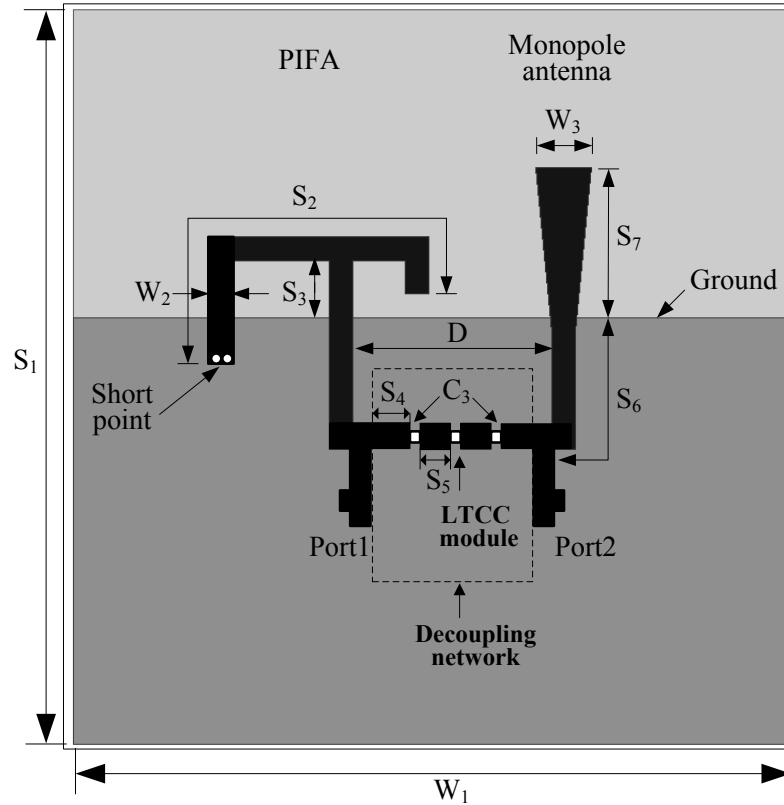
Figure 2.28 Configurations of the asymmetric antenna array.

In the case of array B1 ($D = 0.56\lambda_g$), the isolation of the original coupled array is about 7 dB in the operating frequency band. Here, $S_6 = 16$ mm is used to realize $\text{Re}\{Y_{21}^A\} = 0$ and $\text{Im}\{Y_{21}^A\}$ is about -0.015 over a wide frequency range, thus $\text{Im}\{Y_{21}^N\}$ is designed to be about 0.015 by choosing $C_3 = 1.2$ pF, $S_4 = 4.6$ mm and $S_5 = 6.2$ mm. The simulated and measured S-parameters of the decoupled network are shown in Figs. 2.29 (a) and (b). It is illustrated that the decoupling bandwidth with $|S_{21}| \leq -20$ dB is about 11% (280 MHz), while the impedance matching bandwidth with $|S_{11}| \leq -10$ dB is about 13.5% (330 MHz), and $|S_{22}| \leq -10$ dB is about 13% (320 MHz).
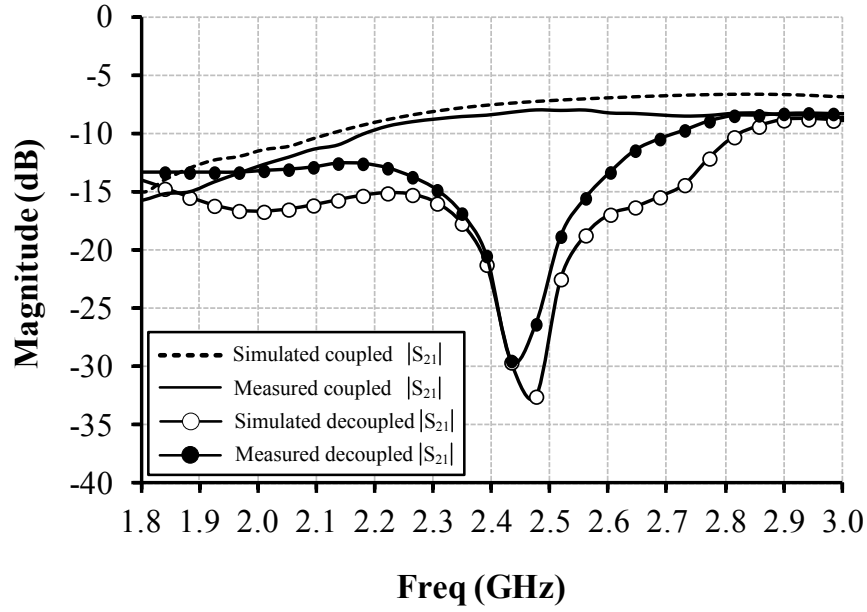
(a)
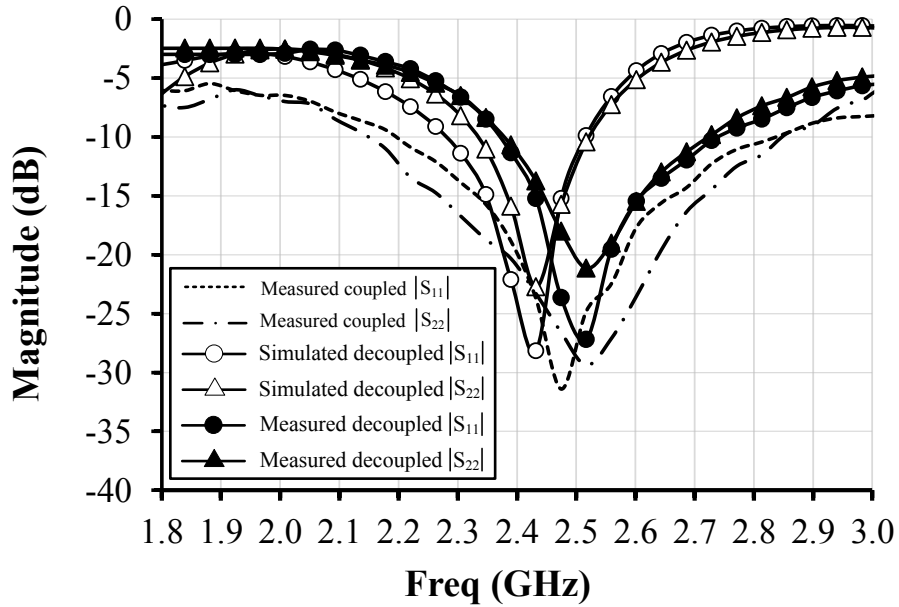
(b)

Figure 2.29 (a) Simulated and measured isolations of the coupled and decoupled array B1. (b) Simulated and measured reflection responses of the coupled and decoupled array B1.

In the case of array B2 ($D = 0.69\lambda_g$), the isolation of the original coupled array is about 9.5 dB from 2.4 GHz to 2.48 GHz. Here, $S_6 = 13$ mm is used for $\mathrm{Re}\{Y_{21}^A\} = 0$ and the corresponding $\mathrm{Im}\{Y_{21}^A\}$ is about -0.012. Accordingly, the other parameters are: $C_3 = 1.5$ pF, $S_4 = 3.2$ mm and $S_5 = 7.7$ mm. Fig. 2.30 shows the simulated and measured S-parameters of the decoupled array B2. The decoupling bandwidth with

$|S_{21}| \leq -20$ dB is about 12% (290 MHz), while the impedance matching bandwidth with $|S_{11}| \leq -10$ dB is about 9% (210 MHz), and $|S_{22}| \leq -10$ dB is about 14% (350 MHz). The photos of the antenna arrays along with some samples of the LTCC CRDN device are shown in Fig. 2.31.

(a)

(b)
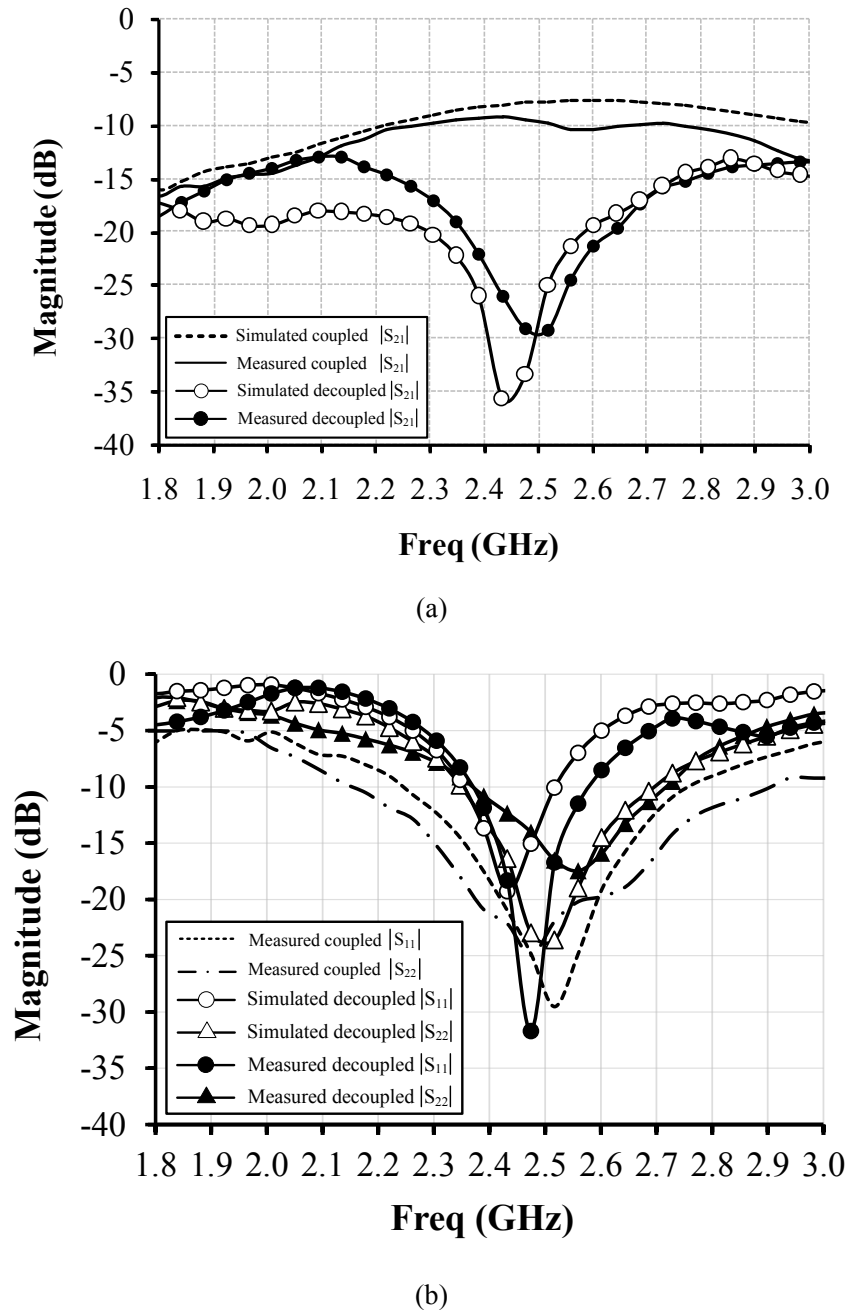
Figure 2.30 (a) Simulated and measured isolations of the coupled and decoupled array B2. (b) Simulated and measured reflection coefficients of the coupled and decoupled array B2.
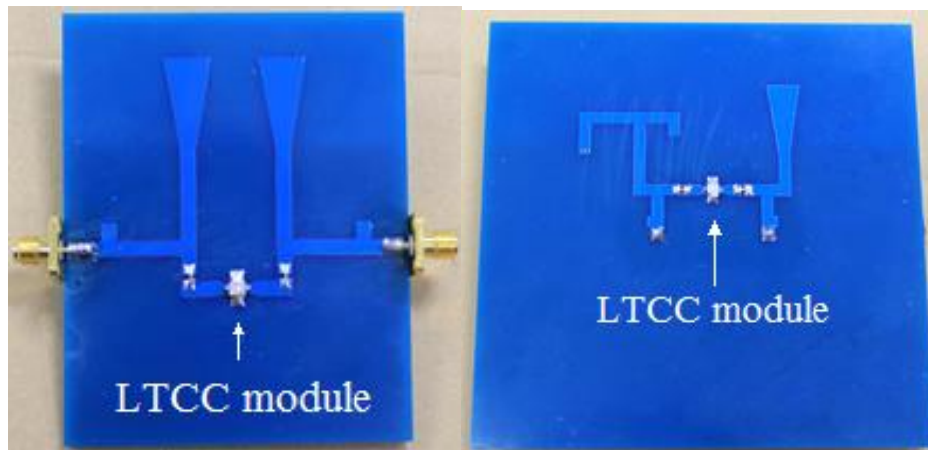
(a)   (b)
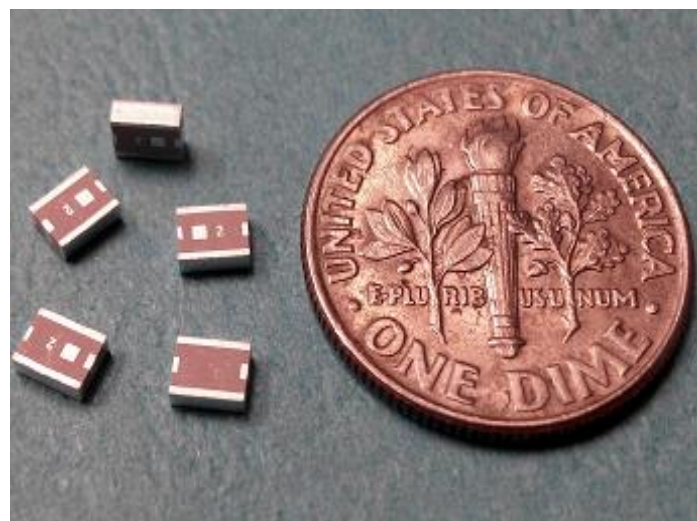
(c)

Figure 2.31 Photos of (a) symmetric antenna array testing board with LTCC CRDN device; (b) asymmetric antenna array testing board with LTCC CRDN device; and (c) samples of LTCC CRDN device.

For all the cases, it should be pointed out that when an LTCC CRDN device is added to a coupled antenna array, the matching bandwidth decreases. The reason for this is that for strongly coupled antennas, one antenna acts as a lossy load for the other one. Thus it is understandable that the matching bandwidth for a lossier antenna is greater. However, despite the matching bandwidth, the radiation efficiencies for the two antennas in a coupled array are poorer than those of decoupled [2].

3. Trade-off Analysis

The prototyped LTCC CRDN device can be used in various decoupling circumstances due to its antenna independence. Furthermore, a tradeoff between the isolation level and decoupling bandwidth can also be realized by adjusting the I/O couplings. A pair of monopole antennas is used here as an illustration of the tradeoff feature. The topology of the CRDN is the same as that of **Example 1**. It can be seen from Fig. 2.32 that by changing the value of C_3 from 4.3 pF to 15 pF, the decoupling bandwidth for 20 dB isolation is reduced from 680 MHz to 600 MHz, whereas the isolation is improved from 20 dB to about 28 dB, while the matching bandwidths remain almost the same.
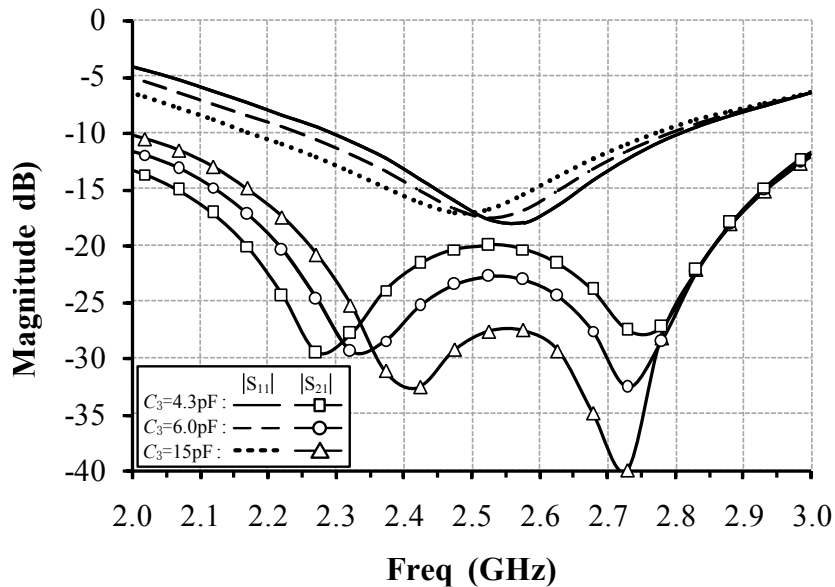
Figure 2.32 A tradeoff analysis between the isolation level and decoupling bandwidth with different values of C_3.

Therefore, with this antenna-independent LTCC CRDN device and appropriate lumped capacitor C_3, a tradeoff between the decoupling bandwidth and level can be realized without reconfiguring the entire CRDN network. This attractive feature allows a mass production of one LTCC device for various applications as long as the frequency band is correct.

2.4. A Dual-Band CRDN

Based on the concept of CRDN for single band applications, a dual-band decoupling technique using dual-band CRDN is proposed in this paper. Compared to the existing dual band decoupling solutions, the proposed scheme has the following unique features:

1) The dual band CRDN can take various form factors in realization and can be very compact in size;

2) The CRDN can be analytically synthesized and designed according to specifications for given antenna characteristics.

3) The characteristics of the decoupled antennas are well-maintained with enhanced efficiency.

2.4.1. The dual-band network model

To decouple the two dual-band antennas, the following *decoupling conditions* must be satisfied within the *two* frequency bands $[\omega_{L1}, \omega_{L2}]$ and $[\omega_{H1}, \omega_{H2}]$, whose center frequencies are ω_L and ω_H, respectively:

$$\mathrm{Re}\left\{Y_{21}^A(\omega)\right\} \approx 0, \, \omega \in \left[\omega_{L1}, \omega_{L2}\right] \tag{2.47a}$$

$$j \cdot \mathrm{Im}\left\{Y_{21}^A(\omega)\right\} + Y_{21}^D(\omega) \approx 0, \, \omega \in \left[\omega_{L1}, \omega_{L2}\right], \tag{2.47b}$$

and

$$\mathrm{Re}\left\{Y_{21}^A(\omega)\right\} \approx 0, \, \omega \in \left[\omega_{H1}, \omega_{H2}\right] \tag{2.48a}$$

$$j \cdot \mathrm{Im}\left\{Y_{21}^A(\omega)\right\} + Y_{21}^D(\omega) \approx 0, \, \omega \in \left[\omega_{H1}, \omega_{H2}\right]. \tag{2.48b}$$

87

Once the antennas are decoupled, they can be independently matched at the low band and the high band, respectively. Using the S-to-Y transformation and conditions (2.47) and (2.48), the *matching conditions* can be written as:

$$\text{Re}\{Y_{kk}^A(\omega)\} \approx 1, \omega \in [\omega_{L1}, \omega_{L2}], k = 1, 2 ,\tag{2.49a}$$

$$j \cdot \text{Im}\{Y_{kk}^A(\omega)\} + Y_{kk}^D(\omega) \approx 0, \omega \in [\omega_{L1}, \omega_{L2}], k = 1, 2 ,\tag{2.49b}$$

and

$$\text{Re}\{Y_{kk}^A(\omega)\} \approx 1, \omega \in [\omega_{H1}, \omega_{H2}], k = 1, 2 , \quad \text{and}\tag{2.50a}$$

$$j \cdot \text{Im}\{Y_{kk}^A(\omega)\} + Y_{kk}^D(\omega) \approx 0, \omega \in [\omega_{H1}, \omega_{H2}], k = 1, 2 .\tag{2.50b}$$

It is worth mentioning that a unique characteristic of a CRDN is that the matching and the decoupling conditions can be satisfied simultaneously. Nevertheless, to further enhance the matching performance, an extra simple matching network always helps.

2.4.2. A dual-band admittance transformer

2.4.2.1 Design Equations

In order to satisfy conditions (2.47a) and (2.48a) simultaneously, the complex mutual admittances of the coupled antenna $Y_{21}^A(\omega)$ must transformed to purely imaginary values within the bands of interest in the first place. For single band application, it is already shown in [10] that with a section of transmission line added to each port, the mutual admittance $Y_{21}^A(\omega)$ of a pair of coupled antennas can be transformed to a purely imaginary value at a specific frequency point. However, this

scheme does not work well for dual-band applications. To best satisfy (2.47a) and (2.48a), a stepped impedance transformer in two sections will be used in this work to accomplish the dual-band admittance transformation.

In general, the two-section stepped-impedance transformer can be formed by two transmission line sections with characteristic impedances Z_1 and Z_2 and lengths l_1 and l_2, respectively. To simplify the design, we chose $Z_1 = Z_0$, where Z_0 is the references port impedance. Consider a simple case first, that the coupled antennas are *identical* and *well matched*, the scattering parameters of the coupled antenna network after inserting the first sections of transmission lines at both antenna ports can be expressed as:

$$\left[S^{A'} \right] = \begin{bmatrix} 0 & S_{21}^{A'} \\ S_{21}^{A'} & 0 \end{bmatrix} = \begin{bmatrix} 0 & S_{21}^{A} \cdot e^{-j2\theta_1} \\ S_{21}^{A} \cdot e^{-j2\theta_1} & 0 \end{bmatrix}, \tag{2.51}$$

where $S_{21}^{A} = \alpha \cdot e^{j\phi}$ is the isolation of the original coupled antennas. The matching condition $S_{11}^{A} = S_{22}^{A} = 0$ is already reflected in (2.51). $\theta_1 = \omega l_1 / c$ is a function of ω while c is the speed of light. Notice that the variable α and ϕ are both frequency dependent.

Since $Z_2 \neq Z_0$, before shifting the reference plane of $[S^{A'}]$, power wave renormalizations [11] with respect to port impedance Z_2 needs to be done, which will result in a renormalized scattering matrix $[S^{A''}]$, whose entries are:

$$S_{11}^{A''} = \frac{r\left[\left(S_{21}^{A'} \right)^2 - 1 \right]}{1 - r^2 \left(S_{21}^{A'} \right)^2}, \tag{2.52}$$

and

$$S_{21}^{A''} = \frac{(1 - r^2) S_{21}^{A'}}{1 - r^2 \left(S_{21}^{A'} \right)^2}, \tag{2.53}$$

with

$$r = \frac{Z_2 - Z_0}{Z_2 + Z_0} \tag{2.54}$$

Shifting the reference plane of the renormalized scattering parameters leads to:

$$\left[S^{A'''} \right] = \begin{bmatrix} S_{11}^{A''} \cdot e^{-j2\theta_2} & S_{21}^{A''} \cdot e^{-j2\theta_2} \\ S_{21}^{A''} \cdot e^{-j2\theta_2} & S_{11}^{A''} \cdot e^{-j2\theta_2} \end{bmatrix} . \tag{2.55}$$

with $\theta_2 = \omega l_1/c$ also being a function of ω. Using S-to-Y transformation, the mutual admittance between the two dual-band antennas can be expressed as:

$$Y_{21}^{A'''} = \frac{1}{Z_0} \cdot \frac{-2 S_{21}^{A''} \cdot e^{-j2\theta_2}}{\left(1 + S_{11}^{A''} \cdot e^{-j2\theta_2} \right)^2 - \left(S_{21}^{A''} \cdot e^{-j2\theta_2} \right)^2} . \tag{2.56}$$

To decouple the antennas without sacrificing the matching performance, it is stipulated that the antennas are matched before connecting a CRDN, which means that $|(2.52)| = 0$, then (2.56) can be simplified to

$$Y_{21}^{A'''} = -\frac{2\alpha\gamma}{Z_0} \frac{e^{-j\tau} + (\gamma - 1)\alpha^2 e^{-j\rho}}{1 - \gamma^2 \alpha^2 e^{-j2\tau}} \tag{2.57}$$

where $\tau = 2\omega l_1/c + 2\omega l_2/c - \phi(\omega)$, $\rho = 6\omega l_1/c + 2\omega l_2/c - 3\phi(\omega)$, and $\gamma = 1 - r^2$.

To set the real part of $Y_{21}^{A'''}$ to zero at frequencies ω_L and ω_H, the following two transcendental equations need to be satisfied:

$$\begin{aligned} &\alpha^4(\omega)\gamma^2(1-\gamma)\cos(\rho(\omega) - 2\tau(\omega)) \\ &+\alpha^2(\omega)(\gamma - 1)\cos\rho(\omega) \\ &+(1 - \alpha^2(\omega)\gamma^2)\cos\tau(\omega) = 0, \ \omega = \omega_L \end{aligned} \tag{2.58a}$$

and

$$\alpha^4(\omega)\gamma^2(1\text{-}\gamma)\cos(\rho(\omega)-2\tau(\omega))$$
$$+\alpha^2(\omega)(\gamma-1)\cos\rho(\omega)$$
$$+(1-\alpha^2(\omega)\gamma^2)\cos\tau(\omega)=0, \ \omega=\omega_H$$

(2.58b)

In practice, when a relatively broader bandwidth is of interest, it is better to evaluate (13) within that band rather than at a single frequency point and try to find the optimum solution rather than an exact one.

There are three variables: r, l_1 and l_2 in (2.58). To find an appropriate solution of the equations, the constraint of $|(2.52)| = 0$ must be considered at ω_L and ω_H, which leads to:

$$e_L = r^2\left(\alpha_L^4 - 2\alpha_L^2\cos\xi_L +1\right)$$
$$\cdot\left(\alpha_L^4 r^4 - 2\alpha_L^2 r^2\cos\xi_L +1\right)\approx 0$$

(2.59a)

and

$$e_H = r^2\left(\alpha_H^4 - 2\alpha_H^2\cos\xi_H +1\right)$$
$$\cdot\left(\alpha_H^4 r^4 - 2\alpha_H^2 r^2\cos\xi_H +1\right)\approx 0$$

(2.59b)

where $\xi_L = 4\omega_L l_1/c - 2\phi_1$ and $\xi_H = 4\omega_H l_1/c - 2\phi_2$. It is obvious that for single band decoupling with one section of transmission line ($r = 0$ or $\gamma = 1$), (2.58) and (2.59) will become the same design equation as that in [11].

Analytically solving the four transcendental equations of (2.58) and (2.59) is not trivial. Therefore, it is better to go through a simple numerical process to find a set of

optimum solution of θ_1, θ_2 and Z_2 from (2.58) and (2.59). To illustrate the process, a pair of practical dual-band monopole antennas is used as an example. The two identical printed dual-band monopoles are placed close to each other on a 1.6 mm FR4 substrate. The separation distance D_A = 9.8 mm, which is less than 0.077 λ_0 at 2.45 GHz and 0.17 λ_0 at 5.25 GHz. For each antenna, Arm 1 mainly controls the low band while Arm 2 determines the high band. The simulated and measured scattering parameters of the strongly coupled dual-band monopole antennas are shown in Fig. 2.33 (b). The isolation between the antennas is around 8 dB at 2.45 GHz and 10 dB at 5.25 GHz. Other antenna dimensions are listed in Table 2-5.
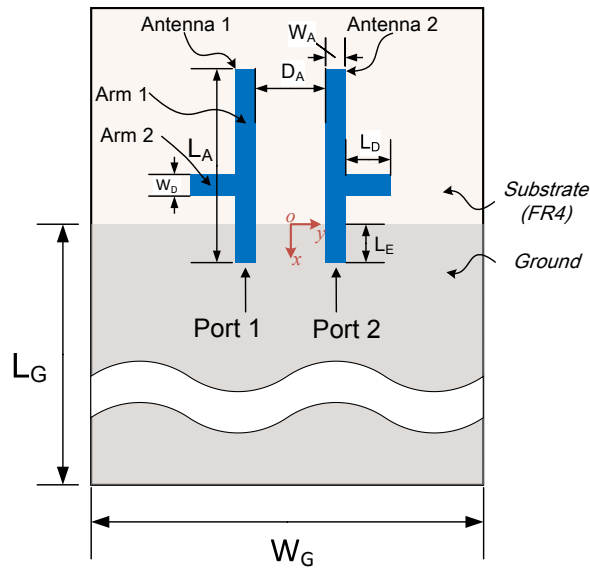
(a)
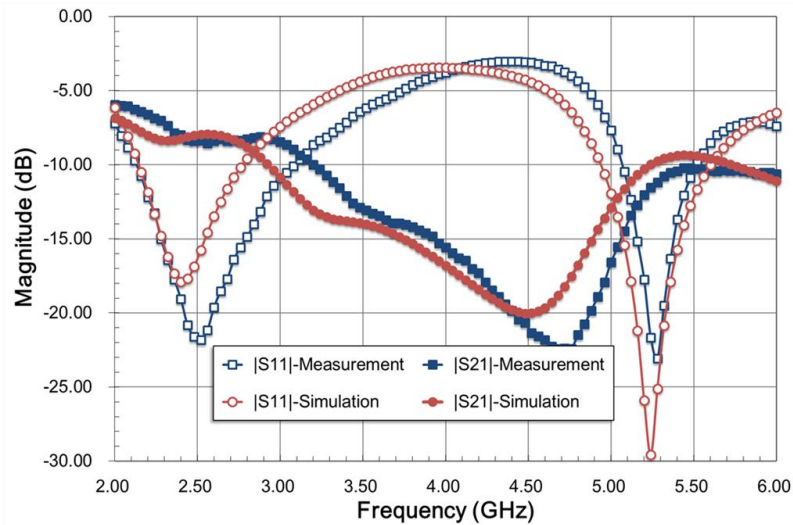
(b)

Figure 2.33 (a) Layout of two coupled dual-band antennas. (b) Simulated and measured S-parameters of the coupled antennas.

Table 2-5 Dimensions of Coupled and Decoupled Antennas (Unit: mm)

Variable	Value	Variable	Value
L_G	80.0	G, G_R	0.3
W_G	55.0	L	17.4
L_A	30.0	W	3.8
L_D	6.3	W_T	2
W_A	3.0	F_R	0.4
W_D	3.5	W_B	4.7
L_E	5.0	W_E	0.6
S	0.6	W_C	1.9

2.4.2.1 Parametric Study

In order to reveal the underlying relation between the parameters of the admittance transformer, several effects of parameter r, l_1 and l_2 are investigated:

1. Effect of r:
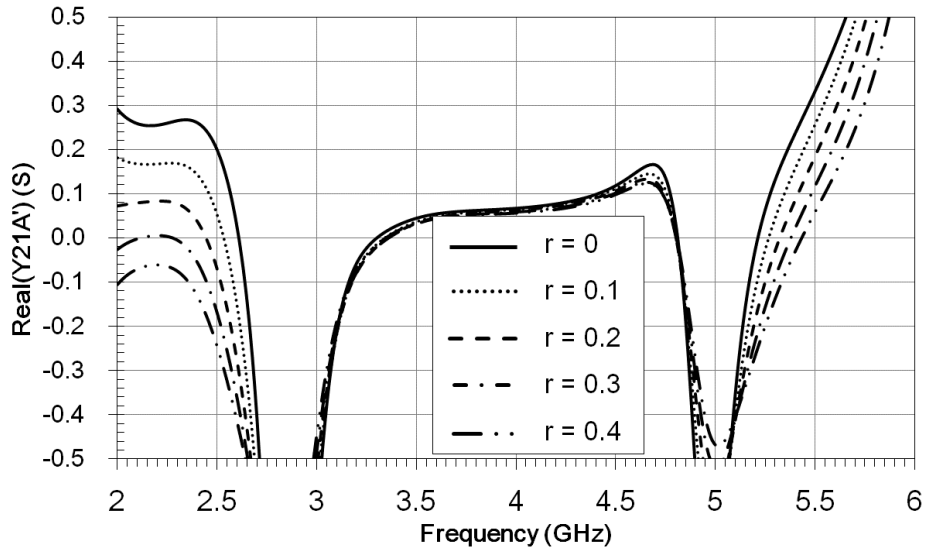
(a)
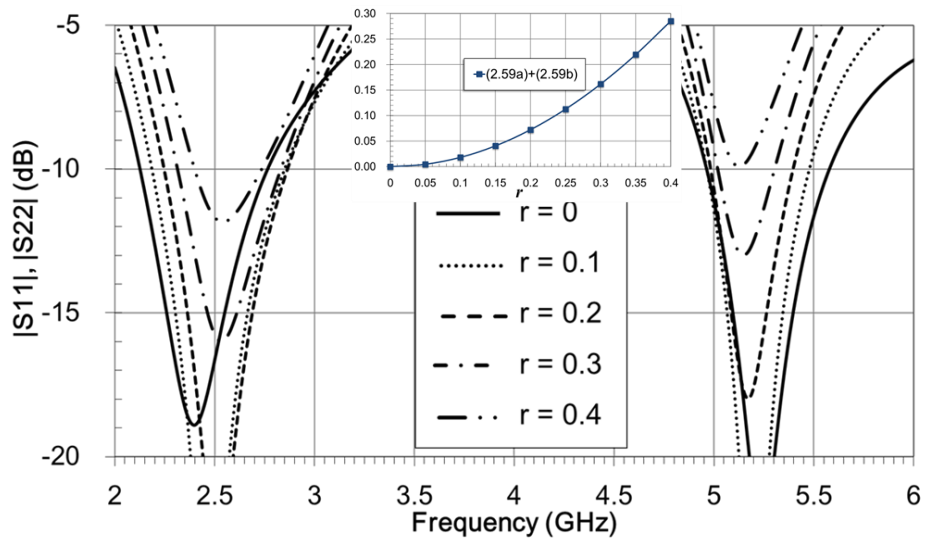
(b)

Figure 2.34 (a) Real part of mutual admittances; and (b) return losses of coupled antennas with respect to different choice of r value. ($\theta_1 = 30°$ and $\theta_2 = 50°$ are assumed in these plots without loss of generality.)

It can be seen from Fig. 2.34 (a) that by adjusting value r, the zero crossing locations of $Re(Y_{21}^A{'''})$ can be efficiently manipulated on the frequency axis. As in this example, if we increase r, the distance between the zero crossings at low band and high band will also increase. $r \approx 0.2$ will be suitable for 2.4 GHz and 5.2 GHz bands.

The increase of r will inevitably cause mismatch at the antenna port. The return loss

of the coupled antennas in Fig. 2.33 (a) with respect to different r values are studied and superposed in Fig. 2.34 (b). It is clear that r cannot be bigger than 0.3 to ensure acceptable matching condition at both the low and high bands, which means that the sum of (2.59a) and (2.59b) cannot be larger than 0.15.

2. Effect of θ_1 and θ_2:
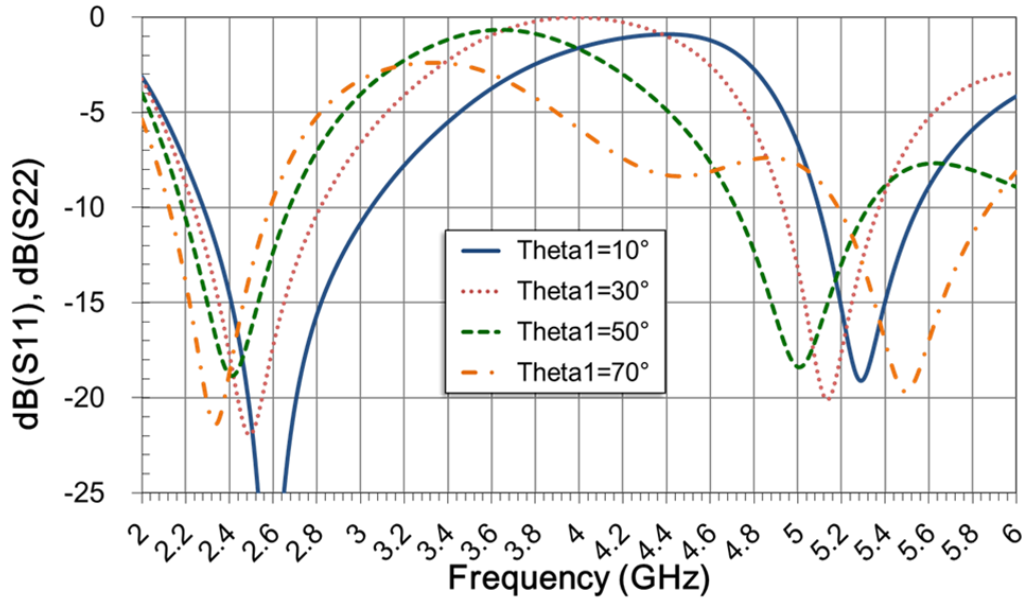
(a)
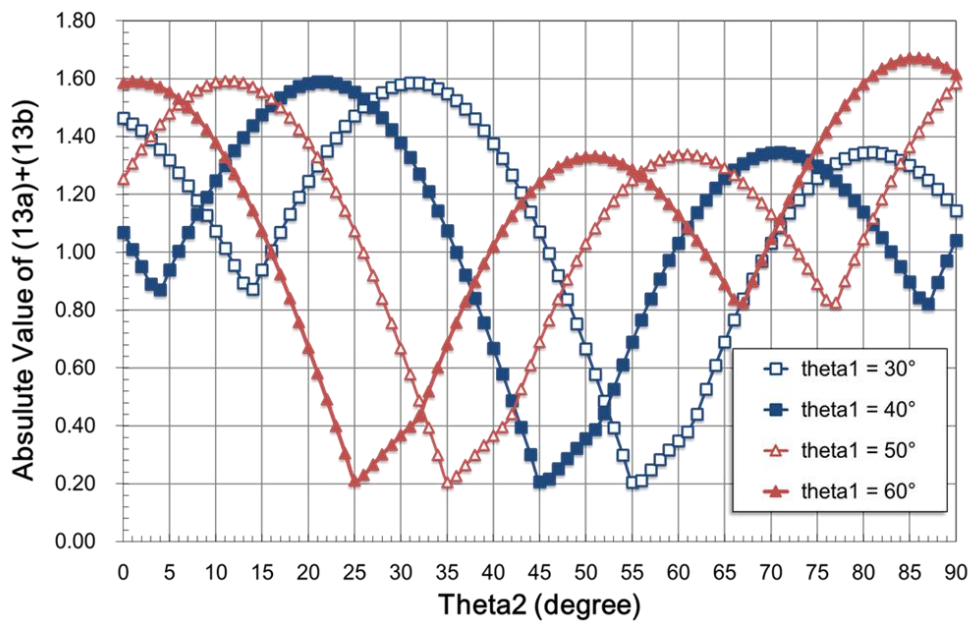
(b)

Figure 2.35 (a) Return losses of coupled antennas with respect to different choice of θ_1 value.

$(\theta_2 = 30^° \ and \ r = 0.2$ are assumed in the figure without loss of generality.) (b) Absolute value of (13a) + (13b) with respect to different θ_1. (r = 0.2)

The effect of transmission line length is also investigated. The return losses with respect to different θ_1 length when r is fixed to be 0.2 and θ_2 is fixed to be 30° are superposed in Fig. 2.35 (a). It can be seen that the matching performances at low and high bands are maintained if θ_1 is around 30° ~ 50°.

If θ_1 and r are fixed, θ_2 can be easily found by examine the absolute value of (13a) + (13b) with respect to different θ_2 as shown in Fig. 2.35 (b). One interesting observation is that there are more than one combinations of θ_1 and θ_2 which will result in desirable $Re(Y_{21}^{A}{}''')$ as long as the sum of θ_1 and θ_2 remains almost the same.

2.4.3. Dual-band CRDNs

2.4.3.1 Design Equations

Since a CRDN and a filter shares some features in common, many matured dual band filter synthesis and design techniques can be utilized with minor modifications. In designing a dual band filter, the specifications are imposed on S-parameters of the filter, whereas the requirements for a CRDN are now imposed on admittance parameters.

The circuit model of the dual-mode CRDN is shown in Fig.1 (a), which is quite similar to the CRDN single band circuit model in [9]. According to [9], the inter-resonator couplings m_{12} has to be designed as large as the physical implementation allows, which is also valid for the dual-band scenario. Having had this requirement fulfilled, the mutual admittances of the CRDN can be almost *constant* with a relatively large frequency band. Therefore, in both the low and high

frequency bands, the relation between the coupling coefficients and the admittance parameter of the dual band CRDN can be found from circuit nodal analysis, which is irrelevant of frequency variable ω:

$$y_{21}^{D}(\omega) \approx j \frac{m_{S1} \cdot m_{2L}}{Z_0 \cdot m_{12}}, \, \omega \in \left[\omega_{L1}, \omega_{L2}\right] , \tag{2.60a}$$

and

$$y_{21}^{D}(\omega) \approx j \frac{m_{S3} \cdot m_{4L}}{Z_0 \cdot m_{34}}, \, \omega \in \left[\omega_{H1}, \omega_{H2}\right] . \tag{2.60b}$$

where Z_0 is the characteristic impedance that is normally 50 ohm. It is obvious in (2.60) that the absolute value of y_{21}^{D} is mainly determined by the input and output couplings. The sign of y_{21}^{D} is controlled by the sign of inter-resonator coupling m_{12}
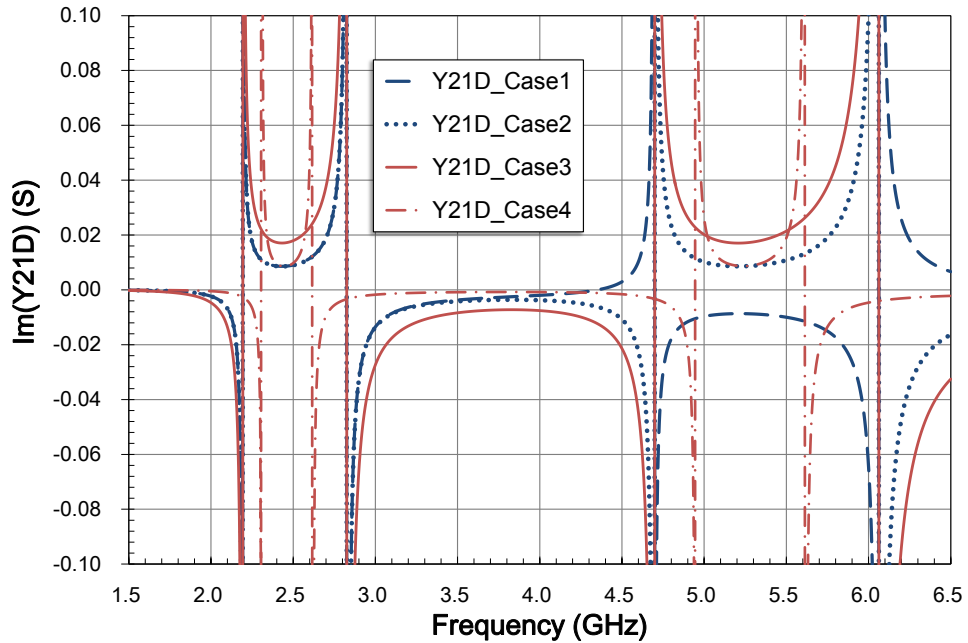
Figure 2.36 Mutual admittance of dual-band CRDNs under different configurations of the coupling coefficients.

and m_{34}. They all need to be designed properly for various coupled antenna pairs

according to conditions (2.47b) and (2.48b).

2.4.3.1 Case Study

To understand the function of all the coupling coefficients, several combination of coupling coefficients of the dual-band CRDN are analyzed, they are:

- *Case1*: A CRDN with opposite inter-resonator coupling coefficients at the low and high bands. ($m_{12} = -m_{34}$)
- *Case2*: A CRDN with the same inter-resonator coupling coefficients at the low and high bands. ($m_{12} = m_{34}$)
- *Case3*: A CRDN with larger input/output coupling coefficients at the low and high bands.
- *Case4*: A CRDN with the smaller inter-resonator coupling coefficients at the low and high bands.

The comparison between *Case 1* and *Case 2* is consistent with (2.60) that the sign of y_{21}^D can be efficiently manipulated by the sign of *m₁₂* and *m₃₄*. The comparison between *Case 2* and *Case 3* shows that the absolute value of y_{21}^D is mainly controlled by the input/output couplings. The comparison between *Case 3* and *Case 4* reveals the fact that the inter-resonator couplings have to be designed as large as possible for a relative flat y_{21}^D within the bands of interest as shown in Fig. 2.36.

Table 2-6 Parameters of the Designed Stepped-Impedance Transformers

	Electrical parameters		Physical dimensions (mm)	
	$Z_0 (\Omega)$	θ (degree)	Width (w)	Length (l)
Section1	50	31	3	5.8
Section2	72	55	1.55	10.7
Section3	50	34.5	3	6.5
Section4	67	20.4	1.83	4
Section5	48	32	3.3	6

2.4.4. A Design Example

2.4.4.1 Design of Dual-band Admittance Transformer

A two-section stepped impedance transformer is designed in the first step using the method discussed in **Section 2.4.2**. The optimum parameters of the transformer are listed in Table 2-6.
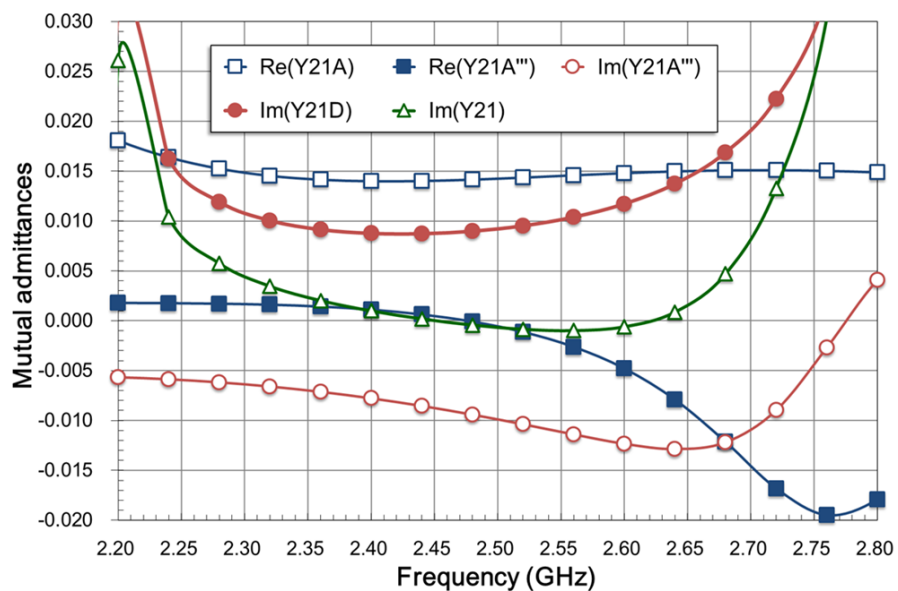
(a)
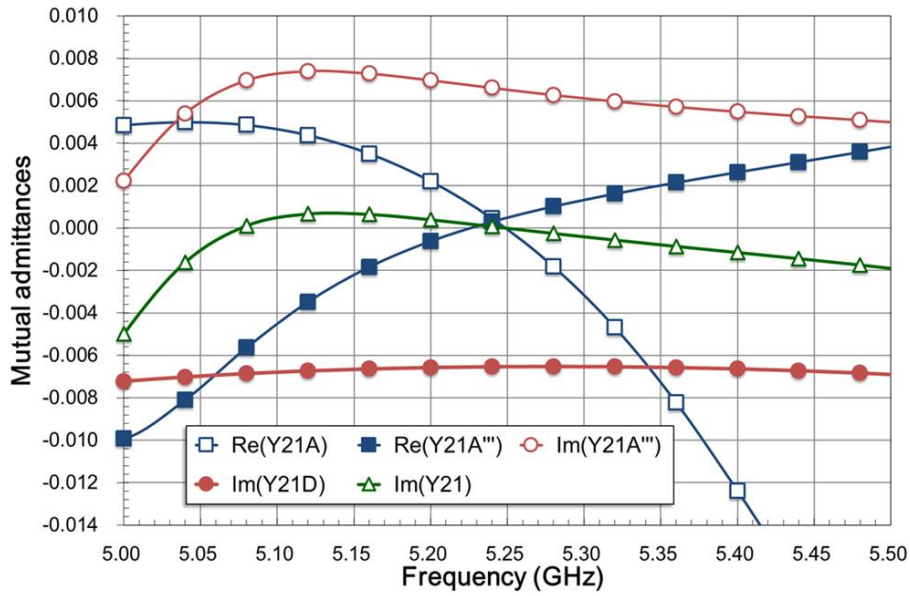
(b)

Figure 2.37 Mutual admittance parameters of the coupled antennas and the CRDN at (c) the low band; and (d) the high band.

The simulated mutual admittance of the coupled antennas are shown in Fig. 2.37 for both the cases with and without the stepped impedance transformers. It should be noted that for the coupled antennas without stepped impedance transformers, a section of transmission lines with characteristic impedance Z_0 and proper length is already included to best satisfy (2.48a) for comparison purpose. It is possible to transform the mutual admittance to purely imaginary at one frequency band using a section of uniform transmission line, but equations (2.47a) and (2.48a) cannot be satisfied at the same time, which is obviously seen in Fig. 2.37 (a). By introducing a stepped impedance transformer in two sections, the real part of the mutual admittance, $\mathrm{Re}(Y_{21}^{A'''})$, becomes zero at 2.45 GHz and 5.25 GHz, which is quite obvious in Fig. 2.37.

2.4.4.2 Design of a Dual-band CRDN
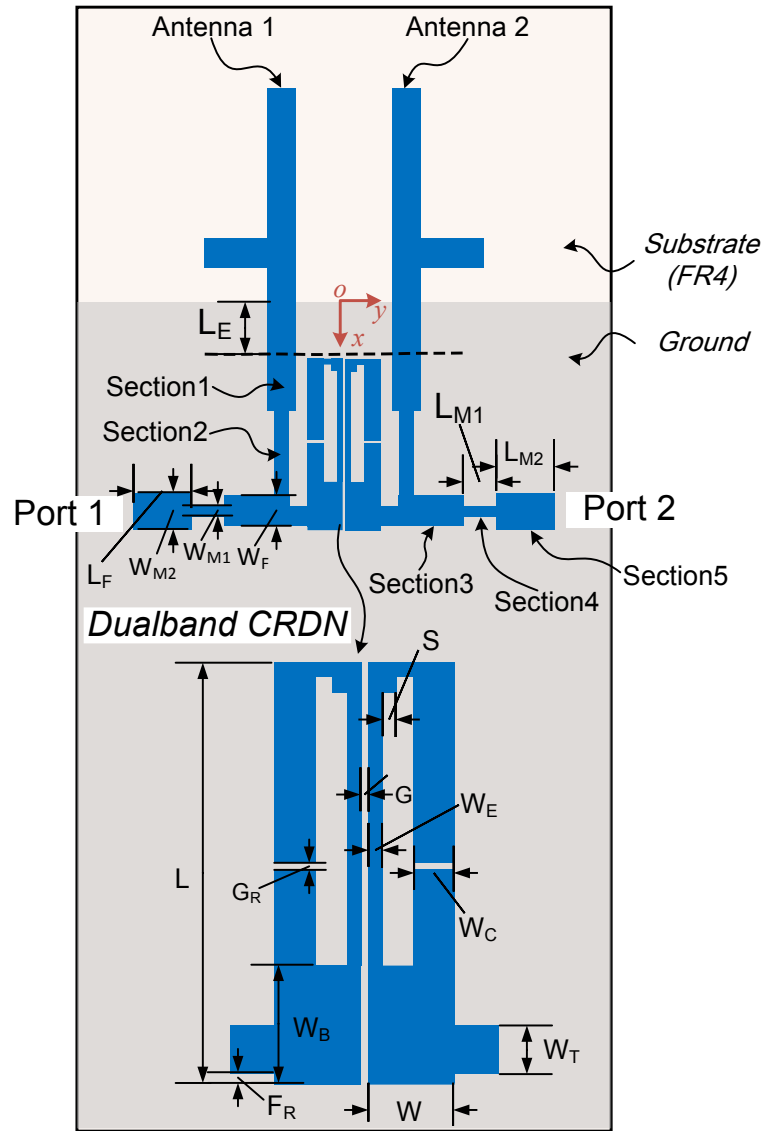
(a)
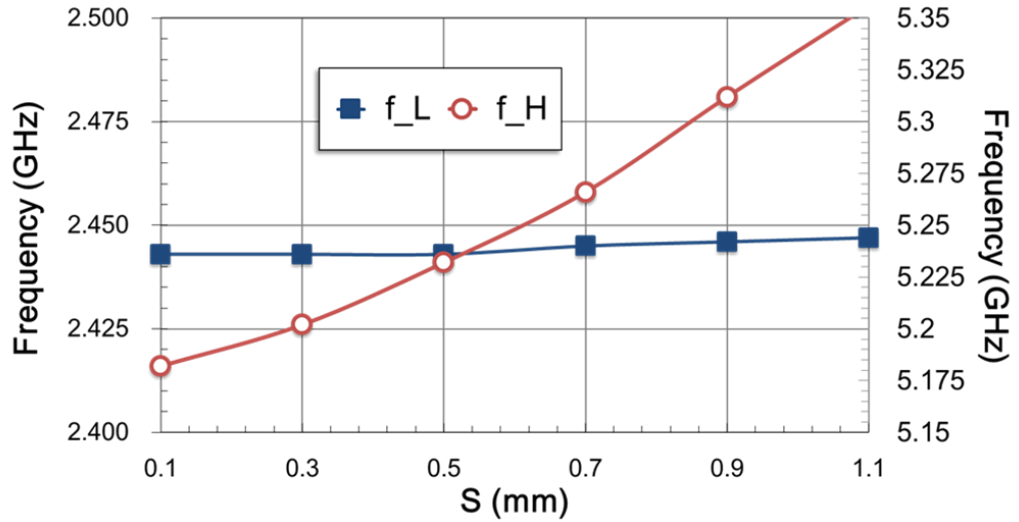
(b)
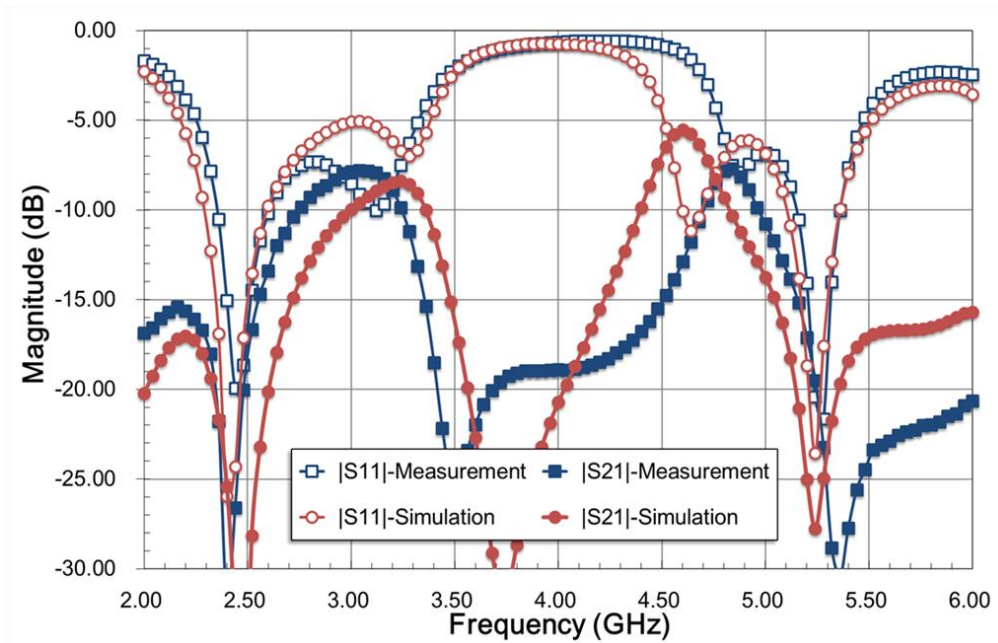
(c)

Figure 2.38 (a) Layout of the dual-band dual-mode CRDN and the dual-band antennas with the CRDN. (b) The first two resonant frequencies against the size of the square perturbation element. (c) Simulated and measured S-parameters of the decoupled antennas.

The coupled but transformed (by the stepped-impedance transformer) two-port antenna network is then connected to the dual-band CRDN in shunt to cancel out the remaining imaginary parts of the mutual admittance at both the low and high bands. It can be seen from Fig. 2.37 that $\text{Im}(Y_{21}^{A'''}) = -0.0086$ at 2.45 GHz and $\text{Im}(Y_{21}^{A'''}) =$

0.0066 at 5.25 GHz. Meanwhile, in the low band (2.4 GHz ~ 2.48 GHz) as well as the high band (5.15 GHz ~ 5.35 GHz), the variation of $\mathrm{Im}(Y_{21}^{A'''})$ is not more than $\pm 10\%$. Therefore, equations (2.47b) and (2.48b) can be further simplified to:

$$Y_{21}^D(\omega) = -j\,\mathrm{Im}\left\{Y_{21}^A(\omega)\right\} \approx -j\,\mathrm{Im}\left\{Y_{21}^A(\omega_L)\right\}, \; \omega \in \left[\omega_{L1}, \omega_{L2}\right] \qquad (2.61\mathrm{a})$$

and

$$Y_{21}^D(\omega) = -j\,\mathrm{Im}\left\{Y_{21}^A(\omega)\right\} \approx -j\,\mathrm{Im}\left\{Y_{21}^A(\omega_H)\right\}, \; \omega \in \left[\omega_{H1}, \omega_{H2}\right] \qquad (2.61\mathrm{b})$$

Based on (2.61), the coupling coefficients are obtained from (2.60) for both the low and the high bands and are listed in Table 2-7. In fact, there are plenty of ways to realize a dual band resonator using a multi-layer PCB board. The dual-band open loop square ring microstrip resonator in [6] are used in light of its attractive features such as easy to be implemented by a planar circuit and compact in size (Fig. 2.38 (a)).

Table 2-7 Coupling coefficients of designed and realized CRDN FBW = 10%)

	m_{S1}, m_{2L}	m_{12}	m_{11}, m_{22}
Designed (Low band)	1.0368	2.5000	0.0000
Realized (Low band)	1.1267	2.6798	-0.0051
Designed (High band)	0.9083	-2.5000	0.0000
Realized (High band)	1.0288	-2.7312	0.1123

The second harmonic mode of the resonator is perturbed by a small square corner element with the size of S by S (mm^2) thus controlling the frequency of the harmonic mode, which is shown in Fig. 2.38 (b). The input couplings are implemented by the

tapper-line scheme. Larger F_R will result in smaller input/output couplings. The inter-resonator coupling is implemented by edge to edge coupling which is mainly magnetic coupling at the fundamental frequency. To keep this coupling as large as possible, the line width W_E and the gap size G have to be as small as the realization allows. The realized coupling coefficients are listed in Table 2-7 and the realized admittance parameters of the dual-band CRDN are shown in Fig. 2.37. It can be seen that in the bands of interest, the designed CRDN significantly reduces the imaginary part of the mutual admittance of the original coupled antennas, whose corresponding S-parameters are shown in Fig. 2.38 (c). To further improve the matching performance, a stepped-impedance transformer is designed according to the method in [12], the resultant dimensions of the stepped impedance transformer as the dual-band matching network (DMN) are listed in Table 2-6. The measured S-parameters demonstrate that the isolation between the decoupled antennas are more than 15 dB while the return losses for both antennas are more than 10 dB in both 2.4 GHz ~ 2.5 GHz and 5.15 GHz ~ 5.35 GHz frequency bands. Other dimensions of the decoupled antennas are listed in Table 2-5.

2.4.4.3 Performance investigation

To reveal the decoupling mechanism of the proposed dual-band CRDN, the simulated current distributions for coupled antennas and decoupled antennas at both the low and the high bands are also presented in Fig. 2.39, in which port 1 is excited while port 2 is terminate with a matched load using the MoM solver in Agilent's Advanced Design System [13]. It is seen that a strong coupling between antennas is cancelled out by the current induced through the dual-band CRDN in the two frequency bands, resulting in two well decoupled dual-band antennas.

$f_L = 2.45$ GHz $f_U = 5.25$ GHz

(a)

$f_L = 2.45$ GHz $f_U = 5.25$ GHz
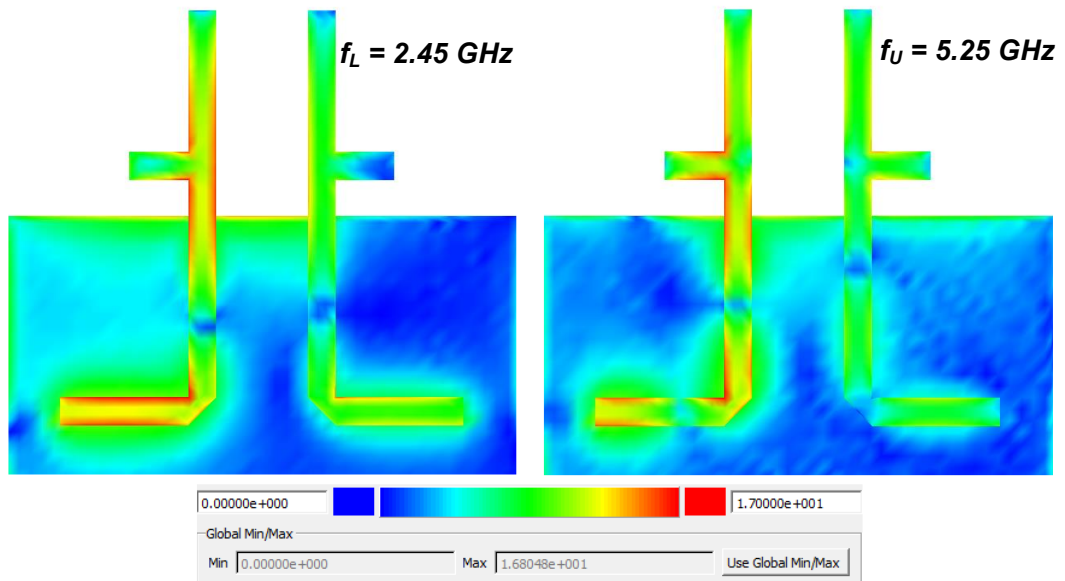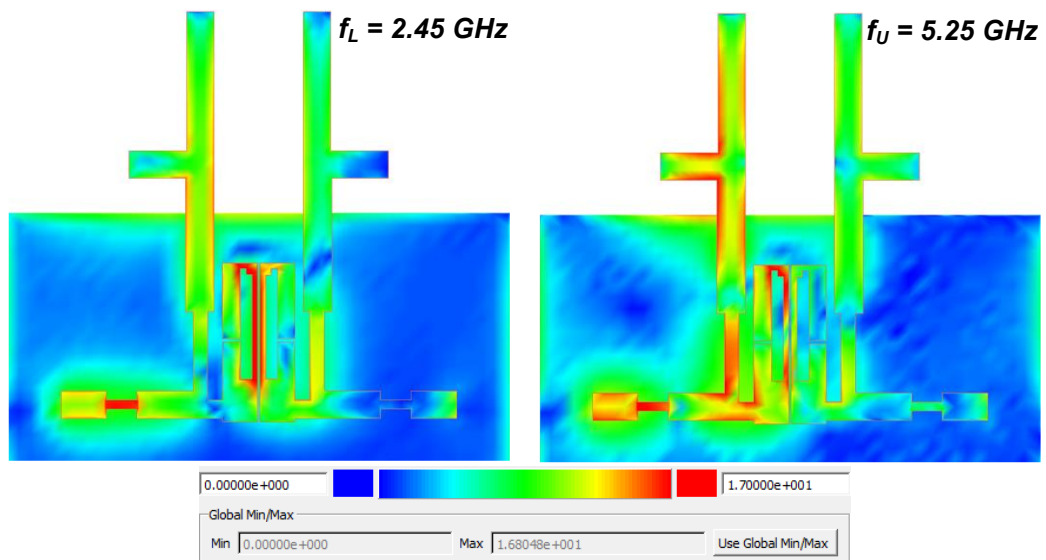
(b)

Figure 2.39 Simulated current distribution of (a) Coupled dual-band antennas; and (b) Antennas decoupled by dual-band CRDN at 2.45 GHz and 5.25 GHz.

2.5. A Third Order Three-Port S-CRDN

Since the CRDN is mainly formed by resonators that are closely coupled, theoretically, it has no limitation on the number of resonators that are coupled to each other, therefore, the second order S-CRDN has the potential to be applied to three or

more element decoupling problem. In this section, the concept of S-CRDN is extended to a three port decoupling network using at least three coupled resonators. An efficient and broadband decoupling can be achieved when the network is connected to a strongly coupled three-element compact array. Then the configuration of the circuit model and underlying working mechanisms for the decoupling network are introduced. An example for decoupling a three-monopole array working at 2.6 GHz band is then presented at the end.

2.5.1. The Network/Circuit Model

The network/circuit model of a strongly coupled compact array with the decoupling network is shown in Fig. 2.40. The CRDN is composed of *three* multi-coupled resonators. The coupling coefficients of these coupled resonators include:

1) The input/output couplings ($m_{pi\_i}, i = 1,2,3$),

2) The inter-resonator couplings ($m_{ij}, i \neq j$) and,

3) The self-couplings ($m_{ii}, i = 1,2,3$).
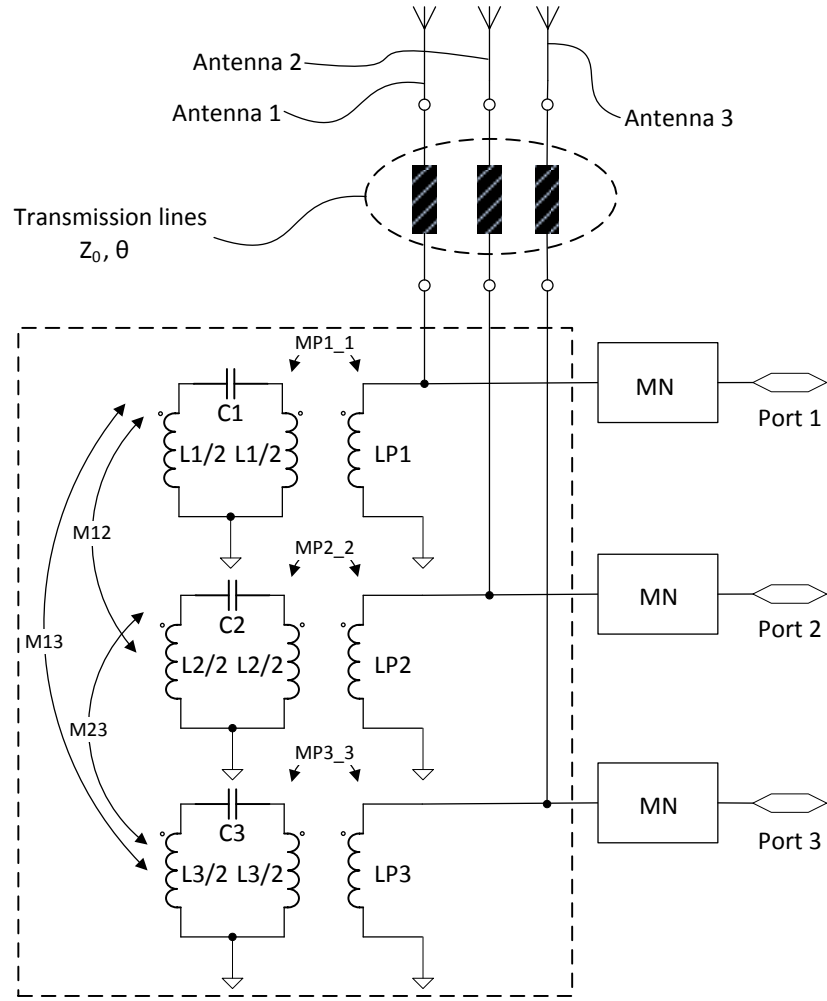
Figure 2.40 The network/circuit model of the three port coupled resonator network in shunt with the compact antenna array.

The CRDN is then connected with the strongly coupled antenna array in shunt. In general, the three coupled antennas can be represented by a 3×3 admittance matrix ($\mathbf{Y}^A$) with complex entries. Being a lossless network, the entries of the admittance matrix $\mathbf{Y}^F$ of the CRDN must all be purely imaginary. Obviously, the admittance of the connected network is the sum of the two admittance matrices as:

$$\mathbf{Y} = \begin{bmatrix} Y_{11} & Y_{12} & Y_{13} \\ Y_{21} & Y_{22} & Y_{23} \\ Y_{31} & Y_{32} & Y_{33} \end{bmatrix} = \begin{bmatrix} Y_{11}^A + Y_{11}^F & Y_{12}^A + Y_{12}^F & Y_{13}^A + Y_{13}^F \\ Y_{21}^A + Y_{21}^F & Y_{22}^A + Y_{22}^F & Y_{23}^A + Y_{23}^F \\ Y_{31}^A + Y_{31}^F & Y_{32}^A + Y_{32}^F & Y_{33}^A + Y_{33}^F \end{bmatrix} \qquad (2.62)$$

For a symmetrical circular array, a symmetrical CRDN is sufficient to de-correlate the three antenna elements. To achieve a better decoupling performance, the mutual admittances of the array are first transformed by three sections of identical transmission lines using the same method in **Section 2.1.2**. Then the decoupling condition can be written as

$$j \cdot \text{Im}\left\{Y_{mn}^A\right\} + Y_{mn}^F \approx 0, \ \ m,n = 1,2,3, \ \ m \neq n \ . \tag{2.63}$$

After the antennas in the compact array are fully decoupled, each antenna can be independently matched to port admittance. The matching condition is then expressed as

$$\text{Re}\left\{Y_{mm}^A\right\} + j \cdot \text{Im}\left\{Y_{mm}^A\right\} + j \cdot \text{Im}\left\{Y_{mm}^F\right\} \approx Y_0, \ \ m = 1,2,3 \ , \tag{2.64}$$

where Y_0 is the port admittance. Extra matching networks (MNs) can also be added to each port to improve the matching bandwidth as shown in Fig. 2.40.

2.5.2. Design of the Three-port S-CRDN

The two-port coupled resonator circuits are widely exploited in the synthesis and design for microwave filters. The concept of coupled resonators is extended to the cases with N ports in general and particularly N = 3 in this paper. The circuit model shown in Fig. 1 can be implemented by the coupling topology shown in Fig. 2.41. In Fig. 40, $L_1 = L_2 = L_3$ and $C_1 = C_2 = C_3$ determine the resonant frequency of the three resonators while the three inductors L_{P1}, L_{P2} and L_{P3} represent three port couplings with zero inductances.
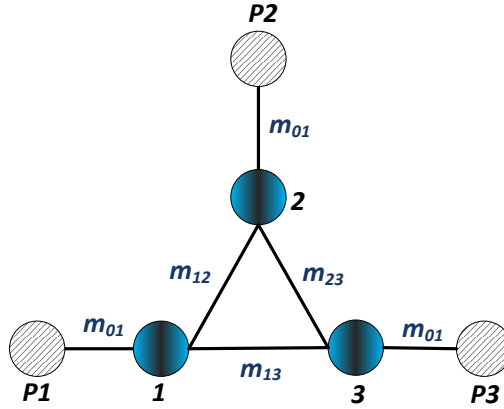
Figure 2.41 The coupling topology of the proposed three-port S-CRDN.

To keep the structure as simple as possible, only the I/O couplings from each port to each resonator as well as the couplings between every two resonators are considered. They are the coupling of port 1 to resonator 1, m_{P1_1}; the coupling of port 2 to resonator 2, m_{P2_2}; the coupling of port 3 to resonator 3, m_{P3_3}; the coupling between resonator 1 and resonator 2, m_{12}; the coupling between resonator 2 and resonator 3, m_{23}; and the coupling between resonator 3 and resonator 1, m_{31}, respectively. Since the three-element antenna array is symmetric, the CRDN must be symmetric, which means that $m_{P1\_1} = m_{P2\_2} = m_{P3\_3} = m_{io}$ and $m_{12} = m_{23} = m_{31} = m_r$. The circuit model in Fig. 2.40 can be easily designed by a simple optimization with (2.63) and (2.64) as objective functions. In the optimization, the coupled antennas can be treated as a black box with either simulated or measured scattering parameters included. The obtained coupling coefficients are then used as the targets in designing the physical layout of the decoupling network.

2.5.3. A Design Example

To validate the concept of the three-port CRDN, a prototype of the S-CRDN together with a compact three-element monopole antenna array is fabricated and measured. Three strongly coupled monopoles are placed with the spacing of 0.2λ. The three-port CRDN is composed of three microstrip open-loop triangular

resonators that are mutually coupled. The layout of the compact array as well as the CRDN is shown in Fig. 2.42 (a). The substrate used is FR4 with the relative dielectric constant of 4.3 and the thickness of 0.8 mm, other design dimensions are listed in Table 2-8.

(a)

(b)
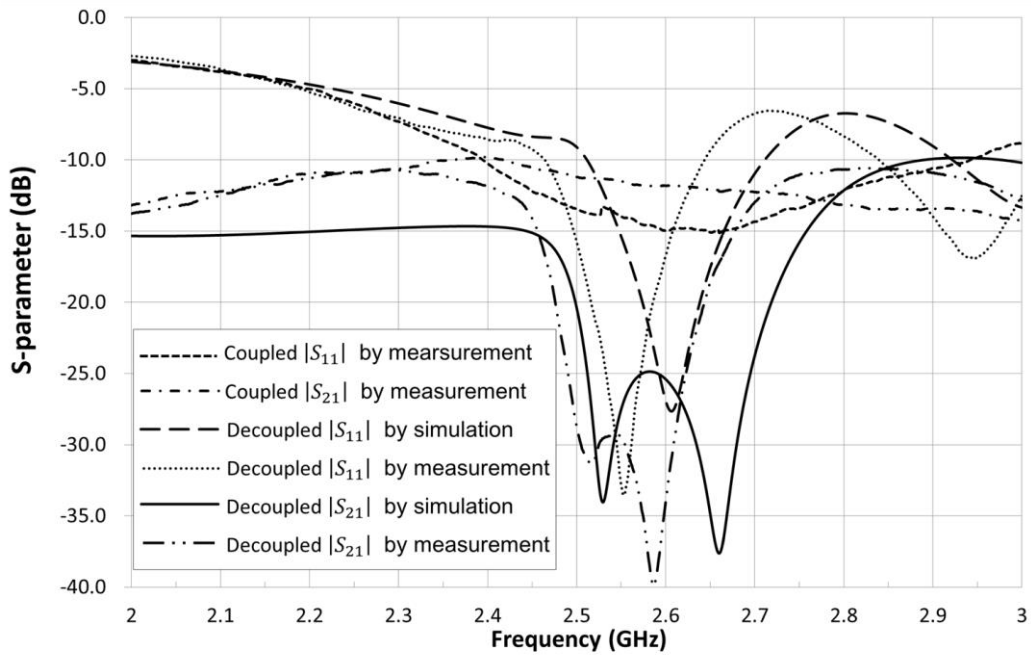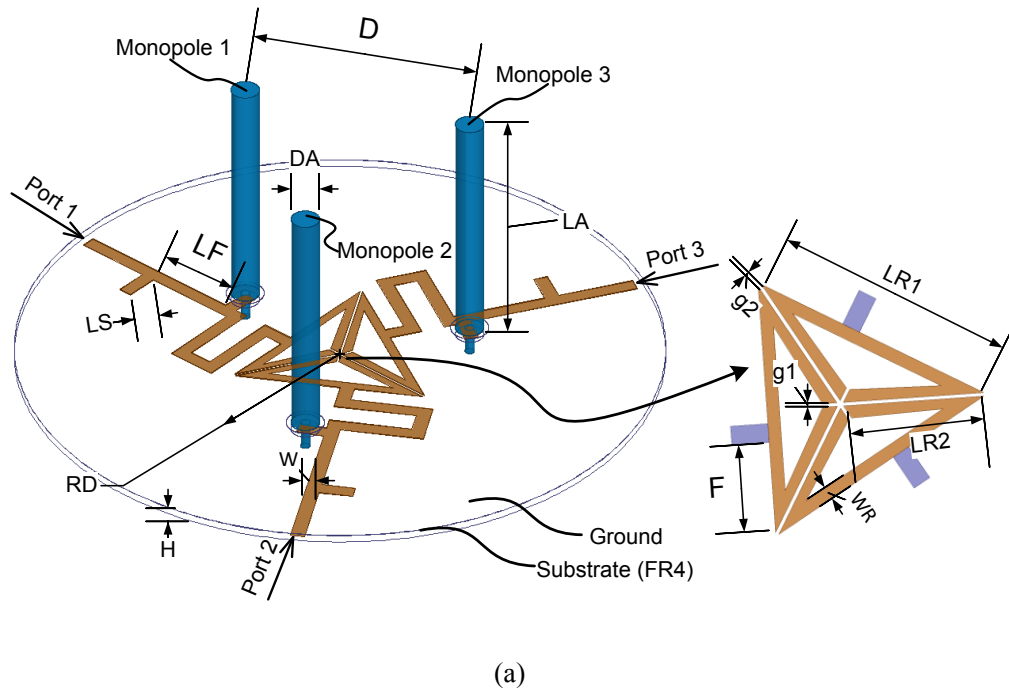
Figure 2.42 (a) A compact monopole array with the CRDN. (b) The simulated and measured

scattering parameters with and without the CRDN.

Table 2-8 Dimensions of the compact array and decoupling network unit: millimeters

Variables	Size	Variables	Size	Variables	Size
RD	34	g1, g2	0.3	LA	26
DA	3	D	24	W	1.5
LS	3.6	LF	10.1	LR2	11.3
F	7.3	WR	1	LR1	19.8

The simulated and the measured scattering parameters of the compact array with and without the CRDN are superposed in Fig. 2.42 (b). Because of the symmetry, only S_{11} and S_{21} are shown. For the coupled antennas, the isolation is as poor as 11 dB at 2.6 GHz. Because of the close spacing, the matching performance is not good either.

Having inserted the CRDN, the isolation is significantly improved. Meanwhile, the matching performance is also improved around the center frequency. To further broaden the matching bandwidth, single-stub matching networks are also designed at each port. The measured decoupling and matching bandwidth with $|S_{11}| < -10dB$ and $|S_{21}| < -20dB$ is 6.4%, which is suitable for LTE 2.6GHz band 7. The realized coupling coefficients are: $m_{io} = 1.7214$ and $m_r = 2.6851$, which are extracted from measurement results by the circuit model shown in Fig. 2.40.
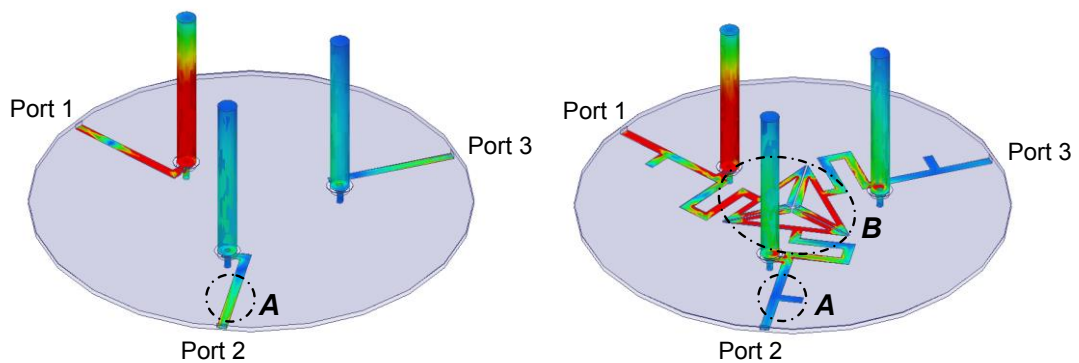
Figure 2.43 Simulated Current distribution on the (a) Coupled Array; and (b) Decoupled Array.

The simulated current distribution of the coupled array and the decoupled array with the S-CRDN are also plotted in Fig. 43. In both simulations, port 1 is excited while the other ports are terminated with matched loads. For the coupled array, strong current can be observed in region A, while for decoupled array, since opposite field are introduced in Region B to cancel out the coupled, there will be almost no current in Region A.

2.6. Reference

[1] D. M. Pozar, Microwave Engineering, 3rd ed. New York: Wiley, 2005.

[2] E. C. Niehenke, "Wireless Communications: Present and Future," *IEEE Microwave Magazine,* vol.15, no.2, pp.26-35, March-April 2014.

[3] G. Shaker, S. Safavi-Naeini, and N. Sangary, "Q-Bandwidth relations for the design of coupled multi-element antennas," in *Proc. IEEE Antennas Propag. Society Int. Symp.*, Jun. 1–5, 2009, pp. 1–4.

[4] G. L. Matthaei, L. Young, and E. M. T. Jones, Microwave Filters Impedance Matching Networks and Coupling Structures. New York: McGraw-Hill, 1980, pp. 355–410.

[5] R. J. Cameron, C. M. Kudsia, and R. R. Mansour, Microwave Filters for Communication systems. New York: Wiley, 2007, ch. 6-8.

[6] M. E. van Valkenburg, Network Analysis, Prentice-Hall, Englewood Cliffs, NJ, 1955.

[7] J.-S. Hong and M. J. Lancaster, Microstrip Filters for RF/Microwave Applications, 2nd ed. New York: Wiley, 2011, Ch. 7-10.

[8] M. Meng and K.-L. Wu, "An analytical approach to computer-aided diagnosis and tuning of lossy microwave coupled resonator filters," *IEEE Trans. Microw.*

Theory Tech., vol.57, no.12, pp.3188-3195, Dec. 2009.

[9] H. Hu and K.-L. Wu, "A generalized coupling matrix extraction technique for bandpass filters with uneven-Qs", *IEEE Trans. Microwave Theory Tech.,* Vol.62, No.2, pp.244-251, February 2014.

[10] L. Zhao, L. K. Yeung, and K.-L. Wu, " A coupled resonator decoupling network for two-element compact antenna arrays in mobile terminals," *IEEE Trans. Antennas Propag.*, vol. 62, no. 5, May 2014.

[11] S. Chang, Y. –S. Wang, and S. –J. Chung, "A decoupling technique for increasing the port isolation between strongly coupled antennas," *IEEE Trans. Antennas Propag.* vol. 56, no. 12, pp. 3650-3658, Dec. 2008.

[12] K. Kurokawa, "Power waves and the scattering matrix", *IEEE Trans. Microw. Theory Tech.*, vol. 13, No.2, pp. 194-202, 1965.

[13] X. Liu, Y. Liu, S. Li, F. Wu and Y. Wu, "A Three-Section Dual-Band Transformer for Frequency-Dependent Complex Load Impedance," *IEEE Microw. and Wireless Components Lett., IEEE* , vol.19, no.10, pp.611-613, Oct. 2009.

[14] Advanced Design System, Version 2012.08, Agilent Technologies, Inc., Santa Clara, CA.

[15] [Online]. Available: http://www.satimo.com/

Chapter 3

Cascaded type CRDN

The S-CRDNs are usually low in orders and quality factors but compact in size, which is suitable for mobile terminal and wireless router. For base station applications, high Q networks are highly desirable. A new breed of microwave passive devices, called cascaded type of Coupled Resonator Decoupling Network (C-CRDN), which can effectively reduce the coupling between two coupled antennas operating at either the same or different frequency bands in a base station (BTS) while providing a good impedance matching will be introduced in this section. Comparing to the existing techniques, the new device has the following unique features:

(1) It is a passive network that does not require any electronic circuits nor any power supply;

(2) It is a generic technique and is applicable to a wide range of co-existence problems;

(3) It provides a significant additional isolation even if the original isolation is already high; the level of the additional isolation is controllable depending on the order of the network;

(4) While providing an additional isolation, the network also significantly improve matching bandwidth of the antennas; and

(5) A C-CRDN device is a filter-like microwave network, so that many filter theory and design technologies [1] can be applied to this new device.

Unlike a conventional microwave filter that is a two-port device, a C-CRDN a four

port coupled resonator network. Although microwave coupled resonator multiport networks is a popular topic in recent years [2]-[5], most of the developed theories and technologies concern with microwave diplexers and multiplexers, which usually possess a common port. Few attention has been paid to problems of decoupling between two radio systems. To the best of authors' knowledge, the proposed C-CRDN concept is the first attempt to address this problem. In this section, the fundamental working principles of the four-port C-CRDN device will be discussed in detail. Two practical design examples will also be given to demonstrate the effectiveness of the device. The measured results have shown that a C-CRDN can effectively mitigate the coexistence interference between two collocated systems by providing at least 20 dB isolation improvement with enhanced matching performance. The proposed technique is generic and can find many applications in future wireless communication systems.

3.1. Nodal Analysis of Multi-port Coupled Resonators

Before discussing the theory for the C-CRDN for two antennas, it is worthy to develop a generalized theory concerning an N-th order coupled resonator network with M ports. For simplicity, M is chosen to be 4 in this section while N can be arbitrary values, normally, $N \geq 4$. The circuit model of such network is shown in Fig. 3.1. The routing diagram of a general ladder coupling topology of the coupled resonators is depicted in Fig. 3.1 (b), where each solid circle represents a microwave resonator resonating at a designed frequency and the dashed line marked by m_{ij} represents for the required coupling between resonators i and j, and the dash line marked by m_{pq-p} represents the coupling between port q and resonator p.

Applying the KVL and KCL to the network representation, following the similar deduction approach in [2] and assuming that there are no couplings between the ports, the admittance matrix $[Y_D]$ of the C-CRDN can be expressed as

$$[Y_D] = j \cdot \left[\mathbf{M_{pr}} \left(\mathbf{M_{rr}} - j \cdot \mathbf{S} \right)^{-1} \mathbf{M_{rp}} \right]^{-1},$$ (3.1)

where

$$\mathbf{M}_{\mathbf{pr}} = \begin{bmatrix} m_{p1\text{-}1} & 0 & \cdots & 0 & 0 \\ 0 & m_{p2\text{-}2} & \cdots & 0 & 0 \\ 0 & 0 & \cdots & m_{p3\text{-}(N\text{-}1)} & 0 \\ 0 & 0 & \cdots & 0 & m_{p4\text{-}N} \end{bmatrix} \in \mathbb{C}^{4 \times N}$$ (3.2a)

$$\mathbf{M}_{\mathbf{rp}} = \mathbf{M}_{\mathbf{pr}}^{\mathbf{T}} \in \mathbb{C}^{N \times 4}$$ (3.2b)

$$\mathbf{M}_{\mathbf{rr}} = \begin{bmatrix} m_{11} & m_{12} & \cdots & m_{1N} \\ m_{12} & m_{22} & \cdots & m_{2N} \\ \vdots & \vdots & \ddots & \vdots \\ m_{1N} & m_{2N} & \cdots & m_{NN} \end{bmatrix} \in \mathbb{C}^{N \times N} \quad ,$$ (3.2c)

$$\mathbf{S} = diag[s, s, \cdots, s] \in \mathbb{C}^{N \times N} \quad ,$$ (3.2d)

with

$$s = j \cdot \frac{1}{FBW}(\frac{\omega}{\omega_0} - \frac{\omega_0}{\omega})$$ (32e)

where ω here means the frequency in the bandpass domain, $\omega_0 L = Z_0$ and the fractional bandwidth (FBW) is a design parameter specified by the designer. Notice that the block matrix inversion relations in **Appendix A4** are used in deducing (3.1).

An interesting finding from (3.1) is that when the port number equals to the number of resonators, such as three port S-CRDN with three resonators, and four port C-CRDN with four resonators, the admittance parameters can be expressed in a very compact form. Take the four-port C-CRDN as an example, (3.2) will become:

116

$$\mathbf{M_{pr}} = \begin{bmatrix} m_{p1-1} & 0 & 0 & 0 \\ 0 & m_{p2-2} & 0 & 0 \\ 0 & 0 & m_{p3-3} & 0 \\ 0 & 0 & 0 & m_{p4-4} \end{bmatrix} = \mathbf{M_{rp}} \qquad (3.3a)$$

$$\mathbf{M_{rr}} = \begin{bmatrix} m_{11} & m_{12} & m_{13} & m_{14} \\ m_{12} & m_{22} & m_{23} & m_{24} \\ m_{13} & m_{23} & m_{33} & m_{23} \\ m_{14} & m_{24} & m_{34} & m_{44} \end{bmatrix} \qquad (3.3b)$$

$$\mathbf{S} = \begin{bmatrix} s & 0 & 0 & 0 \\ 0 & s & 0 & 0 \\ 0 & 0 & s & 0 \\ 0 & 0 & 0 & s \end{bmatrix} \qquad (3.3c)$$

Therefore, (3.1) can be simplified to:

$$[Y_D] = j \cdot \mathbf{M}_{rp}^{-1} \left(\mathbf{M_{rr}} - j \cdot \mathbf{S} \right) \mathbf{M}_{pr}^{-1} \qquad (3.3d)$$

with

$$\mathbf{M}_{pr}^{-1} = \begin{bmatrix} \dfrac{1}{m_{p1-1}} & 0 & 0 & 0 \\ 0 & \dfrac{1}{m_{p2-2}} & 0 & 0 \\ 0 & 0 & \dfrac{1}{m_{p3-3}} & 0 \\ 0 & 0 & 0 & \dfrac{1}{m_{p4-4}} \end{bmatrix} = \mathbf{M}_{rp}^{-1} \qquad (3.3e)$$

More specifically, the self-admittances can be expressed as

$$Y_{ii}^D = \frac{(s + jm_{ii})}{m_{pi-i}^2} \quad i = 1, 2, 3, 4 \qquad (3.4)$$

and

117

$$Y_{ij}^D = \frac{jm_{ij}}{m_{pi-i} \cdot m_{pj-j}} \quad i, j = 1, 2, 3, 4; \ i \neq j \tag{3.5}$$

Equations (3.4) and (3.5) are convenient to use in synthesizing and designing multi-port CRDNs.

(a)

(b)
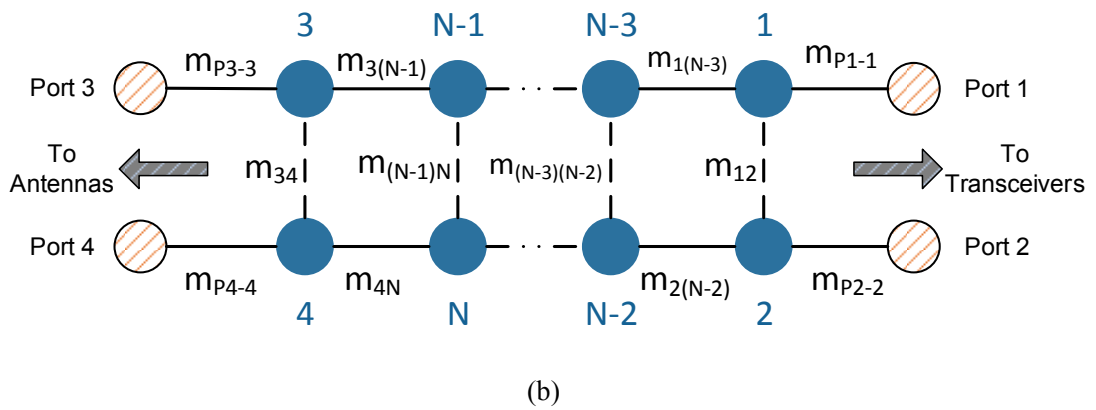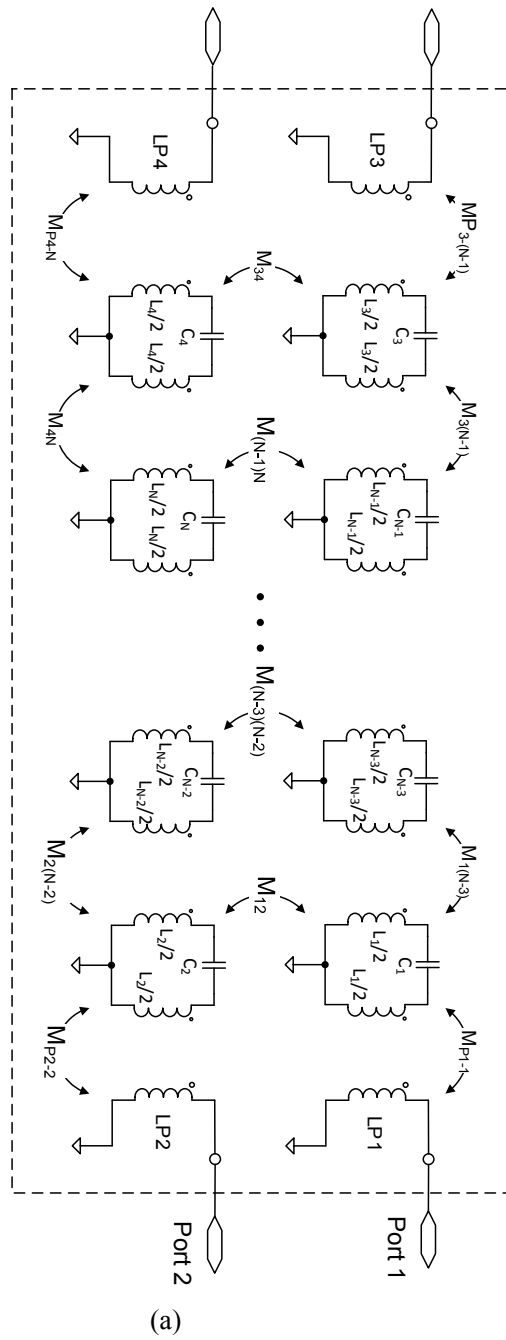
Figure 3.1 (a) The circuit model and (b) The routing diagram of the four-port N-th order CRDN.

3.2. The Network Model of the Cascaded System

For two strongly coupled antennas resonating at adjacent frequency bands, their admittance matrix can be expressed as

$$\left[\mathbf{Y^A} \right] = \begin{bmatrix} Y_{11}^A & Y_{12}^A \\ Y_{12}^A & Y_{22}^A \end{bmatrix}. \tag{3.6}$$

In order to mitigate the coexistence interference caused by the radiating characteristic of the two antennas, a four-port CRDN is cascaded to the coupled antennas as shown in Fig. 3.2.

$$Y_A = \begin{bmatrix} Y_{11}^A & Y_{12}^A \\ Y_{12}^A & Y_{22}^A \end{bmatrix} \qquad Y_D = \begin{bmatrix} Y_{11}^D & Y_{12}^D & Y_{13}^D & Y_{14}^D \\ Y_{12}^D & Y_{22}^D & Y_{23}^D & Y_{24}^D \\ Y_{13}^D & Y_{23}^D & Y_{33}^D & Y_{34}^D \\ Y_{14}^D & Y_{24}^D & Y_{34}^D & Y_{44}^D \end{bmatrix} \qquad Y = \begin{bmatrix} Y_{11} & Y_{12} \\ Y_{12} & Y_{22} \end{bmatrix}$$
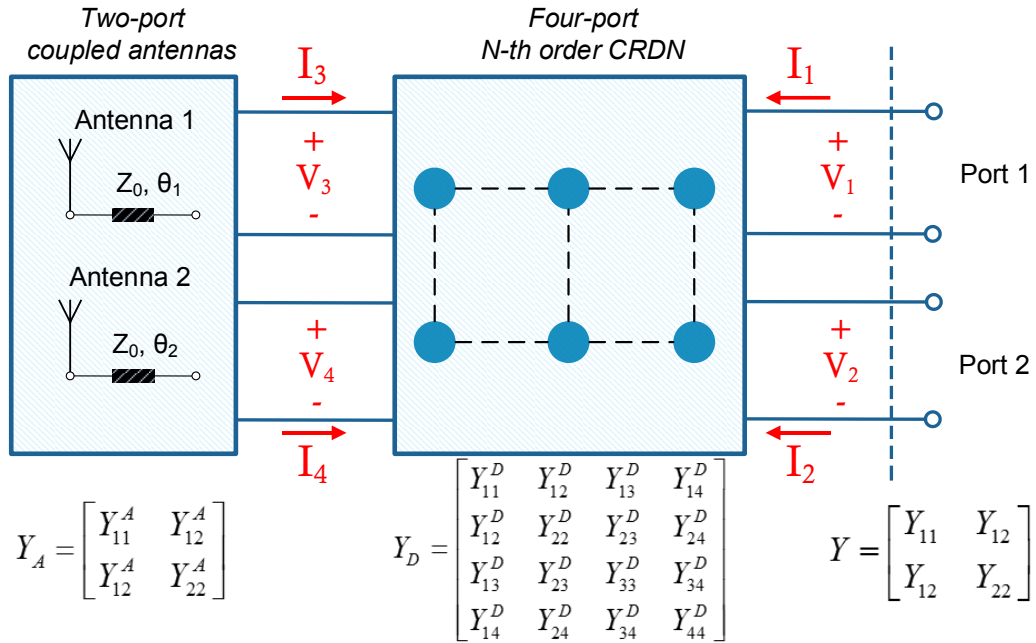
Figure 3.2 The cascaded whole system with coupled antennas and a four-port C-CRDN.

Suppose that the admittance matrix of the CRDN can be written as:

$$\left[\mathbf{Y^D} \right] = \begin{bmatrix} Y_{11}^D & Y_{12}^D & Y_{13}^D & Y_{14}^D \\ Y_{12}^D & Y_{22}^D & Y_{23}^D & Y_{24}^D \\ Y_{13}^D & Y_{23}^D & Y_{33}^D & Y_{34}^D \\ Y_{14}^D & Y_{24}^D & Y_{34}^D & Y_{44}^D \end{bmatrix}. \tag{3.7}$$

the cascaded network becomes a two port network with its admittance parameter expressed as:

$$[\mathbf{Y}] = \begin{bmatrix} Y_{11} & Y_{12} \\ Y_{12} & Y_{22} \end{bmatrix}.$$ (3.8)

To obtain [Y] in terms of $[Y^A]$ and $[Y^D]$, the voltage-current relations of the two coupled antenna network and the C-CRDN are expressed by block sub-matrix representation as

$$\begin{bmatrix} \bar{\mathbf{I}}_1 \\ \bar{\mathbf{I}}_2 \end{bmatrix} = \begin{bmatrix} \bar{\mathbf{Y}}_{11}^{D} & \bar{\mathbf{Y}}_{12}^{D} \\ \bar{\mathbf{Y}}_{21}^{D} & \bar{\mathbf{Y}}_{22}^{D} \end{bmatrix} \cdot \begin{bmatrix} \bar{\mathbf{V}}_1 \\ \bar{\mathbf{V}}_2 \end{bmatrix}$$ (3.9)

and

$$\bar{\mathbf{I}}_2 = -\bar{\mathbf{Y}}^{A} \cdot \bar{\mathbf{V}}_2 \ ,$$ (3.10)

where

$$\bar{\mathbf{I}}_1 = \begin{bmatrix} I_1 \\ I_2 \end{bmatrix}, \quad \bar{\mathbf{I}}_2 = \begin{bmatrix} I_3 \\ I_4 \end{bmatrix}, \quad \bar{\mathbf{V}}_1 = \begin{bmatrix} V_1 \\ V_2 \end{bmatrix}, \quad \bar{\mathbf{V}}_2 = \begin{bmatrix} V_3 \\ V_4 \end{bmatrix}$$ (3.11a)

are port currents and voltages, respectively, and

$$\bar{\mathbf{Y}}_{11}^{D} = \begin{bmatrix} Y_{11}^{D} & Y_{12}^{D} \\ Y_{12}^{D} & Y_{22}^{D} \end{bmatrix}, \quad \bar{\mathbf{Y}}_{12}^{D} = \begin{bmatrix} Y_{13}^{D} & Y_{14}^{D} \\ Y_{23}^{D} & Y_{24}^{D} \end{bmatrix}, \quad \bar{\mathbf{Y}}_{21}^{D} = \begin{bmatrix} Y_{13}^{D} & Y_{23}^{D} \\ Y_{14}^{D} & Y_{24}^{D} \end{bmatrix},$$ (3.11b)

$$\bar{\mathbf{Y}}_{22}^{D} = \begin{bmatrix} Y_{33}^{D} & Y_{34}^{D} \\ Y_{34}^{D} & Y_{44}^{D} \end{bmatrix}, \text{ and } \quad \bar{\mathbf{Y}}^{A} = \begin{bmatrix} Y_{11}^{A} & Y_{12}^{A} \\ Y_{12}^{A} & Y_{22}^{A} \end{bmatrix}.$$ (3.11c)

The admittances for the whole network can then be obtained by substituting (3.10) into (3.9):

$$\bar{\mathbf{I}}_1 = [\mathbf{Y}] \cdot \bar{\mathbf{V}}_1 \tag{3.12a}$$

with

$$[\mathbf{Y}] = \left[\bar{\mathbf{Y}}_{11}^D + \bar{\mathbf{Y}}_{12}^D (-\bar{\mathbf{Y}}^A - \bar{\mathbf{Y}}_{22}^D)^{-1} \bar{\mathbf{Y}}_{21}^D \right] \ . \tag{3.12b}$$

Substituting (3.11) into (3.12b) yields

$$
\begin{aligned}
[\mathbf{Y}] =& \begin{bmatrix} Y_{11}^D & Y_{12}^D \\ Y_{12}^D & Y_{22}^D \end{bmatrix} + \begin{bmatrix} Y_{13}^D & Y_{14}^D \\ Y_{23}^D & Y_{24}^D \end{bmatrix} \cdot \\
& - \begin{bmatrix} Y_{11}^A + Y_{33}^D & Y_{12}^A + Y_{34}^D \\ Y_{12}^A + Y_{34}^D & Y_{22}^A + Y_{44}^D \end{bmatrix}^{-1} \cdot \begin{bmatrix} Y_{13}^D & Y_{23}^D \\ Y_{14}^D & Y_{24}^D \end{bmatrix}
\end{aligned} \tag{3.13}
$$

When the required admittance parameters obtained by appropriately designing the coupling coefficients, either by non-linear optimization or an analytical synthesis approach, the isolation and matching condition of the cascaded system of the coupled antennas and the C-CRDN can be significantly improved. Since for an high order C-CRDN, substituting (3.1) into (3.13) will result in an intricate mathematic expression, circuit level optimization can be conducted using Agilent Advanced Design System [6] more efficiently to find a set of optimum coupling coefficients for a set of given isolation and return loss specifications. Since analytical synthesis of a C-CRDN is highly desired, it should be a focused research topic as a future research work.

In this thesis, the non-linear optimization is used to obtain the desired coupling coefficient. Using S-to-Y transformation, the S_{21} of the whole cascaded system can be expressed as ($Z_0 = 1$):

$$S_{21} = \frac{-2Y_{21}}{(1 + Y_{11})(1 + Y_{22}) - Y_{12}Y_{21}} \ . \tag{3.14}$$

It is obvious that S_{21} will vanish within a certain band of interest as long as:

$$Y_{21}(\omega) \approx 0, \ \omega \in \left[\omega_L, \omega_0\right] \cup \left[\omega_0, \omega_U\right], \tag{3.15}$$

where $\omega \in [\omega_L, \omega_0]$ and $\omega \in [\omega_0, \omega_L]$ are the two adjacent bands of interest.

Having had $Y_{21} \approx 0$, the reflection coefficients can be simplified to:

$$S_{11} \approx \frac{1 - Y_{11}}{1 + Y_{11}}, \qquad S_{22} \approx \frac{1 - Y_{22}}{1 + Y_{22}}, \tag{3.16}$$

Which means that the two ports in Fig 3.2 can be independently matched in their respective band of interest. According to (3.16), to fulfil the matching specification, the constraint on self-admittance parameters should be:

$$Y_{11} \approx 1, \ \omega \in \left[\omega_L, \omega_0\right] \tag{3.17a}$$

and
$$Y_{22} \approx 1, \ \omega \in \left[\omega_0, \omega_U\right] \tag{3.17b}$$

Therefore, the design procedure of a C-CRDN for adjacent frequency bands can be separated into two steps: 1) Design the couplings coefficients such that Y_{21} is minimized; and 2) Match the two ports within their respective band of interest. The coupling coefficients of a C-CRDN can be appropriately designed, either by non-linear optimization or an analytical synthesis approach. Since for an high order C-CRDN, substituting (3.12) into (3.11) will result in an intricate mathematic expression, and there exists no systematic methods to incorporate coupled antenna parameters into a transfer function polynomial, not to mention that the chebyshev polynomials for filters are only two-port, non-linear optimization are used instead. The overall cost function used in this work is given as:

$$K = w_1 \cdot K_{11} + w_2 \cdot K_{22} + w_3 \cdot K_{21}, \tag{3.18a}$$

where:

$$K_{11} = \sum_{i=1}^{N_L} |Y_{11}(\omega_i) - 1|^2 , \qquad (3.18b)$$

$$K_{22} = \sum_{i=1}^{N_U} |Y_{22}(\omega_i) - 1|^2 , \qquad (3.18c)$$

$$K_{21} = \sum_{i=1}^{N_L + N_U} |Y_{21}(\omega_i)|^2 , \qquad (3.18d)$$

w_1 , w_2 and w_3 are weighting coefficients. N_L and N_U are the numbers of sampling frequency points ω_i selected in the lower and upper frequency band which are adjacent.

3.3. Practical Design and Tuning Examples

To validate the theory and prove the concept, two high gain (around 7.6 dBi) sleeve dipole antennas, one resonate at 2.35 GHz and the other resonate at 2.45 GHz, respectively, are placed in close proximity to each other and prepared as the testing bench. Such high gain antennas are used to imitate the characteristic of two high gain base station antennas operating in adjacent bands. The 2.35 GHz antennas is assumed to serve TD-LTE band 40, while the 2.45 GHz antenna is used in a Wi-Fi system. Such situation reflects a popular scenario for 4G femto cells where a Wi-Fi router works as a throughput offload of a TD-LTE wireless system. Fig. 3.3 (a) illustrates the two sleeve dipole antennas, a cascaded C-CRDN and the pre-selection filters for the two radio transceivers. Fig. 3.3 (b) shows the measurement and tuning set up of the examples.

Since the TD-LTE band 2300~2400 (MHz) is immediately adjacent to the ISM band 2400~2483.5 (MHz) as shown in Fig. 3.4, even if the antennas are placed 380 mm (3.04 λ_0 at 2400 MHz) apart, less than 25 dB isolation is observed. For a typical TD-LTE femto cell, whose transmitting power is around 20~23 dBm [8], the unwanted power that is coupled to its neighbor Wi-Fi system can be far above the

receiver sensitivity level that is around -90 ~ -70 dBm, even with a 60 ~ 80 dB filter rejection.

Moreover, for TD-LTE band 40 and 2.4GHz Wi-Fi systems, the frequency bands are contiguous, the isolation between them near the adjacent band edge are most difficult to deal with using conventional means. To demonstrate the C-CRDN device in solving the coexistence problem between two systems, targeting the testing bench shown in Fig. 3.3, two C-CRDNs with different orders are designed, fabricated and measured. Each design process starts with the optimization of the coupled resonator circuit model given in Fig. 3 and minimizing the cost functions in (3.18). It should be noted that in the optimization process, the lengths of two transmission lines θ_1 and θ_2 shown in Fig. 3.2 are also variables to be optimized, since they will change the admittance matrix $[Y^A]$ of coupled antennas. Having had the optimum coupling
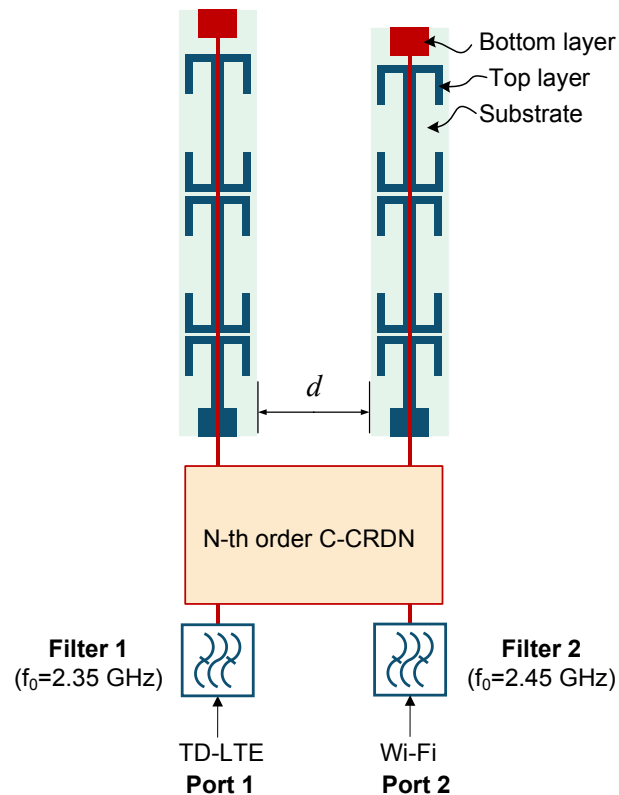
(a)
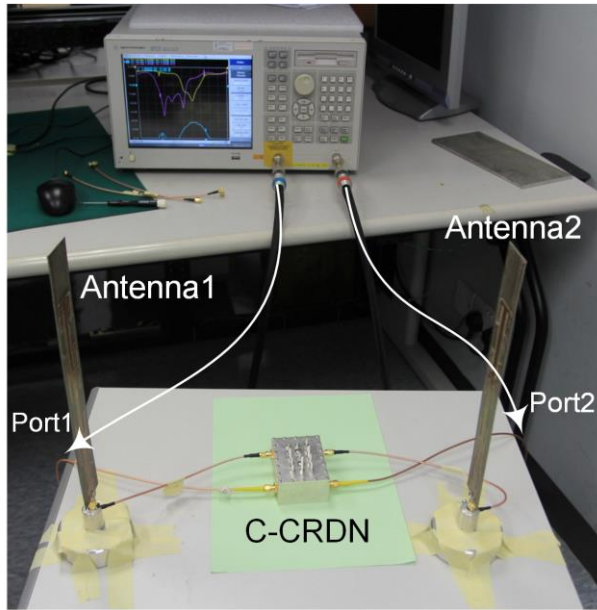
(b)

Figure 3.3 (a) The diagram of the whole communication system with the proposed C-CRDN. (b) Measurement and tuning configuration.

coefficients obtained, a C-CRDN is realized using coaxial combline resonators, which is similar to conventional filter realization, except that a C-CRDN is a *four-port* rather than a two-port device. Additionally, the design of a CRDN strongly depends on the S-parameters of the coupled antennas, therefore, the spacing between the antennas, as well as the surrounding environment must be well maintained during the tuning and measurement process. The detailed design procedure and the performance comparison are given in the following sub-sections.

WCDMA /IMT-200 Downlink (UL) 1920~1980MHz	WCDMA /IMT-2000 Downlink (DL) 2110~2170MHz	TD-LTE Band 40 2300~2400MHz TDD Mode	ISM Band: 2400~2483.5MHz Wi-Fi & Bluetooth	LTE Band 7 Uplink (UL) 2500~2570MHz FDD	LTE Band 38 2570~2620MHz TDD	LTE Band 7 Downlink (DL) 2620~2690MHz FDD
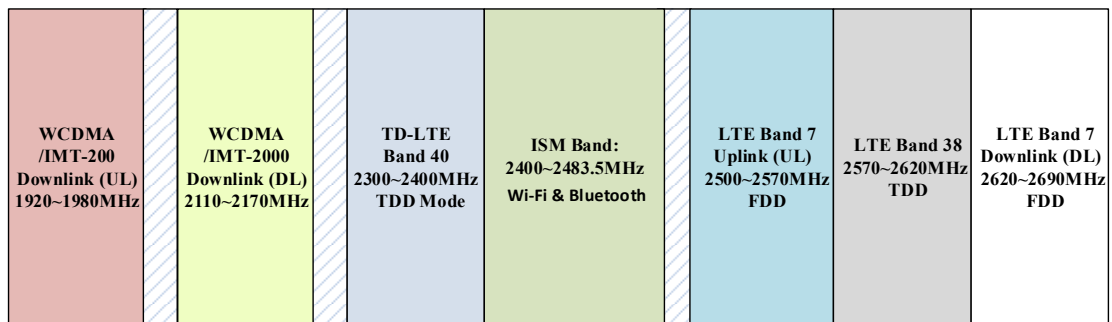
Figure 3.4 Available frequency bands within 2 GHz to 2.7 GHz.

3.3.1. Design of C-CRDNs by Optimization:

At the initial stage, the high gain antennas are fabricated and placed on the test bench as shown Fig. 3.3 (b). The scattering parameters of the coupled antennas are then measured by Agilent PNA N5227A. It can be seen from Fig. 3.5 (a) that the isolation between the two antennas is not more than 25 dB within the frequency bands without a decoupling network. The matching performance in the two bands is also non-ideal. Two fourth order filters with one tri-section, whose coupling coefficients are shown in Table 3-1 (Filter 2-1 and 2-2), are inserted in both the TD-LTE and Wi-Fi channels. It can be seen in Fig. 3.5 (a) that although the isolation between two antennas can be improved to more than 45 dB in most of the bands, the isolation near 2.4 GHz is almost the same before inserting any filters. Therefore, a 4-th order and a 6-th order C-CRDN to further improve the isolation throughout all of the two adjacent bands are optimized and designed.
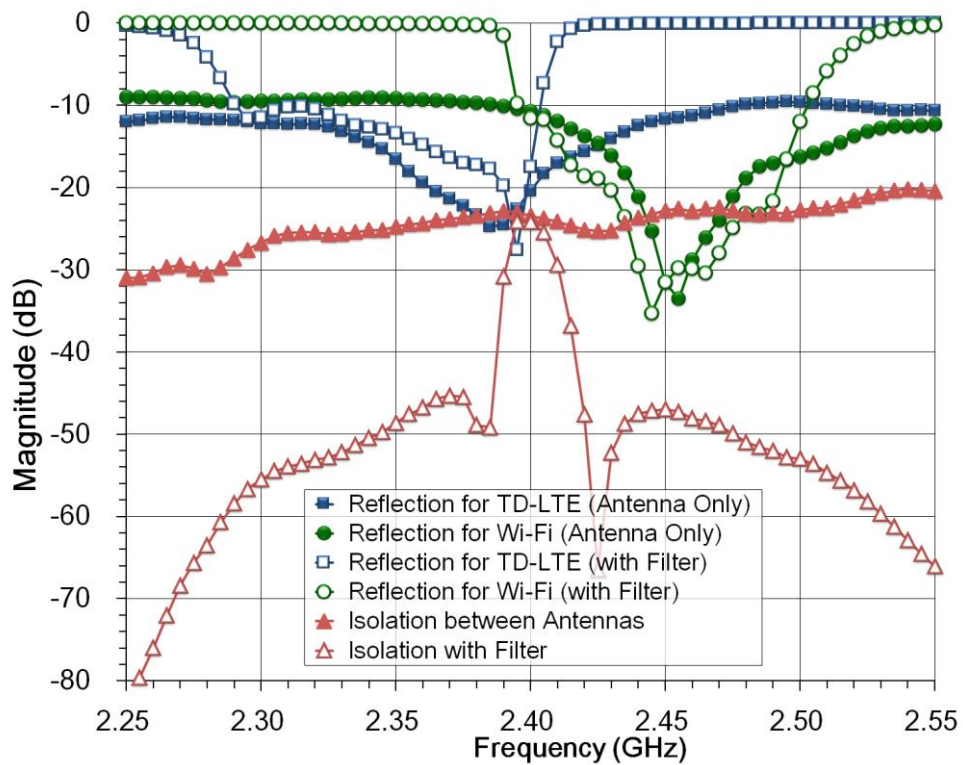
(a)
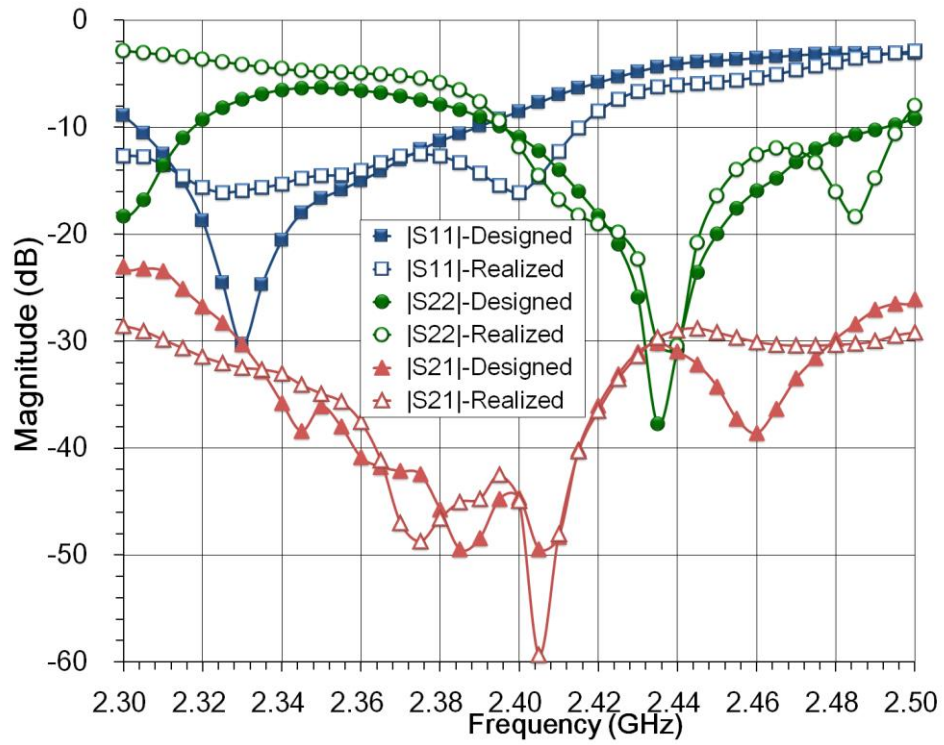
(b)
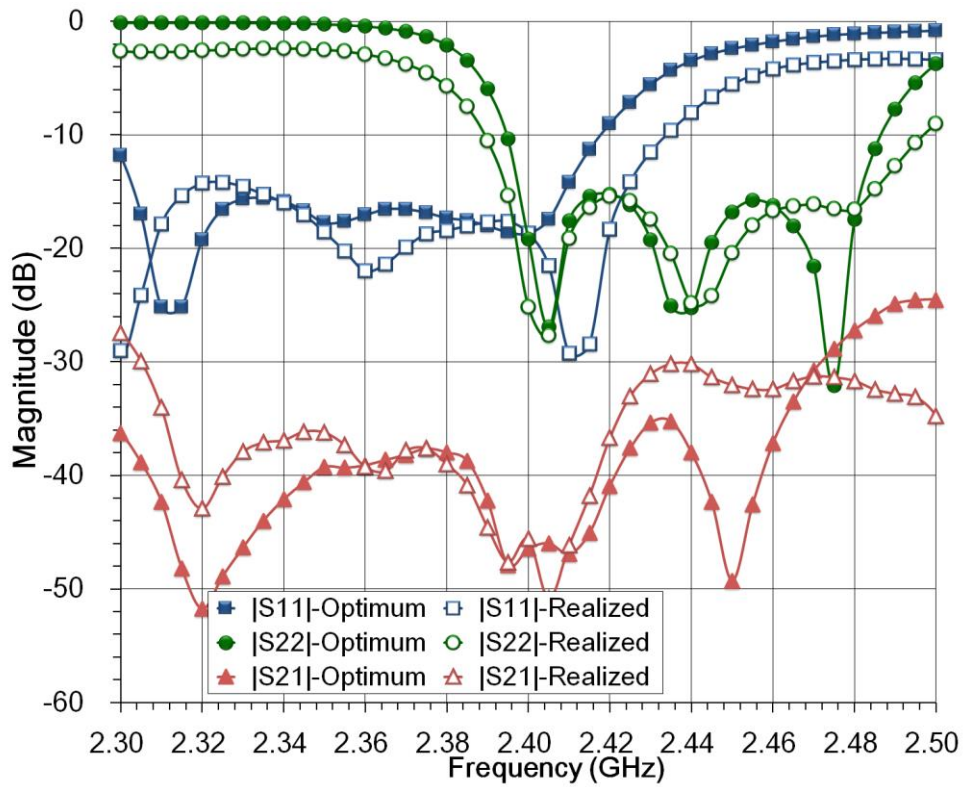
(c)

Figure 3.5 (a) Scattering parameters of two coupled antennas without and with channel filters; The designed and realized scattering parameters of the two antennas with (b) a 4-th order C-CRDN; and (c) a 6-th order C-CRDN.

In the design process, the coupling coefficients in (3.3) and the corresponding transmission line lengths in Fig. 3.2 are the design variables to be optimized. To find the optimum combination of the design variables, the model in Fig. 3.2 are optimized and the cost functions in (3.18) are minimized using a Gradient based algorithm. The optimum solutions of a 4-th order and a 6-th order C-CRDN for the given coupled sleeve dipoles are shown in Table 3-2 and 3-3, with their respective scattering parameters shown in Fig. 3.5 (b) and (c) respectively.

Table 3-1 Coupling coefficients of Filter1 and Filter2 (Designed FBW = 4%)

Filter1-1 (4-th order CRDN)	m_{S1}	m_{12}	m_{23}	m_{34}	m_{4L}	m_{24}
	1.2496	1.1627	0.4658	0.5636	1.120	0.7842
	m_{11}	m_{22}	m_{33}	m_{44}	Q	f_0
	0.2275	0.2650	-0.831	0.2994	2797	2.35GHz
Filter1-2 (4-th order CRDN)	m_{S1}	m_{12}	m_{23}	m_{34}	m_{4L}	m_{24}
	1.4560	1.1961	0.5311	0.8040	1.3575	-0.9147
	m_{11}	m_{22}	m_{33}	m_{44}	Q	f_0
	-0.003	0.000	0.9495	-0.135	2916	2.45GHz
Filter2-1 (6-th order CRDN)	m_{S1}	m_{12}	m_{23}	m_{34}	m_{4L}	m_{24}
	1.2505	1.1311	0.5958	0.6928	0.9605	0.5506
	m_{11}	m_{22}	m_{33}	m_{44}	Q	f_0
	0.1021	0.1678	-0.634	0.1981	2798	2.35GHz
Filter2-2 (6-th order CRDN)	m_{S1}	m_{12}	m_{23}	m_{34}	m_{4L}	m_{24}
	1.0770	0.8605	0.4701	0.7611	1.2194	-0.6672
	m_{11}	m_{22}	m_{33}	m_{44}	Q	f_0
	-0.005	-0.005	0.8044	-0.002	2917	2.45GHz

Table 3-2 Coupling coefficients of designed and realized C-CRDN for the 4-th and 6-th Order C-CRDN (Designed FBW = 5%)

4-th	Designed	Realized		Designed	Realized
$m_{P1\text{-}1}$	1.0640	1.0638	m_{12}	0.6546	0.6895
$m_{P2\text{-}2}$	1.6527	1.7124	m_{34}	2.3489	2.1330
$m_{P3\text{-}3}$	2.1955	2.1067	m_{11}	1.0998	0.8788
$m_{P4\text{-}4}$	1.5500	1.7452	m_{22}	-0.5985	-0.3498
m_{13}	2.8002	3.0000	m_{33}	1.5010	1.8164
m_{24}	2.7006	2.9974	m_{44}	-0.0279	-0.0825
θ_1	101°	103°	θ_2	125°	123°
6-th	Designed	Realized		Designed	Realized
$m_{P1\text{-}1}$	0.9274	1.0405	m_{34}	1.8977	1.7370
$m_{P2\text{-}2}$	0.7704	0.8729	m_{56}	0.2471	0.3639
$m_{P3\text{-}3}$	1.8199	1.5606	m_{11}	0.7868	0.9239
$m_{P4\text{-}4}$	1.9996	1.8106	m_{22}	-0.7574	-0.9238
m_{15}	1.0271	1.2982	m_{33}	0.8116	0.7178
m_{35}	2.0318	2.0891	m_{44}	-0.6754	-0.8590
m_{26}	0.6935	0.8776	m_{55}	0.7868	0.9239
m_{46}	1.6680	1.7445	m_{66}	-0.7574	-0.9238
m_{12}	0.0000	0.0000			
θ_1	105°	103°	θ_2	124°	123°

3.3.2. Parametric Study of the Design Variables:

To further reveal the effect of the design variables on the overall performance, the four cost functions in (3.18) are studied with respect to different combinations of the

variables for the 4-th order C-CRDN. In each step of the study, only one variable is swept while the other variables remain to be their optimum values as shown in Table3-2. The cost functions against different variables are shown in Fig 3.6. It should be noted that all the cost functions are normalized to its maximum value because admittance parameter tends to be singular at poles and a large value of the goal function will desensitize the optimization process.

1) The self-couplings (Fig. 3.6a):

The self-couplings of the two resonators near the antenna end will affect all four cost functions, therefore, only overall cost function K is plotted in Fig. 3.6a. A very intriguing phenomenon is that the self-couplings m_{11} and m_{22} will only affect K_{11} and K_{22} while other cost functions remain unchanged. Meanwhile, as the center frequency is set to 2.4 GHz in this study, the optimum value of self-couplings m_{11} and m_{33} are positive while the optimum value of self-couplings m_{22} and m_{44} are negative.

2) The I/O couplings (Fig. 3.6b):

The parametric study shows that K_{11} is independent of m_{P22} while K_{22} is independent of m_{P11}. While both m_{P11} and m_{P22} have exactly the same effect on K_{21}. However, m_{P33} and m_{P44} are found be related to all cost functions and tend to be larger than m_{P11} and m_{P22}.

3) The main line couplings (Fig. 3.6c):

Similar to the I/O couplings, m_{13} will not affect K_{22} and m_{24} will not affect K_{11}. The optimum values tend to be quite large compared to other couplings.

4) The cross couplings (Fig. 3.6d):

The cross coupling near the antenna end, m_{34} will affect all cost functions while m_{12} will only affect K_{21}. These two couplings mainly control the isolation between two channels. From the parametric study, it is clear that m_{12} can be tuned after m_{34} are tuned to its optimum value and the value of m_{12} are quite smaller than m_{34}.

5) The electric length of transmission lines (Fig. 3.6e):

The electric length θ_1 and θ_2 of the two transmission lines will also change all the cost functions. The optimum values are found to be $\theta_1 = 101°$ and $\theta_2 = 123°$.

Several important conclusion that will be very helpful for physical realization of the C-CRDN can be drawn from the parametric study:

- The two transmission line lengths, θ_1 and θ_2 can be fixed to its optimum value and remain unchanged during the tuning process.

- Since m_{P33}, m_{P44} and m_{34} are found be related to all cost functions, they must be tuned in the first place. m_{P33} and m_{P44} are set to be large enough and $m34$ is mainly used to manipulate K_{21}. Because there are plenty of parameters remain to be tuned, K_{21} should be minimized with best effort at this stage.

- The self-couplings m_{11} and m_{33} must be positive while m_{22} and m_{44} must be negative, this will result in a good initial state in the tuning process.

- Since m_{13}, m_{P11} and m_{11} will not affect K_{22}; m_{24}, m_{P22}, and m_{22} will not affect K_{11}, this means that the matching of the two ports can be independently tuned.

- m_{12} is tuned in the final step to obtain a smaller K_{21}.
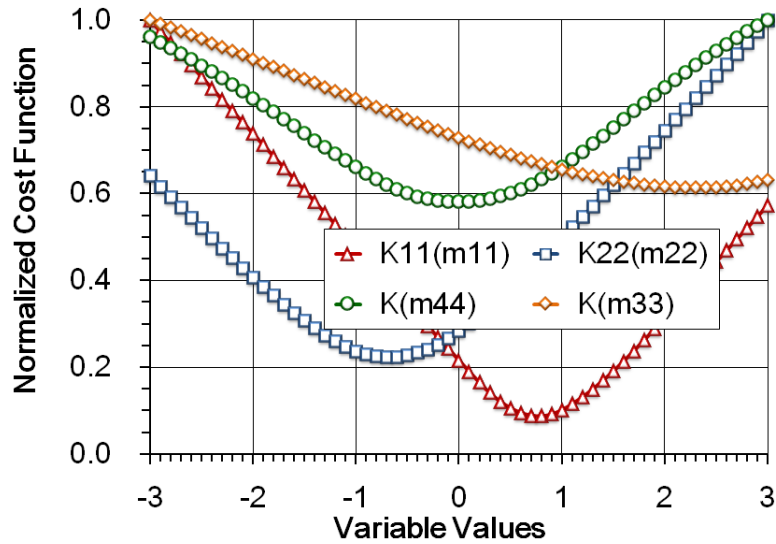
(a)
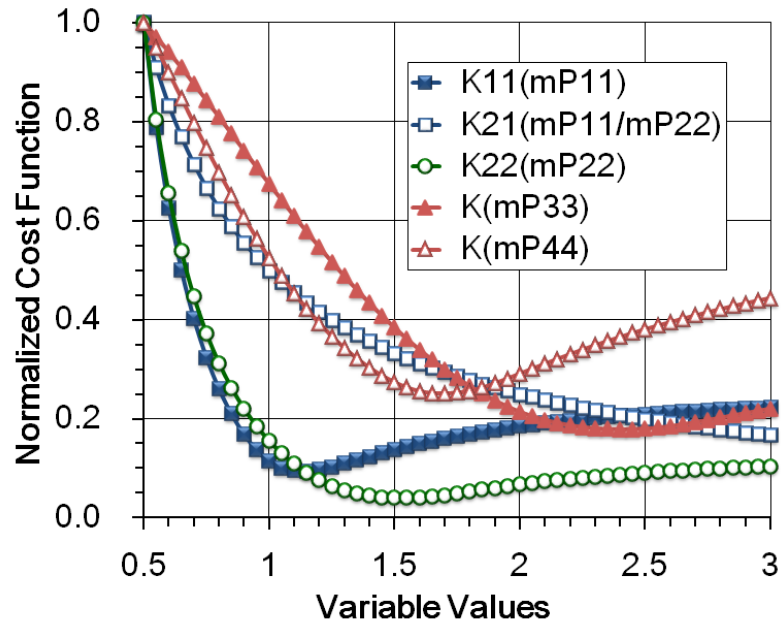
(b)
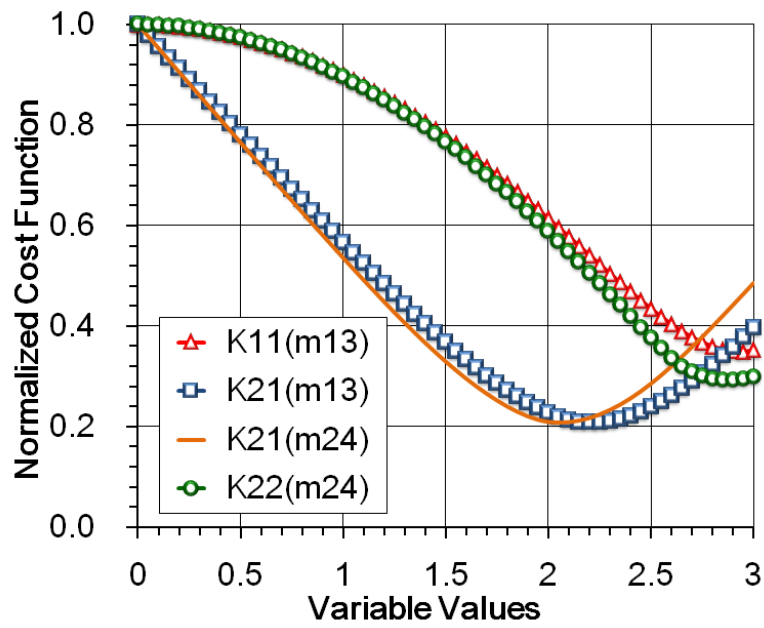
(c)
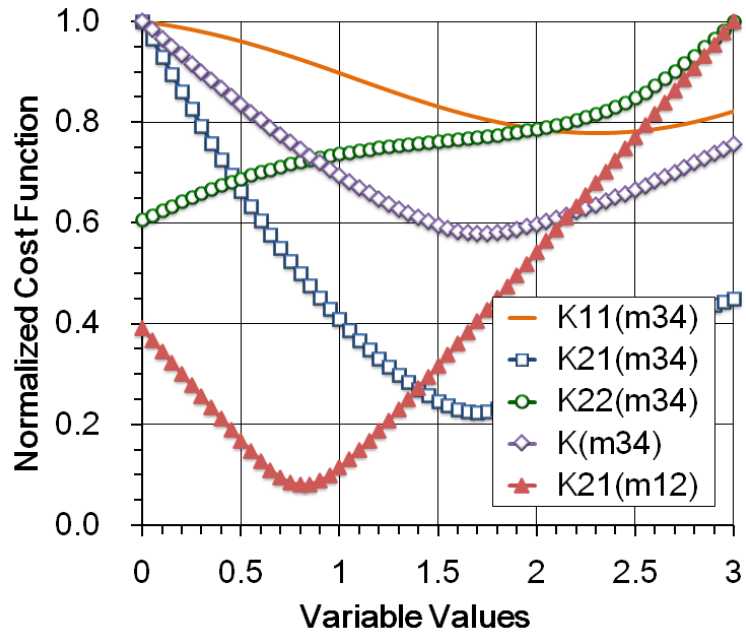
(d)
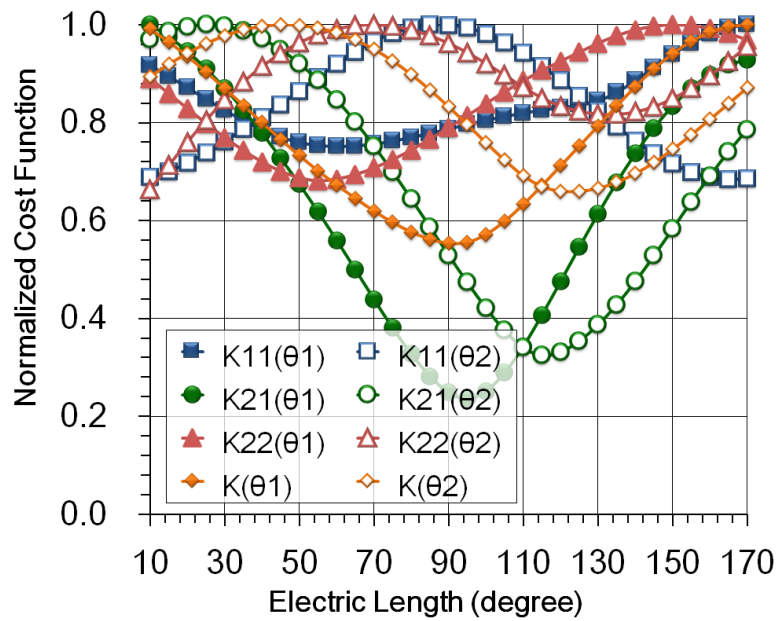
(e)

Figure 3.6 Normalized cost functions against (a) The self-couplings; (b) The couplings between the ports and resonators; (c) The main-line couplings; (d) The cross-couplings; and (e) The lengths of transmission lines for a 4-th order C-CRDN.

3.3.3. Realization and Tuning:

Since the system performance of a C-CRDN is strongly dependent on the antennas, full-wave simulation of the C-CRDN alone to achieve the optimum solution is not practical and suitable for real-world applications. Nevertheless, the physical model can be EM simulated using Agilent EMPro [9] to guarantee that all the resonators in a C-CRDN resonant in the correct frequency bands and there are enough tunability for all the couplings.

The two prototype C-CRDNs are then fabricated according to the EM designed model and is tuned using space-mapping technique [10], by which the circuit model given in Fig. 3.2 serves as the coarse model the parameter extraction process is done using Agilent ADS circuit simulator and optimization engine [6]. At each tuning step, the four port S-parameters of the prototype C-CRDN are first measured using Agilent PNA N5227A, then the realized coupling coefficients are extracted by fitting the circuit model responses to the measured responses. Then, the extracted parameters are compared with the designed ones. The next tuning step will be conducted according to the difference between them. This iteration will be repeated until the realized parameters approach the designed ones by best effort. The realized coupling coefficients at the final stage are also shown in Table 3-2 and 3-3 for comparison. The physical layouts and dimensions of a 4-th and a 6-th order C-CRDN are shown in Fig. 3.7.

After the prototype C-CRDN is well tuned, it is cascaded to the two antennas in the testing vehicle as shown in Fig. 3.2. The measured responses of the two-port cascaded system are shown in Fig. 3.5 (b) and (c). It can be seen that the best improvement in isolation is about 20 dB near 2.4 GHz for both C-CRDNs, but the matching performance of a 6-th order C-CRDN is better than its 4-th order counterpart.

It is understandable that the performance of a C-CRDN is dependent on the characteristic of the coupled antennas. Therefore, the overall two-port responses of the 6-th order C-CRDN when cascaded to two antennas with different spacings is

superposed in Fig. 3.8. Deviations in both the reflection and isolation parameters are observed. Nevertheless, the performance is still acceptable for a $\pm 13\%$ spacing variance.

Dimensions (Unit: mm)

$L_E, W_E = 38$ $T_W = 1$
$R_c = 10$ $R_o = 5$ $R_i = 4$
$G_1 = 4$ $G_2, G_4 = 10$ $G3 = 8$
$H_W = 27$ $H_c = 22$

(a)

Dimensions (Unit: mm)

$L_E = 78$ $W_E = 57$ $T_W = 4$
$R_c = 14$ $R_o = 7$ $R_i = 5$
$G_1, G_4 = 4.5$ $G_2, G_3 = 10.5$
$G_5, G_6, G_7 = 12.5$
$H_W = 30$ $H_c = 23$
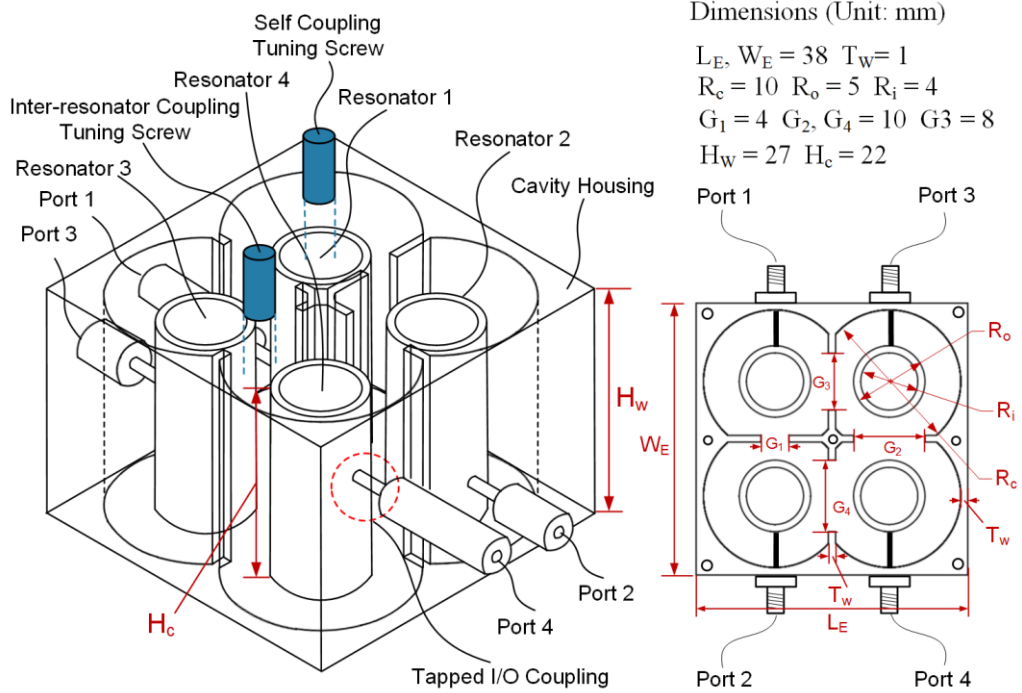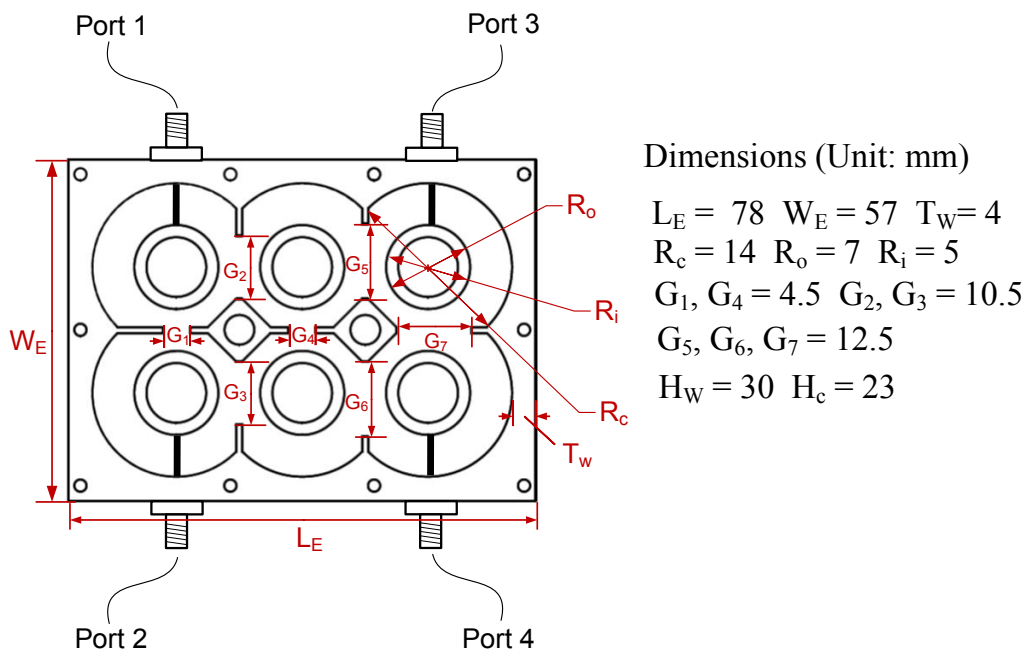
(b)

Figure 3.7 (a) A prototype of a 4-th order; and (b) 6-th order C-CRDN realized by combine cavities. In both design examples, M3 tuning screws are used.
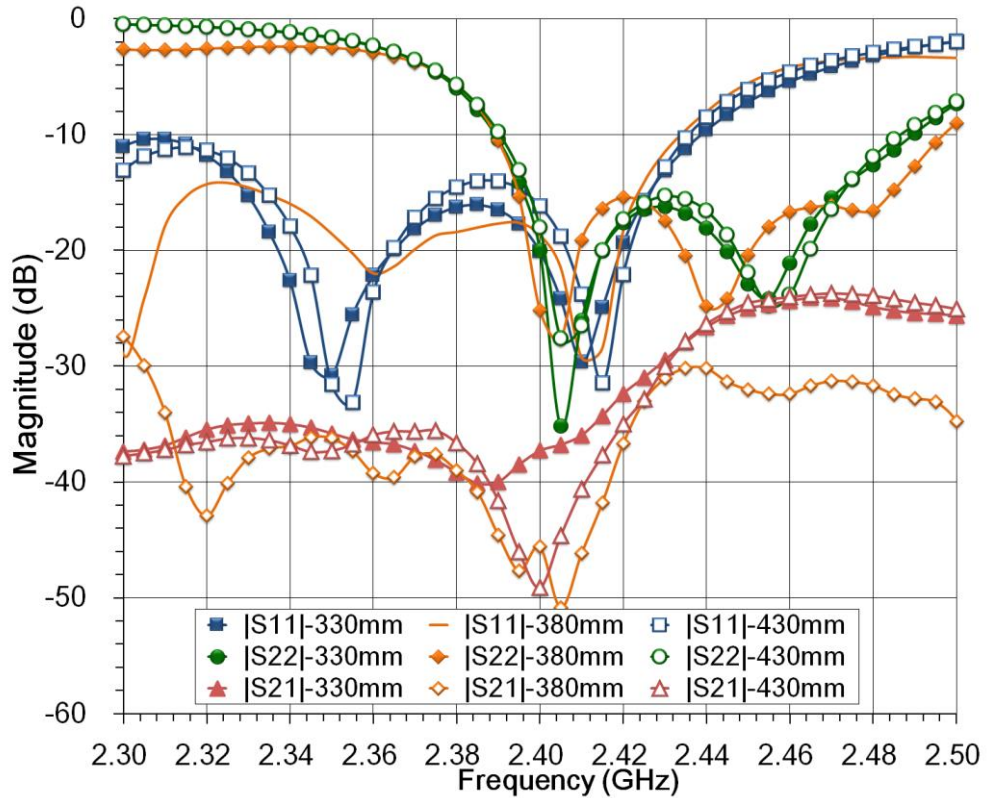
Figure 3.8 The scattering parameters of the whole two-port system when then realized 6-th C-CRDN is cascade to the two coupled antennas with different distance.

3.3.4. Combination of a C-CRDN with Two Channel Filters:

To investigate the performance of the C-CRDN in practical radio systems, two simulated pre-selection channel filters working at the TD-LTE and the ISM bands respectively are also cascaded to the systems as illustrated in Fig. 3.2 (a). Both circuit model simulated filters are fourth-order. The filter for TD-LTE has designed to have a transmission zero at 2.45 GHz while the filter for Wi-Fi has its transmission zero at 2.35 GHz. The S-parameters of the two decoupled channels including channel filters with the 4-th order and 6-th order C-CRDN are superposed in Fig. 3.9 with the couplings coefficients for the filters shown in Table 3-1. It should be noted that the filters used for the 4-th and 6-th order C-CRDNs are different in order to match different complex loads [12].
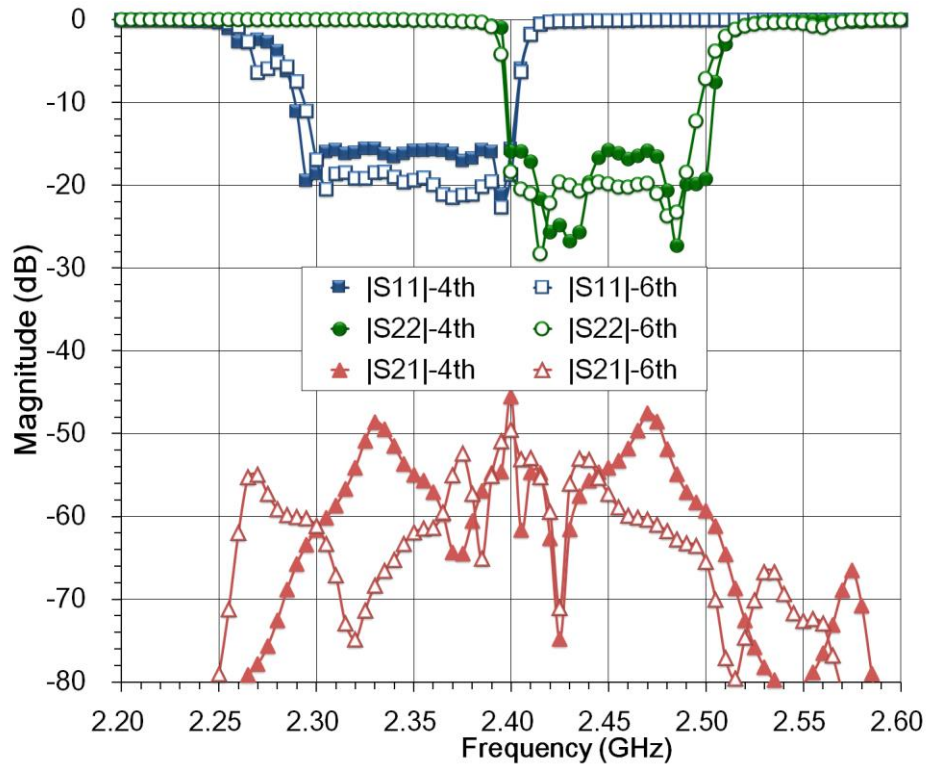
Figure 3.9 Measured scattering parameters of two collocated TD-LTE and Wi-Fi systems with C-CRDNs and channel filters.

3.3.5. The Loss Introduced by a C-CRDN

To quantify extra losses introduced by a C-CRDN, the four port network must be disconnected from the coupled antennas while maintaining its loading effect, therefore, the network models shown in Fig. 3.10 (a) are used to extract the complex loads looking into the port of Antenna 1. The complex load looking into Antenna 2 can be extracted likewise. Meanwhile, the complex loads looking into Port 3 and Port 4 of the C-CRDN should also be extracted. Then, using the network model in Fig. 3.10 (b), the insertion loss between Port 1 and Port 3 can be obtained. By the same token, the insertion loss between Port 2 and Port 4 is also extracted and they are shown in Fig. 3.10 (c). Similar to combline filters, the insertion loss can be improved with increased cavity volume and conductivity as well as roughness of the metal surface.

139
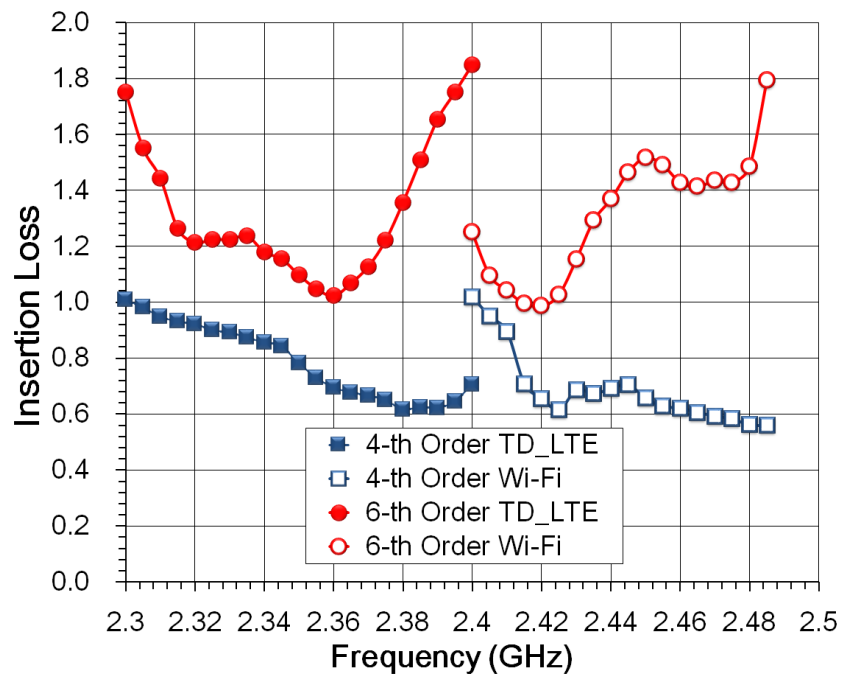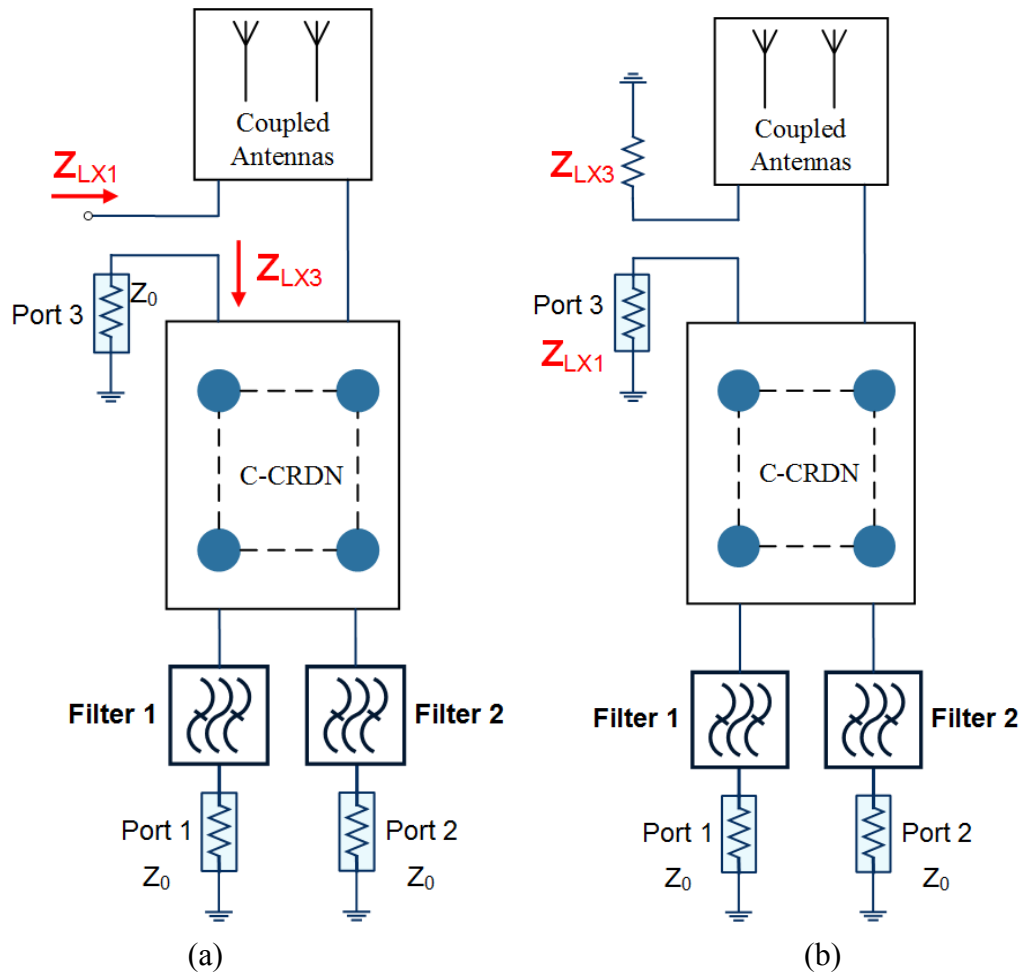
Figure 3.10 The network model to extract the complex load looking into (a) Antenna 1; and (b)

Antennas 2. (c) The extracted insertion losses for the 4-th and 6-th order CRDNs in both the

140

TD-LTE channel and Wi-Fi channel.

3.4. Reference

[1] R. J. Cameron, C. M. Kudsia, and R. R. Mansour, Microwave Filters for Communication systems. New York: Wiley, 2007.

[2] . A. Garcia-Lampérez, M. Salazar-Palma, and T. K. Sarkar, "Analytical synthesis of microwave multiport networks," in *IEEE MTT-S Int. Microw. Symp. Dig.*, 2004, pp. 455–458.

[3] G. Macchiarella, S. Tamiazzo, "Novel Approach to the Synthesis of Microwave Diplexers," *IEEE Transactions on Microwave Theory and Techniques,* vol.54, no.12, pp.4281-4290, Dec. 2006.

[4] T. F. Skaik, M. J. Lancaster, F. Huang, "Synthesis of multiple output coupled resonator circuits using coupling matrix optimization," *IET Microwaves, Antennas & Propagation,* vol.5, no.9, pp.1081-1088, June 27 2011.

[5] U. Rosenberg, S. Amari, "New Power Distribution (Combination) Method with Frequency Selective Properties", EuMC2012 Workshop (CD), Amsterdam, The Netherlands, Oct. 2012.

[6] Advanced Design System, Version 2012.08, Agilent Technologies, Inc., Santa Clara, CA.

[7] [Online]. Available: http://en.wikipedia.org/wiki/Femtocell

[8] D. Lopez-Perez, I. Guvenc, G. de la Roche, M. Kountouris, T. Q. S. Quek, J. Zhang, "Enhanced intercell interference coordination challenges in heterogeneous networks," *IEEE Wireless Communications,* vol.18, no.3, pp.22-30, June 2011.

[9] EMPro 3D EM Simulation Software, Version 2012.09, Agilent Technologies, Inc., Santa Clara, CA.

[10] J. W. Bandler, Q. S. Cheng, S. A. Dakroury, A. S. Mohamed, M. H. Bakr, K. Madsen, and J. Søndergaard, "Space mapping: The state of the art," *IEEE Trans. Microw. Theory Tech.*, vol. 52, no. 1, pp. 337–361, Jan. 2004.

[11] J. I. Choi, M. Jain, K. Srinivasan, P. Levis, and S. Katti, "Achieving single channel,

full duplex wireless communication," in *Proc. 16th Annu. Int. Conf. Mobile Comput. Netw.,* 2010, pp. 1–12.

[12] H. Meng, K.-L. Wu, "Direct Optimal Synthesis of a Microwave Bandpass Filter With General Loading Effect," *IEEE Trans. Microw. Theory Tech.*, vol.61, no.7, pp.2566-2573, July 2013.

Chapter 4

Decoupling with Dummy Antennas

The decoupling solution of two antennas with one extra parasitic antenna/scatter has been previously reported in [1] and [2]. However, they are either highly antenna dependent or lacks the capability to be extended to more than two antennas. This thesis will present a general decoupling technique for a compact array of four uniform elements. Depending on the array configuration; an appropriate decoupling dummy array with optimum reactive loads is demonstrated for effectively decoupling the antenna elements of a compact array. The word "dummy" is used here because in nature, these antennas can be of exactly the same form factor as that of the original radiating antennas in the array but terminated with reactive loads. The theory and design procedures will be given together with two design examples of monopole arrays and a low-profile PIFA "cheesecake" antenna array.

4.1. A Dummy Array for Four Element Arrays

4.1.1. The Basic Theory
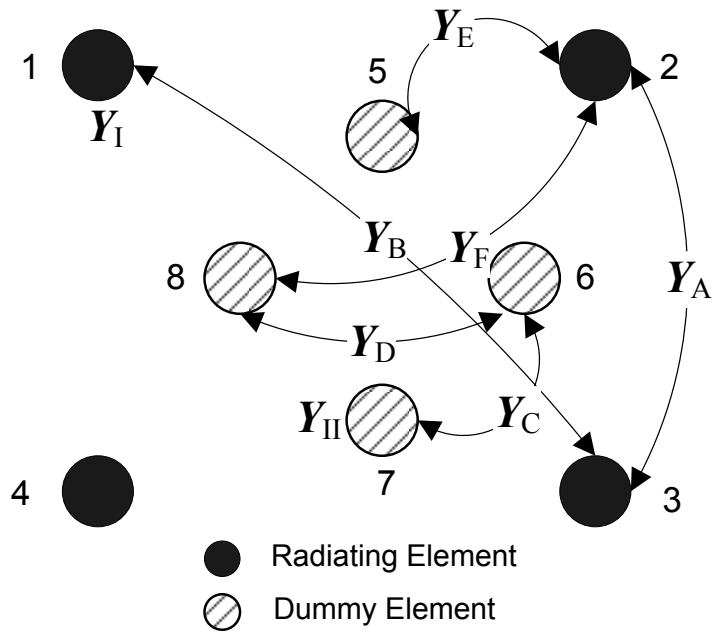
Figure 4.1 The configuration of a four-element array with four dummy elements.

To decouple a compact uniform four-element array, a uniform four-element dummy array is placed at the center of the compact array with its orientation rotated by 45^0 as shown in Fig. 4.1. Generally speaking, the dummy array can also be in other orientations. In Fig.4.1, antennas 1 through 4 are radiating elements that are fed by 50 Ω transmission lines and antennas 5 through 8 are decoupling dummy elements that are terminated with a reactive load. As illustrated by Fig. 4.1, there are six distinct *short- circuit* mutual admittances:

Y_A: Admittance between adjacent radiating elements;

Y_B: Admittance between diagonal radiating elements;

Y_C: Admittance between adjacent dummy elements;

Y_D: Admittance between diagonal dummy elements;

Y_E: Admittance between a radiating element and a nearby dummy element; and

Y_F: Admittance between a radiating element and a distant dummy element.

Due to the symmetry of the two arrays, there are two self-admittances:

Y_I: The self-admittance of the radiating elements; and

Y_{II}:   The self-admittance of the dummy elements

144

Eight-port network with dummy elements

(a)

Four-port decoupled network
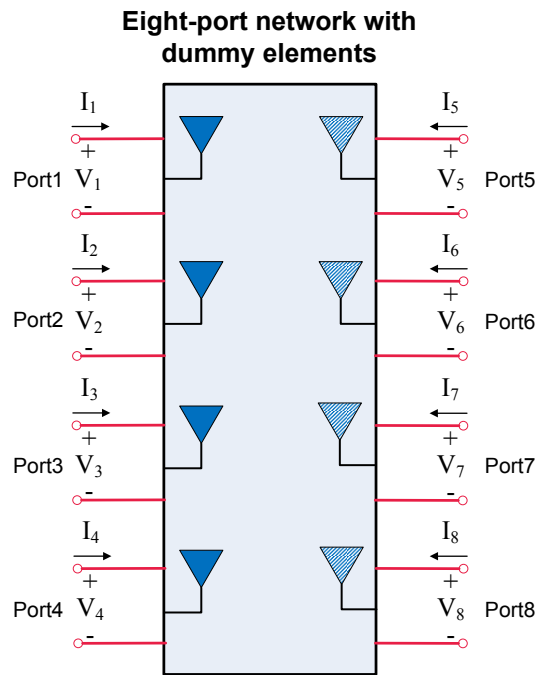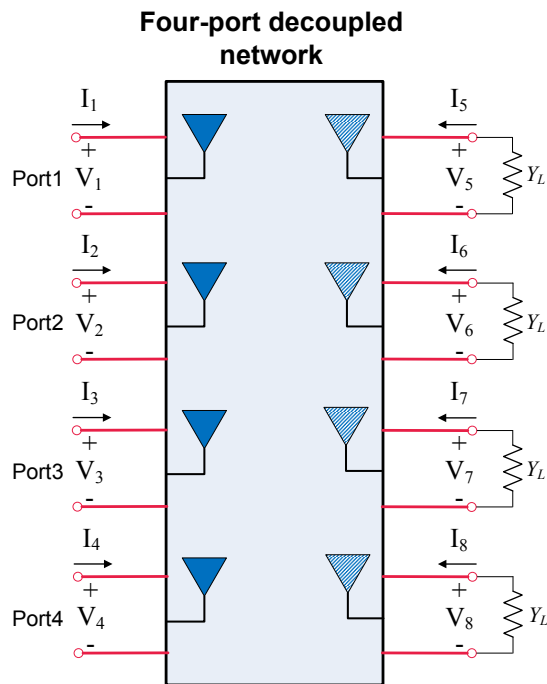
(b)

Figure 4.2 (a) The eight-port network consists of four radiating antennas and four dummy elements. (b) The four port network where the dummy elements are terminated with load Y_L.

Consider the eight antenna elements as shown in Fig. 4.2 (a), including the

radiating and dummy ones, their voltage-current relation can be written as:

$$\begin{bmatrix} \bar{\mathbf{I}}_1 \\ \bar{\mathbf{I}}_2 \end{bmatrix} = \begin{bmatrix} \bar{\mathbf{Y}}_{11} & \bar{\mathbf{Y}}_{12} \\ \bar{\mathbf{Y}}_{21} & \bar{\mathbf{Y}}_{22} \end{bmatrix} \cdot \begin{bmatrix} \bar{\mathbf{V}}_1 \\ \bar{\mathbf{V}}_2 \end{bmatrix} \qquad (4.1)$$

where

$$\bar{\mathbf{I}}_1 = \begin{bmatrix} i_1 \\ i_2 \\ i_3 \\ i_4 \end{bmatrix}, \quad \bar{\mathbf{I}}_2 = \begin{bmatrix} i_5 \\ i_6 \\ i_7 \\ i_8 \end{bmatrix}, \quad \bar{\mathbf{V}}_1 = \begin{bmatrix} v_1 \\ v_2 \\ v_3 \\ v_4 \end{bmatrix}, \quad \bar{\mathbf{V}}_2 = \begin{bmatrix} v_5 \\ v_6 \\ v_7 \\ v_8 \end{bmatrix} \qquad (4.2a)$$

and

$$\bar{\mathbf{Y}}_{11} = \begin{bmatrix} Y_I & Y_A & Y_B & Y_A \\ Y_A & Y_I & Y_A & Y_B \\ Y_B & Y_A & Y_I & Y_A \\ Y_A & Y_B & Y_A & Y_I \end{bmatrix} \qquad \bar{\mathbf{Y}}_{12} = \begin{bmatrix} Y_E & Y_F & Y_F & Y_E \\ Y_E & Y_E & Y_F & Y_F \\ Y_F & Y_E & Y_E & Y_F \\ Y_F & Y_F & Y_E & Y_E \end{bmatrix} \qquad (4.2b)$$

$$\bar{\mathbf{Y}}_{21} = \begin{bmatrix} Y_E & Y_E & Y_F & Y_F \\ Y_F & Y_E & Y_E & Y_F \\ Y_F & Y_F & Y_E & Y_E \\ Y_E & Y_F & Y_F & Y_E \end{bmatrix} \qquad \bar{\mathbf{Y}}_{22} = \begin{bmatrix} Y_{II} & Y_C & Y_D & Y_C \\ Y_C & Y_{II} & Y_C & Y_D \\ Y_D & Y_C & Y_{II} & Y_C \\ Y_C & Y_D & Y_C & Y_{II} \end{bmatrix} \qquad (4.2c)$$

If each dummy element is terminated by a load Y_L as shown in Fig. 4.2 (b), the voltage-current relation at the ports of the dummy elements can be described by

$$\bar{\mathbf{I}}_2 = \bar{\mathbf{Y}}_L \cdot \bar{\mathbf{V}}_2$$

(4.3)

with

$$\bar{\mathbf{Y}}_L = \begin{bmatrix} -Y_L & 0 & 0 & 0 \\ 0 & -Y_L & 0 & 0 \\ 0 & 0 & -Y_L & 0 \\ 0 & 0 & 0 & -Y_L \end{bmatrix} \qquad (4.4)$$

The minus signs in front of Y_L account for the inverse direction of the current defined at the ports of the dummy elements. Substituting (4.3) into (4.1) yields

$$\bar{\mathbf{I}}_1 = \left[\bar{\mathbf{Y}}_{11} - \bar{\mathbf{Y}}_{12}(\bar{\mathbf{Y}}_{22} - \bar{\mathbf{Y}}_L)^{-1}\bar{\mathbf{Y}}_{21} \right] \cdot \bar{\mathbf{V}}_1 \tag{4.5}$$

Taking all dummy elements and their respective loads into account, the voltage-current relation of the four radiating element array shown in Fig. 4.2 (b) can be expressed as:

$$\begin{bmatrix} i_1 \\ i_2 \\ i_3 \\ i_4 \end{bmatrix} = \begin{bmatrix} Y_I' & Y_A' & Y_B' & Y_A' \\ Y_A' & Y_I' & Y_A' & Y_B' \\ Y_B' & Y_A' & Y_I' & Y_A' \\ Y_A' & Y_B' & Y_A' & Y_I' \end{bmatrix} \cdot \begin{bmatrix} v_1 \\ v_2 \\ v_3 \\ v_4 \end{bmatrix} \tag{4.6}$$

Substituting (4.2) and (4.4) into (4.5) and comparing with (4.6), it is apparent that by terminating the dummy elements by load Y_L the original short circuit admittances of the radiating elements are modified to

$$Y_I' = Y_I - \frac{(Y_E + Y_F)^2}{Y_{II} + Y_L + 2Y_C + Y_D} - \frac{(Y_E - Y_F)^2}{Y_{II} + Y_L - Y_D} \tag{4.7a}$$

$$Y_A' = Y_A - \frac{(Y_E + Y_F)^2}{Y_{II} + Y_L + 2Y_C + Y_D} \tag{4.7b}$$

$$Y_B' = Y_B - \frac{(Y_E + Y_F)^2}{Y_{II} + Y_L + 2Y_C + Y_D} + \frac{(Y_E - Y_F)^2}{Y_{II} + Y_L - Y_D} \tag{4.7c}$$

Equation (4.7) states that by appropriately controlling the mutual couplings between dummy elements, the dummy and radiating elements as well as the load Y_L, the mutual couplings between the radiating elements can be cancelled out in certain extent. Although the self-admittance of each radiating element will be altered, one can either compensate the change by a matching circuit or tune the self-admittance of the radiating elements to resonance.

4.1.2. Procedures to Solve the Decoupling Problem

It is clear that to decouple the four symmetric radiating elements, equations (4.7b) and (4.7c) should equal to zero at the same time, which will lead to two simultaneous equations. Solving $Y_A' = 0$ directly will lead to one load condition:

$$Y_{L1} = \frac{(Y_E + Y_F)^2}{Y_A} - Y_{II} - 2Y_C - Y_D.$$ (4.8)

Meanwhile, solving (4.7c) = 0 can also yield another load condition. However, since there is one common term in both (4.7b) and (4.7c), it is more convenient to subtract (4.7b) by (4.7c) in order to find another condition:

$$Y_{L2} = \frac{(Y_E - Y_F)^2}{Y_A - Y_B} - Y_{II} + Y_D.$$ (4.9)

It can be seen from (4.8) and (4.9) that in general $Y_{L1} \neq Y_{L2}$, which means that the values of Y_C, Y_D, Y_E, Y_F and Y_{II} in (4.8) and (4.9) must be properly designed to ensure that Y_{L1} are close to Y_{L2} in the first place. In a practical design, these values depend on the relative spacing between the radiating elements and the dummy elements as well as the form factors of the dummy array. This thesis uses two major steps to find a load that can optimally satisfy (4.8) and (4.9) simultaneously within the frequency band of interest: step 1 is to optimize the form factors of the dummy array, such as the element spacing, such that Y_{L1} and Y_{L2} are most close to each other; and step 2 is to find an optimal load such that (4.8) and (4.9) are best satisfied in the frequency band of interest. Therefore, the effectiveness of the decoupling is dominated by the difference of the two conditions within the frequency band of interest. In general, the optimum load is a complex number. However, for a complex

load whose real part is relatively small, using a purely reactive load is an effective approximation.

Having found the dummy element configuration from a wide range of selections, one can find an optimum reactive load value Y_{Lopt} that achieves a minimum difference by a simple optimization search. If a reactive load Y_L is realized by a section of open ended transmission line, the load is given by $Y_L = -jY_0 \tan \beta l$, where Y_0 and β are the characteristic admittance and phase constant of the transmission line, and l is the length of the line obtained by optimization. The goal function for searching the optimal length that best satisfies $Y'_A, Y'_B = 0$ simultaneously can be defined by minimizing the following function:

$$g(l) = \frac{w_1 \cdot \sum_{i=1}^{N_s} |Y'_A(f_i)|^2 + w_2 \cdot \sum_{i=1}^{N_s} |Y'_B(f_i)|^2}{g(l)_{\max}}, \qquad (4.10)$$

where w_1 and w_2 are normally chosen to be 1, N_s is the number of sampling frequency points f_i selected in the frequency band of interest. The goal function is normalized to the maximum value of $g(l)$, $g(l)_{\max}$ because admittance parameter tends to be singular at poles and a large value of the goal function will desensitize the optimization process.

4.1.3. Four-element Cylindrical Monopole Arrays

A four-element monopole circular array with inter-element spacing $R_A = 25$ mm (0.21 λ_0 at 2.6 GHz) shown in Fig. 4.3 is considered in this example. Due to the limited electric distances between elements, the isolations between the adjacent and the diagonal elements as well as the return losses of each element are poor. If the array is matched at 2.6 GHz with extra matching stubs, the isolations become even

worse. As is shown in Fig. 4.4 (a), the isolations between the adjacent elements and diagonal elements for the coupled array at the center frequency are around 10 dB and 15 dB, respectively. For clarity, the detailed design process will be given step by step:

4.1.3.1. Step 1: Designing a dummy array

In this example, the four dummy monopoles are chosen to be identical to the radiating elements, although different dummy antenna form factors are also possible. The combined array incorporating four *unmatched* radiating elements and four dummy elements can be treated as an eight-port network as shown in Fig. 4.2 (a), whose S-parameters are obtained by a full-wave EM simulation [3]. In the simulation, the conductivity is set to 1.5×10^7 siements/m and the loss tangent of the substrate is set to 0.02. Obviously, the S-parameters of the radiating array depend on not only the geometries of radiating and dummy elements, but also on the relative locations of the dummy elements with respect to the radiating elements, the reactive load and the ground size.
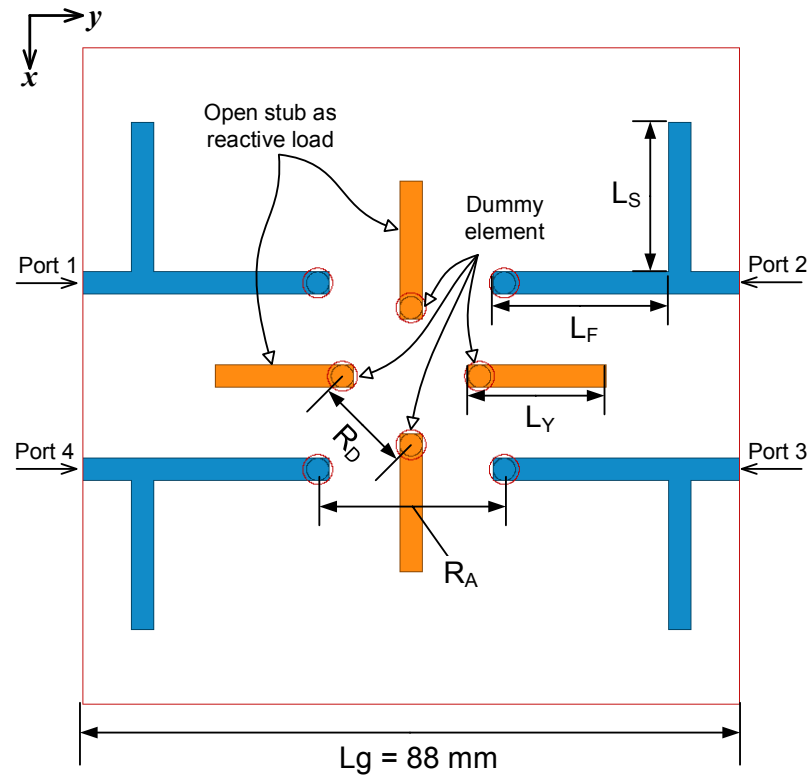
(a)
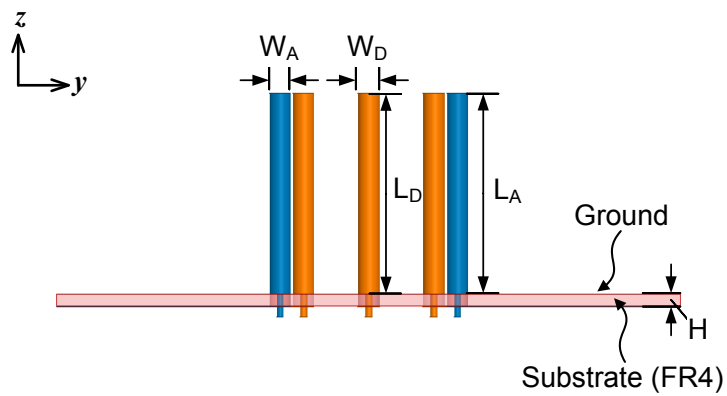
(b)

Figure 4.3 (a) Top view and (b) front view of a four-element coupled monopole array together with a four-element dummy array terminated by open ended transmission lines.
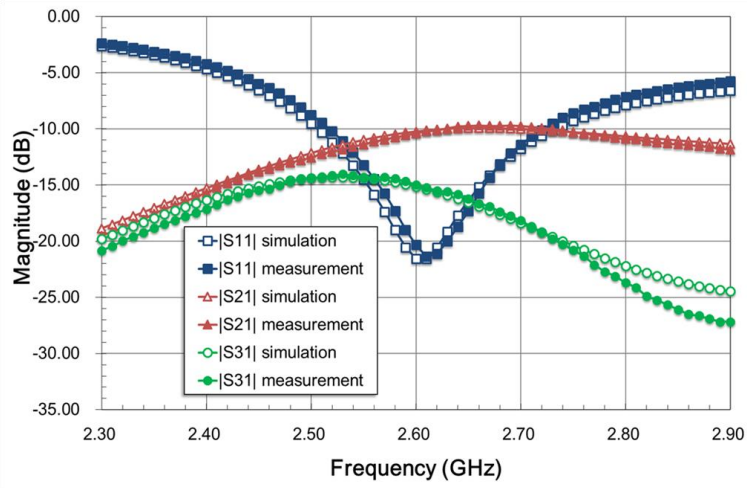
(a)
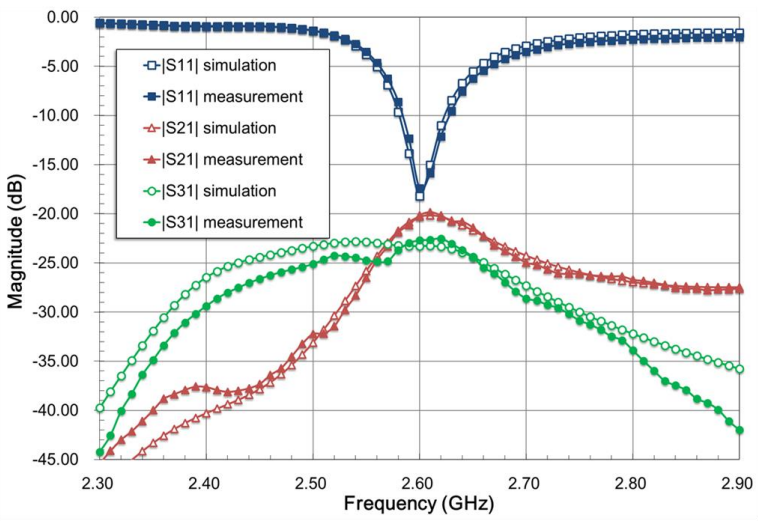
(b)
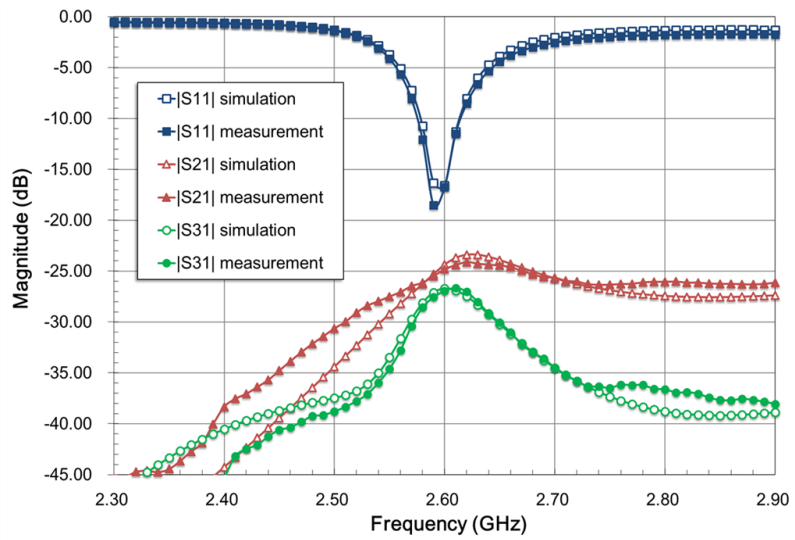
(c)

Figure 4.4 The simulated and measured S-parameters of the four-element monopole array: (a) matched but coupled array; (b) decoupled Array 1; and (c) decoupled Array 2.
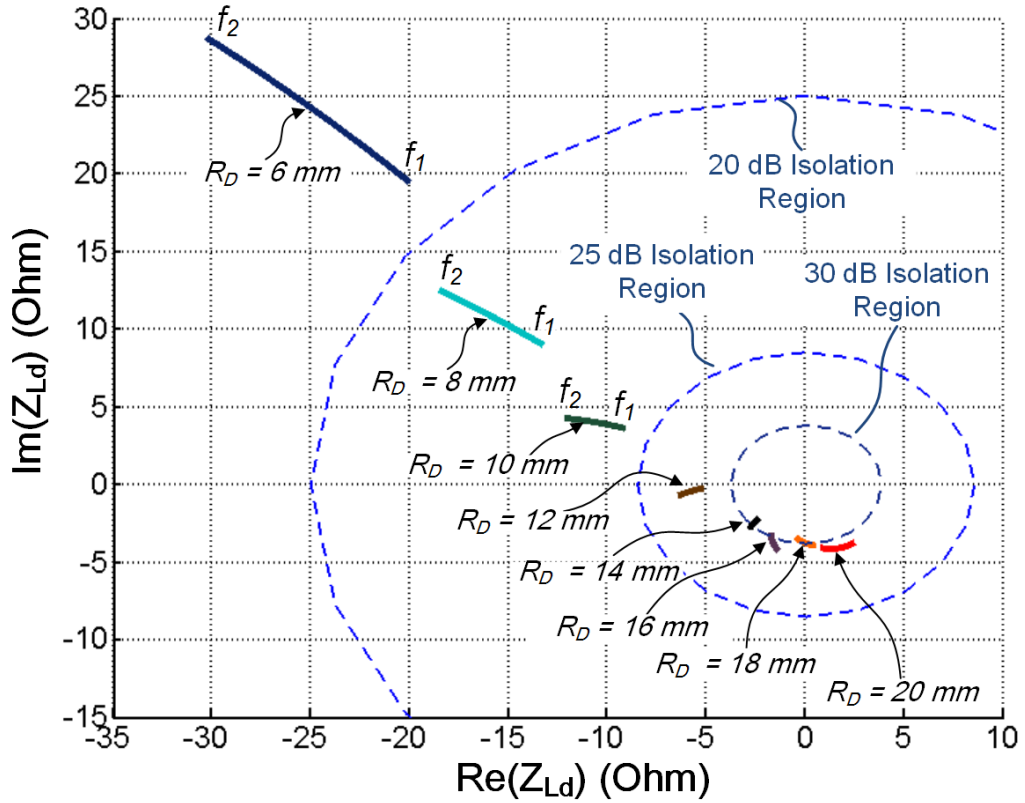
Figure 4.5 Z_{Ld} in a given frequency range (f_1= 2.55 GHz, f_2 = 2.65 GHz) for different dummy element configuration parameter R_D and different illustrative isolation contours.

For convenience, load impedances $Z_L = 1/Y_L$, $Z_{L1} = 1/Y_{L1}$ and $Z_{L2} = 1/Y_{L2}$ are used in the following discussions. Denote the difference of the two loads as $Z_{Ld} = Z_{L1} - Z_{L2}$ and the space between two adjacent dummy elements as R_D. To illustrate the relation between Z_{Ld} and the worst isolations between the radiating elements, several arrays with different R_D are simulated and the locus of Z_{Ld} in a given frequency band for different spacing value R_D is calculated according to (4.8) and (4.9) and they are then plotted in Fig. 4.5. Illustrative contours for different isolation levels are also superposed in the figure. It should be noted that the illustrative isolation contours account for both the adjacent and diagonal isolations. Therefore, if Z_{Ld} is large, the worst isolation becomes dominant. Consequently, the dummy array becomes less effective. It is also observed that the larger the spacing of the dummy elements, the smaller the difference Z_{Ld}. In fact, the observation is consistent with the physical interpretation that when the distance between two

153

dummy elements is large, the difference between Y_E and Y_F also becomes large, so that the difference between Y_A and Y_B can be effectively compensated. It has been demonstrated, through this example, that to decouple an array with multiple elements using reactive loaded dummy elements, there is no exact solution in general. Designing a decoupling network becomes a trade-off between the achievable isolation and the dimension of the whole array.

4.1.3.2. Step 2: Optimizing the reactive load

Once the dummy array configuration is chosen, the reactive load can be obtained by minimizing the worst isolation between the radiating elements. It is apparent that for a given coupled array, different optimum loads are available for different dummy array configurations. For one solution (named Array 1), the side-by-side spacing R_D of the dummy array is chosen to be 12 mm. For another solution (named Array 2), R_D = 18 mm is used. The load value against the normalized goal function defined by (4.10) is plotted in Fig. 6, where the maximum value of the goal function for both Array 1 and Array 2 are used to normalize the goal function. It is observed that the optimum reactive load Z_L for Array 1 and Array 2 are *-j12.5* Ohms and *-j8.5* Ohms, respectively. The dimensions of the two arrays are summarized in Table 4-1.
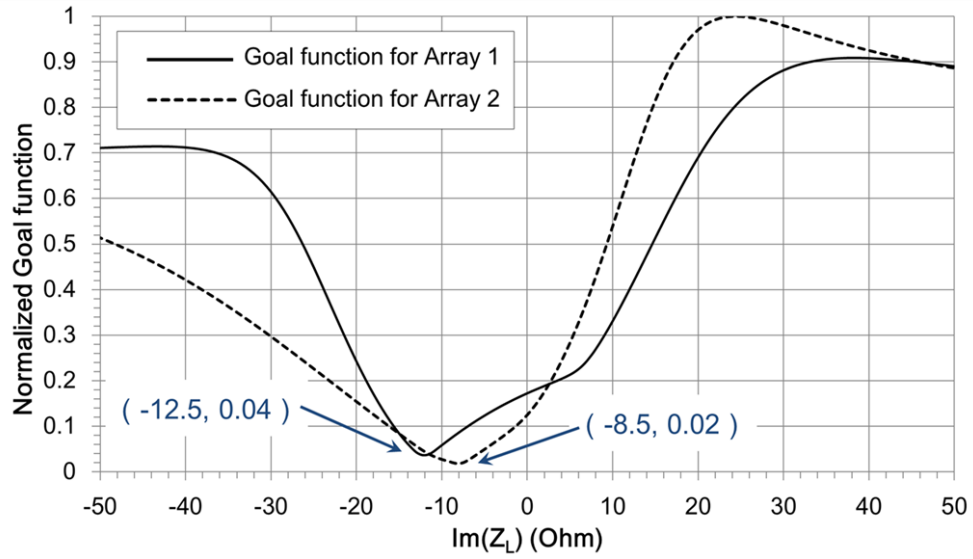
Figure 4.6 The normalized goal functions of the optimum load value for Array 1 and Array 2.

Table 4-1 Dimensions of the four-element monopole array (Unit: mm)

	Decoupled array 1	Decoupled array 2
R_A	25.0	25.0
R_D	12.0	18.0
L_Y	13.0	14.7
L_F	26.5	26.5
L_S	19.0	20.0
L_A, L_D	27.0	27.0
W_A, W_D	3	3

4.1.3.3. Designing matching networks.

As stated by equation (4.7a), decoupling of a radiating array will affect its matching performance. Therefore, a matching network is needed at each port after the array is decoupled. Since the radiating elements are isolated to each other after

155

decoupling, each port can be matched independently. For the decoupled monopole arrays, matching stubs are used.

The simulation and measurement results for decoupled Array 1 and Array 2 are shown in Figs. 4.4 (b) and (c). It can be seen that the adjacent and diagonal isolations at the center frequency are around 20 dB and 23 dB for Array 1, and 25 dB and 27 dB for Array 2, respectively. The fractional bandwidths for isolations below 20 dB are more than 50%. The fractional bandwidths for a return loss better than 6 dB are better than 3%. It is understandable that when the isolation is improved, antenna efficiency and Q factor increase and, consequently, the matching bandwidth decreases. It can be shown, in the following example, that decoupling of a broad band four-element array is also possible using different form factors of the elements and array configurations.

4.1.2. A Four-element "Cheese-cake" PIFA Array

When deploying an indoor MIMO system by a Distributed Antenna System (DAS), the required antenna arrays need to be compact, low-profile, high efficiency, and yet with acceptable bandwidth. To meet the requirements, a "cheese-cake" antenna array is proposed. As shown in Fig. 4.7, the antenna array consists of four planar inverted F radiating antennas (PIFAs) and four planar inverted F dummy elements. As there are sufficient geometric parameters in the dummy array to be tuned, to maintain a relative simple structure, four grounded dummy elements are preferred in this case. In other words, the load impedance should be zero. To decouple the adjacent and diagonal mutual couplings in this example, parameters $F2, P2$ and L_{FD} are fixed and R_D is tunable. A number of radiating and dummy array compositions with different R_D are examined. For each composition, the relation of the load and the normalized goal functions defined in (4.10) is plotted in Fig. 4.8. It can be observed from Fig. 4.8 that the dummy array with $R_D = 30$ mm will have an optimum load impedance of

zero, which means that short-circuited dummy elements are sufficient to decouple all the unwanted mutual couplings.

(a)

(b)

(c)
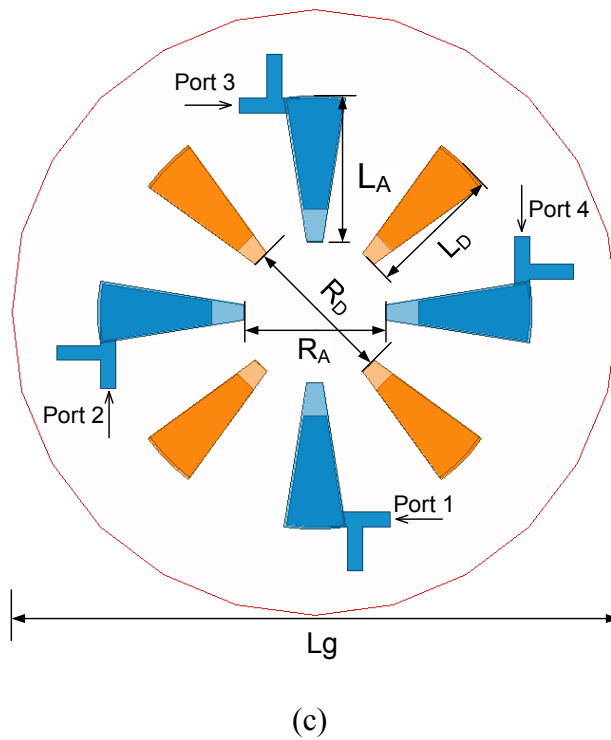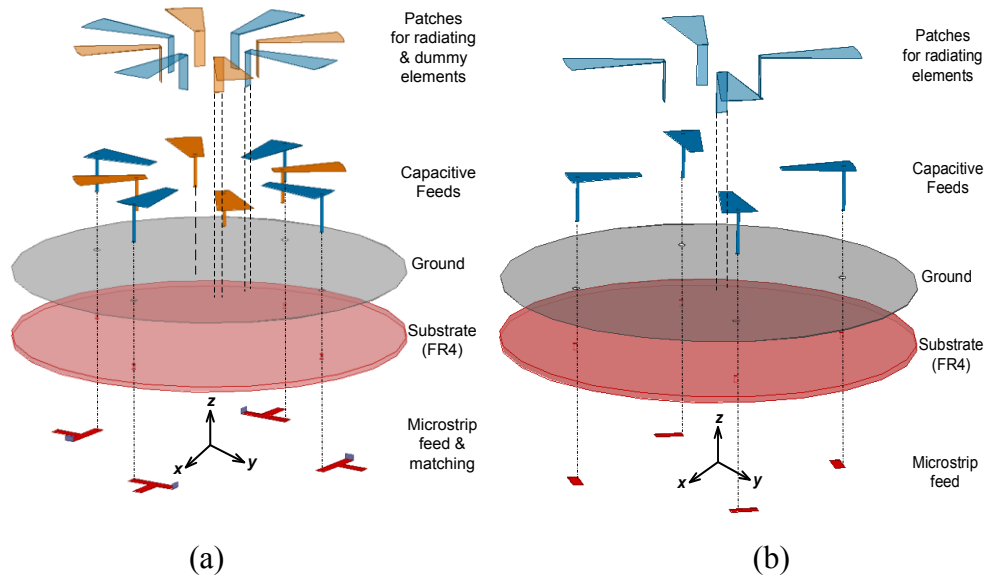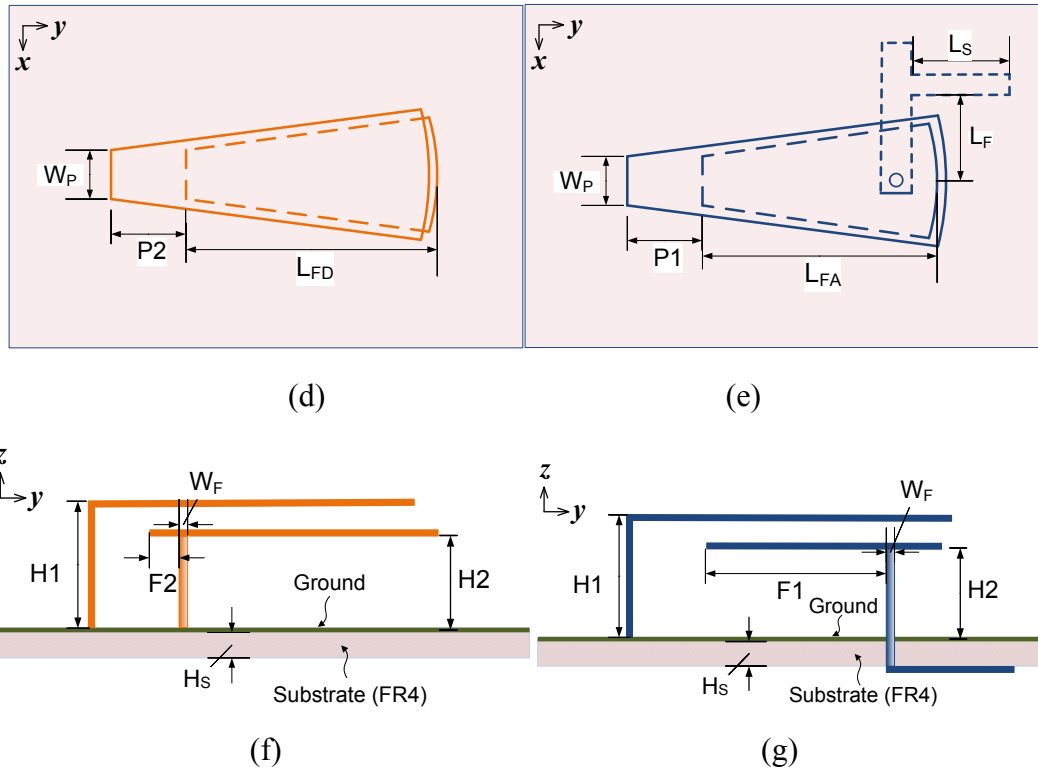
Figure 4.7 The view of (a) the cheese-cake array; (b) the coupled array; (c) top view of the cheese-cake antenna array; (d) top view of a dummy element; (e) the top view of a radiating element; (f) side view of a dummy element and (g) the side view of a radiating element.
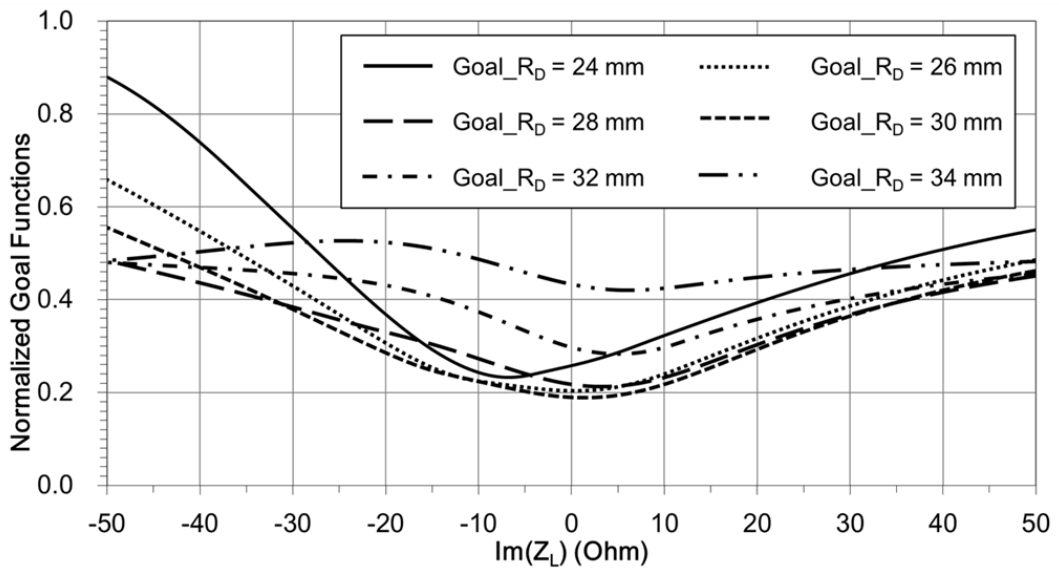
Figure 4.8 The goal functions normalized to the largest goal value of all the cases versus the load Z_L with different R_D values.

Having had an appropriate configuration of the short- circuited dummy array, the

radiating elements are isolated from each other. Extra matching networks can further improve the matching performance.

The final layout of the cheese-cake antenna array is depicted in Fig. 4.7 with the dimensions listed in Table 4-2. To better evaluate the performance of the cheese-cake array, a coupled array as shown in Fig. 4.7 (b) is designed with the best effort under the constraint of similar dimensions and structure. The measured and the simulated S-parameters of the cheese-cake array and the coupled array are superposed in Fig. 4.9. The decoupling performance with $|S_{21}| \leq -20$ dB and $|S_{31}| \leq -26$ dB is achieved from 2.3 GHz to 2.9 GHz. The matching bandwidth with $|S_{11}| \leq -10$ dB is 196 MHz, which is sufficiently large for the required downlink and uplink bands of the LTE 2.6 GHz band.
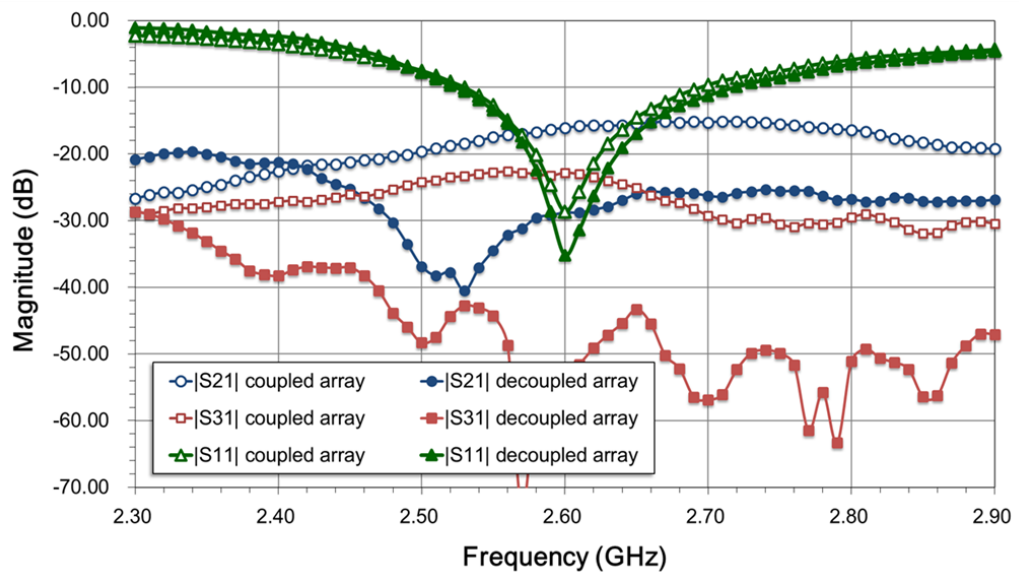
Figure 4.9 Measured magnitude of scattering parameters of the coupled and the decoupled cheese-cake array.

Table 4-2 Dimensions of the cheesecake antenna array (Unit: mm)

Variables	Size	Variables	Size
L_g	120	H1	11
R_D	30	H2	10.2
R_A	28	P1	6.5
L_A	29	F1	20
L_D	26	P2	4.5
L_{FA}, L_{FD}	22	F2	3

4.2. Dummy Array for Three Element Arrays

This section will extend the general theory of dummy array decoupling to decouple a compact isosceles triangle array of three elements. Only one dummy antenna element with an optimum reactive load is sufficient to effectively decouple all the radiating antenna elements of the compact array. Detailed deduction will be given, followed by a design example of monopole array.

4.2.1. The Theory

4.2.1.1. Network Model
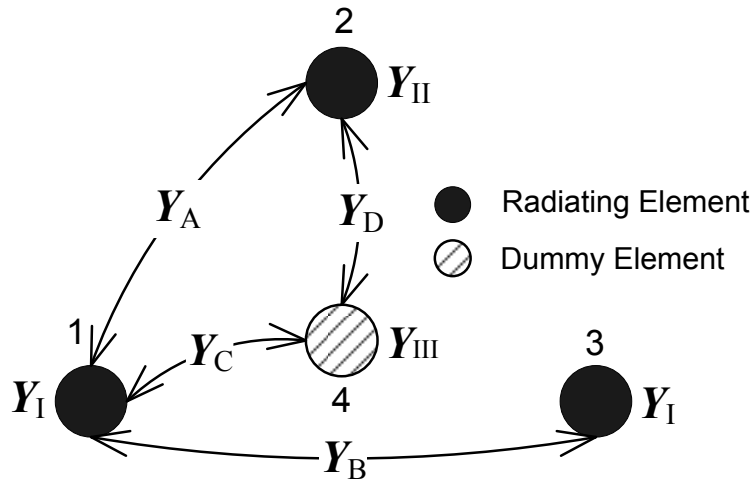
Figure 4.10 The diagram of asymmetrical three-element isosceles triangular array with one dummy element.

The diagram of three radiating elements in an isosceles triangular compact array are shown in Fig. 4.10, in which antennas 1 through 3 are radiating elements that are fed by 50 Ω transmission lines and locate on the vertices of the triangle and antenna 4 is a dummy element, which is terminated with a reactive load and located along the symmetry axis. As illustrated by Fig. 4.10, there are four distinct *short-circuited* mutual admittances according to the configuration:

Y_A: Mutual admittance along the two equal sides of the isosceles triangle (between element 1 and element 2 as well as element 2 and element 3),

Y_B: Mutual admittance along the base side of the isosceles triangle (between element 1 and element 3),

Y_C: Mutual admittance between the dummy element 4 and radiating elements 1 and 3, and

Y_D: Mutual admittance between the dummy element 4 and radiating element 2.

Due to the symmetry of the array, there are three self-admittances:

Y_I: The self-admittance of the radiating elements 1 and 3,

Y_{II}: The self-admittance of the radiating element 2, and

Y_{III}: The self-admittance of the dummy element 4.
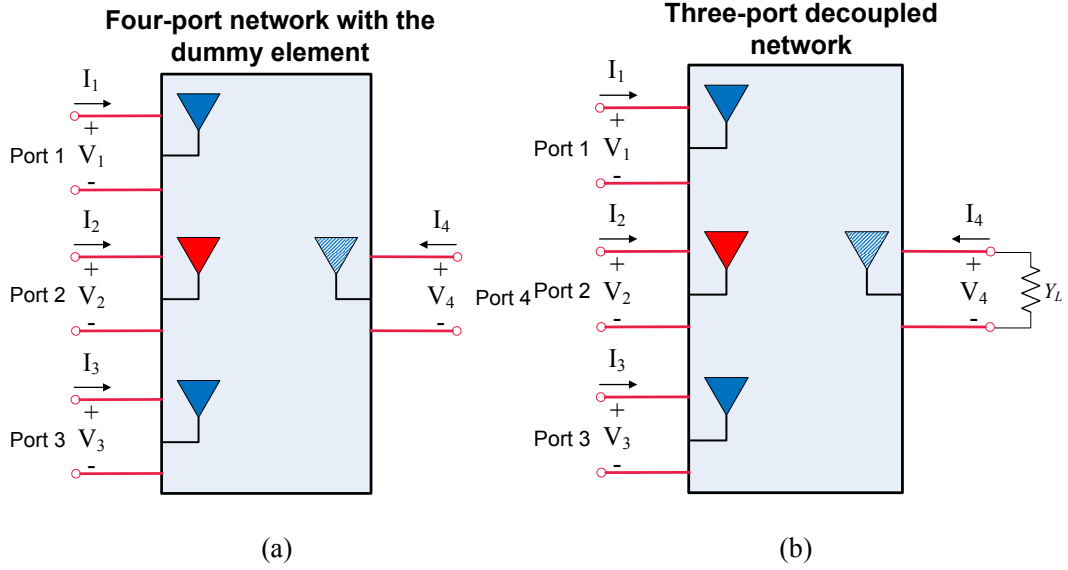
Figure 4.11 (a) The four-port network consists of three radiating elements and one dummy element. (b) The three-port network where the dummy element is terminated with load Y_L.

Consider the four antenna elements as shown in Fig. 4.11 (a), including the radiating and dummy ones, their port voltage-current relation can be written as:

$$
\begin{bmatrix} I_1 \\ I_2 \\ I_3 \\ I_4 \end{bmatrix} = \begin{bmatrix} Y_I & Y_A & Y_B & Y_C \\ Y_A & Y_{II} & Y_A & Y_D \\ Y_B & Y_A & Y_I & Y_C \\ Y_C & Y_D & Y_C & Y_{III} \end{bmatrix} \cdot \begin{bmatrix} V_1 \\ V_2 \\ V_3 \\ V_4 \end{bmatrix}.
\tag{4.11}
$$

If dummy element 4 is terminated by a load Y_L, as shown in Fig. 4.11 (b), the voltage-current relation at the port 4 can be described by:

$$I_4 = -Y_L \cdot V_4. \tag{4.12}$$

Substituting (4.12) into (4.11) yields:

$$\begin{bmatrix} I_1 \\ I_2 \\ I_3 \end{bmatrix} = \begin{bmatrix} Y_I' & Y_A' & Y_B' \\ Y_A' & Y_{II}' & Y_A' \\ Y_B' & Y_A' & Y_I' \end{bmatrix} \cdot \begin{bmatrix} V_1 \\ V_2 \\ V_3 \end{bmatrix}, \tag{4.13}$$

where:

$$Y_A' = Y_A - \frac{Y_C Y_D}{Y_{III} - Y_L} = 0 \tag{4.14}$$

and

$$Y_B' = Y_B - \frac{Y_D^2}{Y_{III} - Y_L} = 0 \tag{4.15}$$

are the two conditions for decoupling the three radiating elements. Further examine (4.14) and (4.15) yields:

$$Y_A' - Y_B' = (Y_A - Y_B) + \frac{Y_D}{Y_{III} - Y_L} \cdot (Y_D - Y_C) = 0 \tag{4.16}$$

Since in general, $Y_A \neq Y_B$, it can be concluded from (4.16) that the necessary condition for decoupling an isosceles triangle array is that $Y_C \neq Y_D$, which can be naturally satisfied for by a proper array configuration in Fig. 4.11 with one dummy element.

4.2.1.2. Design Procedure

In a practical design, the values of Y_A, Y_B, Y_C, Y_D and Y_{III} in (4.11) depend on the relative distances between the radiating elements and the dummy element as well as the antenna radiation characteristics. For a given array configuration, one can choose

the location of dummy element as well as the load admittance Y_L to better satisfy conditions (4.14) and (4.15). For a fixed location of the dummy element, one can find an optimum reactive load value Y_{Lopt} by a simple optimization search method. If a reactive load Y_L is realized by a section of open ended transmission line, whose imaginary input admittance is $Y_L = -jY_0 \tan\beta l$, where Y_0 and β are the characteristic admittance and phase constant of the transmission line, respectively, and l is the length of the line to be optimized. The optimal length that best satisfies (4.14) and (4.15) simultaneously within a frequency band of interest can be found by minimizing the goal function:

$$g(l) = \left(w_1 \sum_{i=1}^{N_s} |Y_A'(f_i)|^2 + w_2 \sum_{i=1}^{N_s} |Y_B'(f_i)|^2\right) \Big/ g(l)_{\max} \qquad (4.17)$$

where w_1 and w_2 are weighting parameters which are normally chosen to be 1, N_s is the number of sampling frequency points f_i selected in the frequency band of interest. This goal function is normalized to the maximum value of $g(l)$.

4.2.2. Implementation of the Decoupling Technique

The concept to use one dummy element for decoupling an isosceles triangle array is demonstrated by a monopole array with circular ground working in the band of 2.5 to 2.6 GHz as shown in Fig. 4.12. The substrate used is FR4 with relative dielectric constant of 4.3 and thickness of 0.8 mm. Since the distances between adjacent elements in the original array without a dummy element are around 0.26λ and 0.21λ, respectively, these elements are not well isolated. The worst isolations in the band of interest are around 9 dB. Therefore, an effective decoupling means must be taken.
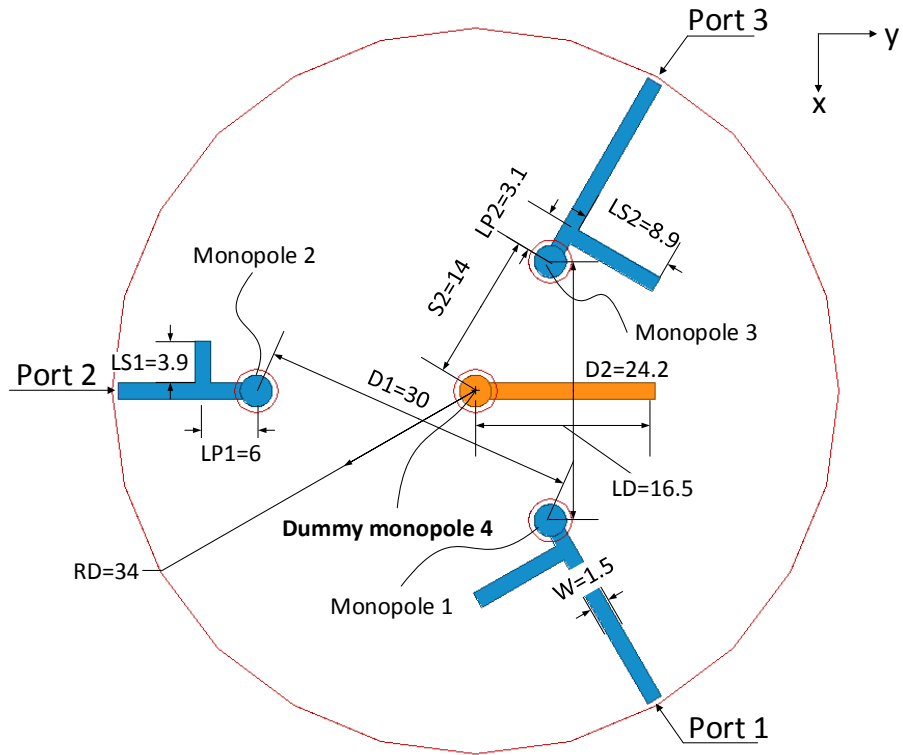
(a)
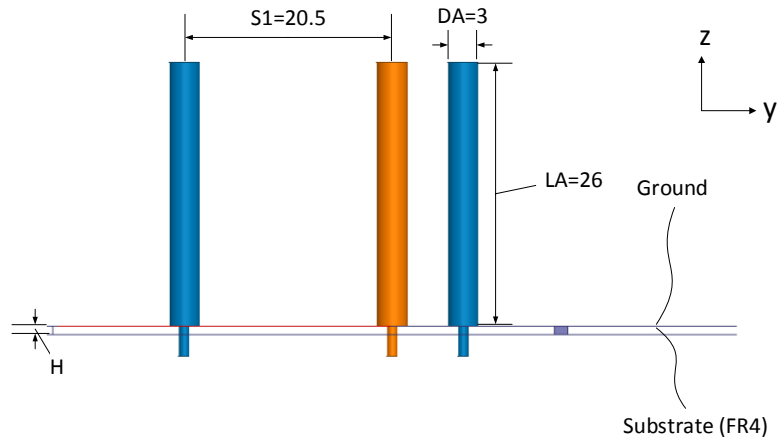
(b)

Figure 4.12 (a) Top view and (b) front view of the three-element array with one dummy element (unit: mm).

One dummy element is to be placed along the symmetry axis of the array. The S-parameters of the new four-element array can be obtained by EM simulation. For different locations of the dummy element, the load value is optimized such that the goal function in (4.17) is minimized. The obtained optimum load Y_{Lopt} is then connected to the fourth-port of the network and the new three-port S-parameters can

be obtained by Agilent Advanced Design System (ADS). Several iterations can be taken to find a proper location of the dummy element and corresponding reactive load. In this example, the dummy element is placed at the point 20.5 mm away from monopole 2. The reactive load is implemented by an open-ended transmission line with length of 16.5mm. After the radiating elements are decoupled, each element can be independently matched using single-stub matching networks.
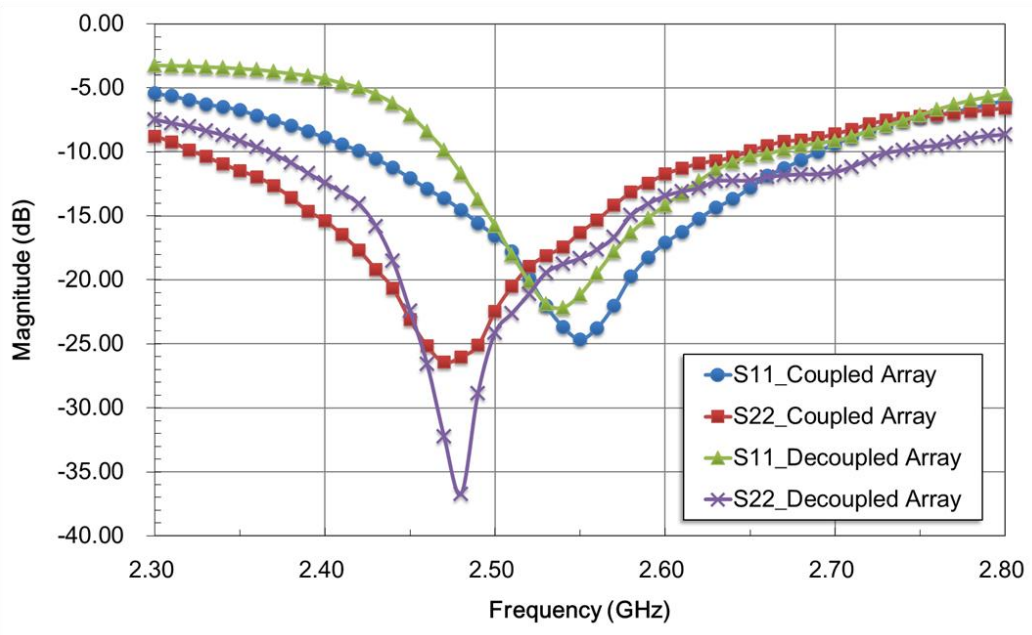
(a)
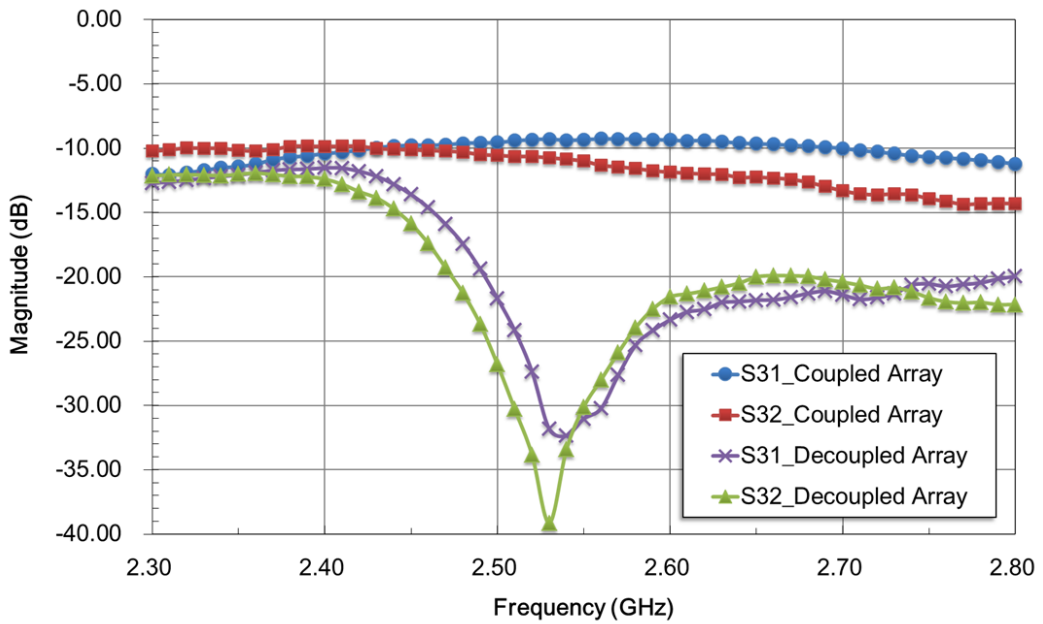
(b)

Figure 4.13 (a) Return losses for the coupled and decoupled array. (b) Isolations for the coupled and decoupled array.

The decoupled array with a dummy element and coupled array without any dummy elements are designed, fabricated and measured. The measurement results

are superposed in Fig. 4.13. It can be seen that the fractional bandwidth with 10 dB return loss and 20 dB isolation is around 6.3% in the band of interest for the decoupled array.

4.3. Reference

[1] A. C. K. Mak, C. R. Rowell, and R. D. Murch, "Isolation enhancement between two closely packed antennas," *IEEE Trans. Antennas Propag.,* vol. 56, no. 11, pp. 3411–3419, Nov. 2008.

[2] B. K. Lau and J. B. Andersen, "Simple and efficient decoupling of compact arrays with parasitic scatterers," *IEEE Trans. Antennas Propag.*, vol. 60, no. 2, pp. 464－472, Feb. 2012.

[3] EMPro 3D EM Simulation Software, Version 2012.09, Agilent Technologies, Inc., Santa Clara, CA.

Chapter 5

Performance Evaluation of multi-antenna systems

To have a thorough understanding of the performance of a multi-antenna system in a practical implementation, several important figures of merit such as scattering parameters, radiation patterns and radiation efficiencies, Envelope Correlation Coefficient (ECC) and throughput are investigated in chapter. For mobile terminal use, the antenna radiation pattern and other characteristics will be significantly altered by the presence of the human hand and head. Therefore, the human interference is a key issue and must be considered [1]-[4]. The human interference on the figures of merit for a multi-antenna system is also discussed in detail in this chapter.

5.1. Radiation Pattern and Correlation

The radiation pattern of multi-antenna systems are investigated using the in-house SATIMO SG128 spherical near-field scanner [5] in an ISO17025 accredited laboratory as shown in Fig. 5.1.
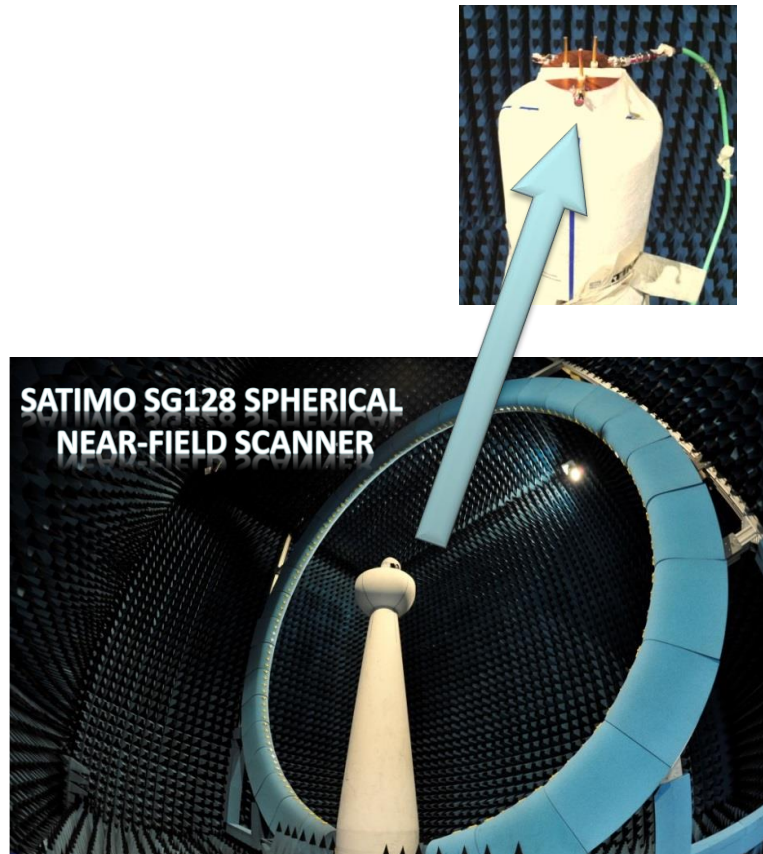
Figure 5.1 The SG-128 near field scanner and multi-antenna system measurement setup (Using the three-element array in **Section 2.5.3** as an illustration).

5.1.1 Radiation Patterns

5.1.1.1 Radiation Pattern Investigation for Antenna Array Decoupled by An S-CRDN

For the two-element asymmetric array in **Section 2.2.1**, radiation power patterns for a single cone-shaped printed monopole, an array of two coupled antennas, and the decoupled array are measured. The measured patterns are superposed in Fig. 5.2. When measuring the coupled and decoupled arrays, port 1 is excited and port 2 is terminated with a 50 Ω load. For the coupled array, the terminated port receives the coupled energy, whereas for the decoupled array, the terminated antenna acts as a 'dummy' element with little current induced at the terminated port. For well

decoupled elements, the radiation pattern is very similar to single antenna, at least in power pattern magnitude.
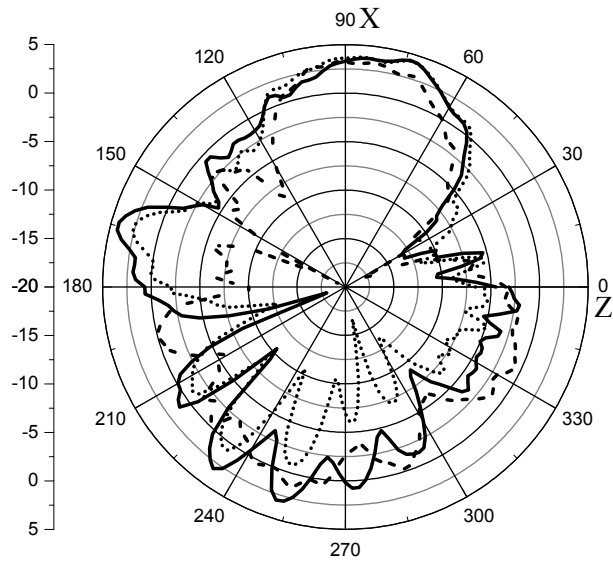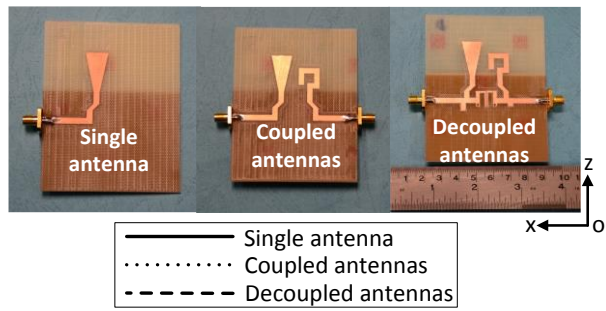
(a)
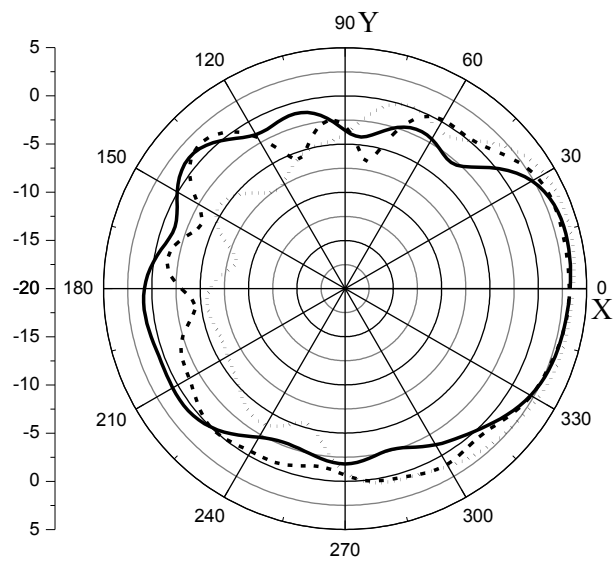
(b)

Figure 5.2 Radiation power patterns (a) in the xoz plane; and (b) in the xoy plane for the two-element symmetric array decoupled by all pole S-CRDN.
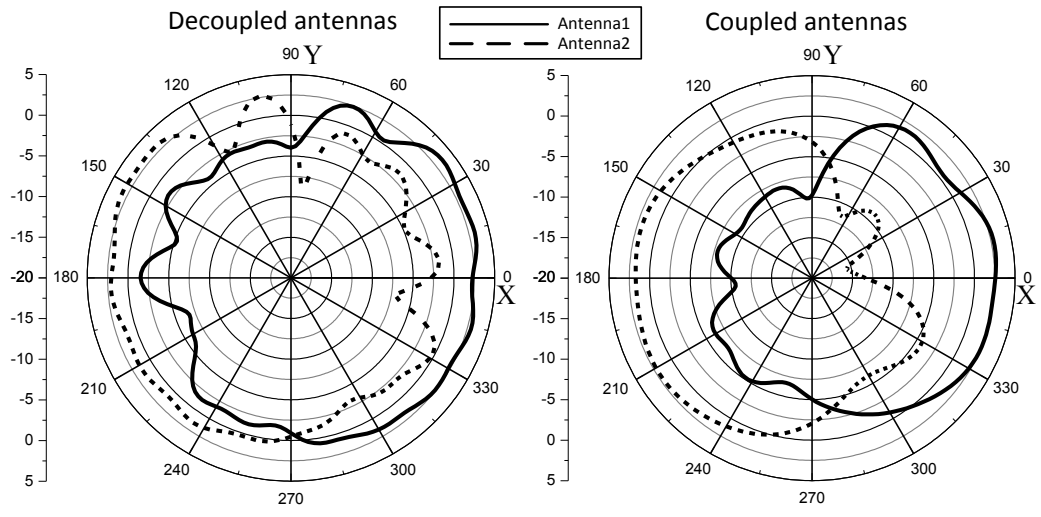
(a)   (b)
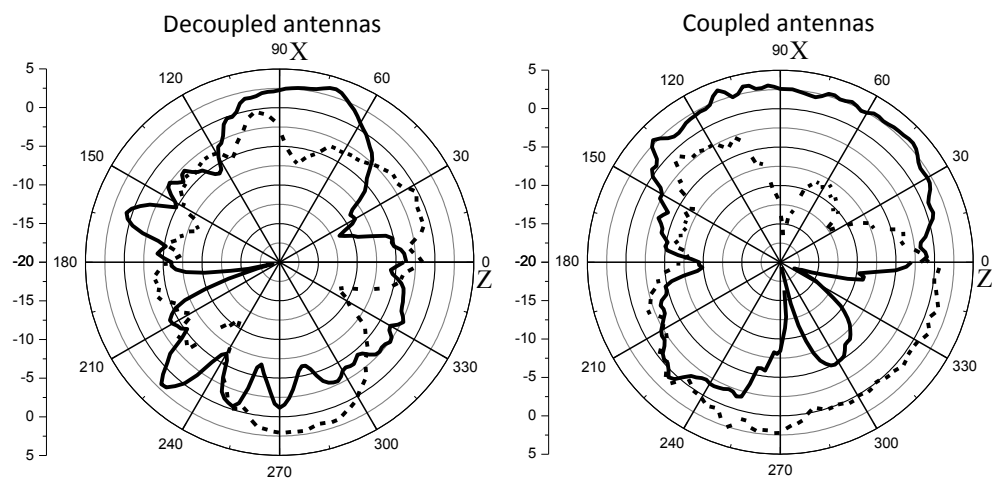
(c)   (d)

Figure 5.3 Radiation power patterns (a) of the decoupled array (by all-pole S-CRDN) in the xoy plane; (b) of the coupled array in the xoy plane; (c) of the decoupled array in the xoz plane; and (d) of the coupled array in the xoz plane.
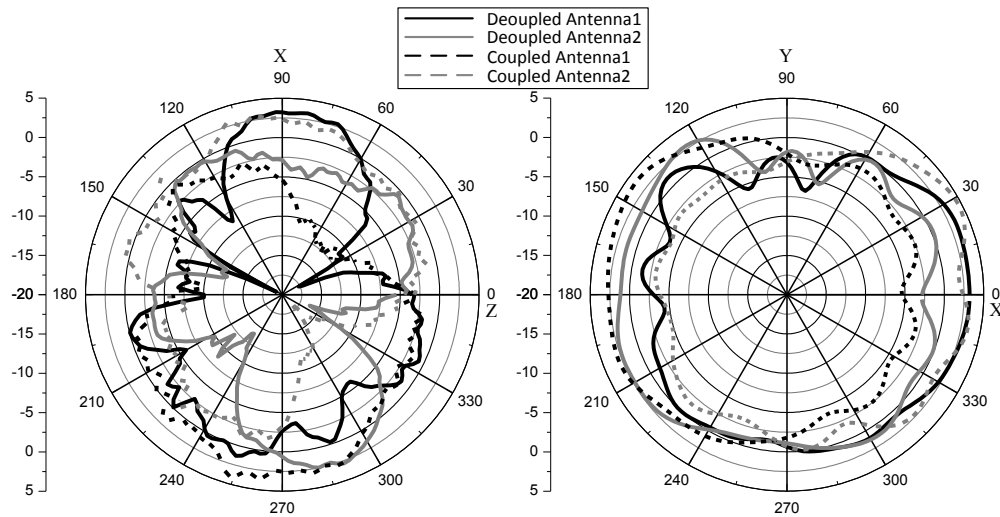
Figure 5.4 Measured radiation patterns of the coupled and decoupled (by CRDN with Source-Load Coupling) arrays.

It is interesting to plot the measured power patterns in Fig. 5.3 of the coupled array and the array decoupled by an all pole S-CRDN for the case with one of the elements is excited while the other element is terminated by a 50 Ω load. Although the phase patterns of the radiated electric fields of the two arrays are not shown, the difference of the phase patterns of the two cases makes significant contribution to the reduction of the correlation. By only comparing the power patterns of the two cases in Figs. 5.3 (a) and 5.3 (b), it seems that the coupled array has a lower correlation. The phenomenon is the same for the array decoupled by an S-CRDN with Source-Load Coupling (**Section 2.2.2**) as shown in Fig. 5.4.

5.1.1.2 Radiation Pattern Investigation for Antenna Array Decoupled by A Dummy Array

The measured radiation patterns for the four radiating elements of the cheesecake array in **Section 4.1.2** are shown in Fig. 5.5. The peak gain for each element is around 5.98 dBi. The dummy array elements act as reflectors such that the radiation

pattern of the whole array with these dummy elements tends to be more directive.
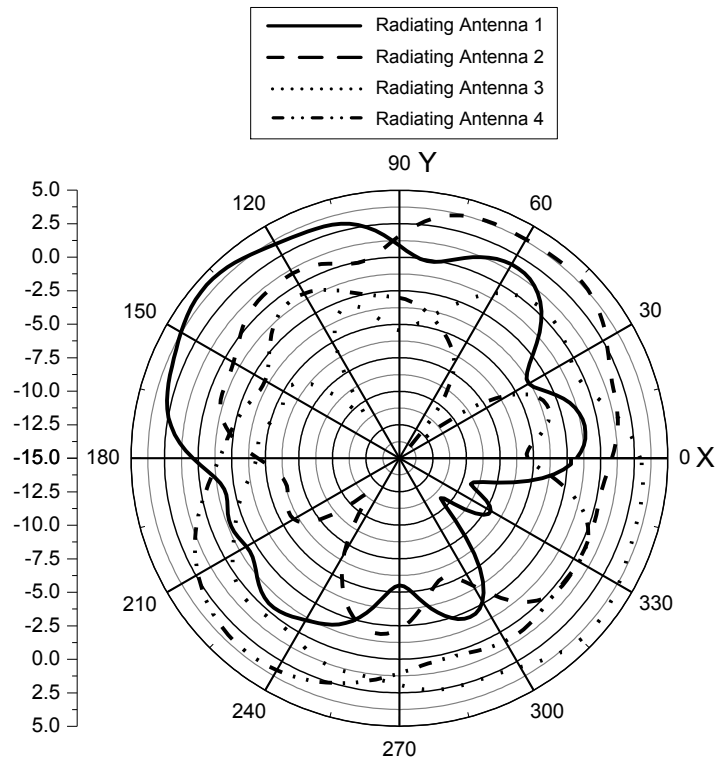
Figure 5.5 Typical radiation power patterns for all four radiating elements in the cheesecake antenna array in the $\theta = 90°$ cutting plane.

5.1.2 Envelop Correlation Coefficient

5.1.2.1 Basic Definition

To achieve a good diversity gain, one of the conditions is to have LOW CORRELATION [6]. There are mainly two metrics of correlation: the complex correlation and the envelop correlation [7]. In practice, it is difficult to measure the correlation between complex fields and signals, but the correlation of their envelopes are easier to measure [8].

The complex correlation is the correlation between the two branch signals, as [8]:

174

$$\rho_{12} = \frac{\mathcal{E}\{(x_1 - \mathcal{E}\{x_1\}) \cdot (x_2 - \mathcal{E}\{x_2\})^*\}}{\sqrt{\mathcal{E}\{|x_1 - \mathcal{E}\{x_1\}|^2\} \mathcal{E}\{|x_2 - \mathcal{E}\{x_2\}|^2\}}} \tag{5.1}$$

For zero mean signals ($\mathcal{E}\{x_1\} = \mathcal{E}\{x_2\} = 0$), (5.1) becomes:

$$\rho_{12} = \frac{\mathcal{E}\{x_1 x_2^*\}}{\sqrt{\mathcal{E}\{|x_1|^2\} \mathcal{E}\{|x_2|^2\}}} = \frac{R_{12}}{\sqrt{\sigma_1^2 \sigma_2^2}} \tag{5.2}$$

where R_{12} is the cross covariance. σ_1^2 and σ_2^2 are the standard deviations of the envelopes of signal 1 and signal 2.

The envelop correlation on the other hand, are defined as the correlation between two signal envelopes as [8], [9]:

$$\rho_e = \frac{\mathcal{E}\{(|x_1|^2 - \mathcal{E}\{|x_1|^2\}) \cdot (|x_2|^2 - \mathcal{E}\{|x_2|^2\})^*\}}{\sqrt{\mathcal{E}\{||x_1|^2 - \mathcal{E}\{|x_1|^2\}|^2\} \mathcal{E}\{||x_2|^2 - \mathcal{E}\{|x_2|^2\}|^2\}}} \tag{5.3}$$

The variables in Equation (5.3) are complex Gaussian signals defined as:

$$x_i = a_i + jb_i \quad i = 1,2 \tag{5.4}$$

where a_i and b_i are real, independent, zero-mean Gaussian random variables of equal variance: $\mathcal{E}\{a_i^2\} = \mathcal{E}\{b_i^2\} = \sigma^2$. Making use of these properties together with some identities of random signal processing, the following relation can be obtained:

$$\rho_e = \frac{\pi}{4(4-\pi)} \left(|\rho_{12}|^2 + |\rho_{12}|^4/16 + |\rho_{12}|^6/64 + \cdots \right) \tag{5.5}$$

The envelope correlation can be good approximated by:

$$\rho_e \approx |\rho_{12}|^2 = \frac{\mathcal{E}\{x_1 x_2^*\}^2}{\mathcal{E}\{|x_1|^2\}\mathcal{E}\{|x_2|^2\}} \tag{5.6}$$

The complex correlation coefficient and envelope correlation coefficient are compared by measurements conducted in [8] and listed in Table 5-1.

Table 5-1 Comparison Between The Complex Correlation and Envelope Correlation

$|\rho_{12}|^2$	ρ_e	$|\rho_{12}|^2$	ρ_e
0.01	0.0092	0.5	0.474
0.1	0.0921	0.6	0.574
0.2	0.185	0.7	0.676
0.3	0.280	0.8	0.780
0.4	0.376	0.9	0.888

5.1.2.2 Correlation Calculation by Antenna Parameters

1. Receiving characteristics of antennas:

In receiving mode, an antenna of any type tries to capture EM waves and to extract power (voltage) from them. The complex effective vector is introduced to characterize the receiving antenna [10]:

$$\vec{l}_e(\theta, \phi) = \hat{a}_\theta l_\theta(\theta, \phi) + \hat{a}_\phi l_\phi(\theta, \phi) \tag{5.7}$$

Having had defined the effective length, the radiated E field in the far-zone is given by:

$$\vec{E}_a = \mathrm{E}_\theta \hat{a}_\theta + \mathrm{E}_\phi \hat{a}_\phi = -j\eta \frac{kI_{in}}{4\pi r} \vec{l}_e e^{-jkr} \tag{5.8}$$

The open-circuit voltage of the receiving antenna is related to the effective length in the following way as:

$$V_{oc} = \vec{E}_{inc} \cdot \vec{l}_e = E_\theta l_\theta + E_\phi l_\phi \tag{5.9}$$

where $\vec{E}_{inc}$ is the incident E-field. This can be understood by the relation between E-field and electric potential: $V = -\int \vec{E} \cdot \overrightarrow{dl}$. As a matter of fact, the effective length quantifies the radiated field relative to the field from a current element of unit length, therefore, we let: $\vec{l}_e \equiv \vec{E}_e$

For multipath sources, the incident field can be represented by: $\vec{E}_{inc} = \vec{E}_{inc}(\Omega, t)d\Omega$, where Ω is the set of incident solid angles of multipath signals. If there are M multipath signals, the incident field can be expressed by:

$$\vec{E}_{inc} = \sum_{m=1}^M \vec{E}_{inc_m}(\Omega_m, t)d\Omega_m \tag{5.10}$$

The total received open circuit voltage is the sum of all the contributions of incident fields over the solid angle that can be captured by the receiving antennas [11], [12]:

$$\mathrm{V}_{oc} = \iint_\Omega \vec{E}_e(\Omega) \cdot \vec{E}_{inc}(\Omega, t)d\Omega \tag{5.11}$$

To be more specific, for multi-antenna systems, the open circuit voltage of the k-th receive antenna is given by:

$$V_{ok}(t) = \iint \vec{E}_{ek}(\Omega) \cdot \vec{E}_{inc}(\Omega, t) d\Omega \qquad (5.12)$$

Substituting (5.12) into (5.6), the complex correlation between antenna j and antenna k in a multi-antenna system can be represented by:

$$\rho_{jk} = \frac{\rho_{jkn}}{\rho_{jkd}} \qquad (5.13)$$

where the numerator

$$\rho_{jkn} = \mathcal{E}\left\{ \iint \vec{E}_{ej}(\Omega_1) \cdot \vec{E}_{inc}(\Omega_1, t) d\Omega_1 \cdot \iint \vec{E}_{ek}^*(\Omega_2) \cdot \vec{E}_{inc}^*(\Omega_2, t) d\Omega_2 \right\} \qquad (5.14)$$

Interchange the order of expectation and integration, we will have:

$$\rho_{jkn} = \iint \vec{E}_{ej}(\Omega_1) \cdot \vec{E}_{ek}^*(\Omega_2) \cdot \vec{E}_{inc}(\Omega_1, t) \cdot \vec{E}_{inc}^*(\Omega_2, t) d\Omega_1 d\Omega_2 \qquad (5.15)$$

For mobile terminals, the antennas are always closely spaced, so that: $\Omega_1 = \Omega_2 = \Omega$. We also have the assumption that orthogonal polarized field are uncorrelated [9]. Therefore, (5.15) becomes:

$$\rho_{jkn} = \iint \left[E_{\theta j}(\Omega) \cdot E_{\theta k}^*(\Omega) + E_{\phi j}(\Omega) \cdot E_{\phi k}^*(\Omega) \right] \left| \vec{E}_{inc}(\Omega, t) \right|^2 d\Omega \qquad (5.16)$$

Similarly, for the denominator, the following expression can be obtained:

$$\rho_{jkd} = \sqrt{ \iint \left[|E_{\theta j}(\Omega)|^2 + |E_{\phi j}(\Omega)|^2 \right] \left| \vec{E}_{inc} \right|^2 d\Omega \cdot \iint \left[|E_{\theta k}(\Omega)|^2 + |E_{\phi k}(\Omega)|^2 \right] \left| \vec{E}_{inc} \right|^2 d\Omega } \qquad (5.17)$$

Using both (5.16) and (5.17) and cancel out the common term $\left| \vec{E}_{inc} \right|^2$ and eventually we have:

$$\rho_{jk} = \frac{\iint_{4\pi}\left[E_{\theta j}(\Omega)\cdot E_{\theta k}^*(\Omega)+E_{\phi j}(\Omega)\cdot E_{\phi k}^*(\Omega)\right]d\Omega}{\iint_{4\pi}\left(G_{\theta j}(\Omega)+G_{\phi j}(\Omega)\right)d\Omega\cdot\iint_{4\pi}\left(G_{\theta k}(\Omega)+G_{\phi k}(\Omega)\right)d\Omega} \qquad (5.18)$$

with $G_{\theta i}(\Omega) = E_{\theta i}(\Omega)\cdot E_{\theta i}^*(\Omega) \quad i = j,k$ and $G_{\phi i}(\Omega) = E_{\phi i}(\Omega)\cdot E_{\phi i}^*(\Omega) \quad i = j,k.$

For two antenna array, with j = 1, k = 2 and using the relation (5.6), (5.18) becomes:

$$\rho_e = \frac{\left|\iint_{4\pi}\left(E_{\theta 1}(\Omega)\cdot E_{\theta 2}^*(\Omega)+E_{\phi 1}(\Omega)\cdot E_{\phi 2}^*(\Omega)\right)d\Omega\right|^2}{\iint_{4\pi}\left(G_{\theta 1}(\Omega)+G_{\phi 1}(\Omega)\right)d\Omega\cdot\iint_{4\pi}\left(G_{\theta 2}(\Omega)+G_{\phi 2}(\Omega)\right)d\Omega} \qquad (5.19)$$

It should be noted that the antenna correlation not only depends on the orthogonality of radiated fields (patterns) but also on the statistical characteristics of the propagation channel. Equation (5.19) needs to be modified as:

$$\rho_e = \frac{\left|\iint_{4\pi}\left(XPD\cdot E_{\theta 1}(\Omega)\cdot E_{\theta 2}^*(\Omega)\cdot p_\theta(\Omega)+E_{\phi 1}(\Omega)\cdot E_{\phi 2}^*(\Omega)\cdot p_\phi(\Omega)\right)d\Omega\right|^2}{\begin{array}{c}\iint_{4\pi}\left(XPD\cdot G_{\theta 1}(\Omega)\cdot p_\theta(\Omega)+G_{\phi 1}(\Omega)\cdot p_\phi(\Omega)\right)d\Omega\\ \cdot\iint_{4\pi}\left(XPD\cdot G_{\theta 2}(\Omega)\cdot p_\theta(\Omega)+G_{\phi 2}(\Omega)\cdot p_\phi(\Omega)\right)d\Omega\end{array}} \qquad (5.20)$$

where XPD is the cross polar discrimination defined as the vertical and horizontal power ratio. $p_\theta(\Omega)$ and $p_\phi(\Omega)$ are the angular distribution of θ and φ components of radiated fields. Equations (5.18) and (5.20) are quite useful both for mobile terminal antennas and base station antennas. The application of them in deducing the well-known Clarke's model [14] and Geometric models for Macrocells [15] will be elaborated in Appendix A6.

For mobile terminal scenario, uniform angular distribution and 0 dB XPD are always assumed, therefore, (5.20) can be simplified as:

$$\rho_e = \frac{\left|\iint_{4\pi}\left(E_{\theta 1}(\Omega)\cdot E_{\theta 2}^*(\Omega)+E_{\phi 1}(\Omega)\cdot E_{\phi 2}^*(\Omega)\right)d\Omega\right|^2}{\iint_{4\pi}\left(G_{\theta 1}(\Omega)+G_{\phi 1}(\Omega)\right)d\Omega\cdot\iint_{4\pi}\left(G_{\theta 2}(\Omega)+G_{\phi 2}(\Omega)\right)d\Omega} \tag{5.21}$$

which is the commonly used equation for ECC calculation [9], [13]. It can be concluded from (5.21) that it is very important to include phase information in the calculation of ECC. Therefore, only investigating the power pattern in Fig. 5.3 and Fig. 5.4 will have little use unless the phases are considered.

5.1.2.3 Correlation Calculation by Scattering Parameters

The calculation of envelope correlation coefficients from antenna radiation patterns are quite complicated. It has to be carried out at every frequency points of interest. Depending on the resolution in solid angles, the integrals on the numerator and denominator of (5.21) can be very time consuming. The calculation of ECC from scattering parameter is first introduced in [16] and then modified in [17] to include antenna efficiency into the calculation. The detailed deduction can be found in [16] and [17], the calculation formula is given here as:

$$\rho_e = \frac{\left|S_{11}^*S_{12}+S_{21}^*S_{22}\right|^2}{(1-(|S_{11}|^2+|S_{21}|^2))(1-(|S_{22}|^2+|S_{12}|^2))\eta_1\eta_2} \tag{5.22}$$

where η_1 and η_2 are the radiation efficiencies of antenna 1 and antenna 2, respectively.

Although not explicitly pointed out in [16], there is one prerequisite in obtaining (5.22), that the antennas must be minimum scattering antennas. A minimum-scattering antenna has identical gain in opposite directions. It scatters with the same antenna pattern that it radiates. It always scatters the same power it absorbs [18]. In practical applications, due to the limited ground size and other interferences such as human hand and head, any antennas that are coupled to other antennas cannot

be viewed as a minimum scattering antenna. Nevertheless, equation (5.22) can always be used as an approximation which can be calculated very fast.

The two methods for ECC calculation are compared. The decoupled antenna array in Fig. 5.2 is used as an example. The ECCs of such array using two methods are superposed in Fig. 5.6.
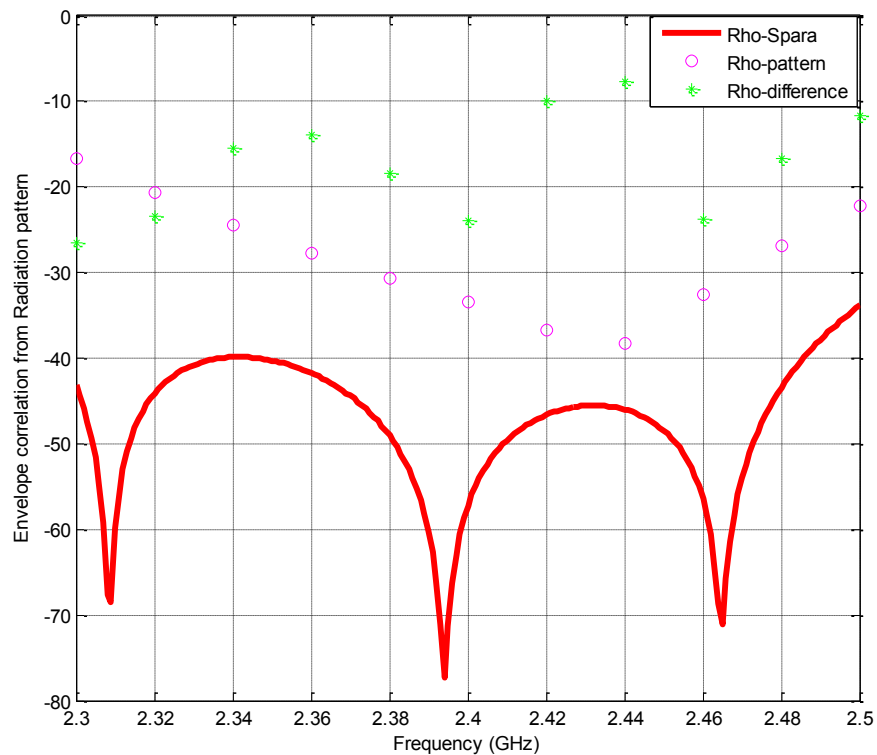
Figure 5.6 ECC (in dB) calculation of the decoupled antenna array in Fig. 5.2 using S-parameter method (Eq. 5.22) and using antenna pattern method (Eq. 5.21)

5.1.2.4 ECC evaluation for Decoupled Antenna Arrays

The benefit of antenna decoupling is revealed by comparing the ECCs of a strongly coupled antenna array, and the same array but decoupled. The ECCs decoupled array by means introduced from Chapter 2 to Chapter 4 together with their

coupled counterpart for comparison purpose are plotted in Figures 5.7 ~ 5.11. The ECCs are obtained from pattern calculation as in (5.21). Significant improvement can be observed for all decoupled arrays.
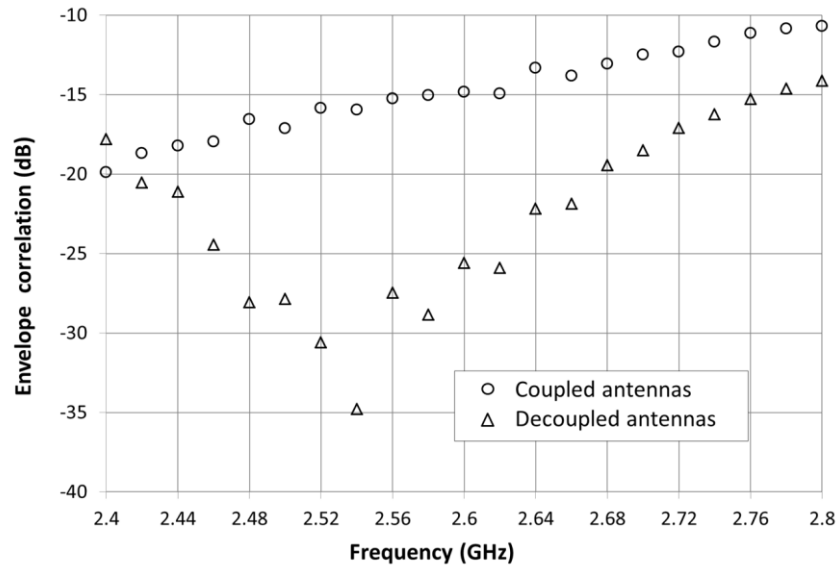
Figure 5.7 The ECCs for coupled asymmetric array (Fig. 2.9 (a)) and the same array decoupled by a second order all pole S-CRDN (Fig. 2.11 (a))
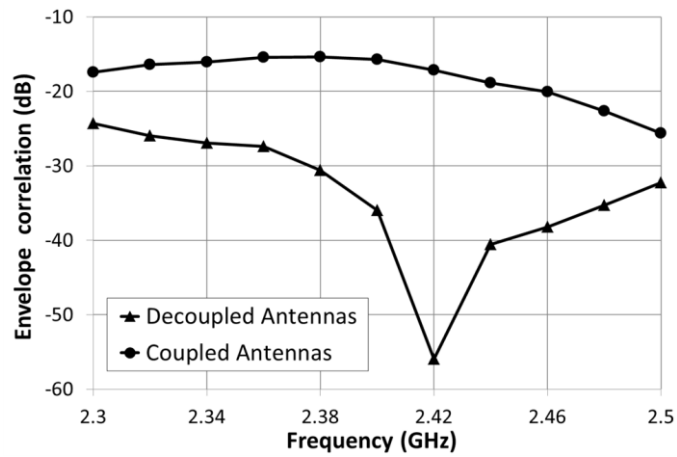
Figure 5.8 The ECCs for coupled array and the same array decoupled by an S-CRDN but with source load coupling (Fig. 2.16)
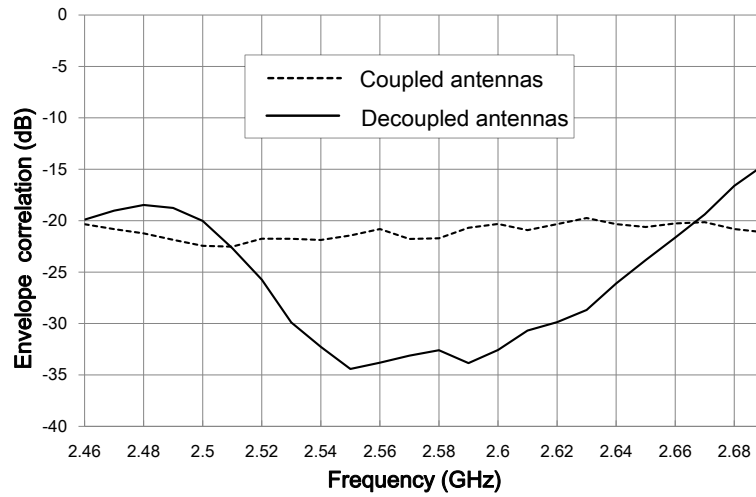
Figure 5.9 The ECCs for coupled array and the same array decoupled by a three port S-CRDN (Fig. 2.42).
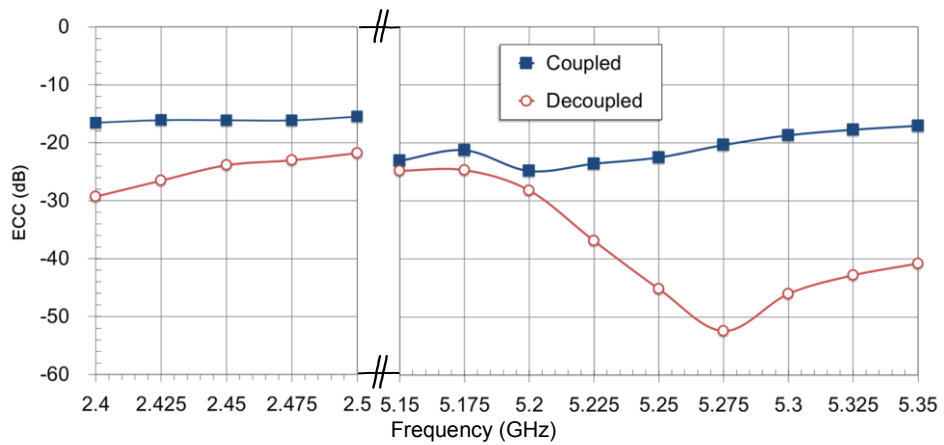
Figure 5.10 The ECCs for dual-band coupled array and the same array decoupled by a dual-band S-CRDN (Fig. 2.42).
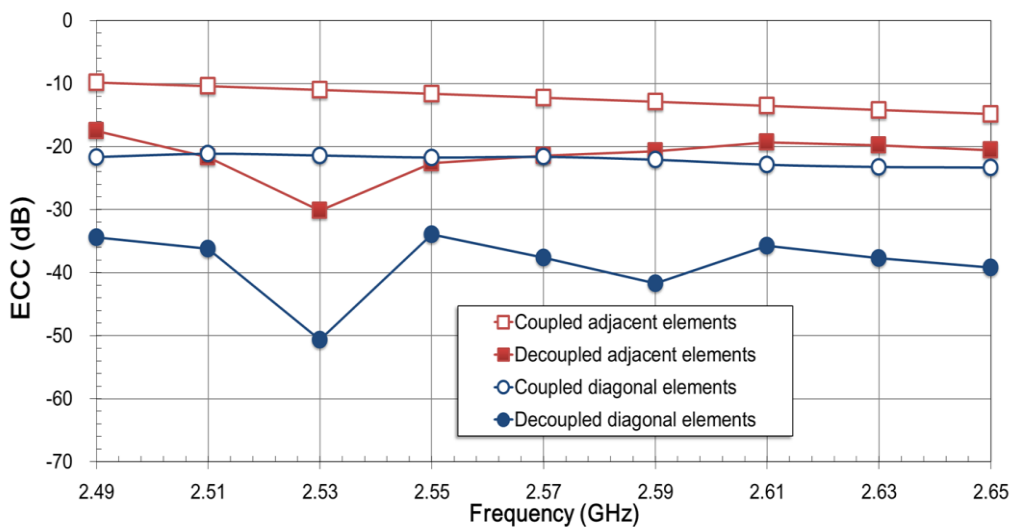
Figure 5.11 The ECCs for the cheesecake array and its coupled counterpart (Fig. 4.7).

An interpretation of the increased ECCs for Fig. 5.7 ~ Fig. 5.10 is that a CRDN increases the

183

phase differences between the two antennas by cancelling out unwanted induced currents.

5.2. Total Efficiency

For coupled antennas, when one antenna is radiating, the other antennas will act as lossy loads. Even if the antenna is well-matched, the power fed into the radiating antenna will not only radiate into free space, but also coupled to the other antennas and eventually absorbed by the matched loads of these antennas. Thus, the efficiency drop is one of the most harmful side effect of mutual couplings in a coupled array. Take the three fabricated prototypes in Fig. 5.2 as an example, the measured total efficiencies of the single antennas, coupled antennas and decoupled antennas are superposed in Fig. 5.12. The measurements are conduction in a Satimo SG-128 near field scanner. It is very clear that for coupled antennas, the total efficiency within the band of interest is around only 64%, which has a degradation of 16% compared to the single antennas. Making use of a well-designed S-CRDN, the decoupled array can improve the efficiency by around 10% as compared to the coupled array. The remaining 6% loss in total efficiency is mainly caused by the conduction and dielectric loss of the passive network. Because the two kinds of loss tend to be higher at high frequencies, the efficiency improvement for decoupled antennas will not be too significant at high bands for the dual-band CRDN case. For example, the total efficiencies of the decoupled dual-band antennas as well as its coupled counterpart are superposed in Fig. 5.13 for comparison. In the low band, the decoupled antenna pair has an improvement of around 3% ~9% in efficiency while at the high band, the improvement in total efficiency is negligible since the conduction and dielectric loss tend to be higher at the high band (5.2 GHz). Using low-loss substrate, such as RT/duroid® 5880, can improve the efficiency, especially at the high band.
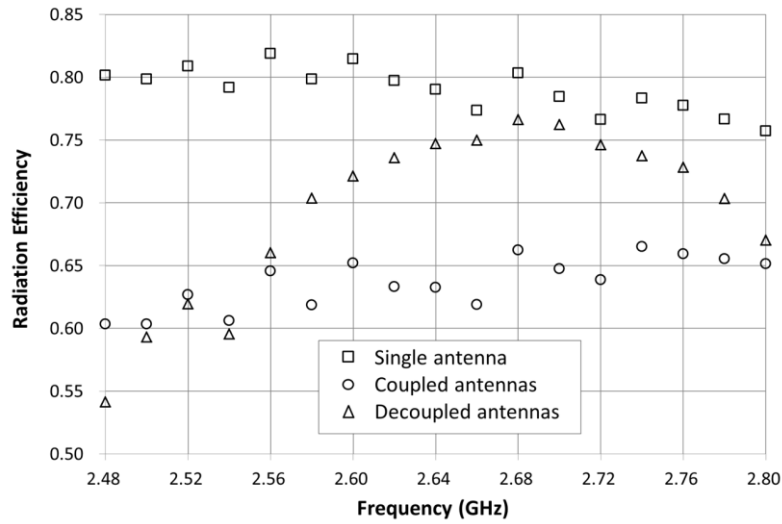
Figure 5.12 Total efficiencies of the single antenna, the coupled antennas and the decoupled antennas in Fig. 5.2.
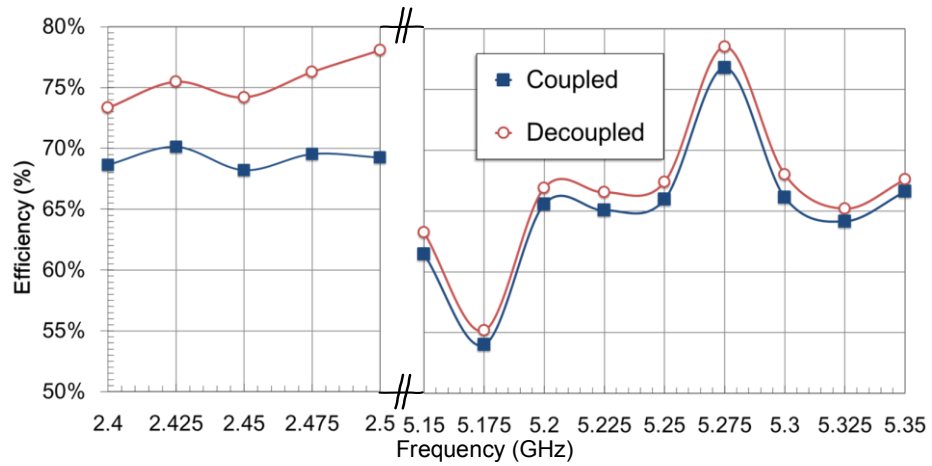
Figure 5.13 Total efficiencies of the coupled and decoupled dual-band antennas in **Section 2.4.4**.

Since the substrate used is FR-4 with relative large loss tangent with copper as the conductor, increasing the conductivity as well as reducing the loss in substrate will definitely reduce the extra loss in a CRDN. For the CRDN module implemented by LTCC technology, the efficiencies of decoupled antennas reach to more than 80%, which is quite significant as shown in Fig. 5.14.
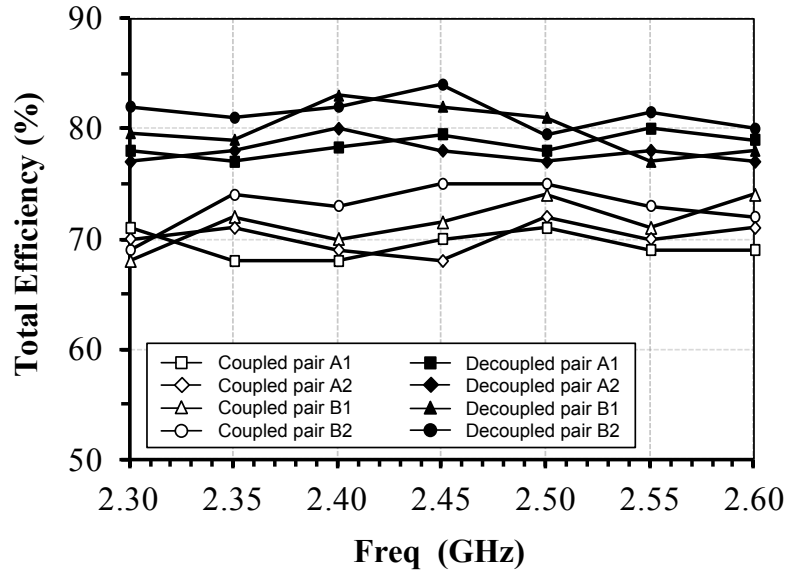
Figure 5.14 Total efficiencies of the coupled and decoupled arrays A1, A2, B1 and B2 in **Section 2.3.2**.

5.3. Channel Capacity

5.3.1 General Capacity Expression

Channel capacity was first introduced by Claude Shannon in the 1940s [19]-[21]. The capacity of a given channel *C*, is the maximum achievable data rate at which reliable communication can be performed, without any constraints on Tx and Rx complexity and coding schemes. The channel capacity is actually the fundamental limit /upper bound of a wireless communication system in a given channel [22].

For simplicity, we assume M = N in equation (1.5). Then the ideal Gaussian channel capacity is given as [23]:

$$\text{C}_{\text{ideal}} = \log_2 \left\{ det \left(\boldsymbol{I_M} + \frac{SNR}{N} \boldsymbol{H} \cdot \boldsymbol{H}^H \right) \right\} \ bps/Hz \qquad (5.23)$$

if $\boldsymbol{H} = \boldsymbol{H_w}$ is the ideal channel (I.I.D.) with the following characteristics:

$$\mathcal{E}\{[H_W]_{ij}\} = 0 \qquad (5.24a)$$

$$\mathcal{E}\left\{\left|[H_W]_{ij}\right|^2\right\} = 1 \qquad \qquad \text{(5.24b)}$$

$$\mathcal{E}\left\{[H_W]_{ij} \cdot [H_W]^*_{mn}\right\} = 0 \text{ if } i \neq m \text{ or } j \neq n \qquad \text{(5.24c)}$$

Therefore, it can be deducted that $\boldsymbol{H_w H_w^H} = \boldsymbol{I_M}$, which will lead to:

$$C_{\text{ideal}} = \log_2\left[\det\left(\boldsymbol{I_M} + \frac{SNR}{M}\boldsymbol{I_M}\right)\right] = M \cdot log_2\left(1 + SNR\right) \qquad \text{(5.25)}$$

For an ideal MIMO system, the channel capacity becomes the linear combination of eigen values of the channel matrix $\boldsymbol{H \cdot H^H}$.

5.3.2 Channel Capacity Considering Correlation and Efficiency

In reality, it is impossible to find an ideally Gaussian I.I.D. channel. There are various factors that cause the capacity to deviate from the ideal limit. One of these is correlation. As discussed in **Section 5.1.2**, the correlations for a strongly coupled antenna array can be quite large. It is well known that for correlated channels, the performance of MIMO systems will definitely deteriorate. To take the correlation into consideration when computing channel capacity from (5.23), the Kronecker model is widely used [23], [24]. The model to obtain the receiver correlation matrix, or the receiver covariance matrix is shown in Fig. 5.15.
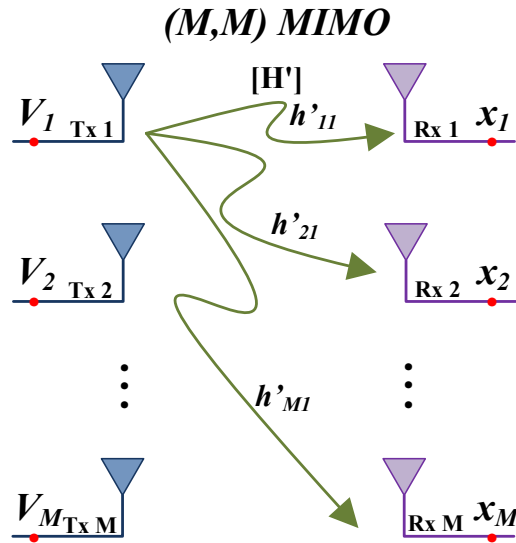
Figure 5.15 The diagram of an M by M MIMO system considering the correlation at receiver end.

The Kronecker model of the channel matrix is expressed as:

$$\mathbf{H} = \sqrt{\mathbf{R_r}} \cdot \mathbf{H_w} \cdot \sqrt{\mathbf{R_t}} \tag{5.26}$$

There are three assumptions in (5.26), they are:

(1) H_w is the independent identically distributed (I.D.D.) (spatially white) channel. All the entries of H_w are IDD complex circular symmetric Gaussian with zero mean and unit variance.

(2) R_r is the $M \times M$ receive covariance matrix and R_t is the $N \times N$ transmit covariance matrix. Both R_r and R_t are positive semi-definite Hermitian matrices. (Positive real eigenvalues and $R_r = R_r^H, R_t = R_t^H$).

(3) This relation is only valid when transmit and receive antennas are closed located and have identical radiation pattern.

According to the third assumption, if we excite any of the transmitting antenna in Fig. 5.15, the signals received at the receiver end will be identical. Then, we can define a $M \times 1$ channel matrix as:

$$H'_r = [h'_{11} \quad h'_{21} \quad \cdots \quad h'_{M1}]^T \tag{5.27}$$

The column vectors h'_{11}, h'_{21}, h'_{M1} is already defined in Fig. 5.15. Finally the covariance matrix R_r is defined as:

$$\mathbf{R_r} = \mathcal{E}\{\mathbf{H'_r} \cdot \mathbf{H'^H_r}\} = \begin{bmatrix} |h'_{11}|^2 & h'_{11} \cdot h'^*_{21} & \cdots & h'_{11} \cdot h'^*_{M1} \\ h'_{21} \cdot h'^*_{11} & |h'_{21}|^2 & \cdots & h'_{21} \cdot h'^*_{M1} \\ \vdots & \vdots & \ddots & \vdots \\ h'_{M1} \cdot h'^*_{11} & h'_{M1} \cdot h'^*_{21} & \cdots & |h'_{M1}|^2 \end{bmatrix} \tag{5.28}$$

The similar definition can apply to the covariance R_t

To be more specific, if the complex correlation between all the antenna elements in the Rx array is known, (5.28) can be expressed as:

$$\mathbf{R_r} = \begin{bmatrix} 1 & \rho_{12} & \cdots & \rho_{1M} \\ \rho_{21} & 1 & \cdots & \rho_{2M} \\ \vdots & \vdots & \ddots & \vdots \\ \rho_{M1} & \rho_{M2} & \cdots & 1 \end{bmatrix} \tag{5.29}$$

Therefore, the channel capacity considering correlation at both the Tx and Rx sides can be represented as [25]:

$$C = log_2\left\{det\left(I_M + \frac{SNR}{M}R_r^{1/2} \cdot H_w \cdot R_t \cdot H_w^H \cdot R_r^{1/2}\right)\right\} \tag{5.30}$$

Equation (5.30) is often used to evaluate the spatial fading correlation and its impact on MIMO capacity.

Meanwhile, the ideal capacity calculation assumes that all the antennas at the Tx and Rx have 100% total efficiency, which is seldom the case in reality. For lossy antennas, the SNR will be lower and the overall MIMO system performance will be affected eventually. According to [23], the impact of SNR drop caused by lossy antennas can be

included by scaling the correlation matrix as:

$$\mathbf{R}_r^{'} = \sqrt{\mathbf{\eta}_r}\mathbf{R}_r\sqrt{\mathbf{\eta}_r} \quad , \tag{5.31}$$

with

$$\mathbf{\eta}_r = diag[\eta_1,\eta_2,\cdots,\eta_M], \tag{5.32}$$

which represents the total efficiency of each elements in the receiver array. The same formulation can be deducted for antenna array at the transmitter.

The overall channel capacity considering correlation as well as total efficiency of the antenna array can be written as:

$$C = \log_2 \det\left[\mathbf{I}_N + \frac{SNR}{M}\sqrt{\mathbf{R}_t^{'}}\mathbf{H}_W\mathbf{H}_W^H\sqrt{\mathbf{R}_r^{'}}\right] \tag{5.33}$$

5.3.3 A Calculation Example

The channel capacities for the decoupled cheesecake array, its coupled counterpart in **Section 4.1.2** and an ideal 4-by-4 MIMO array are calculated using (5.33). The correlation matrix at the transmitter is defined as:

$$\mathbf{R}_t = \begin{bmatrix} 1 & \rho_{12} & \rho_{13} & \rho_{14} \\ \rho_{12} & 1 & \rho_{23} & \rho_{24} \\ \rho_{13} & \rho_{23} & 1 & \rho_{34} \\ \rho_{14} & \rho_{24} & \rho_{34} & 1 \end{bmatrix} \tag{5.34}$$

Since the cheesecake array is symmetric, $\rho_{12} = \rho_{14} = \rho_{23} = \rho_{34} = \rho_{cs}$ and $\rho_{13} = \rho_{24} = \rho_{cd}$. ρ_{cs} and ρ_{cs} are the complex correlation coefficients between the

side-by-side elements and the diagonal elements, respectively, which is shown in Fig. 5.16 (a). The efficiency for one radiating element in the cheesecake array, as well as for its counterpart shown in Fig. 5.16 (b) is also considered in the calculation. For simplicity, the receiver is assume to be uncorrelated, which means $\mathbf{R}_r = \mathbf{I}_4$. The channel capacities for the cheesecake array, the coupled array and the ideal array against SNR in dB are superposed in Fig. 5.17. The average improvement of the cheesecake array compared to its coupled counterpart is 2.01 bps/Hz at 2.51 GHz and 1.15 bps/Hz at 2.59 GHz.
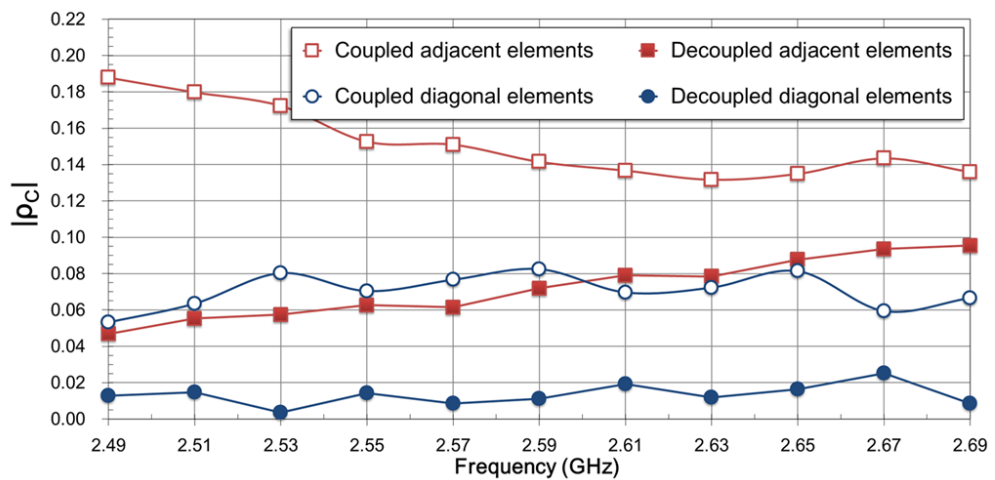
(a)
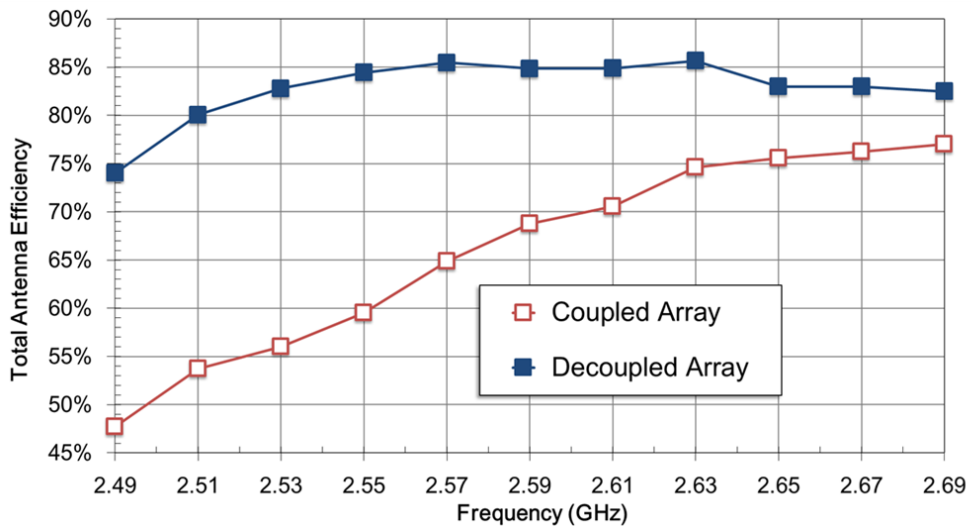
(b)

Figure 5.16 (a) Measured magnitude of complex correlations; and (b) Measured total antenna efficiencies (including reflection losses) for adjacent and diagonal radiating antenna pairs for the cheese-cake antenna array and its coupled counterpart.
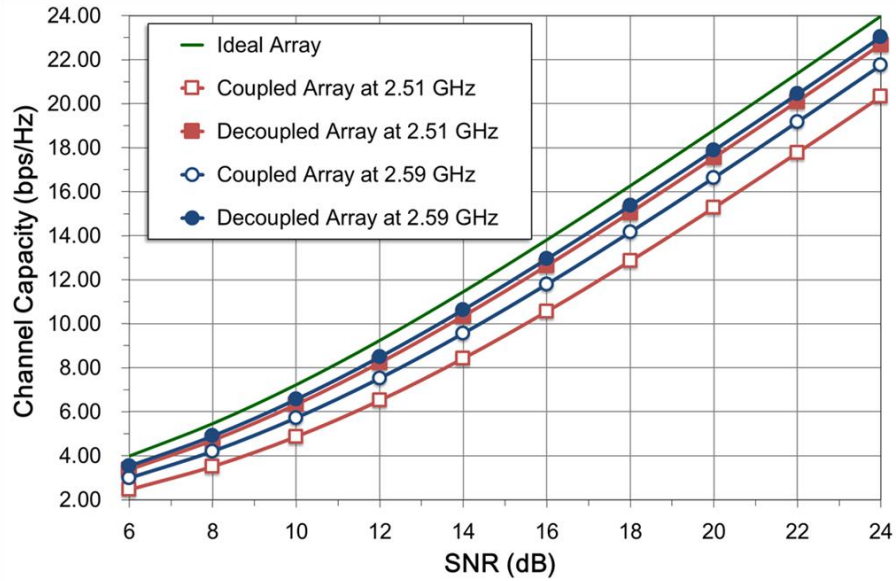
Figure 5.17 Channel capacity comparison between the cheese-cake array and its coupled counterpart and ideal MIMO array.

Following the calculation method described in this section, the channel capacities for all the   coupled and decoupled antenna arrays discussed in Chapters 2 ~ 4 can be calculated, which will not be repeated here.

5.4. Throughput

5.4.1 The concept for two-stage throughput assessment

The channel capacity only gives **an ideal tightest upper bound** on the rate of information that can be reliably transmitted over a communications channel. But to achieve that data rate with a desired probability of error might need an extremely complicated coding scheme with a very long code [22]. Throughput on the other hand, is the sum of the data rates that are successfully delivered to all terminals in a network. It is more practical to evaluate the throughput when the compact antenna array are implemented in a real-world system. According to COST Action 2100, throughput is suggested to be an important system level figure of merit [26]. However,

to assess the throughput of a MIMO system in a given multipath environment is always challenging because it depends not only on the MIMO antenna array itself, but also on *spatial and temporal characteristics* of the radio channel as well as the space-time data processing algorithm. Existing assessment techniques include the reverberation chamber testing method, the anechoic chamber with channel emulators and a two-stage evaluation method. For the first two methods, the measurement must be done after the designed multiple antenna array is implemented in a user equipment (UE), which is very difficult for antenna designers. The two-stage method can be conducted by mathematically importing measured antenna far-field patterns into a MIMO channel model with appropriate setting of a MIMO communication system. This method allows performance prediction performed at an early design stage.

In this section, the WINNER II channel model in Agilent's W1715 MIMO Channel Builder of SystemVue is used [27]. The WINNER II channel model is a geometry-based double directional stochastic channel model. The channel parameters for individual snapshots are determined stochastically, based on statistical distributions extracted from channel measurement. Antenna geometries and field patterns can be defined properly by the user of the model. Channel realizations are generated with geometrical principle by summing contributions of rays with specific small scale parameters like delay, power, Angle of Arrival (AoA) and Angel of Departure (AoD). Superposition results to correlation between antenna elements and temporal fading with geometry dependent Doppler spectrum. An illustration of the MIMO channel is given in Fig. 5.18.
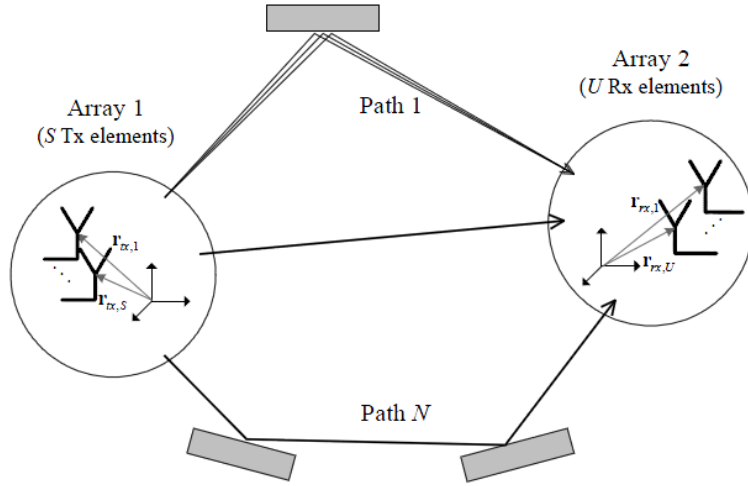
Figure 5.18 The MIMO channel model [28].

The channel transfer matrix of the MIMO channel is written as:

$$\boldsymbol{H}(t;\tau) = \sum_{n=1}^{N} \boldsymbol{H}_n(t;\tau) \tag{5.35}$$

The impulse response matrix is composed of the antenna array response matrices $\boldsymbol{F}_{tx}$ and $\boldsymbol{F}_{rx}$ for the transmitter (Tx) and the receiver (Rx) and the propagation channel response matrix $\boldsymbol{h}_n$ for cluster n as follows:

$$\boldsymbol{H}(t;\tau) = \iint \boldsymbol{F}_{rx}(\varphi)\boldsymbol{h}_n(t;\tau;\phi;\varphi)\,\boldsymbol{F}_{rx}^T(\phi)\,d\phi\,d\varphi \tag{5.36}$$

The channel from the Tx antenna element s to the Rx element u, for cluster n, is expressed as [29]:

$$
\begin{aligned}
\mathrm{H}_{u,s,n}(t;\tau) = \sum_{n=1}^{N} &\begin{bmatrix} F_{rx,u,V}(\varphi_{n,m}) \\ F_{rx,u,H}(\varphi_{n,m}) \end{bmatrix}^T \begin{bmatrix} \alpha_{n,m,VV} & \alpha_{n,m,VH} \\ \alpha_{n,m,HV} & \alpha_{n,m,HH} \end{bmatrix} \begin{bmatrix} F_{tx,s,V}(\phi_{n,m}) \\ F_{tx,s,H}(\phi_{n,m}) \end{bmatrix} \\
&\times \exp\left(j2\pi\lambda_0^{-1}\left(\overline{\varphi}_{n,m}\cdot\overline{r}_{rx,u}\right)\right) \exp\left(j2\pi\lambda_0^{-1}\left(\overline{\phi}_{n,m}\cdot\overline{r}_{tx,s}\right)\right) \\
&\times \exp(j2\pi\upsilon_{n,m}t)\delta(\tau-\tau_{n,m})
\end{aligned}
\tag{5.37}
$$

where

➢ $F_{rx,u,V}$ and $F_{rx,u,H}$ are the antenna element u field patterns for vertical and

194

horizontal polarizations, respectively;

- $\alpha_{n,m,VV}$ and $\alpha_{n,m,VH}$ are the complex gains of vertical-to-vertical and horizontal-to-vertical polarizations of ray n, m, respectively;

- λ_0 is the wavelength of the carrier frequency;

- $\overline{\phi}_{n,m}$ is the AoD unit vector;

- $\overline{\varphi}_{n,m}$ is the AoA unit vector;

- $\overline{r}_{tx,s}$, and $\overline{r}_{rx,u}$, are the location vectors of element s and u, respectively; and

- $v_{n,m}$ is the Doppler frequency component of ray n, m.

A configuration for evaluating MIMO antenna array using different channel models in SystemVue is shown in Fig. 5.19. The Tx and Rx are ideal LTE transmitter and receivers. The two signal streams coming out of LTE Tx will be modulated and sent to the MIMO channel model block, where appropriate parameters of the channel can be configured. Then the signals are received, demodulated and decoded by the Rx. By comparing the signals at the Tx end and Rx end, the system throughput and block error rate can be obtained.

The LTE-Advanced channel model is also available. Similarly, this model implements a MIMO channel model for mobile wireless applications and follows the definition in LTE-A channel model which is compatible with IMT-A channel model. The generic LTE-A channel models follow ray-based channel modeling approach. Channel realizations are generated by summing contributions of rays with specific channel parameters like delay, power, angle-of-arrival and angle-of-departure. The channel parameters are determined stochastically, based on statistical distributions extracted from channel measurement [30].

In this thesis, all the patterns for coupled and decoupled array are first measured in the chamber, then, after converted to a proper format, they are included in the MIMO channel model to accomplish the throughput calculation.
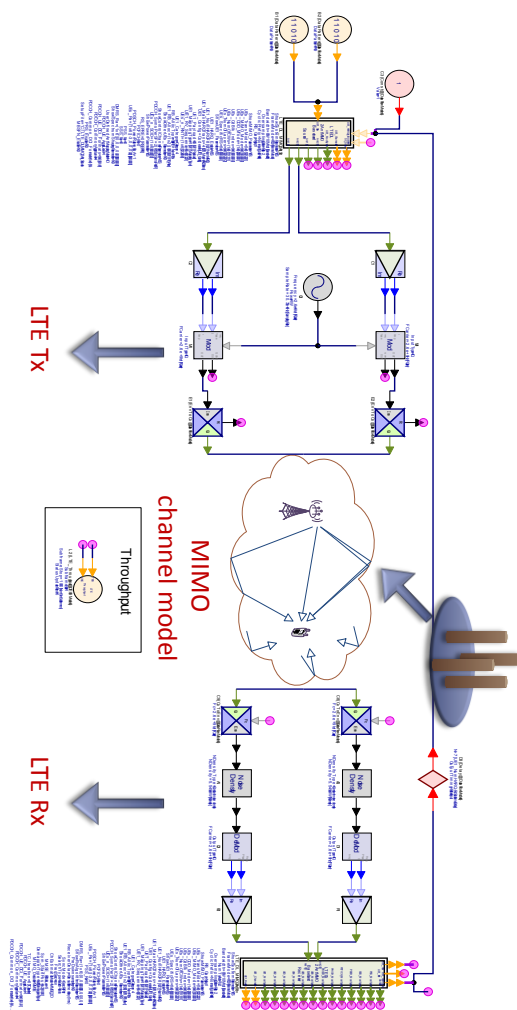
Figure 5.19 The configuration for MIMO antenna performance evaluation in SystemVue.

5.4.2 A Throughput Calculation Example

The throughput for the decoupled cheesecake array and coupled counterpart in **Section 4.1.2** are calculated using SystemVue. The channel model of LTE-A Indoor Hotspot (InH) and Urban Micro (UMi) scenario without line of sight component is used in this example. The indoor hotspot scenario consists of one floor of a building. The height of the floor is 6 m with the transmitter mounted on the ceiling. The floor contains 16 rooms of 15 m × 15 m and a long hall of 120 m × 20 m. The transmitter and

196

receiver are placed in the middle of the hall at 30 m and 90 m with respect to the left side of the building. In urban micro-cell scenario the height of both the antenna at the base station and that at the user terminal is assumed to be well below the tops of surrounding buildings. Both antennas are assumed to be outdoors in an area where streets are laid out in a Manhattan-like grid. [31]. The downlink receiver is assumed to use ideal four-element linear array of omnidirectional elements with one wavelength spacing between each other and the cheese-cake array as well as its coupled counterpart at the transmitter is placed vertically ($\theta = 90^{\circ}$ case) facing to the broadside of the receiver array. Due to the symmetry of the arrays, only $\varphi = 90^{\circ}$ azimuth orientation angle is considered. The patterns of cheese-cake antenna as well as its counterpart are imported from measured far-field results at three frequencies (2.51 GHz, 2.59 GHz and 2.69 GHz). Both of vertical and horizontal polarizations are considered. Other parameters remain to be the default values. The average data throughput fractions of the decoupled and coupled array, which is the normalized throughput with respect to the maximum achievable throughput, and which are average values of the three frequencies, are superposed in Fig. 5.20. It is seen that in the InH scenario, the cheese-cake array demonstrates significant improvement in both poor SNR and medium SNR scenarios, while in UMi scenario, less improvement is observed.
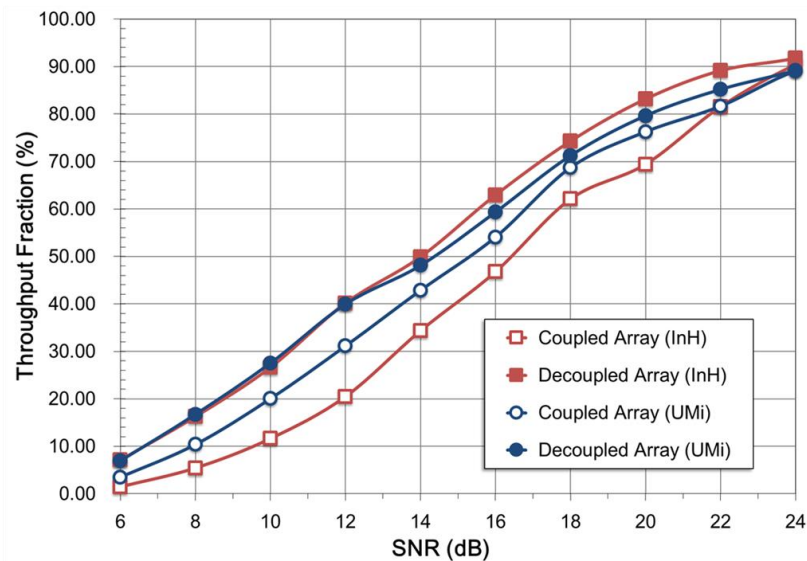
Figure 5.20 Throughput comparison between the cheese-cake array and its coupled counterpart.

5.5. Human interference

For portable devices, such as mobile phones and tablets, the human interference is a major issue to be considered in reality. To have a thorough insight on the physical mechanism of the S-CRDN as well as its performance in mobile terminal applications, several figures of merit such as isolation, radiation patterns and efficiencies, ECC and throughput are investigated in free space and with hand phantom in this section. The SPEAG hand phantoms for mono-block phones SHO V2RB/LB is used as shown in Fig. 5.21 [32]. Four pairs of antennas are compared, including the symmetrical coupled cone-shaped antennas (Pair A), the same antennas decoupled by lumped elements using the same procedure in [33] (Pair B), the same antennas decoupled by an all pole S-CRDN using the method in Section 2.1.2 with a wide band isolation of 20 dB (Pair C, CRDN1) and the same antennas decoupled by a CRDN with a normal band isolation of 30 dB (Pair D, CRDN2), which are also shown in Fig. 5.21. The radiation characteristics of the four pairs of antenna arrays with and without hand phantom are measured using the SATIMO SG128 spherical near-field scanner [5].

(a)

(b)

Radio Frequency Radiation Research Laboratory
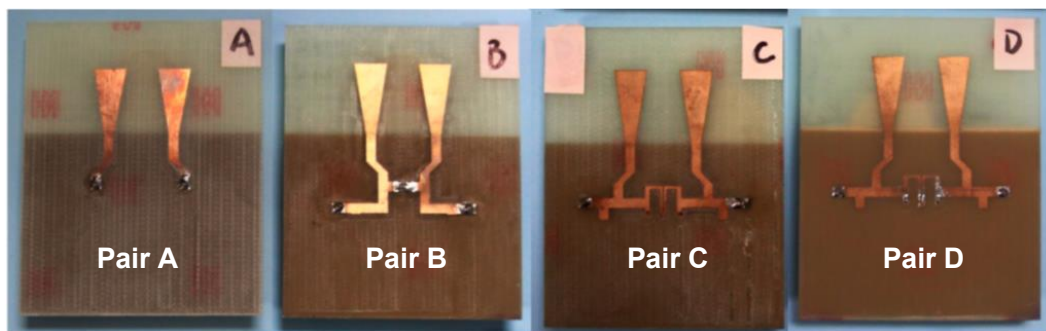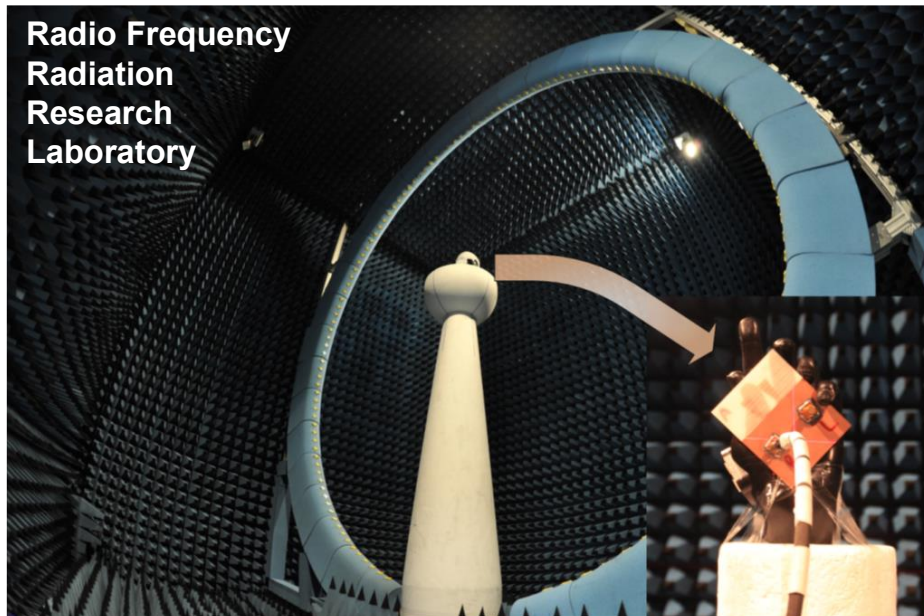
(c)

Figure 5.21 (a) Four pairs of antennas under investigation. (b) Hand phantoms and arrangement.
(c) Radiation characteristic measurements setup.

5.5.1. Matching and Isolation

The reflection and isolation coefficients of antenna pairs A, B, C, and D with and without the presence of the hand phantom are examined and the results are displayed in Fig. 5.22. Since the hand phantom acts as a lossy dielectric medium in close proximity of the antennas, the resonant frequency of all the antenna pairs shifts to a

lower value. However, the impact of the hand phantom on the isolation for the four antenna pairs seems to be quite different. For antenna pairs B, C and D, the isolation increases in certain frequencies while it decreases in other frequencies due to the detuning of resonance frequencies. Nevertheless, both pairs C and D achieve 20 dB isolation with a frequency band that is as wide as more than three times of that of pair B, with and without the presence of a hand phantom.
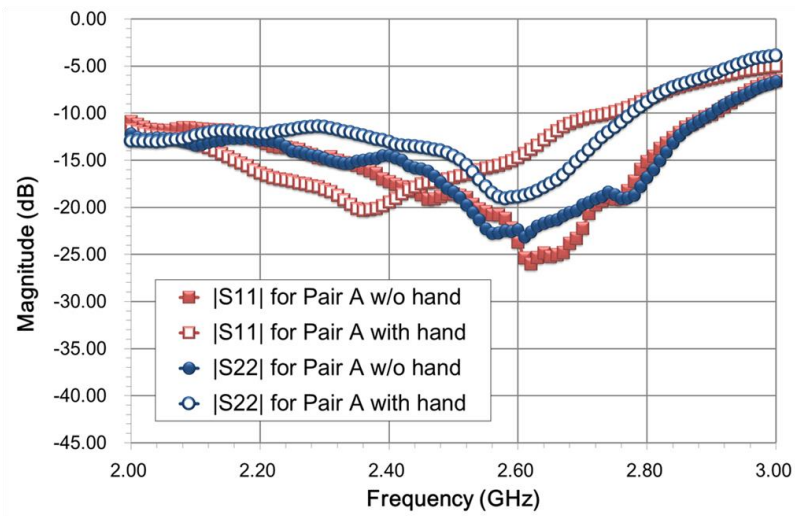
(a)
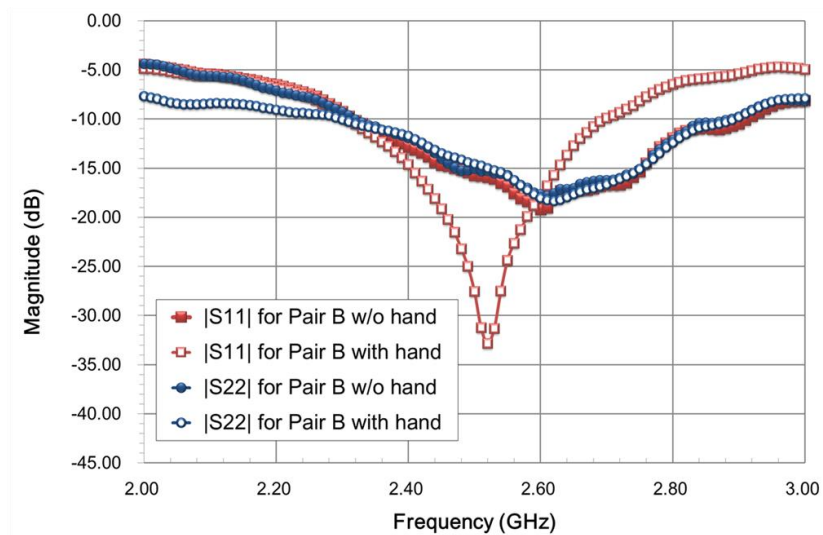
(b)
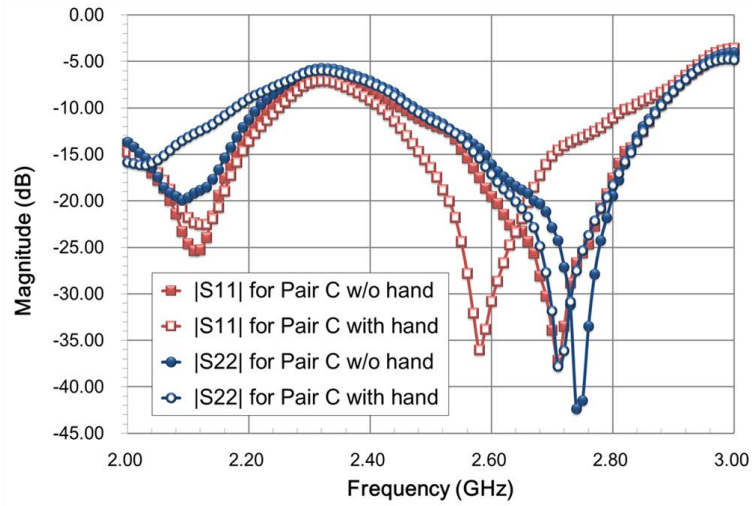
(c)
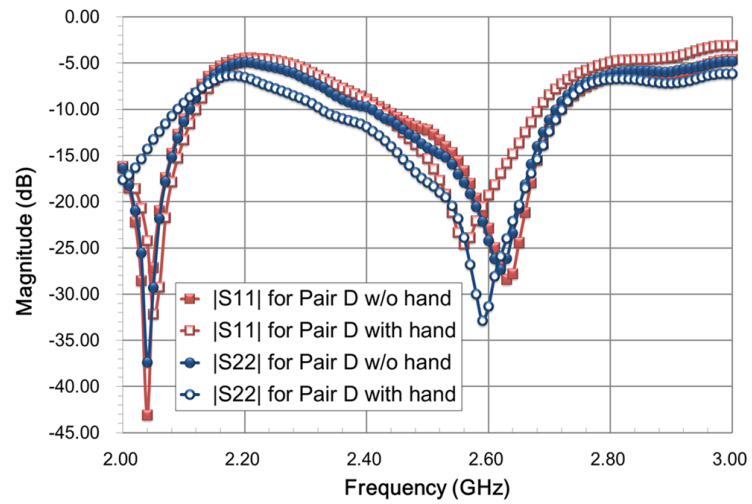
(d)
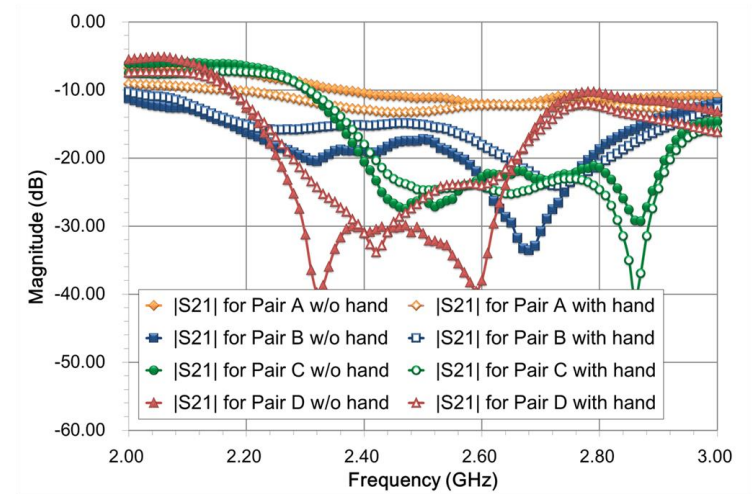
(e)

Figure 5.22 Measured return loss for (a) antenna pair A, (b) antenna pair B, (c) antenna pair C and (d) antenna pair D. (e) Measured isolation for antenna pairs A, B, C, and D.

5.5.2. Total Efficiency

The total efficiencies of the antenna pairs are shown in Fig. 5.23. Under the free-space condition, the total efficiency for the coupled array (Pair A) is no more than 73% from 2.4 GHz to 2.7 GHz, whereas for the decoupled array (Pair B), the efficiency is around 76% for the same band. For Pair C and Pair D using CRDNs, the typical efficiency has improved to 78% and 83%, respectively. Further improvements in efficiency can be expected if substrate with lower loss is used. Due to the lossy nature of the hand phantom, the total efficiencies for all the four pairs of arrays have a huge degradation when the hand phantom is presented. Nevertheless, the Pair D still shows a significant efficiency improvement from 17% to 26% as compared to Pair A.
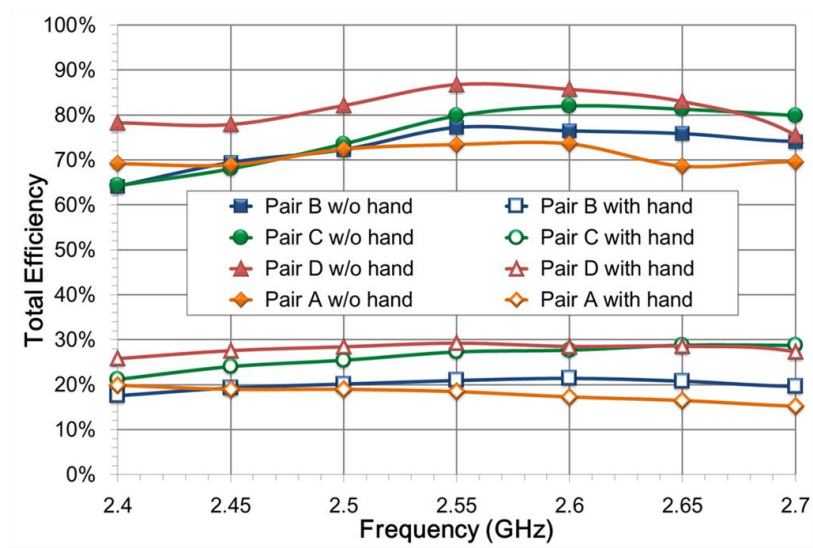
Figure 5.23 Total efficiencies of four antenna pairs. (The efficiencies are averaged values of the two antennas for each pair.)

5.5.3. Envelope Correlation Coefficients (ECC)

The power patterns of the coupled array (Pair A) and one of the decoupled arrays (Pair C) are shown in Fig. 5.24. In the measurements, one of the antennas is excited

while the other one is terminated by a 50 Ω load. Using the measured far-field vector phasor radiation patterns, the ECC of the each antenna pairs can be calculated by the method introduced in **Section 5.1.2**. It is known that a lower envelope correlation leads to a higher channel capacity and a better diversity gain. For the decoupled antenna Pairs B, C, and D under the free space condition, an improvement in ECC from around 0.05 to smaller than 0.01 is seen in Fig. 5.25. But for the cases with the hand phantom, a much higher ECC is obtained for all the four pairs. This phenomenon is consistent with the discovery in [2]. For Pair A, the ECC increases to 0.17 ~ 0.27 within the band of interest. Although the ECCs for Pair B, C, and D are also increased, the ECC for Pair D is below 0.025 from 2.4 GHz to 2.7 GHz due to its wide band decoupling attribute.
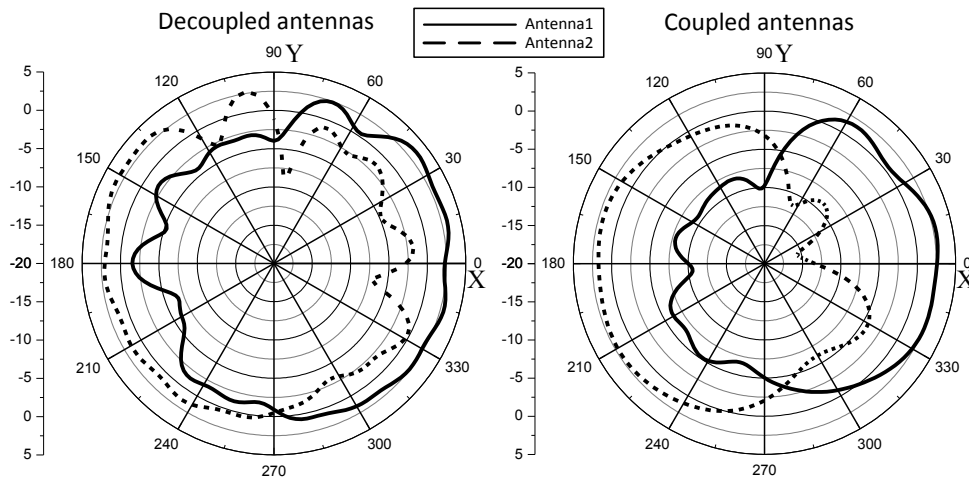
Figure 5.24 Radiation patterns of the decoupled array-Pair C and the coupled array-Pair A in the xoy plane at 2.6 GHz.
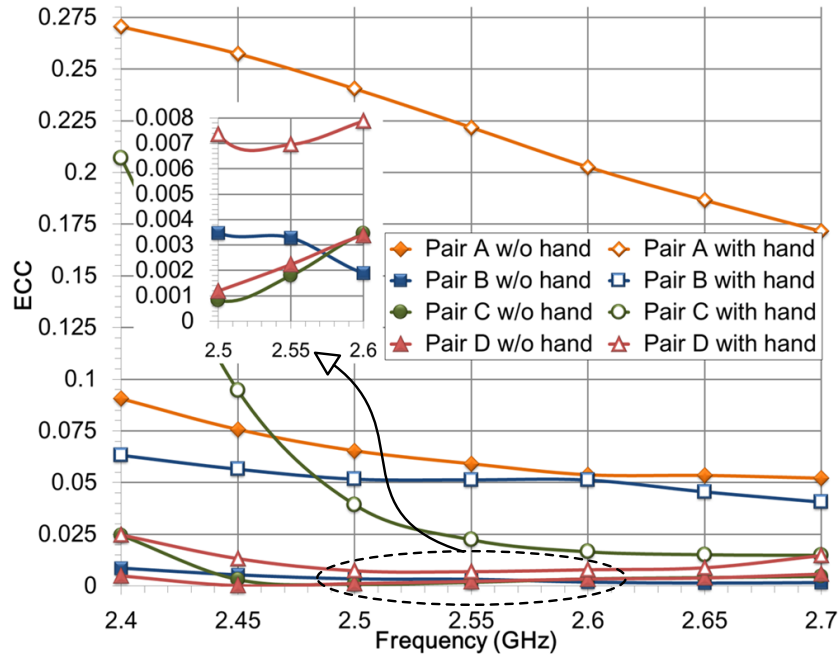
Figure 5.25 Calculated envelope correlation coefficients for the four antenna pairs.

5.5.4. Channel Capacity and Throughput

The channel capacities for an ideal 2-by-2 MIMO system using these four antenna arrays under different SNRs are calculated and are superposed in Fig. 5.26. The channel capacity calculation follows the method given in **Section 5.3**, which takes the antenna array efficiency and correlation into account. The transmitter antennas are assumed to be uncorrelated while all the arrays under investigation are placed at the receiver end. A larger enhancement of channel capacity is observed for cases having a hand phantom. An averaged improvement of around 1 bps/Hz is observed for Pair C and D as compared to Pair A.

The throughputs of the four arrays are also investigated using the method discussed in **Section 5.4**.The channel scenario B1 (Urban Micro-cell) is used in the throughput comparison of the four antenna pairs. The downlink transmitter is assumed to use a two-element linear array with omni-directional elements and half-wavelength spacing. The four antenna pairs under investigation are placed horizontally ($\theta = 0^{\circ}$) at the receiver, facing the transmitter array in the broadside direction. The patterns of

the antenna pairs are imported from measured results at 2.6 GHz. Other parameters are set to be the default values in the model. The fractional data throughputs, which are normalized with respect to their corresponding maximum achievable values, are superposed in Fig. 5.27.
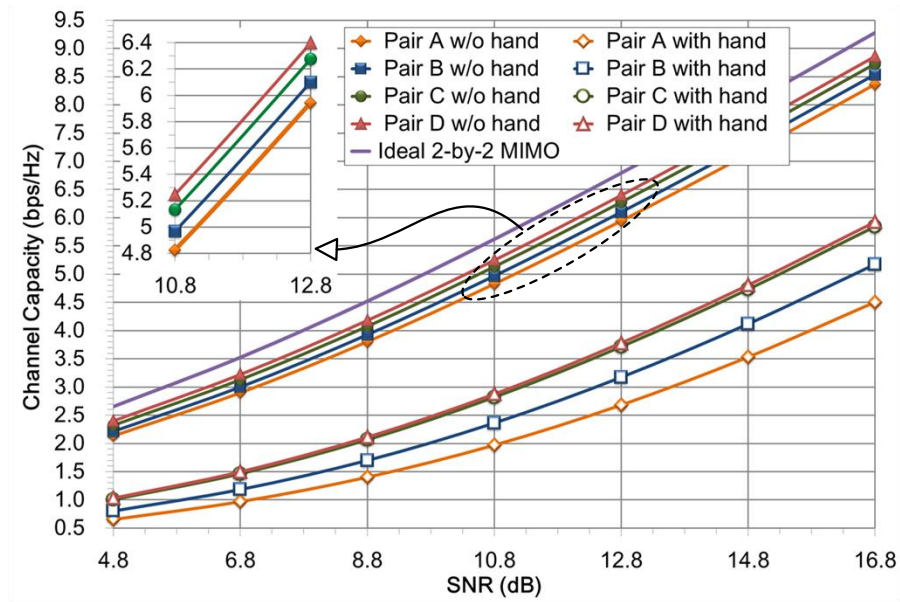
Figure 5.26 Channel capacity for the four antenna arrays together with an ideal 2-by-2 MIMO array.
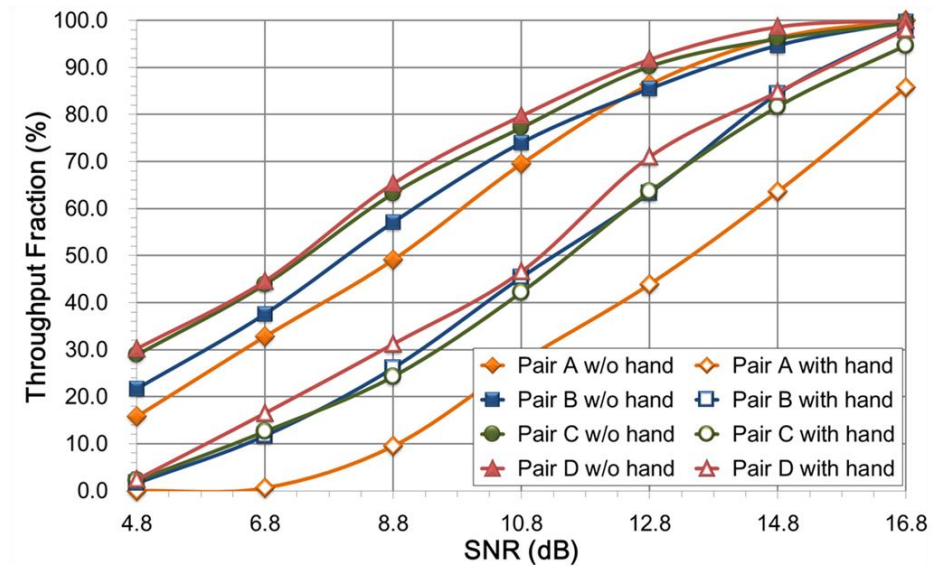
Figure 5.27 Throughput fraction for the four antenna pairs without and with hand phantom in WINNER II channel model B1.

5.6. Reference

[1] M. Okoniewski, M.A. Stuchly, "A study of the handset antenna and human body interaction," *IEEE Trans. Microw. Theory Tech.*, vol.44, no.10, pp.1855-1864, Oct 1996.

[2] M. Pelosi, M. B. Knudsen, and G. F. Pedersen, "Multiple antenna systems with inherently decoupled radiators," *IEEE Trans. Antennas Propag.*, vol. 60, pp. 503–515, Feb. 2012.

[3] B. Yanakiev, J. O. Nielsen, M. Christensen, G. F. Pedersen, "On Small Terminal Antenna Correlation and Impact on MIMO Channel Capacity," *IEEE Trans. Antennas Propag.*, vol.60, no.2, pp.689-699, Feb. 2012.

[4] J. O. Nielsen, B. Yanakiev, I. B. Bonev, M. Christensen, G. F. Pedersen, "User Influence on MIMO Channel Capacity for Handsets in Data Mode Operation," *IEEE Trans. Antennas Propag.*, vol.60, no.2, pp.633-643, Feb. 2012.

[5] [Online]. Available: http://www.satimo.com/

[6] CHIAU C.C.: 'Study of the diversity antenna array for the MIMO wireless communication systems'. PhD thesis, Department of Electric Engineering, Queen Mary, University of London UK, April 2006.

[7] G.F. Pedersen, J. Bach Andersen, "Handset antennas for mobile communications, integration, diversity and performance", *URSI Review of Radio Science*, pp. 119-139, 1996.

[8] M. Schwartz, W. R. Bennet and S. Stein, "Communication systems and techniques", McGraw Hill, 1996.

[9] R. G. Vaughan and J. B. Andersen, "Antenna diversity in mobile communications," *IEEE Trans. Veh. Technol.*, vol. VT-36, pp. 147–172, Nov. 1987.

[10] C. A. Balanis, Antenna Theory: Analysis and Design. New York: Wiley, 2005.

[11] R. E. Collin and F. J. Zucker, Antenna Theory: Part 1. New York: McGraw-Hill, 1969.

[12] T. K. Sarkar, M. Salazar-Palma, and E. L. Mokole, Physics of Multiantenna

Systems and Broadband Processing. Hoboken, NJ: Wiley, 2008.

[13] M. A. Jensen and J. W.Wallace, "A review of antennas and propagation for MIMO wireless communications," *IEEE Trans. Antennas Propag.*, vol., 52, no. 11, pp. 2810–2824, Nov. 2004

[14] R.H. Clarke, "A Statistical Theory of Mobile Radio Reception", Bell System Technical Journal, pp. 957-1000, 1966.

[15] W. C. Y. Lee, Mobile Communications Engineering: Theory and Applications, Second Edition. McGraw-Hill, 1998.

[16] S. Blanch, J. Romeu, I. Corbella, "Exact representation of antenna system diversity performance from input parameter description," *Electronics Lett.*, vol.39, no.9, pp.705-707, May, 2003.

[17] P. Hallbjorner, "The significance of radiation efficiencies when using S-parameters to calculate the received signal correlation from two antennas," *IEEE Antennas Wireless Propag. Lett.*, vol.4, no., pp.97-99, 2005.

[18] C. G. Montgomery, R. H. Dicke and E. M. Purcell, "*Principles of Microwave Circuits*," Vol. 8, Rad. Lab. Series, McGraw-Hill, New York, 1948.

[19] C. Shannon, "A mathematical theory of communication," *Bell Sys. Tech. J.*, pp. 379－423, 623－656, 1948.

[20] C. Shannon, "Communications in the presence of noise," in *Proceedings of IRE*, pp. 10－21, 1949.

[21] C. Shannon and W. Weaver, *The Mathematical Theory of Communication*. Univ. Illinois Press, 1949.

[22] E. Biglieri, R. Calderbank, A. Costantinides, A. Goldsmith, A. Paulraj, and H. Poor, MIMO Wireless Communications. Cambridge, U.K.: Cambridge Univ. Press, 2007.

[23] J. X. Yun and R. G. Vaughan, "Multiple element antenna efficiency and impact on diversity and capacity," *IEEE Trans. Antennas Propag.,* vol. 60, no. 2, pt. I, pp. 529–539, Feb. 2012.

[24] D. Chizhik, F. Rashid-Farrokhi, J. Ling, and A. Lozano, "Effect of antenna separation on the capacity of BLAST in correlated channels," *IEEE Commun.*

Lett., vol. 4, no. 11, pp. 337–339, Nov. 2000.

[25] A. Paulraj, R. Nabar, and D. Gore, *Introduction to Space–Time Wireless Communications*. Cambridge, U.K.: Cambridge Univ. Press, 2003.

[26] R. Verdone and A. Zanella, eds. *Pervasive Mobile and Ambient Wireless Communications: COST Action 2100*. Springer, 2012.

[27] SystemVue Electronic System-Level (ESL) Design Software, Version 2013.01, Agilent Technologies, Inc., Santa Clara, CA.

[28] WINNER II, D1.1.2, "WINNER II Channel Models part I: Channel Models," Tech. Rep., Sept. 2007.

[29] Agilent Application Note, "Accounting for Antenna and MIMO channel effects using Agilent SystemVue," September 2010, 5990-6535EN.

[30] M. Rumney, *LTE and the Evolution to 4G Wireless: Design and Measurement Challenges*, 2nd ed., Wiley, 2013.

[31] "Guidelines for evaluation of radio interface technologies for IMT-Advanced," ITU, Tech. Rep., 2009.

[32] [Online]. Available: http://www.speag.com/

[33] S. Chang, Y. –S. Wang, and S. –J. Chung, "A decoupling technique for increasing the port isolation between strongly coupled antennas," *IEEE Trans. Antennas Propag.* vol. 56, no. 12, pp. 3650-3658, Dec. 2008.

Chapter 6

Concluding Remarks

6.1. Summary

This dissertation is dedicated to various antenna decoupling problems by taking advantages of modern network synthesis, analysis and model extraction techniques. Instead of solving antenna problem intuitively by yielding some ad-hoc and antenna dependent solutions, this thesis has proposed complete theory and practical design procedures for S-CRDN, C-CRDN and dummy array types of decoupling methods.

The S-CRDNs offer a high order decoupling solution as compared to the existing neutralization line and lumped element decoupling schemes. The trade-off between decoupling bandwidth and isolation level can be achieved. It is very suitable for the use in mobile terminals where a compact device is needed without very high Q factor. More importantly, it can be extended to multi-band and multi-element decoupling problems straightforwardly.

Using multiport coupled resonators for decoupling purpose is proposed for the first time. It is a brand new microwave network strategically designed for antenna decoupling problem. It totally changed the "common sense" that coupled resonators are used for designing filters that is a two-port network for most of the time.

The concept of decoupling two coupled antennas with a dummy element is not new, but in this thesis, a general theory of doing so for high number of antenna

element arrays is given for the first time. It has no limitation on array size, antenna form factor and element number. It can be extended to solve a much larger antenna array, say the massive MIMO array for example.

As the antenna interference becomes more and more severe in today's size constrained wireless systems, the proposed theories, methods and components will find numerous applications today and in the near future.

6.2. Future Work

Despite the above-mentioned researches that had been done by the author, there are still more to explore. Possible extensions include:

(1) Implementing the S-CRDN with more advanced techniques, such as Integrated Passive Device (IPD) on silicon.

(2) Broadband decoupling solutions covering around 100% FBW, which is quite useful for mobile terminal applications, which normally occupy 1.7 GHz ~ 2.7 GHz.

(3) Finding a complete synthesis theory on C-CRDNs with various coupling topologies.

(4) Implementing the proposed prototype networks into a real mobile terminal and investigate the MIMO OTA performances.

(5) Extending the proposed dummy array decoupling problems to the applications of massive MIMO with more than 100 antennas.

Appendix

A1. The Low-pass ladder network and its dual-network.

1. The lowpass ladder networks
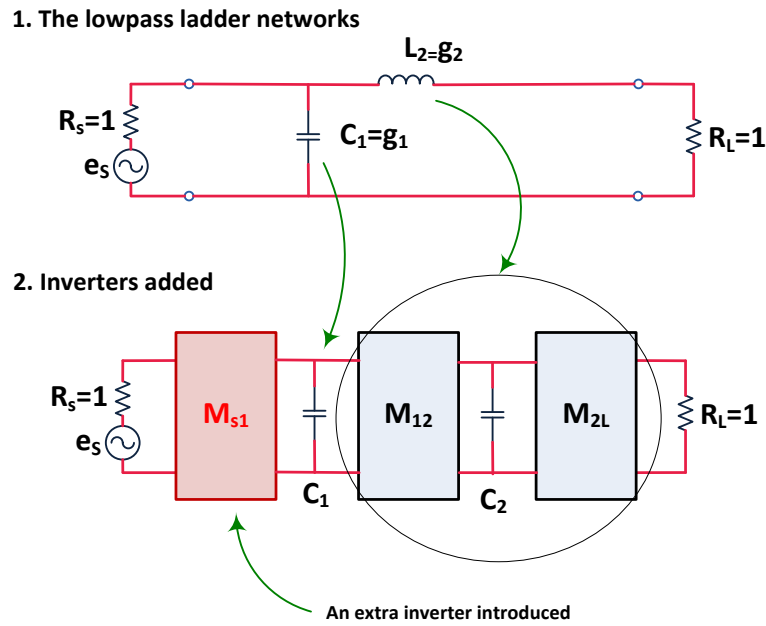
Fig. A1 The comparison between a lowpass ladder network and a low pass prototype circuit model with inverters.

It can be seen in Fig. A1 that an extra inverter M_{s1} is introduced when converting the low-pass prototype circuit into its dual-network.

The ABCD parameter of circuit 1 is given by:

$$\begin{bmatrix} 1 & 0 \\ sC_1 & 1 \end{bmatrix} \cdot \begin{bmatrix} 1 & sL_1 \\ 0 & 1 \end{bmatrix} = \begin{bmatrix} 1 & sL_1 \\ sC_1 & L_1C_1s^2 + 1 \end{bmatrix}$$

$$y_{21} = \frac{-1}{sL_1} = \frac{even}{odd}$$

The ABCD parameter of circuit 2 is given by: ($C_2 = L_2$)

$$j \begin{bmatrix} 0 & 1 \\ 1 & 0 \end{bmatrix} \cdot \begin{bmatrix} 1 & 0 \\ sC_1 & 1 \end{bmatrix} \cdot j \begin{bmatrix} 0 & 1 \\ 1 & 0 \end{bmatrix} \cdot \begin{bmatrix} 1 & 0 \\ sC_2 & 1 \end{bmatrix} \cdot j \begin{bmatrix} 0 & 1 \\ 1 & 0 \end{bmatrix} = j \begin{bmatrix} 0 & 1 \\ 1 & 0 \end{bmatrix} \cdot \begin{bmatrix} 1 & sL_1 \\ sC_1 & L_1C_1s^2 + 1 \end{bmatrix}$$

$$= j \begin{bmatrix} sC_1 & L_1C_1s^2 + 1 \\ 1 & sL_1 \end{bmatrix}$$

The extra inverter M$_{s1}$ change the position of B and D of the ABCD matrix for circuit 1, now we have:

$$y_{21}' = \frac{-1}{L_1C_1s^2 + 1} = \frac{even}{even}$$

Therefore, it is completely fine if the polynomial $Y_{21}^F(s)$ is not the quotient of odd to even or even to odd polynomials. Meanwhile, if we consider frequency-invariant reactances (FIRs) in the filter prototype, the polynomial $Y_{21}^F(s)$ is also not the quotient of odd to even or even to odd polynomials.

A2. Positive Real Functions

According to [1], the positive real functions should have the following properties:

1. The coefficients of the numerator and denominator polynomials in $Y(s) = p(s)/q(s)$ are real and positive, as a consequence:

(a) $Y(s)$ is real when s is real.

(b) Complex poles and zeroes of $Y(s)$ occur in conjugate pairs.

(c) The ratio of the coefficients of the highest order of the numerator and the denominator is real and positive.

2. Poles of $Y(s)$ on the imaginary axis must be simple and their residues must be positive and real.

3. The degrees of numerator and denominator polynomials in $Y(s)$ differs at most by 1; Thus the number of finite poles and finite zeroes of $Y(s)$ differ at most by 1.

Reference:

[1] M. E. van Valkenburg, Network Analysis, Prentice-Hall, Englewood Cliffs, NJ, 1955.

A3. Matrix Rotation to a full matrix topology

The full matrix can be obtained from matrix similarity transformation, with a $N \times N$ rotation matrix $[R]$:

$$[R] = \begin{bmatrix} 1 & 0 & \cdots & 0 & 0 \\ 0 & c_r & 0 & -s_r & 0 \\ \vdots & 0 & 1 & 0 & \vdots \\ 0 & s_r & 0 & c_r & 0 \\ 0 & 0 & \cdots & 0 & 1 \end{bmatrix}$$

With: $c_r = \cos \theta_r$ and $s_r = \sin \theta_r$

For the N=2 case shown in the figure below:

We only need elements in rows and columns 2,3 to be changed by the transformation process, therefore, we choose pivot [2,3]. Other elements will remain the same after the transformation.

The element $[M_3]_{24} = b'$ has the following relation with the rotation matrix and the matrix $[M_1]$:

$$[M_3]_{24} = c_r \cdot [M_1]_{24} - s_r \cdot [M_1]_{34}$$

Also, the element $[M_3]_{13} = b'$ can be represented as:

$$[M_3]_{13} = s_r \cdot [M_1]_{12} + c_r \cdot [M_1]_{13}$$

Therefore, we have:

$$c_r \cdot [M_1]_{24} - s_r \cdot [M_1]_{34} = s_r \cdot [M_1]_{12} + c_r \cdot [M_1]_{13}$$

Or:

$$c_r \cdot a - s_r \cdot b = s_r \cdot a + c_r \cdot (-b)$$

We can conclude that:

$$s_r = sin\,\theta_r = c_r = cos\,\theta_r$$

and

$$\theta_r = \frac{\pi}{4}$$

Similarly:

$$s_r \cdot [M_1]_{24} + c_r \cdot [M_1]_{34} = c_r \cdot [M_1]_{12} - s_r \cdot [M_1]_{13} = a'$$

or:

$$s_r \cdot a + c_r \cdot b = c_r \cdot a - s_r \cdot (-b) = a'$$

$\theta_r = \frac{\pi}{4}$ will also satisfy this equation.

For the diagonal elements:

$$\begin{cases} [M_3]_{22} = c_r^2 \cdot [M_1]_{22} - 2s_r c_r \cdot [M_1]_{23} + s_r^2 \cdot [M_1]_{33} \\ [M_3]_{33} = s_r^2 \cdot [M_1]_{22} + 2s_r c_r \cdot [M_1]_{23} + c_r^2 \cdot [M_1]_{33} \end{cases}$$

with:

$$\begin{cases} [M_1]_{22} = p_1 \\ [M_1]_{23} = 0 \\ [M_1]_{33} = p_2 \end{cases}$$

We have:

$$c_r^2 \cdot p_1 + s_r^2 \cdot p_2 = [M_3]_{22} = [M_3]_{33} = s_r^2 \cdot p_1 + c_r^2 \cdot p_2$$

$\theta_r = \frac{\pi}{4}$ will also satisfy this equation.

Therefore, if the rotation matrix is defined as following:

$$[R] = \begin{bmatrix} 1 & 0 & 0 & 0 \\ 0 & cos\left(\frac{\pi}{4}\right) & -sin\left(\frac{\pi}{4}\right) & 0 \\ 0 & sin\left(\frac{\pi}{4}\right) & cos\left(\frac{\pi}{4}\right) & 0 \\ 0 & 0 & 0 & 1 \end{bmatrix}$$

We will have:

$$[M_3]_{full} = [R] \cdot [M_1]_{trans} \cdot [R]^t = \begin{bmatrix} 0 & a' & b' & k \\ a' & p & c & b' \\ b' & c & p & a' \\ k & b' & a' & 0 \end{bmatrix}$$

which is symmetric with respect to the principal diagonal as well as the anti-diagonal.

The element $[M_1]_{23}$ will also be changed during the transformation:

$$[M_3]_{22} = [M_1]_{23} \cdot (c_r^2 - s_r^2) - s_r c_r \cdot ([M_1]_{22} - [M_1]_{33})$$

Or:

$$c = \cos\left(\frac{\pi}{4}\right) \cdot \sin\left(\frac{\pi}{4}\right) \cdot (p_1 - p_2) = \frac{1}{2}(p_1 - p_2)$$

An Example

For example, if we have the following coupling matrix from the Y-parameter synthesis approach:

$$[M_1] = \begin{bmatrix} 0 & 0.8210 & -0.5709 & 1 \\ 0.8210 & 5.4818 & 0 & 0.8210 \\ -0.5709 & 0 & -2.6511 & 0.5709 \\ 1 & 0.8210 & 0.5709 & 0 \end{bmatrix}$$

It can be transformed to folded coupling matrix:

$$[M_2]_{folded} = \begin{bmatrix} 0 & 1 & 0 & 1 \\ 1 & 2.8306 & 3.8122 & 0.3480 \\ 0 & 3.8122 & 0 & 0.9375 \\ 1 & 0.3480 & 0.9375 & 0 \end{bmatrix}$$

The coupling matrix is asymmetric and the two resonators will have to resonate at different f_0. Therefore, for $N = 2$ case, we need to transform the coupling matrix into a new topology. The new coupling matrix have to be symmetric looking from port 1 and port 2. In general, it may be represented by:

$$[M_3]_{full} = \begin{bmatrix} 0 & a' & b' & k \\ a' & p & c & b' \\ b' & c & p & a' \\ k & b' & a' & 0 \end{bmatrix}$$

while the original transversal coupling matrix will have the following form:

$$[M_1]_{trans} = \begin{bmatrix} 0 & a & -b & k \\ a & p_1 & 0 & a \\ -b & 0 & p_2 & b \\ k & a & b & 0 \end{bmatrix}$$

where:

With the rotation matrix:

$$[R] = \begin{bmatrix} 1 & 0 & 0 & 0 \\ 0 & \cos(\frac{\pi}{4}) & -\sin(\frac{\pi}{4}) & 0 \\ 0 & \sin(\frac{\pi}{4}) & \cos(\frac{\pi}{4}) & 0 \\ 0 & 0 & 0 & 1 \end{bmatrix}$$

We will have:

$$[M_3]_{full} = [R] \cdot [M_1]_{trans} \cdot [R]^t$$

The resultant matrix is:

$$[M_3]_{full} = \begin{bmatrix} 0.0000 & 0.9842 & 0.1768 & 1.0000 \\ 0.9842 & 1.4153 & 4.0664 & 0.1768 \\ 0.1768 & 4.0664 & 1.4153 & 0.9842 \\ 1.0000 & 0.1768 & 0.9842 & 0.0000 \end{bmatrix}$$

A4. Extraction of Source-load Coupling

A4.1 Extraction Formula

Let the frequency variable $s \to j\infty$, all the N-transversal resonator array will be short circuited, leaving only the source load admittance inverter M_{SL}, as shown in Fig. A4.1.
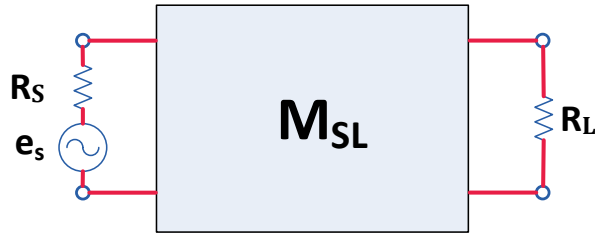
Fig A4.1 The circuit model containing only the source-load coupling in a transversal resonator array.

The input impedance or admittance should be:

$$Z_{11} = \frac{1}{M_{SL}^2} \ or \ Y_{11} = M_{SL}^2$$

Since:

$$\left.|S_{11}|\right|_{s=j\infty} = \frac{|1 - Y_{11}|}{|1 + Y_{11}|}$$

And

$$\left.|S_{21}|\right|_{s=j\infty} = \sqrt{1 - |S_{11}|^2} = \frac{2\sqrt{Y_{11}}}{1 + Y_{11}} = \frac{2M_{SL}}{1 + M_{SL}^2}$$

Therefore we can obtain that

$$M_{SL} = \pm \frac{1 - \sqrt{1 - |S_{21}|^2}|_{s=j\infty}}{\left.|S_{21}|\right|_{s=j\infty}}$$

A4.2 An EM Extraction Example

The source-load coupling structure in Fig. 2.16 is used as an example, which is re-drawn in Fig. A4.2 (a). The simulated |S21| is also shown in Fig. A4.2 (b). Notice

that in the simulation, the two resonators should be removed.
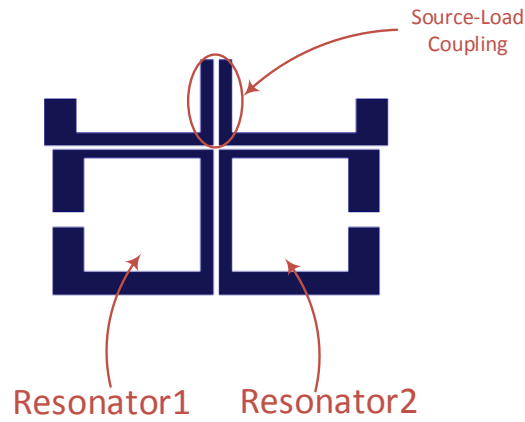
(a)
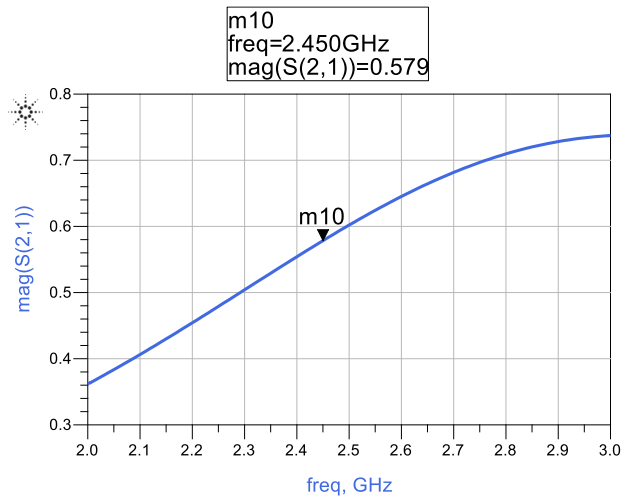
(b)

Fig. A2 (a) The layout of a microstrip source-load coupling structure. (b) Simulated |S21| of the structure (without Resonator 1&2)

The extracted source-load coupling will be:

$$m_{SL} = \frac{1 - \sqrt{1 - 0.579^2}}{0.579} = 0.31$$

A5. The inverse of block matrix

Suppose a block matrix M is defined as:

$$M = \begin{bmatrix} A & B \\ C & D \end{bmatrix}$$

Then its inverse can be represented as:

$$M^{-1} = \begin{bmatrix} A^{-1} + A^{-1}B(D - CA^{-1}B)^{-1}CA^{-1} & -A^{-1}B(D - CA^{-1}B)^{-1} \\ -(D - CA^{-1}B)^{-1}CA^{-1} & (D - CA^{-1}B)^{-1} \end{bmatrix}$$

If D = 0, we have:

$$M^{-1} = \begin{bmatrix} A^{-1} - A^{-1}B(CA^{-1}B)^{-1}CA^{-1} & A^{-1}B(CA^{-1}B)^{-1} \\ (CA^{-1}B)^{-1}CA^{-1} & -(CA^{-1}B)^{-1} \end{bmatrix}$$

A6. Correlation for mobile terminals and base stations

A6.1. Correlation for mobile terminals

Assume a plane wave impinge on the two-element array without mutual coupling as shown in Fig. A6.1. The field at antennas 1 and 2 can be written as: $E_1(\theta, \phi) = E_0(\theta, \phi)$ and $E_2(\theta, \phi) = E_0(\theta, \phi)e^{-jkd\cos\phi\sin\theta}$ [1].
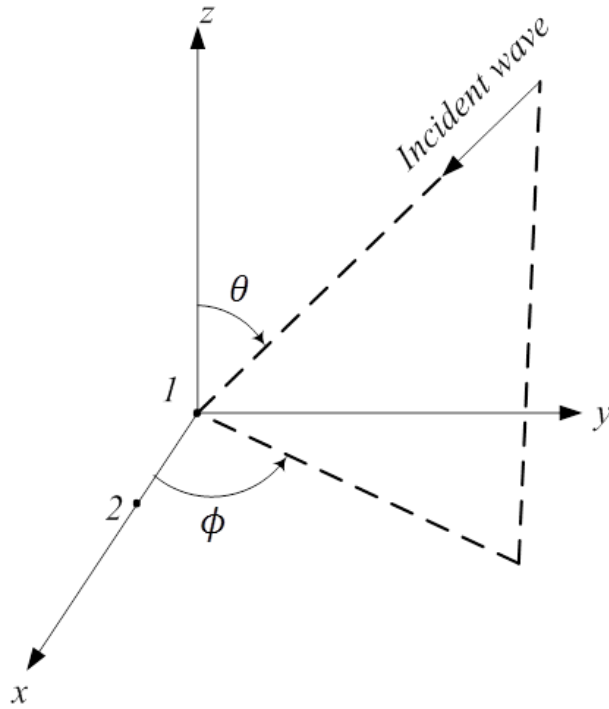
Fig. A6.1 A plane wave impinge on an ideal two-element array.

For ideal isotropic antennas, $E_0(\theta, \phi) = 1$. The complex correlation of two antennas can be expressed as:

$$\rho_{12}^m = \frac{\int_0^\pi \int_0^{2\pi} E_1(\theta,\phi)E_2^*(\theta,\phi)p(\theta,\phi)d\theta d\phi}{\sqrt{\int_0^\pi \int_0^{2\pi}|E_1(\theta,\phi)|^2 p(\theta,\phi)d\theta d\phi \cdot \int_0^\pi \int_0^{2\pi}|E_2(\theta,\phi)|^2 p(\theta,\phi)d\theta d\phi}} \qquad (A6.1)$$

With $E_0(\theta, \phi) = 1$ and $\int_0^\pi \int_0^{2\pi} p(\theta, \phi)d\theta d\phi = 1$, we have:

$$\rho_{12} = \int_0^\pi \int_0^{2\pi} e^{-jkd\cos\phi\sin\theta} p(\theta, \phi) d\theta d\phi \qquad (A6.2)$$

For 2D ideal case, we assume that $p(\theta) = \delta\left(\theta - \frac{\pi}{2}\right)$, we also assume uniform angular distribution in the azimuth plane: $p(\phi) = \frac{1}{2\pi}$, therefore, the classic Clarke's model [2] can be obtained as:

$$\rho_{12}^m = \int_0^{2\pi} \frac{1}{2\pi} \cdot e^{jkd\cos\phi} d\phi = J_0(kd) \qquad (A6.3)$$
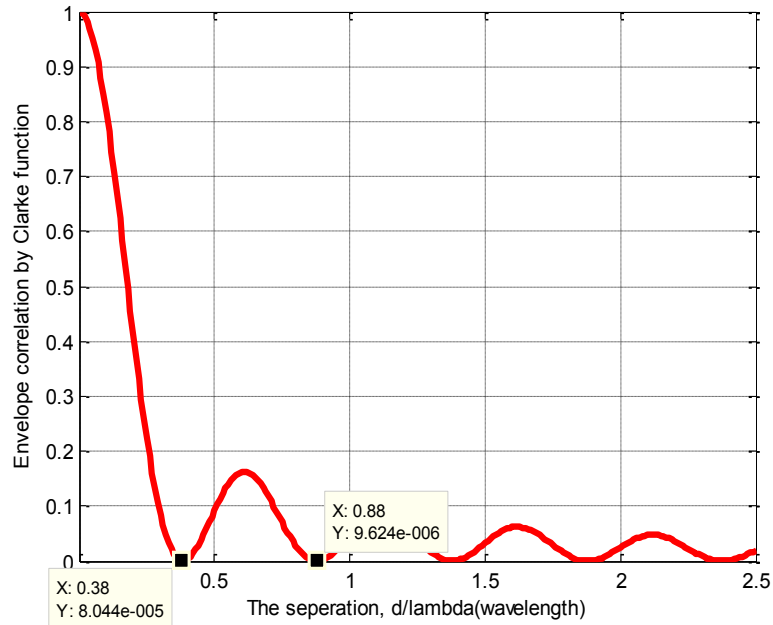
Fig. A6.2 Correlation by Clarke model.

The correlation with respect to different spacing d is plotted in Fig. A6.2. It should be noted that this figure only considers spatial correlation without inter-element mutual couplings.

For the extreme case, only one multipath is considered, we have:

$$p(\theta, \phi) = p(\theta)p(\phi) \qquad (A6.4)$$

222

and

$$\begin{cases} p(\theta) = \delta(\theta - \theta_0) \\ p(\phi) = \delta(\phi - \phi_0) \end{cases}$$ (A6.5)

Substituting (A6.4) and (A6.5) into (A6.2) yields:

$$\rho_{12}^0 = e^{-jkd\cos\phi_0 \sin\theta_0}$$ (A6.6)

Thus we have the magnitude of the correlation to be unity. This is because that incoming wave from one direction will encounter a constant phase difference at the two antennas that is coherent. As more waves coming from different directions, different phase differences will be introduced, the two signals will be de-correlated.

A6.2. Correlation for base stations

For base station antennas, the correlation can be written as:

$$\rho_{12}^b = \int_{\theta=-\pi/2}^{\pi/2} \int_{\phi=0}^{2\pi} e^{-jk_0 d\cos\phi \sin\theta} \, p(\theta)p(\phi)d\phi d\theta$$ (A6.7)

The incident waves are no longer uniformly distributed in the azimuth angle, which is illustrated in Fig. A6.3. Similar to the mobile terminal cases, the two dimensional distribution is assumed, $p(\theta) = \delta(\theta - \theta_0)$. We assume that the scatters around the mobile terminal can be modeled by the "Circular Scattering Model" depicted in Fig. A6.4.
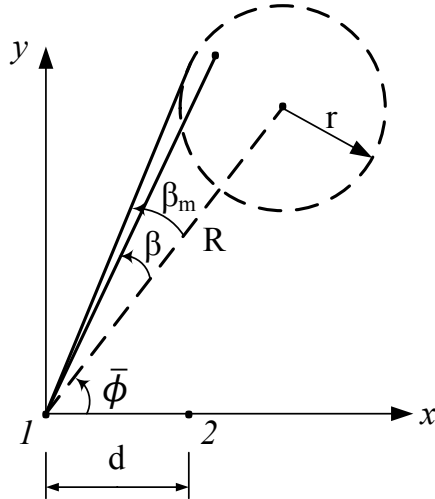
Fig. A6.3 The base station scenario.
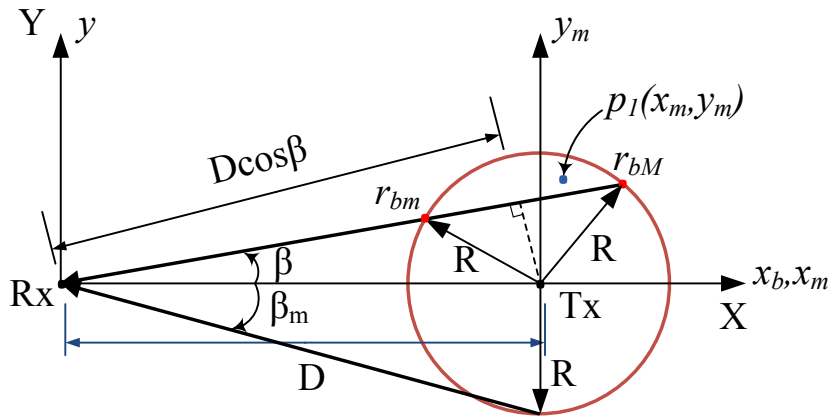
Fig. A6.4 Circular scattering model.

The angular distribution is:

$$p(\beta) = \frac{2b}{\pi} \cos\beta \sqrt{1 - b^2 \sin^2\beta}, \quad |\beta| \leq \beta_m \tag{A6.8}$$

With $b = \frac{R}{r} \gg 1$ and the maximum angular spread β_m should obey $b \sin\beta_m = 1$ because

$$\frac{1}{b} = \frac{r}{R} = \sin\beta_m \tag{A6.9}$$

Then (A6.7) can be written in the following form as:

$$\rho_{12}^b = \int_{\theta=-\pi/2}^{\pi/2} \int_{\phi=0}^{2\pi} e^{-jk_0 d\cos\phi\sin\theta}\, p(\theta)p(\phi)d\phi d\theta$$
$$= \int_{\beta=-\beta_m}^{\beta_m} e^{-jk_0 d\sin\theta_0 \cos(\bar{\phi}+\beta)} \frac{2b}{\pi} \cos\beta\sqrt{1-b^2\sin^2\beta}\, d\beta$$
$$\text{(A6.10)}$$

Without loss generality, we can further assume that $\bar{\phi} = \pi/2$, and let $\tau = b\sin\beta$, we have:

$$\rho_{12}^b = \frac{2}{\pi}\int_{\tau=-1}^{1} e^{\frac{jk_0 d\sin\theta_0\tau}{b}}\sqrt{1-\tau^2}d\tau \qquad\qquad \text{(A6.11)}$$

Since we already have $\sin\beta_m = \frac{1}{b}$. We can further simplify (A6.11) to

$$\rho_{12}^b = \frac{2}{\pi}\int_{\tau=-1}^{1} e^{jk_0 d\tau\sin\beta_m\sin\theta_0}\sqrt{1-\tau^2}d\tau \qquad\qquad \text{(A6.12)}$$

The integral can be calculated using Euler's equation and finally, we can obtain that:

$$\rho_{12}^b = 2\frac{J_1(k_0 d\sin\beta_m\sin\theta_0)}{k_0 d\sin\beta_m\sin\theta_0} \qquad\qquad \text{(A6.13)}$$

where $J_1(x)$ is the Bessel function of the first kind of order one.

The correlations with respect to different element spacing d and angle spread β are superposed in Fig. A6.5. It can be observed that with increased angular spread in incoming waves, the correlation can be reduced significantly.
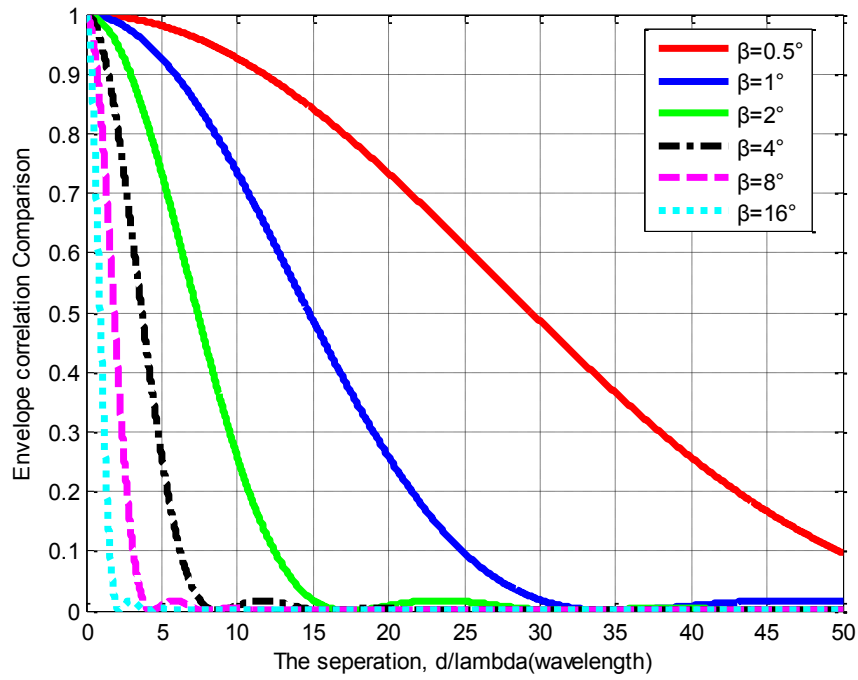
Fig. A6.5 Ideal Correlations w.r.t. different element spacing and angular spread in incoming waves by Circular scattering model.

A6.3. EM simulation verification

To verify the previously mentioned geometric models, we conduct several EM simulations for both the mobile terminal (MT) and base station (BTS) cases. In the EM simulator [3], we set a point source for excitation and several objects with certain dielectric constant as scattering objects, then, two groups of probes are used to obtain the E-field around two antennas with separation *D*. Three simulation cases are investigated for base station scenario as shown in Fig. A6.6.
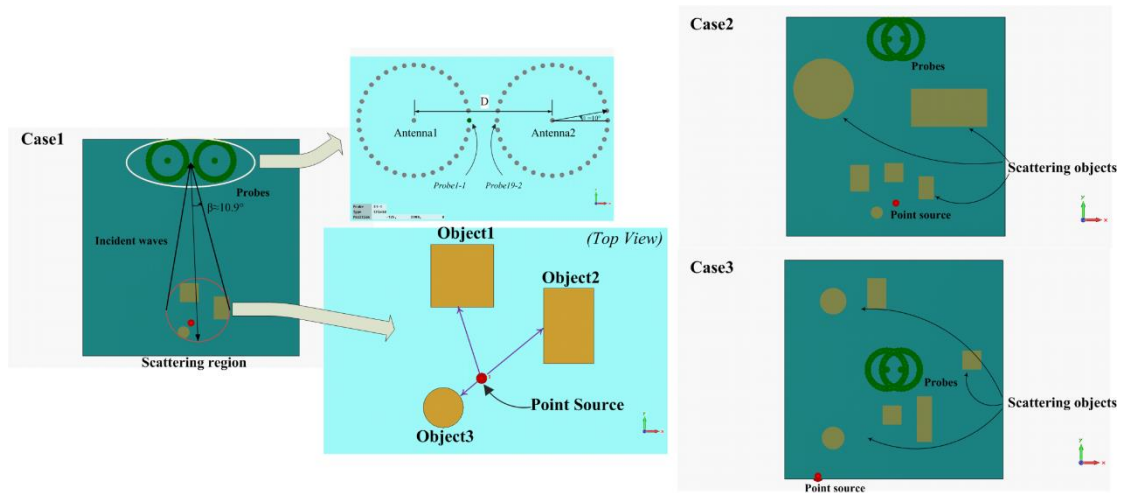
Fig. A6.6 Simulation cases in CST for investigating correlations.

▫ Case1: Small angular spread, only a few scatters.-(Macrocell)

▫ Case2: More scatters than case one, with two large obstacles.-(Microcell)

▫ Case3: Scatters locates around the antenna 1 and 2, which are not far from the source.-(Picocell)

In the simulation, we constrain that there are only one layer of meshes in the Z-axis, which emulates the 2D cases. The size of the simulation region is 10 meters by 10 meters, with PMLs on the boundary. The field distribution can be simulated and obtained. Precise field strength can be obtained by placing a filed probe at the specified coordinates. Simulated filed distributions for case 1 in Fig. A6.6 are shown in Fig. A6.7.
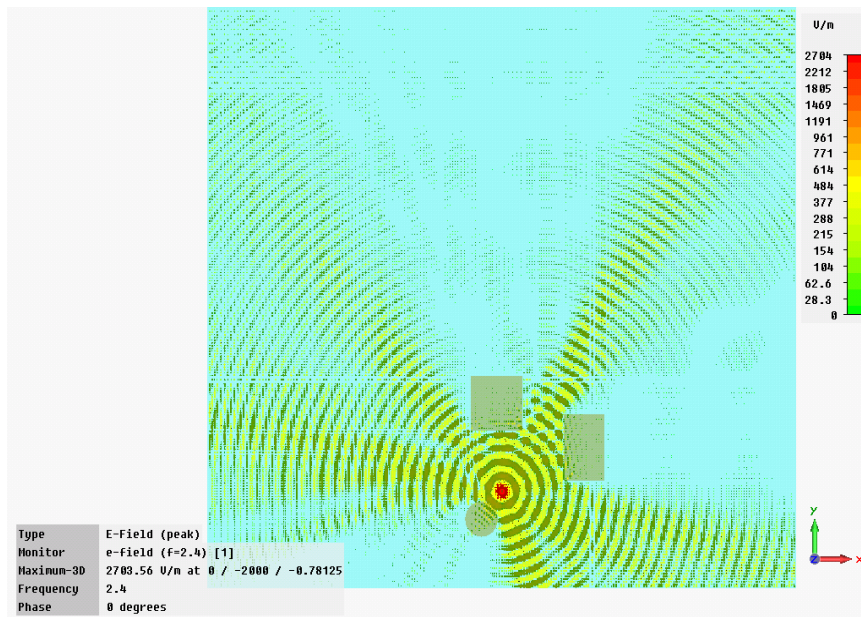
Fig. A6.7 E-Field distributions for Case1 in Fig. A6.6.

The simulated envelope correlations for the three cases are plotted and compared with the circular scattering model with different angular spread in Fig. A6.8. It can be seen that case 1 is similar to $\beta = 8°\sim10°$, case 2 is similar to $\beta = 12°$ and case 3 is similar to $\beta = 18°$, which is quite reasonable.
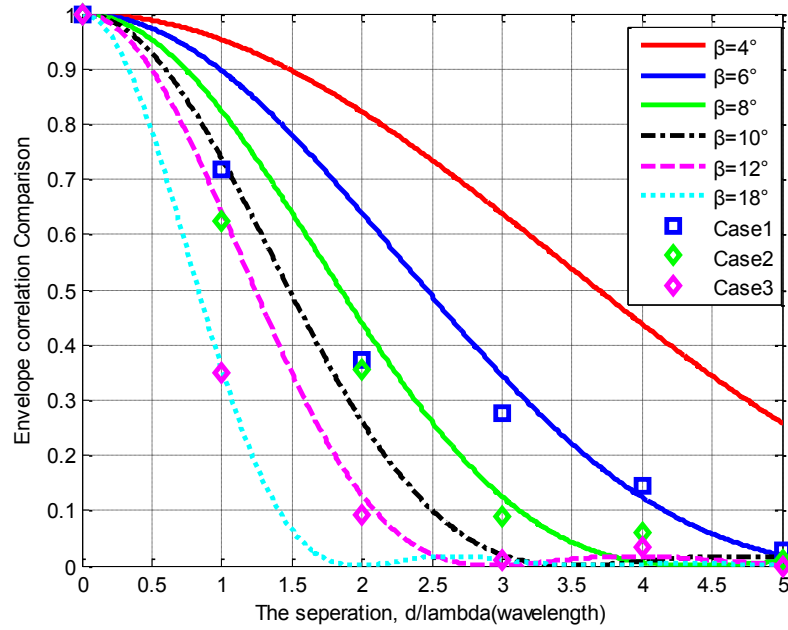
Fig. A6.8 The simulated envelope correlations for the three cases and the correlations calculated by (A6.13) w.r.t. different angular spread.

For the mobile terminal case, we build an indoor environment with scatters randomly located around the receiving antenna 1 and 2. The walls are included in the model with the following parameters:

$$\begin{cases} \epsilon' = 6 \\ tan\delta_c = 0.1 \end{cases}$$

The EM model and simulated field distribution are shown in Fig. A6.9.
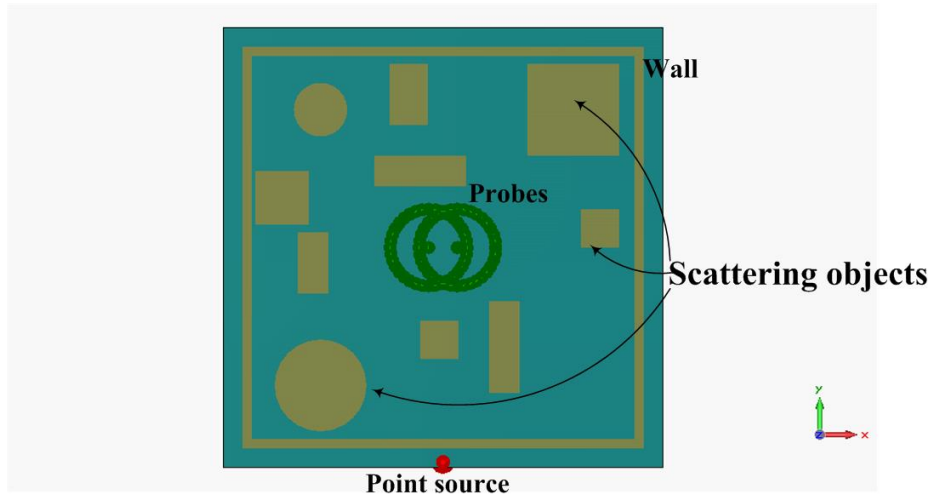
(a)
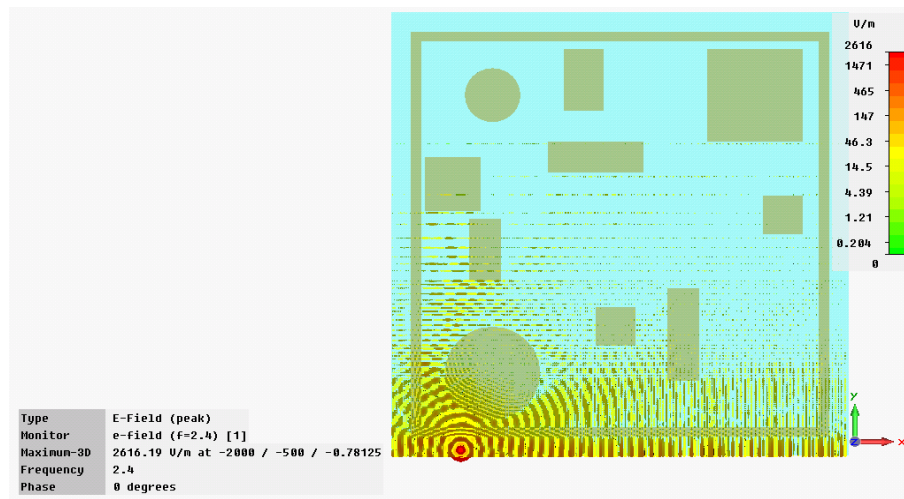
(b)

Fig. A6.9 (a) EM model set-up for indoor propagation simulation in CST. (b) Simulated E-field distribution.

The correlation coefficients are calculated with: $D = 0.25\lambda, 0.5\lambda, 1\lambda, 2\lambda, 3\lambda, 4\lambda$ and compared with the ideal Clarke's model in (A6.3) and shown in Fig. A6.10.
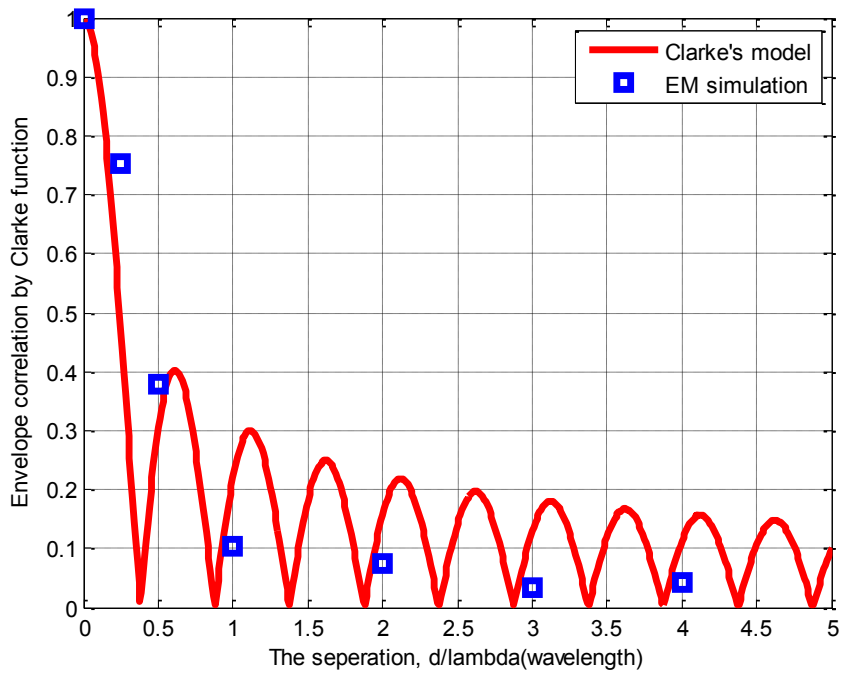
Fig. A6.10 Comparison between the ideal Clarke's model and EM simulated correlations.

Reference:

[1] R. Janaswamy, Radiowave Propagation and Smart Antennas for Wireless Communications. Boston, MA: Kluwer, 2001.

[2] R.H. Clarke, "A Statistical Theory of Mobile Radio Reception", Bell System Technical Journal, pp. 957-1000, 1966.

[3] CST MICROWAVE STUDIO, CST STUDIO SUITE Version 2010, CST Computer Simulation Technology AG.

Author's Publications

Journal papers

[J1] L. Zhao, L. K. Yeung, and K.-L. Wu, " A coupled resonator decoupling network for two-element compact antenna arrays in mobile terminals," *IEEE Trans. Antennas Propag.*, vol. 62, no. 5, pp. 2767-2776, May 2014.

[J2] L. Zhao and K.-L. Wu, "A Decoupling Technique for Four-element Symmetric Arrays with Reactively Loaded Dummy Elements," *IEEE Trans. Antennas Propag.*, vol. 62, no. 8, pp. 4416-4421, August 2014.

[J3] L. Zhao and K.-L. Wu, "A Cascaded Coupled Resonator Decoupling Network for Mitigating Interference between Two Radios in Adjacent Frequency Bands," *IEEE Trans. Microw. Theory Tech.*, to appear

[J4] L. Zhao and K.-L. Wu, "A Dual-band Coupled Resonator Decoupling Network for Two Coupled Antennas," *IEEE Trans. Antennas Propag.*, submitted.

[J5] K. Qian, L. Zhao and K.-L. Wu, "An LTCC Coupled Resonator Decoupling Network for Two Antennas of Same Frequency," *IEEE Trans. Microw. Theory Tech.*, submitted.

[J6] K. Qian, L. Zhao and K.-L. Wu, "An LTCC Coupled Resonator Decoupling Network for Two Antennas of Adjacent Frequency Bands," *IEEE Trans. Microw. Theory Tech.*, submitted.

Conference papers

[C1] L. Zhao, L. K. Yeung, and K.-L. Wu, "A novel second-order decoupling network for two-element compact antenna arrays," *Proc. Asia-Pacific Microwave Conf.,* Dec. 2012.

[C2] L. Zhao and K.-L. Wu, "A Broadband Coupled Resonator Decoupling Network for A Three-element Compact Array," *Proc. IEEE MTT-S Int. Microw. Sym.,* Jun. 2013.

[C3] L. Zhao and K.-L. Wu, "Decoupling of an Isosceles Triangular Three Element Array with One Reactively Loaded Dummy Element," *Proc. IEEE MTT-S Int. Microw. Sym.,* Jun. 2014.

[C4] L. Zhao and K.-L. Wu, "A Coupled Resonator Decoupling Network for In-Device Coexistence of Two Collocated Antennas," to be presented at *Asia-Pacific Microwave Conf.,* 2014.